

©2018

Nicholas V. Faenza

ALL RIGHTS RESERVED

CHEMICAL AND STRUCTURAL LIMITATIONS TO THE PRACTICAL UTILIZATION OF
HIGHLY DELITHIATED LAYERED OXIDE POSITIVE ELECTRODE MATERIALS

By

NICHOLAS VALENTINO FAENZA

A dissertation submitted to the

School of Graduate Studies

Rutgers, The State University of New Jersey

In partial fulfillment of the requirements

For the degree of

Doctor of Philosophy

Graduate Program in Materials Science and Engineering

Written under the direction of

Dr. Glenn G. Amatucci

And approved by

New Brunswick, New Jersey

May 2018

ABSTRACT OF THE DISSERTATION

CHEMICAL AND STRUCTURAL LIMITATIONS TO THE PRACTICAL UTILIZATION OF HIGHLY DELITHIATED LAYERED OXIDE POSITIVE ELECTRODE MATERIALS

By NICHOLAS VALENTINO FAENZA

Dissertation Director:

Dr. Glenn G. Amatucci

Minimizing the difference between the theoretical and practically obtained energy densities of layered oxide positive electrode materials is critical to increasing the energy density of Li-ion batteries. Currently, positive electrode materials are incapable of repetitively accessing the high states of charge necessary to approach the theoretical energy density. Primary factors limiting the operating potential of layered oxide positive electrodes include the structural degradation of the positive electrode material, parasitic reactions between the positive electrode and the liquid electrolyte, and the presence of surface impurity species.

Parasitic electrode-electrode reactions at high states of charge are investigated through an accelerated aging test developed using a thermally and electrochemically strenuous environment. In conjunction with accelerated aging testing, $\text{Li}[\text{Ni}_{0.8}\text{Co}_{0.15}\text{Al}_{0.05}]\text{O}_2$ (NCA) is used as a model positive electrode compound to study the chemical and structural stability of highly delithiated layered oxides in the presence of liquid electrolyte. Furthermore, the surface impurity species that develop on NCA upon ambient atmospheric exposure and their impact on the material's electrochemical performance is thoroughly evaluated. Synthesis and characterization of $\text{Li}_x\text{Co}_{1-y}\text{Al}_y\text{O}_2$ and $\text{Li}_x\text{Ni}_{1-y}\text{Al}_y\text{O}_2$ ($1 \geq x \geq 0$ and $0.2 \geq y \geq 0$) as well as $\text{Li}_x\text{Ni}_{0.8}\text{Co}_{0.2}\text{O}_2$ and $\text{Li}_x\text{Ni}_{0.8}\text{Co}_{0.15}\text{Al}_{0.05}\text{O}_2$ enables the determination of the specific roles that the layered oxide material's

transition metal chemistry has on its structural stability and cycling capabilities at and near full delithiation.

The results presented herein emphasize the importance of proper management of layered oxide positive electrode materials and propose handling procedures based on the formation mechanisms of critical surface impurity species. The surface and sub-surface structural decomposition of highly charged positive electrode materials in the presence of electrolyte causes substantial impedance growth and severe transition metal dissolution. Based on the investigation into these intricate electrode-electrolyte reaction mechanisms, strategies to minimize parasitic reactions and avoid degradation of the electrochemical performance are developed. Additionally, elucidated relationships between the material's transition metal chemistry and stability at high states of charge provide guidelines for designing new positive electrode materials intended to operate near full delithiation.

ACKNOWLEDGEMENT

I would like to express my sincere gratitude to my thesis advisor, Dr. Glenn G. Amatucci, for his extensive guidance and tutelage over the past few years. His unwavering support and patience fostered my instructional development and provided the foundation upon which I explored new ideas. The opportunities and ceaseless encouragement he has given me have enabled me to develop as a scientist and push myself beyond my preconceived potential.

I deeply appreciate my committee members, Dr. Frederic Cosandey, Dr. Dunbar Birnie, Dr. Philip Batson, and Dr. Charles Dismukes, for their dedication and guidance in my graduate development.

I would also like to thank all of the staff members of the ESRG: Ms. Fadwa Badway, Ms. Linda Sung, Ms. Anna Halajko, Ms. Irene Plitz, Ms. Kate Woodside, Mr. Barry Vanning, and Mr. John Gural for their assistance and support over the years. I would especially like to thank Drs. Nathalie Pereira and Kimberly Scott for being instrumental to my educational experience. I am grateful for the help provided to me by my fellow graduate students, Drs. Jonathan Ko, Anthony Ferrer, and Joshua Kim; and by all of our group's undergraduate students, particularly Lejandro Bruce.

I greatly appreciate NECCES, an Energy Frontier Research Center funded by the U.S. Department of Energy, Office of Science, Office of Basic Energy Sciences under Award No. DE-SC0012583 for providing the funding for this work.

The work in Chapter 3 was originally published as “Electrolyte-Induced Surface Transformation and Transition-Metal Dissolution of Fully Delithiated $\text{LiNi}_{0.8}\text{Co}_{0.15}\text{Al}_{0.05}\text{O}_2$,” N. V. Faenza, Z. W. Lebens-Higgins, P. Mukherjee, S. Sallis, N. Pereira, F. Badway, A. Halajko, G. Ceder, F. Cosandey, L. F. J. Piper, and G. G. Amatucci, *Langmuir*, **33**, 2017, pg. 9333-9353. Z. W. Lebens-Higgins, S. Sallis, and L. F. J. Piper performed all XPS and XAS experiments, while P. Mukherjee and F. Cosandey contributed the HRTEM and SAED characterization. F. Badway,

A. Halajko, and N. Pereira assisted in sample preparation and electrochemical analysis. G. Ceder provided useful discussions that helped interpret the results.

Chapter 4 is derived from the work published as “Growth of Ambient Induced Surface Impurity Species on Layered Positive Electrode Materials and Impact on Electrochemical Performance,” N. V. Faenza, L. Bruce, Z. W. Lebens-Higgins, I. Plitz, N. Pereira, L. F. J. Piper, and G. G. Amatucci, *Journal of the Electrochemical Society*, **164** (14), 2017, pg. A3727-A3741. All XPS and XAS experiments were conducted by Z. W. Lebens-Higgins and L. F. J. Piper. L. Bruce assisted with sample preparation and FTIR analysis, while I. Plitz contributed with interpretation of the FTIR results.

As of March 2018, the work presented in Chapter 5 is being prepared to be submitted for publication. A. Halajko performed the FESEM experiments, while P. Mukherjee and F. Cosandey conducted the STEM and EDS analysis. L. Bruce aided in the fabrication and preparation of the layered oxide materials. F. Badway, N. Pereira, and G. G. Amatucci contributed to the electrochemical characterization and analysis of the materials.

DEDICATION

This work is dedicated to my parents, Noel and Thomas Faenza, for their persistent love and support throughout my entire education. I am truly grateful for the sacrifices they made for me throughout my upbringing, which have enabled all of my accomplishments and the pursuit of this endeavor.

TABLE OF CONTENTS

ABSTRACT OF THE DISSERTATION	ii
ACKNOWLEDGEMENT	iv
DEDICATION	vi
TABLE OF CONTENTS.....	vii
LIST OF TABLES.....	x
LIST OF FIGURES	xii
1 INTRODUCTION	1
1.1 Motivation.....	1
1.2 Electrochemistry Basics.....	2
1.3 Lithium Ion Batteries	7
1.4 Positive Electrodes.....	9
1.5 Negative Electrodes	14
1.6 Electrolytes	17
1.6.1 Aqueous Electrolytes	18
1.6.2 Non-aqueous Liquid Electrolytes.....	20
1.6.3 Polymer/Gel Electrolytes	24
1.6.4 Solid-state Electrolytes	25
1.7 Important Topics.....	28
1.7.1 Failure Modes of Layered Oxide Electrodes	28
1.7.2 Bonding in Positive Electrode's at High States of Charge	30
1.7.3 Electrode-Electrolyte Interfacial Reactions	32
1.7.4 Positive Electrode Transition Metal Dissolution	34
1.8 $\text{LiNi}_{0.8}\text{Co}_{0.15}\text{Al}_{0.05}\text{O}_2$	36
1.9 Approach.....	37
2 EXPERIMENTAL TECHNIQUES.....	42
2.1 Introduction.....	42
2.2 Synthesis of Layered Oxide Materials	42
2.3 X-ray Diffraction (XRD)	44
2.4 Microcalorimetry	46
2.5 Thermogravimetric Analysis	49
2.6 Brunauer-Emmett-Teller (BET) Analysis.....	50
2.7 Karl Fischer (KF) Coulometric Titration.....	51
2.8 Inductively Coupled Plasma – Optical Emission Spectroscopy (ICP-OES).....	52
2.9 Fourier Transform Infrared Spectroscopy (FTIR)	52
2.10 Electrochemical Analysis.....	54

2.11	X-ray Photoelectron and Absorption Spectroscopies	56
2.12	Electron Microscopy and Associated Techniques	57
3	ELECTROLYTE INDUCED SURFACE TRANSFORMATION AND TRANSITION METAL DISSOLUTION OF FULLY DELITHIATED $\text{LiNi}_{0.8}\text{Co}_{0.15}\text{Al}_{0.05}\text{O}_2$	59
3.1	Abstract.....	59
3.2	Introduction.....	59
3.3	Experimental	64
3.3.1	Materials Preparation	64
3.3.2	Electrochemical Characterization	65
3.3.3	Physical Characterization.....	65
3.3.4	Operando Microcalorimetry.....	67
3.4	Results.....	68
3.4.1	Reaction Identification.....	68
3.4.2	Three-Electrode Electrochemical Analysis.....	81
3.4.3	Impact of Electrolyte Salt on Heat Flux and Impedance	88
3.4.4	Evolution of the Surface	93
3.4.5	Additional Studies.....	102
3.5	Discussion.....	110
3.6	Conclusion	118
3.7	Acknowledgement	119
3.8	Next Steps	120
4	GROWTH OF AMBIENT INDUCED SURFACE IMPURITY SPECIES ON LAYERED POSITIVE ELECTRODE MATERIALS AND IMPACT ON ELECTROCHEMICAL PERFORMANCE.....	121
4.1	Abstract.....	121
4.2	Introduction.....	121
4.3	Experimental.....	126
4.3.1	Materials Preparation	126
4.3.2	Electrochemical Characterization	127
4.3.3	Physical Characterization.....	127
4.4	Results.....	129
4.4.1	Effect of Atmosphere Exposure.....	129
4.4.2	Isolation and Analysis of Impurity Species	140
4.5	Discussion.....	161
4.6	Conclusion	166
4.7	Acknowledgements.....	167
4.8	Next Steps	167

5	STRUCTURAL EFFECTS ON THE ELECTROCHEMICAL PERFORMANCE OF HIGHLY DELITHIATED LAYERED OXIDE MATERIALS	169
5.1	Abstract.....	169
5.2	Introduction.....	169
5.3	Experimental.....	173
5.3.1	Materials Preparation	173
5.3.2	Electrochemical Characterization	174
5.3.3	Physical Characterization.....	175
5.4	Results.....	178
5.4.1	Overview of Materials	178
5.4.2	Group 1: $\text{LiCo}_{1-y}\text{Al}_y\text{O}_2$	183
5.4.3	Group 2: $\text{LiNi}_{1-y}\text{Al}_y\text{O}_2$	205
5.4.4	Group 3: 20% Substituted LiNiO_2	222
5.5	Discussion	239
5.5.1	Influence of Al	239
5.5.2	Influence of Co	242
5.5.3	Influence of Co and Al.....	243
5.5.4	Transition Metal – Oxygen Bonding at High States of Charge	243
5.5.5	Summary	248
5.6	Conclusions.....	251
5.7	Acknowledgements.....	252
6	CONCLUDING REMARKS	252
7	FUTURE WORK.....	255
7.1	Impact from Substitution with Mn and Other Transition Metals.....	255
7.2	Effect of Electrolyte Composition	255
7.3	Role of Positive Electrode Surface Coatings	256
	REFERENCES	257

LIST OF TABLES

Table 1-I: Commonly studied organic carbonates and esters for use as an electrolyte solvent. The material's structure and important properties are listed for comparison. The materials are arranged by whether they are cyclic (top) or acyclic (bottom).	21
Table 1-II: Promising ether materials for use as an electrolyte solvent in Li-ion batteries. The structure of each material is shown alongside the properties that are important to its performance in an electrochemical cell. The top three materials are acyclic while the remaining five materials are cyclic.	22
Table 1-III: Common Li salts, their structure and relevant properties are listed. More information on each salt, particularly related to the ionic conductivity can be found in publications by Ue and Mori, ⁵⁸ Linden, ¹⁶ and Schmidt et al. ⁶⁸	23
Table 1-IV: Some common chemistries for crystalline solid-state electrolytes are shown along with their corresponding ionic conductivities and a brief description of the material. More extensive descriptions of the perovskite ⁷³ , NASICON ⁷⁴ , thio-LISICON ⁷⁵ , crystalline ⁷⁶ , and garnet ⁷⁷ type materials can be found elsewhere.	26
Table 1-V: Various types of glassy (amorphous) solid state electrodes are listed with their ionic conductivities and a brief a brief description. Additional details on the LiPON, ⁷⁸ sulfide-based glass, ⁷⁹ glass and polymer composites, ⁸⁰ and glass-ceramics ^{81,82} materials are given elsewhere. .	27
Table 3-I: Surface area, Li ₂ CO ₃ content, and average discharge capacities for four variations of NCA. Measured surface area, and Li ₂ CO ₃ content for the four NCA variations are provided. After the constant voltage phase, cells were discharged at 5 mA/g to 2.7 V. The average discharge capacities after testing with either 1M LiPF ₆ or 1M LiBF ₄ in EC:DMC (1:1) are included.	104
Table 3-II: Co and Ni dissolution measurements from NCA determined by ICP-OES. * denotes that the minimum detection limit was reached, and that the listed value is the maximum possible.	108
Table 4-I: Provides the results for the working profile (R _{wp}), goodness of fit (GOF), calculated lattice parameters, and transition metal occupancies from Rietveld simulations on XRD scans of the initial NCA material as well as all baseline and annealed samples. The refined occupancy of Ni atoms in the Li layer is listed as "Ni (3a)," while those in the transition metal layer are denoted as "Ni (3b)."	131
Table 4-II: Quantitative results from KF, TGA, FTIR and electrochemistry experiments on all baseline and annealed materials. KF results are the cumulative ppm of H ₂ O, while the FTIR results are listed as an approximation of the peak area relative to the area of that scan's main PE peak. Some materials had insufficiently sized LiOH·xH ₂ O peaks to determine the relative peak area, and are labeled as "N/A." The % capacity loss results were calculated by using the maximum discharge capacity and the discharge capacity of the 50 th cycle. The % capacity loss for Ambient NCA was "N/A" when cycled to 4.2 V because the discharge capacity was negligible for all cycles, and the % capacity loss was 0.00 when charged to 4.5 V since the 50 th cycle also had the largest discharge capacity of the first 50 cycles. The discharge rate capacity retention data was obtained by dividing the discharge capacity of the 25 th cycle (150 mA/g) by the discharge capacity of the 24 th cycle (15 mA/g). Since Ambient NCA had no discharge capacity	

when cycled to 4.2 V, the capacity retention is listed as “N/A.” The average OCV values for all electrodes are listed in the rightmost column..... 137

Table 5-I: Reitveld calculated unit cell lattice parameters, Ni/Co occupancy, volume and % phase impurity from the overnight XRD scans shown in Figure 1. For the group 1 materials (blue rows) Co_3O_4 is the impurity phase, while $\gamma\text{-LiAlO}_2$ is the impurity phase for the group 2 (red rows) and 3 (green rows) materials. For each Reitveld calculation the weighted profile residual (R_{wp}) and goodness-of-fit (GOF) are provided in the two rightmost columns..... 181

Table 5-II: The OCV taken 1 h after charging finished, the final lithiation in the positive electrode and the % Ni/Co oxidation for each of the ex-situ XRD coin cells (Figure 5-9) are listed. The group 1 materials are shown in the blue rows, while the group 2 and 3 materials are shown in the red and green rows, respectively. The % Ni/Co oxidation was calculated from the measured charging capacity and the theoretical capacity assuming that Al is electrochemically inactive. . 193

Table 5-III: First cycle charge capacity, discharge capacity, and irreversible loss for each coin cell shown in Figure 5-11. The theoretical capacity (assuming Al is electrochemically active) is given for each material. 198

Table 5-IV: Ni and Co transition metal dissolution results determined by ICP-OES. Coin cells using each positive electrode material were charged to 4.75 V at 25 mA/g, held at a constant potential (4.75 V) for 10 h, all while in a 60°C incubator. In an Ar-filled glovebox the cells were disassembled, the negative electrode and adjacent separator were removed and then dissolved in an acidic solution. The Ni and Co concentration in the resulting solution was then measured by ICP-OES, and the average % Ni and % Co dissolution from each positive electrode material is presented. The % Ni and % Co dissolution from the baseline samples was below the instrument’s detection limit. 202

Table 5-V: First cycle charge capacity, discharge capacity, and irreversible loss for each coin cell shown in Figure 5-22. The theoretical capacity (assuming Al is electrochemically active) is given for each material. 219

Table 5-VI: First cycle charge capacity, discharge capacity, and irreversible loss for each coin cell shown in Figure 5-29. The theoretical capacity (assuming Al is electrochemically active) is given for each material. 235

Table 5-VII: For each positive electrode material, important structural and electrochemical results at 4.5 V and at full state of charge are given (4.75 V). The lithiation (x)/%TM oxidation results are from the ex-situ XRD samples, and the listed values are from the end of the potentiostatic hold at each potential. The OCV results are from the same cells and were taken 1 h after the charging commenced. The % change in the c parameter and unit cell volume results were calculated with the in-situ XRD results at 4.5 V and at the end of charge, while the Li^+ diffusivity data is from the PITT experiments shown in Figures 2, 7, and 13. * denotes a two phase transition between 4.5 and 4.75 V, and ** signifies that two phases were present simultaneously. 248

LIST OF FIGURES

Figure 1-1: The specific energy and power capabilities for various electrochemical energy storage systems are shown. Data for the internal combustion (IC) engine are provided for reference.⁴ 2

Figure 1-2: A schematic diagram of a simple electrochemical cell, called a Daniell cell. The cell consists of two electrodes (zinc and copper metals), an electrolyte solution, a separator and an external circuit.⁶ 4

Figure 1-3: A diagram explaining the operation of a Li-ion battery that consists of a graphite based negative electrode, and a LiCoO_2 positive electrode.¹⁰ 9

Figure 1-4: Approximations of the discharge potentials and specific capacities for various classes of positive and negative electrode materials. Experimentally determined ranges for (a) intercalation-based positive electrodes and (c) conversion-based negative electrodes are shown. The theoretical potentials and capacities for conversion-based positive electrodes are displayed in (b), while (d) presents an overview for all intercalation and conversion electrodes.¹¹ 11

Figure 1-5: An illustration of the CoO_6 -octahedra and Li atoms from a crystal structure of layered ($R\bar{3}m$) LiCoO_2 .¹⁵ 14

Figure 1-6: Potential curves (vs. Li/Li^+) for a graphite electrode at various C-rates. The following rates were tested; 0.2C (2nd cycle), 1C (5th cycle), 5C (10th cycle), 10C (15th cycle), 15C (20th cycle), and 20C (25th cycle). For all cycles the cell was charged at a constant current (C/5) and a 1M LiPF_6 EC:DMC (1:1) electrolyte was used.³³ 15

Figure 1-7: Discharge capacity versus cycle number for Si-C-composite (top) and graphite-based (bottom) negative electrodes. For each electrode material, two binder compositions with different chemistries were employed.³⁹ 16

Figure 1-8: Possible Li-ion electrode materials for aqueous batteries. The potentials for H_2 and O_2 evolution are shown as a function of pH relative to both the neutral hydrogen electrode (NHE) and the Li/Li^+ redox potential.⁵⁴ 19

Figure 2-1: Schematic diagram of the coin cell holder, heat flux sensor and electrochemical leads of a MMC 274 Nexus multimode calorimeter is shown.¹⁵² 47

Figure 3-1: Voltage and current profiles as a function of time for NCA and SP/PVdF-HFP half-cells that were charged to and held at the upper cutoff potential while at 60°C. The upper cutoff potential was either 4.1, 4.5, or 4.75 V. Voltage and current data is scaled according to the left and right axes, respectively. 70

Figure 3-2: Heat flux and electrochemical measurements from an operando microcalorimetry experiment of an LCO half-cell as it was charged to and held at 4.75 V, while isothermal at 30°C. The heat flux (black), temperature (red), voltage (green), and current (blue) data are each scaled according to an individual axis. 71

Figure 3-3: Heat flux (black) and electrochemical (blue and green) measurements from an operando microcalorimetry experiment of an NCA half-cell as it was charged to and held at 4.75 V. The NCA cell was charged to 4.75 V, and held at constant potential while the temperature (red) was incrementally stepped up from 30°C to 45°C to 60°C. 73

Figure 3-4: LCO microcalorimetry cell charged to 4.75 V, and held at constant potential while the temperature was incrementally stepped up from 30°C to 45°C to 60°C. The heat flux (black), temperature (red), voltage (green), and current (blue) data are each scaled according to an individual axis.	74
Figure 3-5: Heat flux (black) and electrochemical (blue and green) measurements from an operando microcalorimetry experiment of an NCA half-cell as it was charged to and held at 4.75 V. The NCA cell was charged to 4.75 V, and held at constant potential while the temperature (red) was incrementally stepped up from 30°C to 45°C to 60°C.	75
Figure 3-6: (a) General and (b) enhanced view of selected impedance scans from the 4.75 V potentiostatic segment of the microcalorimetry test shown in Figure 3-3.	76
Figure 3-7: Comparison of XRD results of the pristine powder (black) and the positive electrodes before (red) and after (blue) exothermic reactions at 4.75 V and 60°C for NCA. The peaks associated with the layered (<i>R3m</i>) structure are indexed for the pristine material.	77
Figure 3-8: Comparison of XRD results of pristine powder (black) and positive electrodes before (red) and after (blue) exothermic reactions at 4.75 V and 60°C for LCO. The O3 and O1 structures are indexed when appropriate. The peaks associated with the layered (<i>R3m</i>) structure are indexed for the pristine material.	78
Figure 3-9: SEM images of Li negative electrodes (a) before and (d) after exothermic reactions. Corresponding Ni (b,e) and Co (c,f) EDS measurements taken from the (b-c) pre-exotherm and (e-f) post-exotherm Li negative electrodes. Noted areas of the negative electrodes were scraped to remove any products deposited on the surface, thereby creating an internal standard for baseline Ni and Co concentrations.	79
Figure 3-10: XRD plot of a Li foil negative electrode retrieved from an NCA microcalorimetry cell after testing at 4.75 V and 60°C. The main Li, Ni and Co metal peak locations are marked by a black circle, red diamond, and blue asterisk, respectively. For each phase the main peaks are indexed according to the listed space groups.	80
Figure 3-11: Three-electrode electrochemical cells with an NCA positive, Li metal negative, and a (a) Ag metal quasi-reference or a (b) $\text{Li}_x\text{V}_2\text{O}_5$ reference electrode. The cell potential was charged to 4.75 V (vs. Li negative electrode) at 25mA/g and then held at 4.75 V at 60°C. The positive and negative electrode potentials are each relative to the reference electrode, while the cell potential is the difference between the positive and negative electrodes. The cell (black), positive (red) and negative (blue) potentials are scaled according to the left axis, while the current (green) is correlated to the right axis. The three-electrode cells in figures (a) and (b) were identically made, except for the reference electrode used.	82
Figure 3-12: Nyquist plots taken at the beginning (solid lines) and end (dotted lines) of the three-electrode experiments. Scans were taken between the working – reference (black), counter – reference (red), and working – counter (blue) electrodes. All scans were taken at 60°C. The final working – reference scan (black dotted line) is only partially visible in the inset graph. This scan intersects the x-axis at approximately 8 ohms higher than the initial scan, suggesting a slight increase in the electronic impedance. The final working –reference scan reaches the Warburg impedance at roughly the same impedance as the initial scan.	85

- Figure 3-13: A three-electrode electrochemical cell with an NCA positive, Li metal negative, and a $\text{Li}_x\text{V}_2\text{O}_5$ reference electrode. The cell potential was charged to 4.75 V (vs. Li negative electrode) at 25mA/g and then held at 4.75 V at 60°C. The positive and negative electrode potentials are each relative to the reference electrode, while the cell potential is the difference between the positive and negative electrodes. The cell (black), positive (red) and negative (blue) potentials are scaled according to the left axis, while the current (green) is correlated to the right axis. 87
- Figure 3-14: Nyquist plots taken at the beginning (solid lines) and end (dotted lines) of the three-electrode experiments. Scans were taken between the working – reference (black), counter – reference (red), and working – counter (blue) electrodes. All scans were taken at 60°C. 88
- Figure 3-15: (a) Heat flux and (b) current profiles for microcalorimetry experiments of NCA half-cells made with 1M LiPF_6 (black) and 1M LiBF_4 (red) salt in EC:DMC (1:1) solvent. Cells were charged to 4.75 V at 25mA/g and held potentiostatically, while the temperature of the microcalorimeter was changed from 30°C to 45°C to 60°C. 89
- Figure 3-16: Selected scans from Nyquist plots of NCA microcalorimetry electrodes at 4.75 V, 60°C with either 1M (a) LiPF_6 or (b) LiBF_4 salt in EC:DMC (1:1). A visual representation of the R1, R2, and R3 values measured for the 229 h Nyquist plot of the LiBF_4 sample is shown in (b). 90
- Figure 3-17: R1, R2, and R3 impedance values extracted from the LiPF_6 (black) and LiBF_4 (red) impedance spectra in Figure 3-16 are plotted versus time in figures (a), (b), and (c), respectively. Note the differences in the scale of the y axis. 92
- Figure 3-18: (a) TEY O K-edge spectra of 2 week exposed (dashed lines) and pristine (solid lines) NCA powder. (b) TEY O K-edge spectra of powder electrodes of pristine and 2 week exposed NCA that were charged to and held at 4.75 V, and then discharged to 2.7 V while in a 60°C incubator. All measurements were taken on beamline I09 at DLS. 94
- Figure 3-19: (a,c) TEY O K-edge and (b,d) Ni L_3 -edge XAS spectra taken at ALS for NCA samples before (red) and after (green) exothermic reactions. Samples with electrolyte containing LiPF_6 are shown in (a-b) and those with LiBF_4 are presented in (c-d). All figures show reference spectra of “NiO” (black) and of NCA charged to 4.75 V at room temperature (blue). 95
- Figure 3-20: O K-edge (a,c) and Ni L-edge (b,d) PFY measurements taken at ALS of NCA charged to 4.75 V at room temperature (blue), pre-exotherm (red), and post-exotherm NCA (green) with either LiPF_6 (a-b) or LiBF_4 (c-d) salts. 96
- Figure 3-21: (a) P 2p XPS spectra for NCA electrodes with LiPF_6 and (b) B 1s spectra for identical samples with LiBF_4 salt. NCA electrodes charged to 4.75 V at room temperature are shown in blue, while pre-exotherm (10 h hold) and post-exotherm (295 h hold) samples are displayed in red and green, respectively. 97
- Figure 3-22: A HRTEM image of the (a) pristine, uncycled NCA material, and enhanced HRTEM images of the (b) sub-surface and (d) surface structure are provided. FFT images taken along the $[241]_{\text{Trigonal}}$ zone axis corresponding to figures (b) and (d), are shown in (c) and (e), respectively. Both of the surface and sub-surface have a layered ($R3m$) structure. 99

Figure 3-23: (a-b) HRTEM images of the surface and subsurface regions of NCA aged in LiPF_6 at 4.75 V, 60°C for 10 h. The surface region in (a) is enhanced and shown in (b). (c) FFT and (d) SAED of the surface layer are also provided. The SAED image (d) is indexed with a zone axes of either $[-110]_{\text{layered}}$ or $[121]_{\text{spinel}}$ in images (e) and (f), respectively. 100

Figure 3-24: (a-b) HRTEM images of NCA particles aged in LiBF_4 at 4.75 V, 60°C for 10 h. SAED figures corresponding to surfaces (c) 1, (d) 2, and (e) 3 in image (b) are provided. Additional rows of weak reflections in (c) are indicative of the formation of the spinel phase. . 101

Figure 3-25: Current (solid lines) and accumulated capacity (dotted lines) comparison for NCA microcalorimetry coin cells (black) and incubator (red) coin cells. All cells were charged to 4.75 V at 25mA/g, and then held at 4.75 V under potentiostatic conditions. As previously described, the microcalorimetry cells were subjected to dynamic and isothermal conditions, while the coin cells in the incubator were isothermal at 60°C for the entirety of the test. 103

Figure 3-26: Comparison of the current from the parasitic reactions for 0.12 wt% Li_2CO_3 , 0.46 m^2/g (black), 0.82 wt% Li_2CO_3 (blue), 0.24 wt% Li_2CO_3 , 7.40 m^2/g (red), and 1.74 wt% Li_2CO_3 , 7.40 m^2/g (green) NCA materials when using (a) LiPF_6 or (b) LiBF_4 salt in a EC:DMC (1:1) solvent. All samples were charged at 25 mA/g to 4.75 V, and then held potentiostatically at 4.75 V in a 60°C incubator. 106

Figure 4-1: Intermittent (a) temperature and (b) relative humidity measurements collected during baseline NCA exposure to various atmospheres. Pristine NCA was stored in an Ar-filled glovebox in our laboratory, as such, the temperature history should be similar to that of Ambient NCA. Additionally, since Pristine and CO_2 NCA were stored in exceedingly dry gases the relative humidity for both materials is assumed to be negligible. 129

Figure 4-2: XRD scans of (a) the initial NCA material, as well as (b) Pristine, (c) Ambient, (d) Dryroom, and (e) CO_2 NCA. Each scan was performed on a powder sample that was sealed in an Ar-filled glovebox to prevent subsequent atmospheric exposure. The $R3m$ layered oxide peaks are indexed for the initial NCA material. 130

Figure 4-3: FTIR spectra of the (a) Pristine, (b) Ambient, (c) dryroom, and (d) CO_2 baseline materials as well as (e) Li_2CO_3 and (f) LiOH reference materials. A break in the x-axis was included to emphasize the regions with relevant peaks. In contrast to the samples presented in Figure 4-4, none of these materials were mixed with PE. Additional spectra, taken with 1,000 scans instead of 250, show the effect of annealing at 150°C on (g) Ambient and (h) CO_2 NCA. In all spectra the Li_2CO_3 , $\text{LiOH}\cdot x\text{H}_2\text{O}$ and H_2O peaks are denoted by red stars, blue caret, and green exclamation points, respectively. The exact composition of $\text{LiOH}\cdot x\text{H}_2\text{O}$ cannot be determined because the visible peak is very broad and has low intensity. 132

Figure 4-4: FTIR measurements of the (a) Pristine, (b) Ambient, (c) Dryroom and (d) CO_2 baseline materials mixed with 26 wt% PE. The spectra focus on the Li_2CO_3 (red star), PE (black dot), and hydroxyl (blue caret) peaks in the ranges of 750 to 1650 cm^{-1} , and 3550-3850 cm^{-1} . Both absorbance ranges for the FTIR spectra are normalized to the size of each spectrum's 2912 cm^{-1} PE peak. Mass loss curves from (e) TGA and the moisture content from cumulative (f) KF experiments on Pristine (black), Ambient (red), Dryroom (blue) and CO_2 (green) NCA baseline materials are also presented. TGA experiments had 2 h isothermal holds at 150°C, 350°C, and 500°C to systematically remove H_2O , LiHCO_3 , and LiOH , respectively. The fourth and final isotherm, at 750°C, lasted 4 h and measured the mass loss from Li_2CO_3 decomposition. 134

Figure 4-5: TGA mass loss curves during heating, isothermal, and cooling segments in dry air for Pristine (black) and Ambient (red) NCA. Samples were tested identically to previously described TGA experiments, except that they were also cooled to 30°C at 5°C/min after completing the heating and isothermal segments. The part of each mass loss curve that correlates to heating or cooling is labeled for clarity. 136

Figure 4-6: Comparison of the discharge capacities as a function of cycle number for all four baseline materials. Electrodes were charged to an upper cutoff potential of either (a) 4.2 V or (b) 4.5 V. Cells were charged at 20 mA/g to V_{\max} (4.2 V or 4.5 V), held under potentiostatic conditions until the current dropped below 10 mA/g and then discharged to 2.75 V at -15 mA/g. Starting on the 6th cycle, and every 19 cycles afterwards, the cells were discharged at -150 mA/g instead of -15 mA/g. All of the cycling was done in a temperature controlled chamber set at 24°C. 138

Figure 4-7: First cycle voltage profiles for Pristine (black), Ambient (red), Dryroom (blue), and CO₂ (green) NCA electrodes cycled with an upper cutoff potential of 4.5 V. Electrodes were charged at 20 mA/g to 4.5 V, and then held at 4.5 V until the current dropped below 10 mA/g before being discharged at 15 mA/g to 2.75 V. 140

Figure 4-8: Plots of the (a) a and (b) c lattice parameters, and (c) cell volume as determined by Rietveld analysis of XRD scans of each annealed sample. The calculated parameters for the baseline materials are shown as having an anneal temperature of 24°C. 142

Figure 4-9: FTIR data showing the normalized 870 cm⁻¹ carbonate peak area as a function of the baseline material and annealing conditions. Carbonate peak intensities are normalized to the area of the 2912 cm⁻¹ PE peak in each scan, and show the changes in the LiHCO₃/Li₂CO₃ content as a result of annealing. 144

Figure 4-10: Quantification of H₂O, LiHCO₃, LiOH, and Li₂CO₃ contents as determined by TGA. The surface impurity mass loss results of the baseline and annealed samples for Pristine, Ambient, Dryroom, and CO₂ NCA materials are displayed in panels (a-d), respectively. The magnitude of the H₂O (black square), LiHCO₃ (red circle), LiOH (green upward triangle), and Li₂CO₃ (blue inverted triangle) contents were determined by the mass loss from the 20-150°C, 150-350°C, 350-500°C, and 500-750°C regions, respectively. 146

Figure 4-11: Comparison of the FTIR spectra from baseline and post-TGA versions of (a) Pristine and (b) Ambient NCA. The post-TGA scans show no carbonate (red star), hydroxide or moisture peaks (green exclamation point), indicating their complete removal during the TGA experiment. None of the samples were mixed with PE. 148

Figure 4-12: Li₂CO₃ mass loss determined by TGA measurements on 750°C annealed Pristine NCA. The solid bars show experiments where the 150°C, 350°C, and 500°C isothermal temperature segments were systematically removed to isolate the temperature range where Li₂CO₃ develops. All TGA experiments used heating rates of 5°C/min and were run with flowing dry air. The white and black patterned bar shows the Li₂CO₃ mass loss from an experiment using a specialty dry air gas with no CO₂ (<0.1 ppm), and was tested according to the standard TGA procedure (black bar). 151

Figure 4-13: KF coulometry results for all anneals of (a) Pristine, (b) Ambient, (c) Dryroom, and (d) CO₂ NCA. Results from the measured moisture content of the first test (black) and the cumulative result from successive experiments (red) are provided. Note that the scale of the

measured H₂O axis varies significantly between samples. All KF samples were prepared and sealed in an Ar-filled glovebox to prevent atmospheric exposure. 152

Figure 4-14: XPS spectra of the (a) O 1s region for select samples and (b) the percent composition of surface and lattice oxygen for Pristine NCA and all Ambient materials. The amount of surface and lattice oxygen were determined by the relative intensities of the higher binding energy peaks (530-533 eV) and NCA (529 eV) peaks. Peak intensities of the spectra in the (a) are normalized to the size of the NCA peak. The peak locations from a Li₂CO₃ reference and NCA are denoted by vertical bars. (c-d) show the Ni 2p, Co 3p, and Li 1s regions for the same samples shown in (a). For reference, the Ni 2p region of a NiO reference material is displayed in (c). 154

Figure 4-15: (a) The XPS O 1s spectra of Pristine NCA and all Ambient exposed materials. The approximate LiHCO₃/Li₂CO₃ and LiOH regions are shown by the horizontal green and black brackets, respectively. The LiOH peak position is based on previous work by Dupin et. al.²¹⁷ (b) A comparison of the O 1s region for Ambient NCA, 150°C annealed Ambient NCA, and a Li₂CO₃ reference material is provided. The expected peak locations for Li₂CO₃ and NCA are denoted by vertical bars, while the approximate location for LiOH is indicated by a horizontal bracket. 155

Figure 4-16: Discharge capacity vs. cycle number for cells made with positive electrodes of (a) 150°C, (b) 350°C, (c) 500°C, and (d) 750°C annealed Pristine and Ambient NCA materials. All cells were cycled at 24°C by charging to V_{max} (4.2 or 4.5 V) at 20 mA/g, holding at constant voltage until the current fell below 10 mA/g, and then discharging at 15 mA/g to 2.75 V. Starting on the 6th cycle and every 19 cycles afterwards, the cells were discharged at 150 mA/g instead of 15 mA/g. (e) The 50th cycle discharge capacity as a function on annealing temperature for all Pristine and Ambient materials is provided. A breakdown of the surface impurity species on Ambient exposed materials as a function of anneal, and the total impurity species on Pristine materials is shown in part f. 157

Figure 4-17: The voltage profiles of the 1st and 50th cycles from cells cycled to 4.5 V for (a) all baseline materials, and annealed (b) Pristine and (c) Ambient materials. All cells were charged at 20 mA/g to 4.5 V, held at constant voltage until the current dropped below 10 mA/g, and then discharged at 15 mA/g to 2.75 V. Starting on the 6th cycle and every 19 cycles afterwards the cells were discharged at 150 mA/g. All of the cells shown here were discharged at 15 mA/g. 160

Figure 5-1: Representative FESEM images of cNCA and LiNi_{0.8}Co_{0.15}Al_{0.05}O₂ particles at a magnification of (a-b) 40 KX and (c-d) 84.6 KX. Both materials were coated with a thin Au layer to prevent charging by the electron beam. 179

Figure 5-2: Overnight powder XRD scans of all fabricated and commercial materials are shown according to group number in (a-c), respectively. All XRD scans were measured over of a two theta range of 15-70° at a scan rate of 0.08 °/min under ambient lab conditions. The peaks associated with the layered (*R3m*) structure are indexed, while the peaks corresponding to the impurity phase are denoted by a *. 180

Figure 5-3: Reitveld calculated a (black) and c (blue) lattice parameters for the (a) the synthesized LiCo_{1-y}Al_yO₂ and (b) the LiNi_{1-y}Al_yO₂ materials from the XRD scans shown in Figure 1. LiNi_{0.8}Al_{0.2}O₂ (DO) is excluded because the disordered structure gave distorted lattice parameters. All lattice parameters were calculated based on an *R3m* unit cell. 182

Figure 5-4: The (a) voltage (black) and differential charge (blue) profiles from the first charge of coin cells that were cycled at a constant current of 5 mA/g between 4.75 – 2.75 V are shown for all group 1 materials. Duplicate cells were cycled under PITT conditions (10 mV steps, 1 mA/g current cutoff) and the resulting first cycle (b) voltage (black) and current (blue) profiles, and (c) the voltage (black) and diffusivity (blue) plots of each material are also presented. The red boxes in the three graphs denote the theoretically inaccessible lithiation regions based on the amount of transition metals that can be electrochemically oxidized in each material. 184

Figure 5-5: In-situ XRD contour plots of the (003) peak and corresponding electrochemical profiles for (a) cLCO, (b) LiCoO₂, (c) LiCo_{0.95}Al_{0.05}O₂, (d) LiCo_{0.9}Al_{0.1}O₂, and (e) LiCo_{0.8}Al_{0.2}O₂. Cells were charged at a constant current of C/50 to 4.75 V, and then held at a constant potential indefinitely, all while 1 h XRD scans were continuously running. To avoid missing any features, the experimental parameters were chosen such that $\Delta x \leq 0.02$ for every scan. A red dashed line corresponding to when the potential reached 4.75 V is superimposed on each sub-figure to enable easy comparison between materials. 187

Figure 5-6: Calculated (a) c and (b) a lattice parameters as a function of delithiation for the in-situ XRD experiments of cLCO (black), LiCoO₂ (red), LiCo_{0.95}Al_{0.05}O₂ (blue), LiCo_{0.9}Al_{0.1}O₂ (green), and LiCo_{0.8}Al_{0.2}O₂ (orange) positive electrodes. Lattice parameters were calculated from a rhombohedral unit cell using the peak locations of the (003) and (101) peaks. Note that a break was included in the y-axis of (b). 189

Figure 5-7: The % change of the c and a lattice parameters relative to the unit cell parameters of the material in OCV was calculated as a function of lithiation. The calculations are based on the c and a lattice parameters derived from the in-situ XRD experiments. (a-c) Shows the % change of the c parameter for the group 1-3 materials, while the % change of the a parameter are presented in (d-f). 190

Figure 5-8: Ex-situ XRD scans of positive electrodes that were charged to 4.75 V under PITT conditions (10 mV step, 1 mA/g cutoff). Results are presented in the regions of the (003) (18-21.5°) and (104) (42-47°) peaks for cLCO (black), LiCoO₂ (red), LiCo_{0.95}Al_{0.05}O₂ (blue), LiCo_{0.9}Al_{0.1}O₂ (green), and LiCo_{0.8}Al_{0.2}O₂ (orange). All coin cells were disassembled in an Ar-filled glovebox and the XRD samples were sealed with a Kapton film to temporarily prevent hydrogen intercalation upon exposure to ambient atmosphere. 191

Figure 5-9: Voltage vs. lithiation profiles for coin cells made with each positive electrode material. Cells were charged under PITT conditions (10 mV step, 1 mA/g current cutoff) in a 24°C incubator. The charging profiles for group 1, 2, and 3 electrode materials are shown in (a), (b), and (c). 192

Figure 5-10: Operando isothermal microcalorimetry voltage (black) and heat flux (blue) measurements are presented during the first cycle for each group 1 material. Coin cells were cycled at a constant current (25 mA/g) between 4.75 V and 2.75 V, while the chamber was isothermal at 30°C. 195

Figure 5-11: Discharge capacity vs. cycle results for coin cells charged to either (a) 4.5 V or (b) 4.75 V. Cells were charged at 20 mA/g to V_{\max} (4.5 or 4.75 V), held at a constant potential until the current dropped below 10 mA/g, and were then discharged at 10 mA/g to 2.75 V, all at room temperature. Duplicate cells of each positive electrode material were made to ensure reproducibility. 197

Figure 5-12: The voltage vs. capacity curves of the 1st, 5th, 10th and 15th cycles from a 4.75 V cycling cell is shown for (a) C. LCO, (b) LiCoO₂, (c) LiCo_{0.95}Al_{0.05}O₂, (d) LiCo_{0.9}Al_{0.1}O₂, and (e) LiCo_{0.8}Al_{0.2}O₂. Each cell was charged to 4.75 V at 20 mA/g, held at 4.75 V until the current went below 10 mA/g, and then was discharged at 10 mA/g to 2.75 V, all at room temperature. 200

Figure 5-13: The % discharge capacity retention during cycling for cells charged to 4.5 V (a-c) and 4.75 V (d-f). The results for the (a, d) group 1, (b, e) group 2, and (c, f) group 3 materials are presented. The % capacity retention was calculated by normalizing the discharge capacity of each cycle to the cell's first cycle discharge capacity. 201

Figure 5-14: The current profiles for all of the ICP-OES coin cells listed in Table I. The group 1, 2 and 3 materials are shown in (a), (b), and (c), respectively, while the reference materials are presented in (d). Cells were charged to 4.75 V at a constant current (25 mA/g), and then held at constant potential (4.75 V) for 10 h, all while in a 60°C incubator. Some cells show a temporary increase in current at the beginning of the potentiostatic segment, but the current was never above 25 mA/g for more than 1 data point (10 sec). 204

Figure 5-15: (a) The (a) voltage (black) and differential charge (blue) profiles from the first charge of coin cells that were cycled at a constant current of 5 mA/g between 4.75 – 2.75 V are shown for all group 2 materials. Duplicate cells were cycled under PITT conditions (10 mV steps, 1 mA/g current cutoff) and the resulting first cycle (b) voltage (black) and current (blue) profiles, and (c) the voltage (black) and diffusivity (blue) plots of each material are also presented. The red boxes in the three graphs denote the theoretically inaccessible lithiation regions based on the amount of transition metals that can be electrochemically oxidized in each material. 205

Figure 5-16: (a) A HAADF image of a representative LiNi_{0.8}Al_{0.2}O₂ (DO) particle and EDS maps of the (b) Ni, (c) Al, and (d) Ni and Al signals is shown. A similar HAADF image and EDX maps are given for LiNi_{0.8}Al_{0.2}O₂ (O) in (e-h), respectively. The EDS images show relatively poor Ni and Al mixing for LiNi_{0.8}Al_{0.2}O₂ (DO) and a homogenous distribution for LiNi_{0.8}Al_{0.2}O₂ (O)... 208

Figure 5-17: In-situ XRD contour plots of the (003) peak and corresponding electrochemical profiles for (a) LiNiO₂, (b) LiNi_{0.95}Al_{0.05}O₂, (c) LiNi_{0.9}Al_{0.1}O₂, (d) LiNi_{0.8}Al_{0.2}O₂ (O), and (e) LiNi_{0.8}Al_{0.2}O₂ (DO). Cells were charged at a constant current of C/50 to 4.75 V, and then held at constant potential indefinitely, all while 1 h XRD scans were continuously running. To avoid missing any features, the experimental parameters were chosen such that $\Delta x \leq 0.02$ for every scan. A red dashed line corresponding to when the potential reached 4.75 V is superimposed on each sub-figure to enable easy comparison between materials. 210

Figure 5-18: Visualizations of the Reitveld calculated crystal structures for (a, d) NiO₂ fit to C2/m, (d, e) NiO₂ fit to R3m, and (c, f) CoO₂ fit to P-3m1 are shown. For each structure, images with (a-c) and without (d-f) the transition metal octahedra are provided. Oxygen, Ni and Co atoms are represented by red, maroon, and pink balls, respectively. All structures are oriented so that the a axis (red line) is directed to the left, and the b axis (green line) is indirectly positioned towards the reader. 212

Figure 5-19: Calculated (a) c and (b) a lattice parameters as a function of delithiation for the in-situ XRD experiments of LiNiO₂ (black), LiNi_{0.95}Al_{0.05}O₂ (red), LiNi_{0.9}Al_{0.1}O₂ (blue), LiNi_{0.8}Al_{0.2}O₂ (O) (green), and LiNi_{0.8}Al_{0.2}O₂ (DO) (orange) positive electrodes. Lattice parameters were calculated from a rhombohedral unit cell using the peak locations of the (003) and (101) peaks. 213

Figure 5-20: Ex-situ XRD scans of positive electrodes that were charged to 4.75 V under PITT conditions (10 mV step, 1 mA/g cutoff). Results are presented in the regions of the (003) (18-21.5°) and (104) (42-47°) peaks for LiNiO₂ (black), LiNi_{0.95}Al_{0.05}O₂ (red), LiNi_{0.9}Al_{0.1}O₂ (blue), LiNi_{0.8}Al_{0.2}O₂ (O) (green), and LiNi_{0.8}Al_{0.2}O₂ (DO) (orange). All coin cells were disassembled in an Ar-filled glovebox and the XRD samples were sealed with a Kapton film to temporarily prevent hydrogen intercalation upon exposure to ambient atmosphere. 215

Figure 5-21: Operando isothermal microcalorimetry voltage (black) and heat flux (blue) measurements are presented during the first cycle for each group 2 material. Coin cells were cycled at a constant current (25 mA/g) between 4.75 V and 2.75 V, while the chamber was isothermal at 30°C. 217

Figure 5-22: Discharge capacity vs. cycle results for coin cells charged to either (a) 4.5 V or (b) 4.75 V. Cells were charged at 20 mA/g to V_{max} (4.5 or 4.75 V), held at a constant potential until the current dropped below 10 mA/g, and were then discharged at 10 mA/g to 2.75 V, all at room temperature. Duplicate cells of each positive electrode material were made to ensure reproducibility. 218

Figure 5-23: The voltage vs. capacity curves of the 1st, 5th, 10th and 15th cycles from a 4.75 V cycling cell is shown for (a) LiNiO₂, (b) LiNi_{0.95}Al_{0.05}O₂, (c) LiNi_{0.9}Al_{0.1}O₂, (d) LiNi_{0.8}Al_{0.2}O₂ (O), and (e) LiNi_{0.8}Al_{0.2}O₂ (DO). Each cell was charged to 4.75 V at 20 mA/g, held at 4.75 V until the current went below 10 mA/g, and then was discharged at 10 mA/g to 2.75 V, all at room temperature. 221

Figure 5-24: The (a) voltage (black) and differential charge (blue) profiles from the first charge of coin cells that were cycled at a constant current of 5 mA/g between 4.75 – 2.75 V are shown for all group 3 materials. Duplicate cells were cycled under PITT conditions (10 mV steps, 1 mA/g current cutoff) and the resulting first cycle (b) voltage (black) and current (blue) profiles, and (c) the voltage (black) and diffusivity (blue) plots of each material are also presented. The red boxes in the three graphs denote the theoretically inaccessible lithiation regions based on the amount of transition metals that can be electrochemically oxidized in each material. 223

Figure 5-25: In-situ XRD contour plots of the (003) peak and corresponding electrochemical profiles for (a) LiNiO₂, (b) LiNi_{0.8}Co_{0.2}O₂, (c) LiNi_{0.8}Al_{0.2}O₂ (O), (d) LiNi_{0.8}Co_{0.15}Al_{0.05}O₂, and (e) cNCA. Cells were charged at a constant current of C/50 to 4.75 V, and then held at constant potential indefinitely, all while 1 h XRD scans were continuously running. To avoid missing any features, the experimental parameters were chosen such that $\Delta x \leq 0.02$ for every scan. A red dashed line corresponding to when the potential reached 4.75 V is superimposed on each sub-figure to enable easy comparison between materials. 228

Figure 5-26: Calculated (a) c and (b) a lattice parameters as a function of delithiation for the in-situ XRD experiments of LiNiO₂ (black), LiNi_{0.8}Co_{0.2}O₂, LiNi_{0.8}Al_{0.2}O₂ (O)(blue), LiNi_{0.8}Co_{0.15}Al_{0.05}O₂ (red)(green), and cNCA (orange) positive electrodes. Lattice parameters were calculated from a rhombohedral unit cell using the peak locations of the (003) and (101) peaks. 229

Figure 5-27: Ex-situ XRD scans of positive electrodes that were charged to 4.75 V under PITT conditions (10 mV step, 1 mA/g cutoff). Results are presented in the regions of the (003) (18-21.5°) and (104) (42-47°) peaks for LiNiO₂ (black), LiNi_{0.8}Co_{0.2}O₂ (red), LiNi_{0.8}Al_{0.2}O₂ (O) (blue), LiNi_{0.8}Co_{0.15}Al_{0.05}O₂ (green), and cNCA (orange). All coin cells were disassembled in an Ar-filled

glovebox and the XRD samples were sealed with a Kapton film to temporarily prevent hydrogen intercalation upon exposure to ambient atmosphere. 231

Figure 5-28: Operando isothermal microcalorimetry voltage (black) and heat flux (blue) measurements are presented during the first cycle for each group 3 material. Coin cells were cycled at a constant current (25 mA/g) between 4.75 V and 2.75 V, while the chamber was isothermal at 30°C. 233

Figure 5-29: Discharge capacity vs. cycle results for coin cells charged to either (a) 4.5 V or (b) 4.75 V. Cells were charged at 20 mA/g to V_{\max} (4.5 or 4.75 V), held at a constant potential until the current dropped below 10 mA/g, and were then discharged at 10 mA/g to 2.75 V, all at room temperature. Duplicate cells of each positive electrode material were made to ensure reproducibility. 234

Figure 5-30: The voltage vs. capacity curves of the 1st, 5th, 10th and 15th cycles from a 4.75 V cycling cell is shown for (a) LiNiO₂, (b) LiNi_{0.8}Co_{0.2}O₂, (c) LiNi_{0.8}Al_{0.2}O₂ (O), (d) LiNi_{0.8}Co_{0.15}Al_{0.05}O₂, and (e) C. NCA. Each cell was charged to 4.75 V at 20 mA/g, held at 4.75 V until the current went below 10 mA/g, and then was discharged at 10 mA/g to 2.75 V, all at room temperature. 237

Figure 5-31: (a) Charge and (b) discharge capacities vs. cycle # results for coin cells with LiCo_{0.8}Al_{0.2}O₂ positive electrodes. Cells were made with either 1M LiPF₆ EC:DMC (1:1) (black), or 1M LiBF₄ EC:DMC (1:1) (red). Electrodes were charged at 20 mA/g to 4.75 V, held at a constant potential until the current dropped below 10 mA/g, and were then discharged at 10 mA/g to 2.75 V, all while at room temperature. Duplicate cells with each electrolyte were made to ensure reproducibility. 241

1 INTRODUCTION

1.1 Motivation

Improvements in clean energy storage systems are critical to the successful development of technologies that reduce fossil fuel dependence and improve quality of life. Major sectors dependent upon advanced energy storage technologies include transportation, portable electronics, and electrical utilities. Each application has unique energy requirements, but current energy storage technologies are generally incapable of meeting future demands in each of these sectors. Particularly, the cost efficiency, safety, and specific and volumetric energy densities of modern energy storage systems must be advanced and improved to support commercial development without unduly tarnishing the environment.^{1,2} Traditional clean energy storage systems like flywheels, compressed air, and pumped water storage are mature technologies, but they often suffer from low efficiencies, high costs, and poor response times.³ Consequently, recent research efforts have focused upon advancing a variety of electrochemical storage systems to better meet the stringent energy requirements of future technologies.

Specific energy and power densities for common electrochemical systems are presented in Figure 1-1. Electrochemical capacitors demonstrate exceptional power performance and lifetimes, which is attributed to their high surface areas and use of double-layer capacitance (instead of material conversion from one redox state to another). Electrochemical capacitors thus excel in high rate applications, but they are limited by modest energy storage capabilities.^{2,3} Conversely, fuel cells – which draw electrical power from irreversible chemical reactions – have very high energy densities, but often inadequate rate capabilities. Batteries, however, generally balance both specific power and energy density needs.² Lithium (Li)-ion batteries, in particular, are the only electrochemical energy storage system of those depicted in Figure 1-1 capable of simultaneously delivering 100 Wh/kg, and 100 W/kg. As a result, Li-ion batteries are currently

used in the majority of rechargeable portable electronic devices and power the rapidly growing industry of electric vehicles.¹

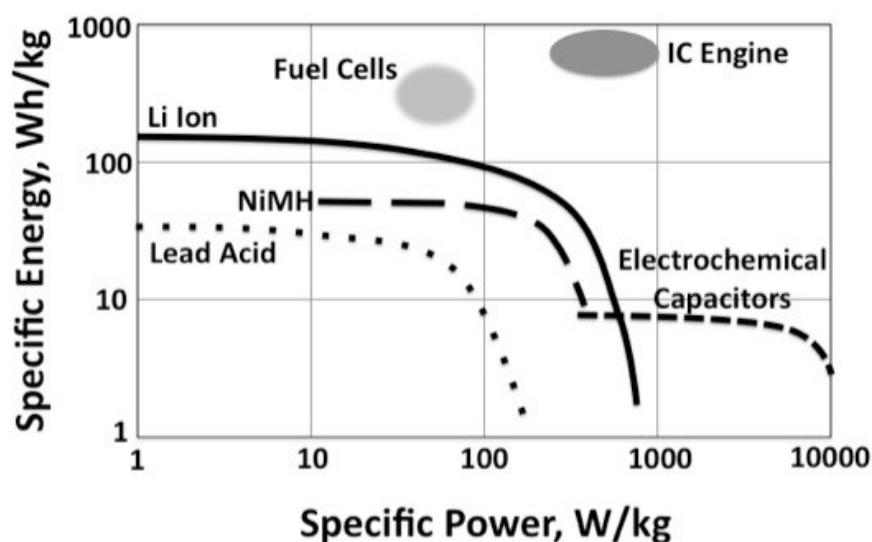


Figure 1-1: The specific energy and power capabilities for various electrochemical energy storage systems are shown. Data for the internal combustion (IC) engine are provided for reference.⁴

Despite the advantages that Li-ion batteries have over other clean energy storage methods, current battery technologies also struggle to satisfy the requirements of new generations of portable electronic devices and electric vehicles. Like other clean energy storage systems, Li-ion batteries need substantial advancements in relative cost, safety, energy density, and environmental impact to support effective current and future use.^{1,5} In order to assertively address Li-ion battery deficits, however, one must first understand the deficits' origin. This work focuses upon furthering the understanding of the failure mechanisms prevalent in current Li-ion batteries such that new materials and strategies can be intelligently designed and successfully developed.

1.2 Electrochemistry Basics

Electrochemistry is a subset of chemistry that encompasses the relationship between electrical and chemical phenomena, where an electrical input results in a chemical change or visa

versa. This work will specifically focus upon electrochemical energy storage, particularly of secondary (rechargeable) Li-ion batteries.

Electrochemical energy storage devices, generally, are designed to store electrical energy within chemical changes such that the stored energy can be subsequently accessed by inducing chemical state changes in the material or device. In their simplest state, electrochemical devices consist of four active components: a positive electrode, negative electrode, electrolyte and separator. The energy stored by these systems is used to power an external circuit, which is directly connected to the electrodes in the device. As shown in Figure 1-2, the systems are constructed in a manner where both electrodes are in direct contact with the electrolyte, but a porous partition (separator) prevents the two electrodes from contacting each other. Oxidation and reduction reactions with the electrolyte induce chemical changes to the positive and negative electrodes that enable the device to store energy in the form of a chemical charge separation. The electrolyte and the porous separator enable ionic transfer from one electrode to the other, but are sufficiently electrically insulating to force the electron transfer to happen via the external circuit.

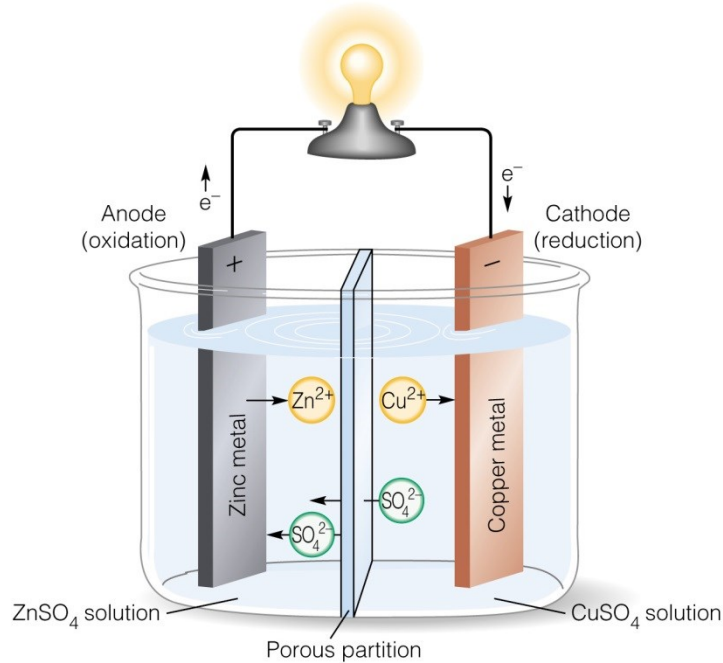


Figure 1-2: A schematic diagram of a simple electrochemical cell, called a Daniell cell. The cell consists of two electrodes (zinc and copper metals), an electrolyte solution, a separator and an external circuit.⁶

The electric potential of the cell is derived from the chemical potential of each electrode when in a shared electrolyte. In the Daniell cell shown in Figure 1-2, the chemical potential of the Zn and Cu metals are equivalent to the sum of the chemical potential of their metal ions in the solution and in the electrode as well as the chemical potential of the electrons in each metal electrode. The resulting equation (Equation 1-1) for each metal (M) is shown below, where μ is the chemical potential, n is the number of electrons involved in the oxidation of the metal, and e denotes an electron:

$$\text{Equation 1-1:} \quad \mu_M = \mu_{M^{n+}} + n\mu_e^M$$

Since the chemical potential of the electrons in the Cu electrode (μ_e^{Cu}) are different from those in the Zn electrode (μ_e^{Zn}) a chemical potential gradient is developed between the two electrodes. When the two electrodes are electronically connected, this in turn creates an electric potential (E). The magnitude of E is related to the change in free energy (ΔG) of the reaction, as shown in Equation 1-2:

Equation 1-2:
$$\Delta G = -nFE$$

F in Equation 1-2 is Faraday's constant, which is the amount of charge in each mole of electrons with units of "Farads." This relationship, of the cumulative equilibrium voltage between two electrodes, is further delineated in the Nernst equation (Equation 1-3), which additionally incorporates the effects of ionic concentrations and temperature:

Equation 1-3:
$$E_{cell} = E^o - \frac{RT}{nF} \ln(Q_r)$$

In the Nernst equation, E^o represents the standard cell potential, R is the universal gas constant, T is the temperature (in Kelvins) and Q_r is the reaction quotient. Q_r is dependent upon the activities of all of the reactants and products. Simply put, the potential of an electrochemical cell is the difference in the potentials of each electrode, as shown in Equation 1-4.

Equation 1-4:
$$E_{cell}^o = E_{positive}^o - E_{negative}^o$$

In summary, the electrochemical cell's voltage is the difference between the electromotive forces of two electrodes and is directly related to the Gibbs free energy difference between the two electrodes.⁷

It is important to note, however, that E_{cell}^o is the electric potential of the cell at equilibrium and not under dynamic conditions. E_{cell}^o can be measured by the open circuit voltage (OCV) when the electrochemical cell is at equilibrium. In open circuit conditions, measurement of the cell's potential is assumed to use an infinitesimal current that has a negligible effect upon the reactants activities and thus does not perturb the equilibrium potential, E_{cell}^o . When non-negligible changes are made to the cell, the Nernst equation (Equation 1-3) is used to determine the cell's actual potential (E_{cell}). Since inducing current causes the development of concentration gradients which affect the activities of the reaction's reactants and products, the potential of the cell will differ from the equilibrium voltage. The greater the magnitude of the current that is applied to the cell, the larger the potential deviation from E_{cell}^o will be. The difference between E_{cell} and E_{cell}^o is often referred to as the "overpotential" or "underpotential" depending upon

whether E_{cell} is larger or smaller than E_{cell}^o . Thus, practical cycling conditions always produce a deviation in the cell's potential away from the equilibrium potential, but this deviation is minimized with relatively small cycling currents.

In electrochemistry, “capacity” is a measure of the relative accumulated charge necessary to take the cell (or an electrode) from one state to another. Capacity is usually the amount of charge (mAh) normalized to the mass (g), and thus to the number of moles, of the active material. While the capacity of an electrode could be normalized to other factors such as volume, in this work all capacity values are related to the material's active mass, and units of mAh/g (specific capacity) are used. When electrical energy is added to an electrochemical cell, the amount of capacity necessary to go from an initial to a predetermined “charged” state is called the “charging capacity.” Similarly, when the cell provides electrical work on an external circuit, the magnitude of capacity required to transform from the “charged” to a “discharged” state is referred to as the “discharging capacity.”

Two other important terms in electrochemical energy storage are “power” and “energy.” In general, power is a measure of the rate in which work is being done. Electrical power, though, is specifically defined as the rate that electrical energy is transferred. This latter definition is more applicable to this work. As shown by Equation 1-5, electrical power (measured in Watts) is simply the rate that current (I) flows multiplied by the voltage (V).

$$\text{Equation 1-5:} \quad P = IV$$

Electrical energy (U_E) can then be expressed as the integral of the electrical power as a function of time. Furthermore, if the power is constant over a period of time, then energy is just the power multiplied by time (Equation 1-6).

$$\text{Equation 1-6:} \quad U_E = \int_{t_1}^{t_2} P(t)dt \approx Pt$$

To enable easy comparison between different systems, both a system's power and energy are often normalized to the system's mass or volume; the resulting values are, respectively, referred to as specific energy/power and energy/power density.

In many electrochemical systems, the rate at which an electrode is charged or discharged is described as the "C-rate." The C-rate is simply "C" divided by how many hours are required to fully charge or discharge the electrode. For example, if an electrode requires 2 hours to discharge, the C-rate would be $C/2$, whereas if only 15 min (0.25 h) were necessary the C-rate would be $4C$. In most practical applications the average discharging rate for an electrode is low ($< 1C$) because the device is generally designed to be able to provide power over multiple hours of operation. Rates greater than $1C$ are often considered to be high, but are investigated to gain an understanding of the high rate capabilities of an electrochemical cell.

1.3 Lithium Ion Batteries

Li-ion batteries are electrochemical cells where lithium ions are transferred between the positive and negative electrodes during operation. All of the previously described electrochemical principles are applicable to Li-ion batteries. While Li-ion technology is found in both primary (irreversible) and secondary (reversible) batteries; the low mass, relatively high diffusivity, and the large electrochemical potentials of many lithium based compounds make Li-ions particularly desirable in high performance secondary batteries. Similar to the previously described Daniell cell (Figure 1-2), Li-ion batteries consist of a positive electrode, negative electrode, electrolyte and separator.

While there are numerous Li-ion battery technologies, the most common systems use layered oxide ($R\bar{3}m$) positive electrodes, graphite-based negative electrodes, and a non-aqueous electrolyte.³ As will be described in more detail in section 1.6, non-aqueous electrolytes are preferentially used instead of aqueous electrolytes because of their increased stability against both oxidation and reduction. Similarly, fluorinated electrolyte salts are frequently used because of

their high electrochemical stability and relatively fast ionic conductivities.⁸ A schematic of an electrochemical cell utilizing these materials is shown in Figure 1-3, where a separator (not shown) is placed between the positive and negative electrodes. The separator is generally a porous membrane that permits Li-ion transport via the electrolyte from one electrode to the other and prevents the two electrodes from contacting each other (which would short-circuit the cell).⁹ A cell potential is generated from the difference in electrochemical potentials between the positive (LiCoO_2) and negative (graphite) electrodes. The potential of each electrode is dependent upon its state of lithiation, which changes as Li ions are shuttled through the electrolyte from one electrode to the other during operation.

When *charging* the cell, an external potential oxidizes the positive electrode material and releases a Li ion into the electrolyte to maintain charge neutrality. Simultaneously, the negative electrode is reduced and a Li ion from the electrolyte is intercalated into the graphite material. As the Li ions are shuttled through the cell, an equivalent number of electrons flow via an external circuit and recombine with the Li ions on the electrodes. Then, as the battery is *discharged*, the reactions occur in reverse. In other words, the negative electrode is oxidized, causing a Li ion to enter the electrolyte solution, and subsequently another Li ion is reduced on the positive electrode.¹⁻³ These highly reversible reactions enable Li-ion secondary batteries to be a practical source of repetitive energy storage. The flow of electrons that transverse the external circuit provide electrical work on the circuit and are what gives the electrochemical cell its practical functionality.



Figure 1-3: A diagram explaining the operation of a Li-ion battery that consists of a graphite based negative electrode, and a LiCoO_2 positive electrode.¹⁰

Lithium ion batteries are complex systems that need to balance a variety of factors, such as energy density, cost, safety and societal impact. As a result, a vast amount of research and development has been performed on these systems over the past half-century, and has resulted in the discovery and investigation into an extensive list of materials for each of the system's functional components. More detailed reviews of previous and current Li-ion battery systems can be found in the following sections and elsewhere.^{1,5,9,11-13}

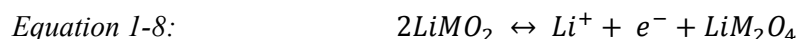
1.4 Positive Electrodes

Materials suitable for positive electrodes in Li-ion batteries can generally be designated to operate via an intercalation or conversion reaction mechanism.¹ Li-ion intercalation-based electrodes operate through a “topotactic” reaction mechanism, where the Li ions are inserted and removed from the material with only minimal changes to the crystal structure.^{14,15} To maintain charge neutrality, as each Li atom leaves the positive electrode another atom within the positive electrode is oxidized. This type of reaction is considered to be a single phase reaction and an example reaction is shown in Equation 1-7, where LiMO_2 and $\text{Li}_{1-x}\text{MO}_2$ share the same crystallographic structure.



Most intercalation-based electrodes have a transition metal atom present in the structure, which can be easily oxidized or reduced between two or more valence states, enabling a low energy barrier for Li^+ intercalation into and out of the structure.^{15,16} Since the host structure is stable with or without any Li ions present, generally only small structural changes are observed during lithiation and delithiation.^{14,17,18}

While an ideal intercalation-based electrode would have only single phase transitions during lithiation/delithiation, it is common for “intercalation” electrodes to have some two phase reactions. During these two phase reactions, two distinct crystallographic phases are simultaneously present and as the chemistry of the system changes, one of the phases is converted to the other. An example of this reaction is provided by *Equation 1-8*, where $LiMO_2$ and Li_2MO_4 have distinct structures.



Even though two phase reactions are distinct from single phase reactions, where no structural phase transition occurs, many electrodes which have both types of reactions are classified as “intercalation-based” because their reaction mechanism is mainly single phase or since the structural transition is minor. As a result of having relatively little structural changes, intercalation-based materials are capable of reproducibly intercalating and deintercalating Li ions from their structures. The high reversibility of intercalation-based electrodes is the main reason why nearly all secondary Li-ion battery positive electrodes belong to this group of materials.

In contrast, electrodes that participate in a conversion reaction mechanism experience substantial chemical and structural changes as Li^+ is inserted and removed.¹⁹ In conversion electrodes, the Li ions aren’t simply accommodated by a pre-existing structure during lithiation as they are in intercalation-based materials. Instead, when conversion electrodes are cycled the positive electrode material undergoes a three phase reaction. This generally requires the nucleation and growth of new, chemically distinct phases from the original electrode material.^{19,20}

As a result, many conversion-based electrodes are synthesized as a nanocomposite, which helps aid the kinetics of the transformation from one phase to another. Equation 1-9 provides an example of a positive electrode material that undergoes a three phase conversion reaction.

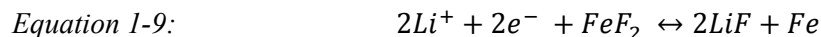


Figure 1-4 presents a comparison between different intercalation-based (Figure 1-4 (a)) and conversion-based (Figure 1-4 (b)) positive electrode materials.¹¹ While the intercalation-based materials tend to have an average discharge potential of ~4 V, which is much higher than for the conversion-based materials (~2-3 V), the specific capacities for the conversion-based materials is substantially larger. Figure 1-4 (b) shows the high theoretical specific capacities for the conversion-based materials, which should be slightly higher than the experimentally obtained results. Regardless, the capacities for conversion-based materials are still expected to be 3-4 times larger than for intercalation-based electrodes.¹¹

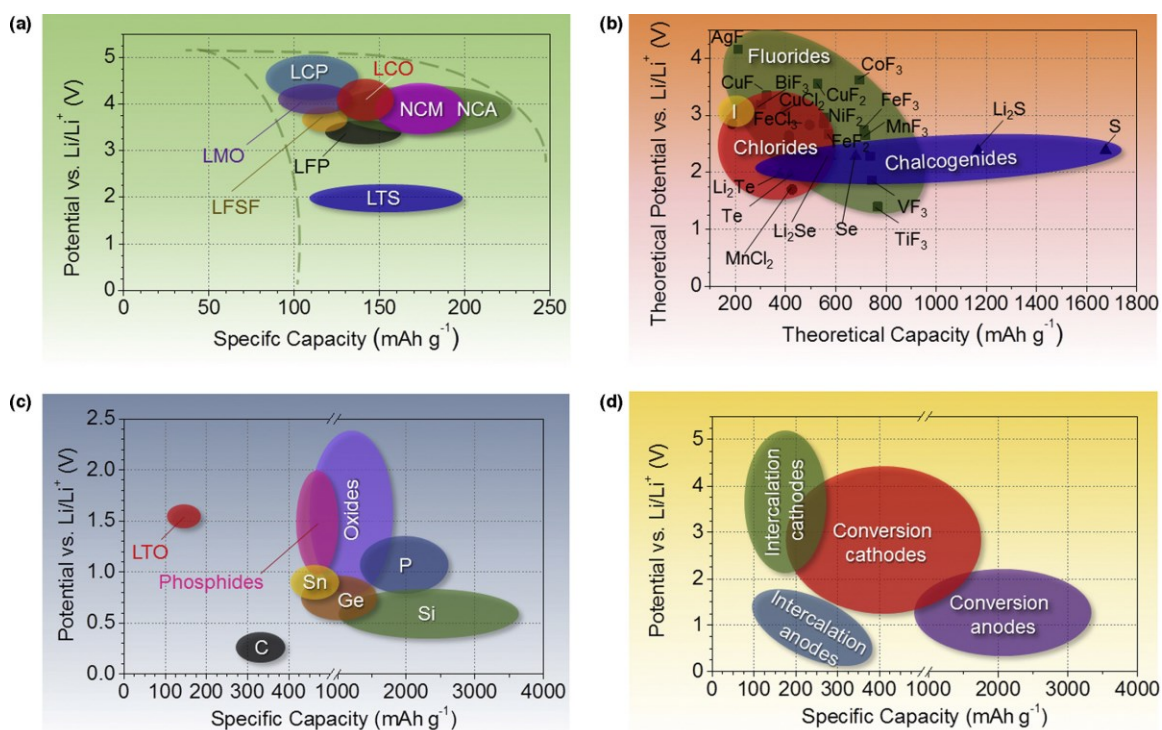


Figure 1-4: Approximations of the discharge potentials and specific capacities for various classes of positive and negative electrode materials. Experimentally determined ranges for (a) intercalation-based positive electrodes and (c) conversion-based negative electrodes are shown. The theoretical potentials and capacities for conversion-based

*positive electrodes are displayed in (b), while (d) presents an overview for all intercalation and conversion electrodes.*¹¹

The exceedingly high theoretical capacities and moderate operating potentials for conversion-based electrodes make them attractive for use in energy dense Li-ion batteries, but these materials are currently plagued by a host of issues which has prevented their application. Among the primary technical obstacles restricting the utilization of conversion-based electrodes are their characteristically poor cycling stability, sluggish kinetics, and low electronic conductivity.^{21–24} The slow reaction kinetics arise from the transition from one structural and chemically distinct material to another. While engineering the electrode material on the nano-scale has improved the rate of the conversion reaction, it is still markedly slower than most intercalation-based materials.^{22,24} Conversion-based electrodes often consist of metal fluorides, oxides or sulfides, which help maximize the electrode's energy density, but also result in poor electrical conductivities.^{11,22,25} Sufficiently high electrical conductivities are necessary in electrodes to enable the extraction of the generated electron from the oxidation reaction. If the electrode's electrical conductivity is prohibitively low then the reaction cannot occur because the reaction's charge balance condition would not be satisfied. A commonly used strategy to improve the electrical conductivity in these electrodes is to finely mix a conductive material like carbon with the conversion material and to then allow the conductive carbon to act as an electronically conducting scaffold.^{22–24}

While there are many obstacles preventing the implementation of conversion-based materials, intercalation-based electrodes also have multiple challenges that need to be overcome in order to increase their operating energy densities. Although there has been some recent research into new classes of intercalation-based materials, the bulk of the efforts to increase the energy density of intercalation electrodes have been focused on optimizing the transition metal ratios in current chemistries and in raising the upper potential limitation. Through changing the transition metals in many intercalation-based materials, researchers aim to reduce the electrode's

mass and cost, as well as stabilize the material against structural changes during cycling. By increasing the electrode's maximum charging potential, additional Li^+ can be extracted from the same material, thus improving the electrode's specific energy density.²⁶ A major difficulty in both approaches is maintaining the cycling stability of current positive electrodes, which are dependent upon a wide range of factors such as electrolyte oxidation, structural stability, Li^+ diffusivity and electronic conductivity, while improving the electrode's energy density.²⁷⁻²⁹

Many positive electrode materials have been studied for use in Li-ion batteries and the vast majority of those commercially available consist of a layered oxide ($R\bar{3}m$) positive electrode. The crystal structure of LiCoO_2 (LCO) is depicted in Figure 1-5; it is the most notable positive electrode material and the electrode material for the first rechargeable commercial Li-ion batteries.¹⁵ Materials such as LCO have a rhombohedral $\alpha\text{-NaFeO}_2$ structure with alternating layers of negatively charged CoO_6 octahedra and positively charged lithium ions. The CoO_6 octahedra share edges with each other and form CoO_2 sheets, as visualized in Figure 1-5. The Li atoms, which reside on the 3a sites of the $R\bar{3}m$ structure, have octahedral coordination with the surrounding O atoms. The tightly packed CoO_2 sheets and large Li-O bond lengths cause the Li atoms to have high two dimensional mobility.^{17,21} $\text{LiNi}_{0.8}\text{Co}_{0.15}\text{Al}_{0.05}\text{O}_2$ (NCA) is isostructural with LCO and only differs by the transition metal elements located in the 3b site. NCA is used in state of the art batteries instead of LCO because of its reduced cost and higher practical cycling capacity.³⁰ Substituting Ni for Co significantly lowers the material cost and eliminates many of the supply chain difficulties in obtaining Co, which is a relatively rare metal. Additionally, the solid solution mixture of multiple transition metals is known to increase the structural stability of the layered oxide, enabling higher states of charge and cycling rates to be practically achieved.^{1,30}

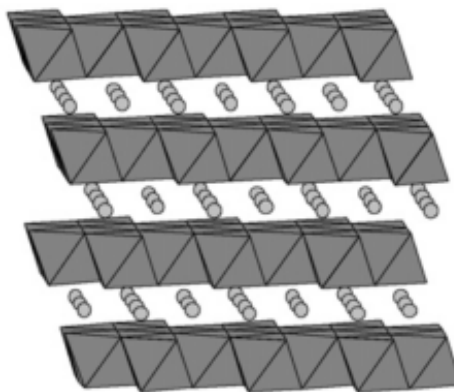


Figure 1-5: An illustration of the CoO_6 -octahedra and Li atoms from a crystal structure of layered ($R\bar{3}m$) LiCoO_2 .¹⁵

1.5 Negative Electrodes

Negative electrodes operate in a nearly identical manner as positive electrodes, but differ in their significantly lower average potential. As explained in section 1.2, the potential difference between the positive and negative electrodes determines the cell's voltage. Thus, having a negative electrode with a low potential is desirable. Relative to a standard hydrogen electrode, Li metal has one of the lowest potentials of all materials, and as a result ample research on Li metal negative electrodes has been performed.¹⁶ However, Li metal electrodes suffer from the formation of dendrites during cycling which can puncture the separator and develop an internal electronic short. A short-circuited cell not only drastically reduces the cell's performance, but also presents a substantial safety hazard.^{12,31} Because of the inability to use Li metal as a negative electrode, most negative electrodes are comprised of a graphite-based material.^{32,33}

Figure 1-6 shows the potential curves (vs. Li/Li^+) for a graphite-based negative electrode when discharged at various rates. At the slowest rate (0.2C – the closest to the equilibrium potential), it is evident that the potential of the graphite electrode is only slightly above that of the Li/Li^+ redox potential.³³ During lithiation (charging of the cell) the potential curve of the graphite electrode has a faceted profile, which is associated with the structural transitions of the graphite material as its Li concentration changes. When a cell containing a graphite-based negative electrode is discharged, the graphite material goes from LiC_6 to $\square\text{C}_6$, where \square represents

vacancies between the graphite sheets.³² Throughout the transition from LiC_6 to $\square\text{C}_6$ there are many individual phases corresponding the energetically favorable Li ordering structures, which are well described by *Ohzuku et al.*³² Figure 1-6 also shows that as the discharging rates are increased so are the potentials at each state of charge. As alluded to in section 1.2, the deviation from the equilibrium potential is caused by concentration gradients and other sources of impedance, which are more pronounced at higher cycling rates. Even at fast discharging rates ($> 5\text{C}$), the average potential of the graphite-based electrode is still relatively low and little capacity is lost.

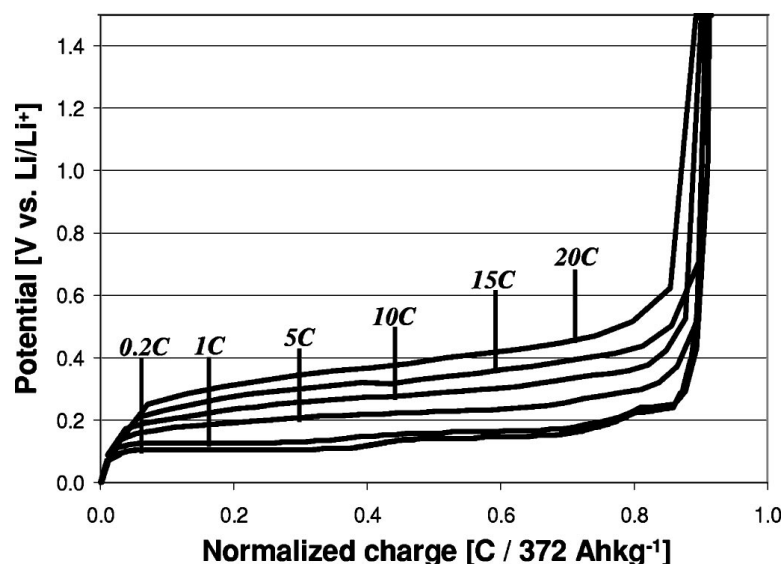


Figure 1-6: Potential curves (vs. Li/Li^+) for a graphite electrode at various C-rates. The following rates were tested; 0.2C (2nd cycle), 1C (5th cycle), 5C (10th cycle), 10C (15th cycle), 15C (20th cycle), and 20C (25th cycle). For all cycles the cell was charged at a constant current (C/5) and a 1M LiPF_6 EC:DMC (1:1) electrolyte was used.³³

Graphite-based electrodes also have good cycling performance, which can be attributed to their high in-plane ionic and electronic conductivities and relatively small structural changes during intercalation.^{11,34–38} The discharge capacities vs. cycle number for a graphite-based negative electrode are presented in the bottom panel of Figure 1-7.³⁹ As is typical for graphite-based negative electrodes, a discharge capacity greater than 300 mAh/g and good cycling stability are observed.^{33,40} On account of the low average

potential, modest discharge capacity and high cycling stability, graphite-based electrodes are widely used as negative electrodes in Li-ion batteries.

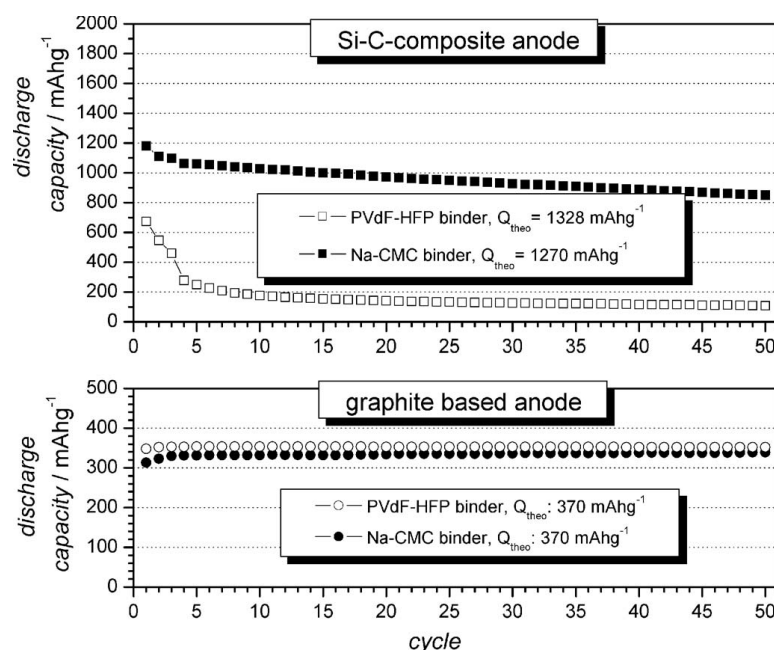


Figure 1-7: Discharge capacity versus cycle number for Si-C-composite (top) and graphite-based (bottom) negative electrodes. For each electrode material, two binder compositions with different chemistries were employed.³⁹

Similar to the positive electrode materials, negative electrodes can utilize either an intercalation-based or conversion-type material. Additionally, many proposed negative electrode materials operate by a third mechanism which is considered to be metal alloying. The graphite-based electrodes are a prime example of an intercalation-based negative electrode, although many other intercalation-based chemistries exist. Because most Li-ion conversion-based materials have relatively high potentials, only a few materials have received attention as possible negative electrodes. Of those proposed, many are divalent transition metal oxides, which are all plagued by large irreversible capacities and exceedingly poor cycling performances.^{25,41–46}

Recently, alloying-type negative electrode materials, particularly Si, have been popular as a next generation negative electrode. Figure 1-4 (c) shows that Si negative electrodes have enormous theoretical capacities which are an order of magnitude larger than graphite-based materials, and have relatively low potentials (< 0.7 vs. Li/Li^+). Materials like Si and other metals

have such high theoretical capacities because each metal atom can accommodate multiple Li atoms. For example, an average of 4.4 Li ions per Si atom can be alloyed into a Si negative electrode, which creates an incredibly high specific capacity.⁴⁷⁻⁵¹ However, because so much Li is being inserted and removed from these materials, the electrodes have large volumetric expansions and contractions during cycling, which cause a structural degradation of the electrode and poor cycling performance. During full lithiation, a Si electrode can have a volumetric expansion of approximately 300%, which leads to substantial micro-cracking, particle isolation, and increased parasitic electrode-electrolyte reactions.^{48,50,51}

In an effort to combine the high theoretical capacity of alloying-type materials and the stability of carbon-based materials, new electrode compositions like those in the top panel of Figure 1-7 have been explored.^{12,13,39,52} As shown by the data depicted in solid black points, these Si-C composite electrodes can provide significantly higher capacities than graphite and sufficient cycling performance. Additional research is needed for these composite materials, especially related to their interactions with the electrolyte, but they are employed in some advanced technology systems and are beginning to be implemented in some commercial products.^{5,12,13,51}

1.6 Electrolytes

During the charging and discharging of an electrochemical cell, the ionic charge transfer between the positive and negative electrodes is enabled by the electrolyte. A “good” electrolyte will be chemically stable against both electrode materials and be able to maintain a high ionic conductivity and electrical resistivity over a wide temperature range. Other desirable properties would include low cost, toxicity, and flammability, especially when exposed to air. The four main types of electrolytes used in secondary batteries are:

- 1) Aqueous
- 2) Non-aqueous liquids
- 3) Polymer/Gel

4) Solid-state

Furthermore, the aqueous, non-aqueous liquid, and polymer/gel electrolytes all consist of a mixture of salt and solvent materials to transport an ionic species. The following text will provide a brief description of each type of electrolyte as well as their individual advantages and challenges.

1.6.1 Aqueous Electrolytes

Aqueous electrolytes, which are used in nickel-metal hydride, nickel-cadmium, and lead-acid batteries, are rarely used in Li-ion cells. Despite being cheaper, more environmentally friendly, less toxic, and having reduced flammability than their non-aqueous liquid electrolytes counterparts; aqueous electrolytes are severely limited by their relatively small stability window. The operating potentials of aqueous electrolyte are restricted by the oxidation and reduction potentials of H_2O . When these potentials are exceeded O_2 and H_2 will be evolved from the solution, leading to the degradation of the cell's electrochemical performance and posing a significant safety hazard.⁵³ Figure 1-8 shows the potential ranges for some possible electrode materials for a Li-ion aqueous battery relative to the potentials at which O_2 and H_2 will be evolved.

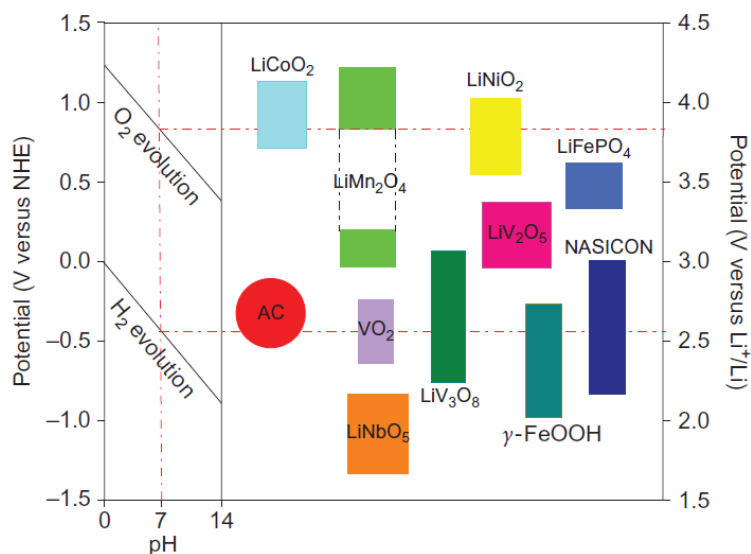


Figure 1-8: Possible Li-ion electrode materials for aqueous batteries. The potentials for H_2 and O_2 evolution are shown as a function of pH relative to both the neutral hydrogen electrode (NHE) and the Li/Li^+ redox potential.⁵⁴

Luo *et al.* recently identified that the four main problems plaguing the cycling stability of aqueous Li-ion batteries are: the instability of electrode materials in the presence of air and H_2O , the thermodynamic stability of H_2O , proton intercalation into highly delithiated electrodes, and the solubility of electrodes in water.⁵⁴ When in the presence of both O_2 (from air) and H_2O , Li-ion intercalated compounds decompose forming Li^+ and OH^- ions. The equilibrium potential ($V(x)$) at which this reaction takes place is determined by the chemical potential of the Li in electrode material and the pH of the aqueous electrolyte. A simplified formula is shown in Equation 1-10.⁵⁴

$$\text{Equation 1-10:} \quad V(x) = 4.268 - 0.059 * pH$$

Even in extremely basic solutions, the equilibrium potential for reduction of the electrode material would be ~ 3.5 V, which is too high for any practical negative electrode materials. Thus, the stability of an aqueous electrolyte in Li-ion batteries is dependent upon preventing any O_2 from coming in contact with the electrode and electrolyte. Even in the absence of O_2 , at certain potentials H_2O will be unstable. Equation 1-11 provides the theoretical potentials in which a lithium intercalated electrode will reduce H_2O and form Li^+ , OH^- , and H_2 gas.⁵⁴

$$\text{Equation 1-11:} \quad V(x) = 3.039 - 0.059 * pH$$

At a pH of 7, the equilibrium potential where H_2O oxidizes an electrode is ~ 2.6 V, but this is decreased to ~ 2.2 V when the pH is 14. Another concern is the oxidation of H_2O at higher potentials. Based on the thermodynamic stability of H_2O , the oxidation of water should occur at 1.23 V above the reduction potential, but due to kinetic limitations this window can be occasionally expanded to up to 2 V. As a result, multiple groups have demonstrated that tailoring the pH of the aqueous electrolyte can minimize the chemical decomposition of H_2O and enable stable cycling of an aqueous Li-ion battery.^{54,55} Since some positive electrode chemistries are more susceptible to proton intercalation than others, proper selection of the electrode materials can eliminate the proton intercalation and electrode solubility degradation mechanisms.

The thermodynamic stability of H_2O generally limits aqueous batteries to a potential window of ~ 1.5 V. While aqueous Li-ion batteries have been previously demonstrated, including some with exceptional cycling performance, the low potentials prevent suitable energy densities for most applications.⁵³ The specific energy density of aqueous Li-ion cells are often between 30-50 Wh/kg, which is comparable with Pb-acid and Ni-Cd technologies but are significantly inferior to Li-ion batteries using other types of electrolyte.⁵⁴⁻⁵⁶

1.6.2 Non-aqueous Liquid Electrolytes

As previously mentioned, non-aqueous liquid electrolytes are comprised of a mixture of salt and solvent materials. When in a suitable solvent, Li salts dissociate to produce cations (Li^+) and anions. The degree of dissociation is correlated to the salt's and solvent's dielectric constant, where a high dielectric constant encourages more dissociation.⁵⁷ In salts with a high solvation power, the Li^+ is closely surrounded by the solvent species, which enables rapid conduction of the Li^+ .^{57,58} Salts with larger anionic molecules are advantageous because the anions easily disperse throughout the electrolyte and prevent ionic pairing.⁵⁹ While the salt's solvation power and dispersion of the ionic species in the electrolyte are important factors to the electrolyte's ionic conductivity, the viscosity and solvation power of the solvent also have a profound impact. To

obtain fast ionic conductivities, the electrolyte's solvent should have a low viscosity and high solvation power.^{58,59} This will enable sufficient formation and dispersion of the Li^+ in the electrolyte, as well as the ability for those ions to quickly transfer charge throughout the solution.

The main materials investigated for use as a solvent in Li-ion batteries are organic carbonates, esters, and ethers.^{60,61} The most commonly studied solvents belong to these families; relevant properties are listed in Table 1-I and Table 1-II, respectively.⁶¹ A large difference in properties is observed between cyclic and acyclic materials (Table 1-I). For example, cyclic carbonates and esters contain high dielectric constants but are relatively viscous. Acyclic materials, in contrast, are weakly polar and fluid. In further contrast, all ether materials in Table 1-II, regardless of whether they were cyclic or acyclic, showed moderate dielectric constants and good viscosities.⁶¹

Table 1-I: Commonly studied organic carbonates and esters for use as an electrolyte solvent. The material's structure and important properties are listed for comparison. The materials are arranged by whether they are cyclic (top) or acyclic (bottom).

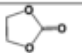
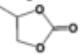
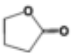
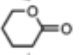
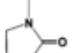

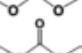
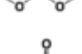
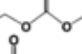
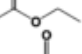
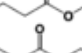
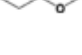




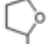
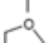
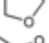
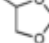
Solvent	Structure	M. Wt	$T_m/^\circ\text{C}$	$T_b/^\circ\text{C}$	η/cP 25 $^\circ\text{C}$	ϵ 25 $^\circ\text{C}$	Dipole Moment/debye	$T_f/^\circ\text{C}$	d/gcm^{-3} , 25 $^\circ\text{C}$
EC		88	36.4	248	1.90, (40 $^\circ\text{C}$)	89.78	4.61	160	1.321
PC		102	-48.8	242	2.53	64.92	4.81	132	1.200
BC		116	-53	240	3.2	53			
γ BL		86	-43.5	204	1.73	39	4.23	97	1.199
γ VL		100	-31	208	2.0	34	4.29	81	1.057
NMO		101	15	270	2.5	78	4.52	110	1.17
DMC		90	4.6	91	0.59 (20 $^\circ\text{C}$)	3.107	0.76	18	1.063
DEC		118	-74.3 ^a	126	0.75	2.805	0.96	31	0.969
EMC		104	-53	110	0.65	2.958	0.89		1.006
EA		88	-84	77	0.45	6.02		-3	0.902
MB		102	-84	102	0.6			11	0.898
EB		116	-93	120	0.71			19	0.878

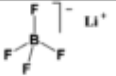
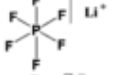
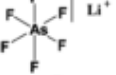
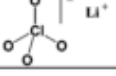
Table 1-II: Promising ether materials for use as an electrolyte solvent in Li-ion batteries. The structure of each material is shown alongside the properties that are important to its performance in an electrochemical cell. The top three materials are acyclic while the remaining five materials are cyclic.

Solvent	Structure	M. Wt	T _m / °C	T _b / °C	η/cP 25 °C	ε 25 °C	Dipole Moment/debye	T _f / °C	d/gcm ⁻³ , 25 °C
DMM		76	-105	41	0.33	2.7	2.41	-17	0.86
DME		90	-58	84	0.46	7.2	1.15	0	0.86
DEE		118	-74	121				20	0.84
THF		72	-109	66	0.46	7.4	1.7	-17	0.88
2-Me-THF		86	-137	80	0.47	6.2	1.6	-11	0.85
1,3-DL		74	-95	78	0.59	7.1	1.25	1	1.06
4-Me-1,3-DL		88	-125	85	0.60	6.8	1.43	-2	0.983
2-Me-1,3-DL		88			0.54	4.39			

Other than ionic conductivity, the stability of the electrolyte with both electrode materials is of primary importance. Because of the high potential range (> 4 V) of current Li-ion batteries, carbonate based liquid electrolytes are frequently operated outside of their thermodynamic stability window.^{61–63} The electrolyte decomposition, however, is often kinetically limited, which enables use in electrochemical devices amidst thermodynamically unstable conditions. Ethylene carbonate (EC) is present in nearly all commercially used electrolytes because of its high dielectric constant and since it quickly forms a passivation layer at low potentials which prevents the continual reduction of the solvent.⁶¹ However, because EC has a high melting point and relatively high viscosity, it is mixed with other solvents to improve the electrolyte's conductivity.⁶² Linear carbonates, particularly dimethyl carbonate (DMC), have low viscosities and melting temperatures, and are frequently mixed with EC to improve the electrolyte's ionic conductivity.⁶¹ Furthermore, electrolyte mixtures of EC and linear carbonates have been demonstrated to be stable against oxidation even when cycled up to 5 V at elevated temperatures for hundreds of cycles.^{64,65} As a result, of their high solvation power, low viscosity and stability against reduction and oxidation, mixtures of EC and linear carbonates are the most commonly used solvents for Li-ion electrolytes.

While there are numerous possible candidates for the solvent component of the electrolyte, the quantity of viable salt materials is limited. Li-ion salts have a demanding list of properties required for use, such as; *i)* the ability to dissolve and dissociate well in the solvent, *ii)* be inert against the solvents, separator, electrode substrates and cell casing, *iii)* thermal stability, and *iv)* for the anion to be able to endure high potentials without oxidation on the positive electrode.^{16,61} As a result, many lithium salts fail to adequately meet the necessary requirements and only a few salts are used in electrolyte solutions. Table 1-III provides a short list of the most common salts for Li-ion electrolytes and displays some of their important properties.⁶¹ LiPF₆ is the most frequently used salt due to its high conductivity and stability against oxidation. However, because of the manufacturing mechanisms used to produce LiPF₆, H₂O is always present in trace amounts with the salt. When moisture is in the presence of any the fluorinated salts, the H₂O reacts with the salt and produces HF, which then subsequently degrades the positive electrode material.^{66,67}

Table 1-III: Common Li salts, their structure and relevant properties are listed. More information on each salt, particularly related to the ionic conductivity can be found in publications by Ue and Mori,⁵⁸ Linden,¹⁶ and Schmidt et al.⁶⁸

Salt	Structure	M. Wt	T _m /°C	T _{decomp} / °C in solution	Al-corrosion	σ /mScm ⁻¹ (1.0 M, 25 °C)	
						in PC	in EC/DMC
LiBF ₄		93.9	293 (d)	> 100	N	3.4 ^a	4.9 ^c
LiPF ₆		151.9	200 (d)	~ 80 (EC/DMC)	N	5.8 ^a	10.7 ^d
LiAsF ₆		195.9	340	> 100	N	5.7 ^a	11.1 ^c
LiClO ₄		106.4	236	>100	N	5.6 ^a	8.4 ^d
Li Triflate	Li ⁺ CF ₃ SO ₃ ⁻	155.9	>300	>100	Y	1.7 ^a	
Li Imide	Li ⁺ [N(SO ₂ CF ₃) ₂] ⁻	286.9	234 ^b	>100	Y	5.1 ^a	9.0 ^e
Li Beti	Li ⁺ [N(SO ₂ CF ₂ CF ₃) ₂] ⁻				N		

Room temperature ionic liquids are another class of inorganic electrolytes. While all previously described non-aqueous liquid electrolytes involved the combined use of a salt and a solvent, ionic liquids are essentially a single ionic salt material operating above its melting temperature. Since these ionic materials need to be liquid at or near room temperature, they must have a low melting point, which severely limits the quantity of possible chemistries.⁶⁹ Although, an in-depth description of ionic liquids and their applications to Li-ion batteries is outside the scope of this work it is important to note that these materials are being researched for potential use as an improved electrolyte. In general, ionic liquids are advantageous because they are non-flammable, have high-thermal stability, and good electrochemical stability, however, they are limited by their ionic conductivities that are 3-4 orders of magnitude below carbonate electrolytes, and their poor low temperature performance.^{59,69}

1.6.3 Polymer/Gel Electrolytes

The use of polymers as a Li-ion electrolyte can be separated into two groups; *i*) solid polymer electrolytes (SPE) and *ii*) gel polymer electrolytes (GPE). As the name suggests, SPEs are dry, solid polymers that solvate lithium salts, which enables ionic charge transfer throughout the material. In contrast, GPEs consist of a polymer network that is soaked with a liquid electrolyte. Since the liquid electrolyte comprises between 60-95% of the GPEs, these materials solvate lithium salts similarly to liquid electrolytes and have ionic conductivities within an order of magnitude of pure liquid electrolytes.^{31,61,62,70} Both types of polymer electrolytes benefit from possessing high processability, flexibility, and safety compared to liquid electrolytes. In both cases, a polymer network provides dimensionality to the electrolyte which can enable the elimination of the separator, thus reducing the cost and complexity of the electrochemical system.^{61,70}

Investigations into SPEs originated with poly(ethylene oxide) (PEO), which effectively solvates Li salts and has suitable mechanical properties.⁶¹ Since it was discovered that the

conductivity is best in the amorphous regions of the polymer, ample effort has been invested in decreasing the crystallinity of PEO-based and other SPE materials. The addition of other polymer materials, plasticizers, and ceramic nanoparticles has been demonstrated to reduce the crystallinity of the SPE and increase the conductivity.^{31,62,70} However, despite decades of research, the ionic conductivities of PEO-based SPEs are still too low for commercial applications at room temperature.³¹ Additionally, PEO-based SPEs are unstable at high potentials and their practical use is limited to lower voltage positive electrodes.^{71,72}

Unlike SPEs, GPEs have seen widespread commercial application, which is attributed to their much higher conductivities than SPEs and increased safety relative to liquid electrolytes. The most commonly used polymer in GPEs is poly(vinylidene fluoride) (PVdF) to which hexafluoropropylene (HFP) is added to reduce the material's crystallinity and improve processibility.⁷⁰ Because GPEs have both polymer and liquid components, they have properties resembling both materials. For example, they take the high ionic conductivity and good electrode-electrolyte interfacial contact from liquid electrolytes and the mechanical integrity of SPEs.⁶¹ Similar to SPEs, plasticizers, ceramic nanomaterials, and other polymers have been mixed into GPEs in an effort to tailor their conductivity and mechanical properties.^{62,70} Current research on GPEs mainly focuses upon improving their ionic conductivities and in reducing the amount of liquid electrolyte used, which will improve the safety and toxicity of these electrolytes.

1.6.4 Solid-state Electrolytes

Solid-state electrolytes consist of a high elastic modulus ceramic material, which can have either a crystalline or amorphous structure. Examples of common crystalline and glassy (amorphous) solid-state electrolytes, their ionic conductivities, and a brief description of each material are shown in Table 1-IV and Table 1-V, respectively.⁵⁹ Similar to the polymer/gel electrolytes, solid-state electrolytes are advantageous because they are much safer than liquid carbonate electrolytes. Additionally, solid-state electrolytes are more resistant to vibrations,

pressures or elevated temperatures and can have a much wider electrochemical stability window relative to liquid electrolytes. One of the primary benefits of the rigid nature of solid-state electrolytes is that they are more resilient against Li dendrites. However, the commercial applications for solid-state electrolytes have been muted because they tend to be more expensive to fabricate and have substantially lower ionic conductivities.^{59,70}

Table 1-IV: Some common chemistries for crystalline solid-state electrolytes are shown along with their corresponding ionic conductivities and a brief description of the material. More extensive descriptions of the perovskite⁷³, NASICON⁷⁴, thio-LISICON⁷⁵, crystalline⁷⁶, and garnet⁷⁷ type materials can be found elsewhere.

Type	Ionic conductivity (S cm^{-1})	Description	Measurement technique
Crystalline (perovskite)	<ul style="list-style-type: none"> • 1.0×10^{-3} ($x=0, 0.1$) 	<ul style="list-style-type: none"> • Solid solution, $x\text{LaAlO}_3-(1-x)\text{La}_{0.5}\text{Li}_{0.5}\text{TiO}_3$: amount of LaAlO_3 (x) is varied 	EIS
Crystalline (NASICON)	<ul style="list-style-type: none"> • 1.0×10^{-8} ($x=0.3$) • 1.0×10^{-11} ($x=0.4$) • 6.7×10^{-7} (at 250°C) 	<ul style="list-style-type: none"> • Phosphate compound ($\text{Li}_2\text{AlZr}[\text{PO}_4]_3$): effect of substitution of Al and Zr for Ti in $\text{Li}_2\text{Ti}_2[\text{PO}_4]_3$ 	EIS
Crystalline (thio-LISICON)	<ul style="list-style-type: none"> • 4×10^{-6} ($x=0$) • 5×10^{-6} ($x=0.05$) 	<ul style="list-style-type: none"> • $\text{Li}_{4-2x}\text{Zn}_x\text{GeS}_4$ • Composition dependent ionic conductivity 	EIS
Crystalline	<ul style="list-style-type: none"> • 4×10^{-7} ($x=0.1$) • 2×10^{-9} ($x=1$) • 5×10^{-4} ($x=0$) 	<ul style="list-style-type: none"> • Chlorine compound ($\text{Li}_3\text{InBr}_{6-x}\text{Cl}_x$): effect of substituting Br with Cl 	EIS
Crystalline (Garnet)	<ul style="list-style-type: none"> • 5×10^{-5} ($x=2.0$) • 4×10^{-4} ($x=3.0$) • 5×10^{-7} ($x=4.0$) • 5×10^{-5} • 5×10^{-4} • 5×10^{-4} • 5×10^{-3} 	<ul style="list-style-type: none"> • Pristine sample: $\text{Li}_5\text{La}_3\text{Ta}_2\text{O}_{12}$ • Substituting La with Ca: $\text{Li}_6\text{CaLa}_2\text{Ta}_2\text{O}_{12}$ • Substituting La with Sr: $\text{Li}_6\text{SrLa}_2\text{Ta}_2\text{O}_{12}$ • Substituting La with Ba: $\text{Li}_6\text{BaLa}_2\text{Ta}_2\text{O}_{12}$ 	EIS

Table 1-V: Various types of glassy (amorphous) solid state electrodes are listed with their ionic conductivities and a brief a brief description. Additional details on the LiPON,⁷⁸ sulfide-based glass,⁷⁹ glass and polymer composites,⁸⁰ and glass-ceramics^{81,82} materials are given elsewhere.

Type	Ionic conductivity (S cm^{-1})	Description	Measurement technique
Glass (LiPON)	<ul style="list-style-type: none"> • 1.8×10^{-6} to 8.0×10^{-7} • 8.0×10^{-7} to 1.8×10^{-6} • 9.0×10^{-7} to 5.0×10^{-7} • 2.5×10^{-7} to 8.0×10^{-7} 	<ul style="list-style-type: none"> • Effect of RF power on ionic conductivity ($2.2\text{--}5.7 \text{ W cm}^{-2}$) • Effect of N_2 gas pressure ($0.5\text{--}2 \text{ Pa}$) • Effect of target-substrate distance ($7\text{--}11.5 \text{ cm}$) • Effect of target density ($1.48\text{--}2.22 \text{ g cm}^{-3}$) 	AC impedance
Glass	<ul style="list-style-type: none"> • 1.2×10^{-4} (25 kpsi) • 2.0×10^{-4} (50 kpsi) • 3.0×10^{-4} (125 kpsi) 	<ul style="list-style-type: none"> • Sulfide-based Li glass: $0.375\text{SiS}_2\text{--}0.375\text{Li}_2\text{S--}0.25\text{LiCl}$ • Effect of isostatic pressure on ionic conductivity 	AC impedance
Composite (glass + polymer)	<ul style="list-style-type: none"> • 5×10^{-3} • 1×10^{-3} (dry process) • 1×10^{-4} (wet process) 	<ul style="list-style-type: none"> • Sulfide-based Li glass: $0.36\text{SiS}_2\text{--}0.63\text{Li}_2\text{S--}0.01\text{Li}_3\text{PO}_4$ • Sulfide-based Li glass particles + SBR (8 vol%) • Sulfide-based Li glass particles + SBR (4 vol%) 	AC impedance
Glass-ceramics	<ul style="list-style-type: none"> • 1.12×10^{-8} • 6.53×10^{-4} • 5.98×10^{-9} • 3.99×10^{-4} • 1.00×10^{-3} 	<ul style="list-style-type: none"> • Glass; $\text{Li}_2\text{O--Al}_2\text{O}_3\text{--TiO}_2\text{--P}_2\text{O}_5$ • Glass-crystalline mixed phase; $\text{Li}_{1-x}\text{Al}_x\text{Ti}_{2-x}(\text{PO}_4)_3$, $x=0.3$ • Glass; $\text{Li}_2\text{O--Al}_2\text{O}_3\text{--GeO}_2\text{--P}_2\text{O}_5$ • Glass-crystalline mixed phase; $\text{Li}_{1-x}\text{Al}_x\text{Ge}_{2-x}(\text{PO}_4)_3$, $x=0.3$ • Glass-crystalline mixed phased by heat treating ($30\text{P}_2\text{S}_5\text{--}70\text{Li}_2\text{S}$) glass 	AC impedance

Ionic conduction in solid-state electrolytes is mainly through ion hopping between energetically favorable sites in the lattice, and it is often observed that diffusion along the grain boundaries is orders of magnitude slower than through the material's bulk.^{59,74} Because the ionic diffusivity is largely dependent upon the magnitude of the activation barriers restricting ion hopping, the ionic diffusivity in solid-state electrolytes is closely correlated to the operating temperature.⁷⁴ At higher temperatures, the ionic species have more energy and can more easily overcome the activation barriers. As a result, the ionic diffusivity often varies by a couple orders of magnitude as a function of temperature.^{70,75,77} Since nearly all of solid-state electrolyte compounds are highly stable ceramic materials, solid-state electrolytes are the most suitable type of electrolytes for high temperature applications.

Three main classes of solid-state electrolyte materials exist: sulfides, oxides, and phosphides.^{70,73–75,79} While an in-depth explanation of each type material is outside the scope of

this thesis, it is important to note that all of the materials operate by the same fundamental mechanisms. Even though there are a few outliers, each type of solid-state electrolyte material is a ceramic material that is chemically and structurally stable at elevated temperatures, and ionic conduction proceeds mainly through ion hopping via vacant sites within the lattice. The entire surfaces of both electrodes, the rigid structure of the ceramic material does not contort itself around the shape of the electrode material. As a result, there is substantially less electrode-electrolyte interfacial area, which results in a significantly higher interfacial impedance.^{80,83} The high interfacial impedance and the lower ionic diffusivity are the primary limitations of solid-state electrolytes, especially for high rate applications.

1.7 Important Topics

This section will briefly introduce the reader to more advanced topics that are particularly relevant to this work. The three key issues that will be discussed are: *i*) the nature of the chemical bonds in the positive electrode material at high states of charge; *ii*) the electrode-electrolyte interfacial reactions that occur on the positive electrode; and *iii*) transition metal dissolution from the positive electrode structure. It is important to note that all three topics are areas of active research and discussion so only the established basics are provided.

1.7.1 Failure Modes of Layered Oxide Electrodes

Despite being the most widely used class of positive electrodes in secondary Li-ion batteries, layered oxide materials are known to have multiple failure mechanisms. The material's surface is known to form an electrode-electrolyte interface upon submersion in a non-aqueous liquid electrolyte.⁸⁴⁻⁸⁶ This interface can cause substantial charge transfer impedance that subsequently reduces the electrochemical performance and will be described in more detail in section 1.7.3.⁸⁷ It is important to note, that commonly observed consequences of electrode-electrolyte reactions are transition metal dissolution and oxygen loss from the layered oxide structure. Transition metal dissolution reduces the amount of electrochemically active material,

thus lowering the capacity, and can generate impedance throughout the cell.⁸⁸ The mechanisms and effects of transition metal dissolution are more extensively described in a following section (1.7.4). Oxygen loss from the layered oxide material creates a host of decomposition structures which have been observed to increase the electrode's impedance. Moreover, the evolved oxygen can react with the electrolyte and present a significant safety hazard.^{89,90}

Since the layered oxides materials used as electrodes are brittle, they are prone to micro-cracking when subjected to high strains. As these materials crack new surfaces are created and subject to parasitic reactions with the electrolyte, which results in increased impedance.^{91,92} A primary source of the large strains needed to induce micro-cracking is the structural changes that occur within the layered oxide as it is reversibly charged and discharged. This failure mechanism is especially prevalent when charging to high states of charge which requires additional structural transformations.^{91,93} A potential consequence of positive electrode micro-cracking is particle isolation. Particle isolation occurs when a particle or portion of the electrode becomes electronically or ionically insulated from the current collector or electrolyte. As a result, the isolated particle becomes inactive since the redox reaction is either electronically or ionically limited.⁴⁰ It is important to note that particle isolation can occur even in the absence of micro-cracking, due to either excessive development of an electrode-electrolyte interface or from a poorly constructed electrode.⁹⁴

Another main bulk failure mode of layered oxide materials is the migration of transition metal ions into undesired sites, such as the Li 3a site or a tetrahedral site. In either of these sites, transition metals are a large detriment to the reversible capacity because they either occupy a Li site making less available to Li, or they significantly increase the energy for Li to occupy a neighboring octahedral site.⁹⁵ Furthermore, transition metals in either of these undesirable locations reduce the Li^+ diffusivity by blocking part of the diffusivity pathway between the MO_2 slabs.⁹⁶ Once in these sites the transition metal ions are relatively immobile and cause permanent

damage to the electrode's electrochemical performance.⁹⁷ Due the differences in the electron configurations of the transition metal elements some metals, such as Ni, are more susceptible to migrating into unfavorable sites.^{96,98} Since Ni is easily reduced to the divalent state it is more prone to occupying the 3a site and as a result well layered LiNiO₂ is very difficult to fabricate.^{98–}

100

The reversible capacity of the positive electrode can also be diminished by loss of the Li ions to formation of an electrode-electrolyte interface or other to parasitic reactions. The more Li that is consumed by these side reactions the less that is available for intercalation, and as a result a decrease of capacity is observed.¹⁰¹ While not an exhaustive list of the failure modes of layered oxide materials, these mechanisms are amongst the most prevalent degradation pathways that limit the stability and performance of layered oxide electrodes.

1.7.2 Bonding in Positive Electrode's at High States of Charge

In the Positive Electrode section (1.4), the important structural features of layered oxide materials were discussed. In a lithiated LiMO₂ (M = transition metal) material, the Li ions reside between sheets of MO₆ octahedra. In conventional theory, the transition metal is subsequently oxidized from one valence state to another as the electrode is charged and Li ions are removed from the material. During the delithiation and lithiation process, the layered oxide material will often undergo subtle transformations from the original crystal structure to a more stable phase depending on the amount of lithium in the electrode.¹⁷ These structural transitions are often attributed to Jahn-Teller distortions, which are distortions to the original geometry of the MO₆ octahedra induced by changes in the electronic structure of the transition metal ion.¹⁰² As M is oxidized and reduced the number of electrons in its outer electron shell varies. This correspondingly causes changes in its bonding nature with the neighboring oxygen ions.¹⁰³ A common example of Jahn-Teller distortions is the hexagonal to monoclinic to hexagonal transition in Li_xCoO₂, which is due to the Jahn-Teller active Co ions.¹⁰⁴ In the fully lithiated state,

the electronic structure of the Co in LiCoO_2 is $t_{2g}^6 \cdot e_g^0$ and has fully occupied t_{2g} orbitals. When LiCoO_2 is charged, some of the Co ions are oxidized and their resulting electronic structure is $t_{2g}^5 \cdot e_g^0$ (low-spin state) or $t_{2g}^3 \cdot e_g^2$ (high-spin state), with the low-spin state being more stable.¹⁸ To accommodate the missing electron in the t_{2g} orbital, a distortion of the CoO_6 octahedra is induced and the energy of the octahedra is changed. Once enough of the Co is in the 4+ valence state, the overall energy of the positive electrode structure is sufficiently altered to induce a phase change. While the valence structure of Ni and other transition metal ions are different, a similar mechanism occurs, albeit at different states of charge.^{14,103,105}

Under the conventional theory, oxidation of these positive electrode materials always results in the extraction of the highest energy transition metal electron and thus oxidation of that transition metal. This causes a contraction of the M-O bond lengths and a polarization of the oxygen ion's electrons towards the M ion.¹⁰⁶ However, recent results indicate that at high states of charge not all of the oxidation activity is localized to the transition metal, and instead the oxygen ions participate in a charge compensation reaction.¹⁰⁷⁻¹⁰⁹ While the exact mechanism of oxygen charge compensation is still being debated, there is a general consensus that as some transition metals are partially oxidized an overlap of the transition metal and oxygen electronic bands occurs and results in some charge transfer from the oxygen ion as further oxidation of the positive electrode occurs.^{109,110} In layered oxides, the oxygen charge compensation occurs simultaneously with the oxidation of the transition metal, not in two separate stages.^{110,111} Furthermore, *Yoon et al.* has demonstrated that the presence and degree of oxygen charge compensation is dependent upon the material's transition metal chemistry.^{106,112}

The presence of oxygen charge compensation has significant ramifications on the nature of the metal-oxygen bonding in the material and on the electrode's electrochemical performance. Previous reports show that changes in the electronic state of the oxygen ions can lead to substantial voltage hysteresis and even the degradation of the material's structure through oxygen

loss, and transition metal migration.^{98,108,113} Moreover, the identification of oxygen charge compensation forces researchers to re-conceptualize the bonding environments in these materials, particularly at high states of charge where oxygen activity is pronounced.

1.7.3 Electrode-Electrolyte Interfacial Reactions

The electrode-electrolyte interfaces are crucial to the performance of an electrochemical cell. At these interfaces, the Li ions transfer between the solid electrode and the electrolyte, and this charge transfer reaction is a major source of the cell's impedance.^{114,115} If there is poor contact between the electrode and the electrolyte, then the charge transfer reactions are restricted to a limited area, which results in a higher charge transfer density, and subsequently increased charge transfer impedance.¹¹⁶ Additionally, the presence of any impurity or degradation species at this interface can impede the charge transfer process by restricting the flow of ions.¹¹⁷ Electrode-electrolyte interfacial reactions are complex because they are influenced by numerous factors including: the electrode and electrolyte chemistries, the state of charge, temperature, and the presence of impurity species.^{114,117,118}

The low potentials of the negative electrode in Li-ion batteries are generally outside of the electrolyte's stability window and reduce the electrolyte at the interface.³¹ The electrolyte degradation products form a solid-electrolyte interface (SEI) on the surface of the negative electrode.^{114,115} If electrolyte reduction continually occurs, the SEI layer can grow to be thick and cause substantial impedance.¹¹⁶ As a result, EC is generally included in the electrolyte because it quickly reduces on the negative electrode and develops a passivating layer that prevents further electrolyte decomposition.^{31,119} The SEI formed from EC decomposition on the negative electrode has been well characterized and is thoroughly described elsewhere.¹²⁰

An electrode-electrolyte interface is also formed on the positive electrode and is referred to as the cathode-electrolyte interface (CEI). Unlike the SEI, the chemical composition and the formation mechanisms of the CEI are complex, and vary extensively based on the type of positive

electrode and electrolyte materials.^{115,119} Since the potential of the positive electrode changes by ~1 V during cycling, a wide range of degradation products are observed on the positive electrode.^{119,121} Furthermore, positive electrode materials rapidly degrade upon exposure to ambient air, and even brief exposure can result in the formation of surface impurity species that reduce the electrochemical performance.^{117,122}

Similar to the SEI, the composition of the CEI is heavily influenced by electrolyte salt and solvent materials, which at high potentials are oxidized on the positive electrode.^{114,115} The electrochemical stability of each salt and solvent material is dependent upon its chemistry, and as a result a multitude of degradation species have been observed.^{121,123} Impurities in the electrolyte, mainly H₂O, are also particularly impactful to the CEI and have been shown to not only form surface products such as LiF, but to also chemically attack and etch the positive electrode material.¹²¹ Electrode-electrolyte reactions can also induce a degradation of the positive electrode material. In layered oxides, especially at higher potentials, electrode-electrolyte reactions can be responsible for transition metal dissolution, oxygen evolution, and structural transformations to spinel-like and rocksalt-like phases.^{85,123–125} As with the products created by electrolyte decomposition, changes to the positive electrode material can result in a loss of electrochemically active material and substantial impedance growth.^{120,121,124} Surface impurity species, namely Li₂CO₃, can induce and accelerate the reactions between the electrode and electrolyte, leading to a richer and thicker CEI.^{117,119} These impurity species have been correlated to increased impedance and reduced cycling stability.¹²²

Since the charge transfer impedances at the SEI and CEI can account for a large portion of the cell's cumulative impedance, understanding and controlling the electrode-electrolyte interfaces is critical to maintaining good performance of the electrochemical cell.^{114,118,121} While much effort has been invested into characterizing and identifying the formation mechanisms of the CEI, there are still significant questions that remain unanswered. The dearth of knowledge

concerning the CEI at high states of charge is an important obstacle to enabling the operation of positive electrodes at these potentials.

1.7.4 Positive Electrode Transition Metal Dissolution

Positive electrode transition metal dissolution occurs when the positive electrode material chemically decomposes and causes transition metal ions to irreversibly enter the electrolyte. Transition metal dissolution is particularly relevant for layered oxide positive electrodes because it has been identified as one of the primary degradation mechanisms of these materials.^{85,104} When transition metal ions are dissolved from the positive electrode material, there is a loss of the electrochemically active material which reduces the energy storage capabilities.^{27,120} The resulting decomposed positive electrode structure after dissolution is known to be a large source of impedance, and is often accompanied by electrolyte degradation products that further increase the electrode-electrolyte interfacial impedance.^{88,126} Furthermore, after dissolution the transition metal ions have been observed to poison the electrolyte and the negative electrode, which can induce substantial increases in impedance throughout the cell.^{103,126} *Blyr et. al* have shown that Mn dissolution from the positive electrode was reduced to Mn metal on both Li and $\text{Li}_4\text{Ti}_5\text{O}_{12}$ electrodes, and caused substantial shifts to the potentials of those electrodes.¹²⁷

While the transition metal dissolution degradation mechanisms aren't fully understood, two main mechanisms have been frequently proposed. The first mechanism is a disproportionation reaction, where transition metal ions at a given valence state spontaneously separate into two ions with two different valence states, but with a cumulative charge that is equivalent to the initial ions.²⁷ This type of reaction is commonly attributed to Mn ions, which initially have a 3+ valence state.^{85,126} The electronic valence configuration of Mn^{3+} is $t_{2g}^4 * e_g^0$, which is unstable since only one t_{2g} orbital is completely filled while the other two are partially filled. As a result, Mn^{3+} ions equally split into $\text{Mn}^{2+} t_{2g}^3 * e_g^2$ and $\text{Mn}^{4+} t_{2g}^3 * e_g^0$, which both have only a single electron in each orbital and are thus much more stable electronic configurations than

Mn^{3+} .¹⁰³ These divalent transition metal ions are more susceptible to dissolution because they are less tightly bound to the neighboring oxygen ions and can more easily enter the electrolyte.^{126,128}

The second transition metal dissolution reaction mechanism is related to acid-induced degradation of the positive electrode material. An acid, usually HF, parasitically reacts with the positive electrode material, resulting in the formation of LiF, M ions, and H_2O .^{27,85,103} As alluded to earlier, the H_2O produced by this reaction will further degrade the fluorinated electrolyte to create more HF, which subsequently repeats the acidic attack of the positive electrode.^{120,127,129} Thus, this transition metal dissolution mechanism is autocatalytic and proceeds until a passivation layer (e.g. MO_x) is developed throughout the entire electrode-electrolyte interface.^{27,120}

Of the multiple factors that influence the propensity for transition metal dissolution from positive electrode materials, the main variables are the composition of the electrode and electrolyte, the electrode's surface chemistry, the presence of any impurities within these materials, the temperature, and the cell's potential.^{27,104,127} Since fluorinated electrolyte salts and moisture are required for the formation of HF, minimizing the moisture content and the use of different salt chemistries can drastically reduce the amount of acid-induced transition metal dissolution.^{85,127,129} Similarly, proper selection of the electrolyte salt and solvent materials can reduce the transition metal solvation power of the electrolyte and diminish the degree of transition metal dissolution.^{27,126} Changes to the positive electrode material structure and chemistry can also have a profound impact on the magnitude of metal dissolution.^{85,104} Because the electronic structure of the metal ion is critical to its propensity to enter solution, substitution of metals with different valence states or electronic configurations can have a profound impact.¹⁰³ The potential of the cell, which is directly related to the stability of the electrolyte and the state of charge of the positive electrode (i.e. electrode composition), has been correlated to transition metal dissolution.^{104,130} Both dissolution mechanisms are highly dependent upon the temperature, either because it affects the activation energy for dissolution to occur or the kinetics of the ionic movement.^{85,127,129} As a result of its importance to the electrochemical performance of the cell and

its complex reaction mechanisms, transition metal dissolution remains critically important to the development of improved positive electrode materials.

1.8 $\text{LiNi}_{0.8}\text{Co}_{0.15}\text{Al}_{0.05}\text{O}_2$

As previously mentioned, NCA is a state of the art positive electrode material that is structurally akin to the other layered oxide materials. It operates via the same topotactic intercalation mechanism and has a similar active mass as the other $R\bar{3}m$ materials, yet has enhanced electrochemical and structural properties. Practically, NCA is attractive because its main transition metal is Ni, which is much cheaper and easier to source than Co. The addition of even some Al is also beneficial in reducing the cost of the material.¹³¹ Fundamentally, NCA is advantageous since it forms a highly ordered layered structure, the structure is both thermally and electrochemically stable, and because the material has good electrochemical performance.⁵

Ni-rich layered oxide materials, especially LiNiO_2 , can be difficult to fabricate due to the propensity for the Ni ions to be reduced to a divalent state and migrate into the Li 3a site.^{132,133} The relatively high concentrations of Ni in this site is a main reason why many Ni-rich compounds severely underperform their theoretical capabilities.¹⁰³ The substitution of Co and Al ions for Ni in LiNiO_2 to form NCA, has been shown to greatly reduce the amount of transition metals in the Li site and improve the overall ordering of the structure.^{132–134} Not only do the Co and Al ions help synthesize a well ordered structure, but they also improve the material's structural stability.^{135,136} In terms of layered oxide electrode materials, NCA is thermally and electrochemically stable.^{5,137} The combination of Ni, Co, and Al ions has been demonstrated to make the lattice more robust during cycling even over large lithiation ranges. The increased structural stability stems from the smoothing or removal of phase transitions during cycling which reduces the strain that the lattice is subjected to and minimizes the degree of mechanical degradation.^{102,138,139}

NCA's layered structure is also stable against bulk decomposition throughout the entire lithiation range. Unlike some similar electrode materials, NCA's bulk doesn't have the propensity to form the spinel structure, even when at the ideal lithiation for transitioning to this structure ($\text{Li}_{0.5}\text{Ni}_{0.8}\text{Co}_{0.15}\text{Al}_{0.05}\text{O}_2$). The presence of 0.15 Co and 0.05 Al ions, which remain in the 3+ valence state at that state of charge, is sufficient to prevent bulk migration of any of the transition metals to the tetrahedral site necessary to form the spinel structure. While the bulk layered structure is stable against degradation, decomposition phases have been observed on NCA's surface.^{95,140} Since the surface is susceptible to oxygen loss the energy barrier to forming spinel and rocksalt-type structures is significantly reduced.¹³⁷

As a result of the enhanced structural stability, particularly the more gradual phase changes during lithiation/delithiation, NCA has great electrochemical properties. Not only can the material be reversibly charged to high degrees of delithiation, but the Co and Al ions also help increase the voltage profile relative to LiNiO_2 .^{132,134,141,142} Additionally, NCA benefits from a relatively high Li^+ diffusivity, and an impressive cycling stability.^{91,143} In summary, NCA is a great layered oxide positive electrode material, because its particular mixture of Ni, Co, and Al ions lowers its fabrication cost, increases its structural stability, and enables its superior electrochemical capabilities.

1.9 Approach

While Li-ion batteries suffer from inefficiencies on all of the electrochemically active and inactive components, the positive electrode material is frequently identified as a main obstacle to increasing the energy density, safety, and relative cost. A multitude of strategies have been proposed to improve the electrochemical performance of the positive electrode. Some include replacing the layered oxide materials with lithium spinel materials, which have similar chemistries but different crystal structures.¹⁴⁴ These materials generally operate at high potentials, but are limited by their relatively low capacities and propensity for transition metal dissolution

from the positive electrode.¹ Other approaches promote the use of a different class of intercalation electrodes, which consist of metal-phosphate based materials. This approach has received substantial investment and has been made commercially available because of the relatively low production cost and superior safety characteristics. However, the volumetric and specific energy densities for these materials are low because the phosphate-based (PO_4) anions are significantly larger and heavier than the oxygen atoms (O_2) in layered oxide materials.¹⁴⁵ Recently, an abundance of attention and resources have been devoted to investigating completely new types of lithium ion batteries, such as Li-air, Li-sulfur, and fluoride-based conversion materials. While these approaches are tantalizing because of their substantially higher theoretical energy densities, both technologies are still in their early stages of development and are far from being suitable for mass market implementation.

Since the practically obtained capacities from current layered oxide materials, such as LCO or NCA, are far from their theoretical limitations much effort has been devoted to improving their performance. While full delithiation and thus attainment of the theoretical capacity has been obtained for LCO and other layered oxides at potentials greater than 4.7 V, commercial Li-ion batteries are limited to ~ 4.2 V.⁵ As a result, only $\sim 60\%$ of the theoretical energy density of the layered oxide material is utilized. The charging potential of the positive electrode is limited to ~ 4.2 V in order to maintain a suitable cycling stability and to prevent safety issues that occur at higher potentials. The rapid degradation of electrochemical performance when layered oxide materials are charged to higher potentials is mainly attributed to the structural decomposition of the layered structure and parasitic reactions between the electrode and electrolyte.^{14,17,101,146}

At high potentials ($> \sim 4.3$ V) the liquid electrolytes become unstable and react with the positive electrode materials. These parasitic reactions cause the breakdown of the electrolyte salt and solvent species and the formation of a rich cathode-electrolyte interface (CEI) on the surface of the positive electrode. The thickness and composition of the CEI is directly correlated to the

electronic and ionic impedance of the positive electrode. Thus, when layered electrodes are charged to higher potentials in the presence of a liquid electrolyte, the parasitic reactions create a thicker CEI layer on the positive electrode, which substantially increases the electrodes' impedance and reduces its electrochemical performance. As previously discussed, the thickness and chemical composition of the CEI is highly dependent upon the electrolyte salt and solvent materials, as well as the presence of any impurity species on the positive electrode or in the electrolyte. Impurity species that develop on the positive electrode when exposed to ambient air, such as LiHCO_3 , LiOH , and Li_2CO_3 , and trace amounts of moisture often react with the fluorinated electrolyte salts and form HF. The highly reactive HF molecules then react with both the positive electrode and electrolyte and decompose both materials. These parasitic reactions lead to substantial transition metal dissolution, oxygen evolution and CEI formation, which severely hamper the cell's cycling capacity and stability.

Even in the absence of a liquid electrolyte, structural degradation of the positive electrode material and a rise in impedance will occur as a result of accessing higher states of charge.^{147,148} During delithiation, the layered oxide structure endures substantial structural transitions which cause large volumetric changes to the unit cell and high internal stresses. The instability of the highly delithiated layered oxide material can cause irreversible transformations to "spinel-like" and "rocksalt-like" structures.¹⁴⁸ Furthermore, large internal stresses caused by volumetric changes during cycling have been shown to cause micro-cracking within individual particles as well as particle isolation.⁹³ Micro-cracking of the primary positive electrode particles increases the positive electrode's surface area which can result in additional CEI formation and particle isolation.⁹⁴ Particle isolation occurs when an individual or group of particles becomes electronically disconnected from the rest of the positive electrode and cannot participate in electrochemical reactions. All of these mechanisms contribute to higher electrode impedance, reduced capacity, and diminished cycling stability.

Multiple approaches have been pursued to alleviate the obstacles to increasing the charging potential limit and accessing the capacity at higher states of charge. By coating the surface of the positive electrode with a thin barrier material, researchers have minimized the electrode-electrolyte reactions that occur at elevated potentials, and mitigated the resulting impedance development.^{149–151} While their results are promising, the exact mechanisms in which these coatings restrict parasitic reactions aren't well understood, and the coatings don't reduce the internal stresses and subsequent micro-cracking. Moreover, the deposition methods generally used to coat the positive electrode materials are too expensive and impractical for mass market implementation. Other strategies have attempted to minimize the undesirable electrode-electrolyte reactions by tailoring the CEI composition through changes to the positive electrode and electrolyte chemistries. In terms of the number of ways to implement this concept, this approach is broad. Efforts have been made to control the CEI through the use of electrolyte additives, dopants to the positive electrode, as well as complete substitution of the electrolyte salt, solvent, and the layered oxide material. Presently, the success of this methodology has been limited by an insufficient comprehension of the complex reactions that occur between the electrode and electrolyte. Additionally, the effects that many of the positive electrode dopants and electrolyte additives have on the structural stability of the positive electrode are not well understood. In general, a poor understanding of the electrode-electrolyte reactions and the structural transitions that occur in the positive electrode at high states of charge have prevented the discovery and implementation of strategies to enable reliable utilization of the capacity at elevated potentials.

To enable the development of informed approaches towards reducing the parasitic reactions and structural instabilities of layered oxide materials at high states of charge, the following chapters are devoted to investigations into the underlying science behind these reactions and the structural transitions that occur in highly delithiated layered oxide materials. Chapter 3 provides insight into the electrode-electrolyte reactions that occur at high states of charge and the resulting impact on the positive electrode material's structure. Particular attention

was given to the cause and consequences of transition metal dissolution from the positive electrode. The following section, Chapter 4, was focused on the formation mechanisms of the main surface impurity species that develop on layered oxide materials and their individual impacts on the electrode's electrochemical performance. This work clarifies considerable ambiguity regarding which impurity species have profound impacts on the material's impedance and cycling stability. In Chapter 5, relationships were established between the transition metal composition of the layered oxide material and the material's structural stability during full delithiation. The use of *in-situ* XRD, *operando* microcalorimetry, and multiple electrochemical techniques enabled the elucidation of the phase changes within the positive electrode material during cycling to 4.75 V, and the influence that these structural transitions have on the material's cycling stability. Together, this work addresses critical issues in current Li-ion batteries by building upon the collective understanding of the failure mechanisms prevalent when layered oxide electrodes are highly charged and encouraging the progression of technologies designed to increase the operating potential of these electrode materials.

2 EXPERIMENTAL TECHNIQUES

2.1 Introduction

To investigate the behavior of layered oxide positive electrode materials at high states of charge, multiple characterization and experimental techniques were used; these techniques are briefly introduced in the following sections of this chapter. The methods applied to this work are diverse and span from material synthesis to bulk and surface characterization to electrochemical analysis of the positive electrode materials. The following brief overviews of each technique are intended in to introduce the reader to the advantages, limitations, and basic operating principles of the technique in order to facilitate an enhanced comprehension of the work presented in the subsequent chapters. Particular focus is given to how the techniques were applied to this work and to the materials that they characterized.

2.2 Synthesis of Layered Oxide Materials

The goal of the material synthesis portion of this work was to develop and investigate high quality positive electrode materials, with the aim of correlating the material's chemistry and structure to its electrochemical performance. Many materials with differing chemistries and crystal structures were synthesized using nearly identical fabrication methods for use as layered oxide positive electrodes. All the synthesized materials derive from mixtures of metal-acetate precursors. The precursors were individually measured so that the lithium and transition metal ratios present in the precursors are identical to that of the desired oxide material. The metal-acetate mixture was then dissolved in deionized water, mixed thoroughly, and heated to remove all of the moisture. By dissolving the precursors, a solution of the metal and acetate ions was created and was stirred until well mixed. As the water was subsequently removed during a heating process, the ions precipitated into small particles with a homogenous distribution. The dried powder was then thoroughly ground with a mortar and pestle, which decreased the average particle size and increased the surface area of the material. A higher surface area and decreased

particle size is advantageous because it aids the evolution and evacuation of undesired reaction products (i.e. H_2O , O_2 , and CO_2), which in turn improves the reaction kinetics and purity of the desired product.

Each material was annealed twice in a sealed tube furnace with a flowing O_2 atmosphere. The flowing O_2 atmosphere was critical to removing gas byproducts and maintaining high oxygen partial pressure, which was necessary to form a pure oxide material with good lithium/transition metal ordering. After each anneal, the reaction product was ground with a mortar and pestle to again reduce the average particle size and create a homogenous mixture. Ensuring that the material was well mixed prior to the second anneal was crucial to offsetting any thermal gradients within the reaction chamber that may have caused an inhomogeneous product after the first anneal. Other than the chemistry of the reactants, the annealing step's thermal procedure is the primary determinant of the product's ultimate chemical and structural identity. While the heating and cooling ramp rates were restricted by the limitations of the tube furnace (which could crack with large thermal gradients), there was flexibility in choosing the annealing temperature and dwell time. The annealing temperature needed to be precisely controlled to ensure the temperature was high enough for the precursor reaction to proceed, but low enough to prevent degradation of the layered oxide material. Moreover, the temperature has a direct impact on the reaction kinetics and on the competing nucleation and growth mechanisms. Thus, the annealing temperature and the dwell time at that temperature were carefully chosen and iteratively tested to achieve the desired material, crystal structure, and approximate particle size.

In order to produce a high quality product, precaution was taken to avoid any potential contamination. Only high grade chemicals were used; all instruments contacting reactants or products were thoroughly cleaned prior to use. At the conclusion of the synthesis process, materials were stored in either an inert or dry atmosphere to preserve their structural and chemical integrity.

2.3 X-ray Diffraction (XRD)

X-ray diffraction (XRD) is a commonly used technique to glean information about a material's structure, chemistry, crystallite size and internal stress. This characterization technique operates by radiating a sample with a monochromatic x-ray source that predictably scatters upon interaction with the sample. The angles in which the x-rays are scattered are measured by a detector, or – more commonly – the intensity of the scattered x-rays at a particular angle is incrementally measured over a wide diffraction range. Solid materials can have either a crystalline (long order repeating unit cell), amorphous (no long order repetition) structure, or some combination of the two. The uniformly repeating structure in crystalline materials enables coherent diffraction of the x-rays, which is measured as higher x-ray intensities at certain angles. On the other hand, amorphous materials diffract the x-ray radiation randomly in all directions and the measured signal cannot be discerned from the background noise. For crystalline materials, the angle at which the incident x-ray beam is diffracted is based on the d-spacing (d) between the crystallographic planes, and is numerically shown in Equation 2-1, where n is the order of reflection (usually 1), λ is wavelength of the incident x-ray photons, and θ is the angle of the diffracted x-rays relative to the crystallographic plane off of which they are diffracted:

$$\text{Equation 2-1:} \quad n\lambda = 2d \sin \theta$$

Since a lattice structure will have a multitude of crystallographic planes, each crystalline sample will have multiple diffraction peaks and each peak is individually correlated to a particular d-spacing between a unique set of planes.

Crystallographic planes are often denoted by their Miller indices, which is a notation system based on how often a plane repeats itself in a lattice. Generally, a crystallographic plane has three Miller indices (hkl), where each of the indices relates to the frequency of repetition within a Cartesian axis. Although, some planes in a hexagonal lattice can be described with four indices. The high degree of symmetry for crystalline structures enables a geometric relationship

between the Miller indices of a crystallographic plane and its d-spacing. As a result, measurement of the angle in which x-rays of a known incident wavelength are diffracted is directly related to the unique orientation of the diffracting plane within the structure. By measuring a sufficient number of these diffracting planes, the specific crystal structure of a sample can be discerned.

Beyond the diffracting crystallographic plane, the intensity and angle of the scattered x-rays are strongly influenced by the type of the atoms in the sample, the crystallite size of the material, and the stress within the sample. Since an incident x-ray is diffracted by an atom's electrons, the electron density surrounding an atom will affect how efficiently the incoming radiation is scattered, and is quantified by the atomic scattering factor. In general, elements with a higher Z number are more effective at scattering x-rays because of their higher number of electrons, and additional electrons in lower energy states. Because x-rays aren't scattered coherently at the grain boundaries between particles, the average crystallite size of a material has significant ramifications on the breadth of the measured diffraction peak. Scherrer's equation (Equation 2-2) numerically relates the crystallite size (τ) to the line broadening (β_τ) of a diffracted peak.

$$\text{Equation 2-2:} \quad \tau = \frac{K\lambda}{\beta_\tau \cos \theta}$$

Here, K is a dimensionless shape factor, and θ is the angle at the most intense point of the diffraction peak. Strain within a lattice causes the distortion of the atomic arrangement and thus alters the d-spacings of the crystallographic planes. A compressive stress will shrink the d-spacing while a tensile stress would enlarge it. As was shown by Equation 2-1, a change to the d-spacing between planes will distort the angle in which the x-rays are diffracted. Since the lattice defects which often cause the strain, generally cause both compressive and tensile stresses, slight positive and negative deviations to the diffracted angle are measured. The effect of strain

broadening (β_e) on the diffracted angle is represented by Equation 2-3, and a cumulative equation representing both types of broadening is given in Equation 2-4.

$$\text{Equation 2-3:} \quad \beta_e = C\varepsilon \tan \theta$$

$$\text{Equation 2-4:} \quad \beta_{total} = \beta_\tau + \beta_e = C\varepsilon \tan \theta + \frac{K\lambda}{\tau \cos \theta}$$

Where C is a dimensionless relationship constant and ε is the lattice strain.

XRD is a particularly useful technique for measuring the chemistries and crystal structures present throughout the entire sample, especially given its relative ease of use. The technique is a bulk characterization method so it is limited in its precision and spatial resolution compared to some other techniques. Each XRD scan is influenced by numerous factors, such as: particle size, strain, chemistry, crystallographic structures, temperature, and sample orientation. This makes calculation of any particular parameter extremely tedious and dependent on multiple assumptions. Reitveld refinement uses a least squares regression analysis to simultaneously calculate every input parameter, and makes analysis of XRD scans substantially faster and more comprehensive. The user exercises ample control over which parameters the simulation should focus on, and in providing approximate sample information (e.g. crystal structure or chemistry). While Reitveld refinement is a powerful and robust tool, it is highly dependent on accurate inputs from the user. Since Reitveld is a least squares calculation it will always produce a result and the responsibility is on the user to ensure the methodology and relevance of the calculation.

2.4 Microcalorimetry

Microcalorimetry is a method of thermal characterization that measures the heat flux from a sample as a function of time and temperature. In this work, microcalorimetry was utilized to measure the heat flux of Li-ion cells as they were electrochemically and thermally stressed. A MMC 274 Nexus multimode calorimeter with a high-temperature coin cell module (Netzsch) was used for all microcalorimetry measurements, and a schematic diagram of the sample holder and heat flux sensors is shown in Figure 2-1.¹⁵² This instrument was specifically designed to test

batteries, particularly those with a coin cell geometry. As is evident from Figure 2-1, the sample coin cell is pinned flush to the heat flux sensor by a copper arm that doubles as one of the two electronic leads. The other lead is the thin Al foil that covers the heat flux sensor, and together these two leads enable the cell to be electrochemically tested while the microcalorimeter is in operation. On the opposing side of the sample coin cell is a reference cell that is comprised of the inactive coin cell parts and negates the thermal impact of those components. The instrument operates by measuring the difference between the heat fluxes measured from the sample and reference cells. During operation, the entire apparatus shown in Figure 2-1 is enclosed in a thermally insulating chamber that is precisely set at a desired temperature.

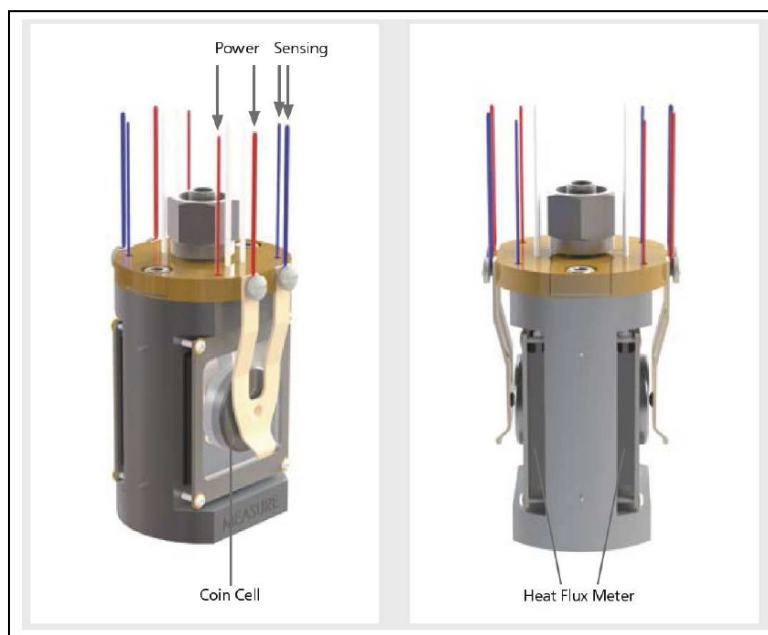


Figure 2-1: Schematic diagram of the coin cell holder, heat flux sensor and electrochemical leads of a MMC 274 Nexus multimode calorimeter is shown.¹⁵²

In an electrochemical cell the 5 main sources of heat that will contribute to the measured heat flux include: entropic heating, resistive heating, heat of mixing, heat capacity, and the heat derived from side reactions. Entropic heating is a reversible heat source that comes from the thermodynamically determined heat released or absorbed by a material as it undergoes a reaction or phase transition, and can be quantified by Equation 2-5 for each unique reaction.

$$\text{Equation 2-5:} \quad Q_{\text{entropy}} = T \Delta S \frac{I}{nF} = IT \frac{dU}{dT}$$

Where Q_{entropy} is the entropic heat, T is temperature, S is entropy, I is current, F is Faraday's constant and n is the number of moles in the reaction. As shown by Equation 2-5, Q_{entropy} can be more broadly described as the change in energy with temperature multiplied by the absolute temperature and current. When a current is passed through a material, imperfections in the electronic pathway cause a resistance and parasitically convert some of the electrical energy into heat. This resistive heating is irreversible and in accordance with Equation 2-6 is directly related to the electrical current and the resistance of the electronic pathway.

$$\text{Equation 2-6:} \quad Q_{\text{resistive}} = I^2 R = I \eta$$

$Q_{\text{resistive}}$ is the heat from resistive heating, R is the electronic resistance of the material or cell and η is the overpotential of the cell.

As an electrochemical reaction proceeds within a material, concentration gradients are developed due to the kinetic limitations of the diffusing ionic species. These concentration gradients induce a thermal signature called the heat of mixing, which can be either endothermic or exothermic. As the concentration gradients diminish over time, so does the heat of mixing. The magnitude of this type of heating is proportional to the magnitude of the concentration gradient, and becomes particularly pronounced when the electrochemical cell is charged or discharged rapidly. A material's heat capacity is the amount of heat necessary to raise the temperature of the material by one degree. Thus, in order to change the temperature of a material or system, a heat transfer is necessary, and is numerically shown in Equation 2-7.

$$\text{Equation 2-7:} \quad Q_{C_p} = C_p \frac{dT}{dt}$$

Here, the heat capacity (C_p) of a material and the rate in which the temperature is changed with time directly contributes to the heat from the material's heat capacity (Q_{C_p}). The final source of heat is the heat derived from the side or parasitic reactions. While these reactions produce heat from the entropic changes of their reactants similar to the entropic heat source previously

mentioned (Equation 2-5), these reactions are outside of the scope of the desired electrochemical reaction and are thus difficult to anticipate and theoretically quantify. The most common sources of parasitic heat are from the formation of the SEI/CEI and from any decomposition of the electrolyte.

During the calorimetric analysis of the battery all of these heat sources may be present, sometimes simultaneously, and the difficulty lies in the deconvolution of the measured heat flux. By carefully designing the experimental procedure in which the cell is tested, each heat source can be isolated or calculated, which enables microcalorimetry to be an extremely useful technique for determining an active material's intrinsic properties. One of the key advantages to microcalorimetry is that the chamber temperature can be finely controlled and the instrument can operate isothermally or with a varying temperature.

2.5 Thermogravimetric Analysis

Another thermal characterization technique is thermogravimetric analysis (TGA) which measures the change in mass as a function of temperature and time. The sample is loaded onto an inert pan which is subsequently placed in a small, thermally insulated chamber. As the material is heated, a gas is flowed through the reaction chamber and the mass of the sample is continuously measured. By correlating the magnitude of the change in mass to the temperature in which the mass change occurred, the specific reaction can be elucidated. A change in mass can result from the evolution of species such as moisture evaporating from the sample, from the decomposition of the sample that produces a gaseous product, or from a chemical interaction between the sample and the atmospheric environment. In all of these cases, the temperature in which the reaction occurs is directly related to the thermodynamic stability of the reactants. Furthermore, the magnitude of the mass change is associated with the amount of material participating in the reaction and with the specific chemical reaction. Thorough analysis of these two measurements

permits the determination of the exact reaction and thus gives insight into the chemical and thermal stability of the sample.

The two main parameters that can be adjusted to tailor the TGA experiment are the thermal procedure and the atmospheric environment. TGA can operate under constant heating or isothermal conditions, or a combination of the two. While a slower heating rate facilitates a more accurate identification of the temperature that a reaction starts and ends, it also extends the total measurement time. Similarly, isothermal segments are advantageous for isolating particular reactions that occur at a specific temperature, and for allowing a reaction to be completed before continuing the temperature change, but prolonged isothermal segments may increase the experiment time significantly. While the main objective of the atmospheric environment or “flow gas” is to carry away any evolved gases from the sample, it can also be used to react with the sample. An inert gas, such as Ar, will permit the measurement of the intrinsic thermal stability of the sample, while using a flow gas that reacts with the sample will give insight into the tendency for the sample to react with that gas.

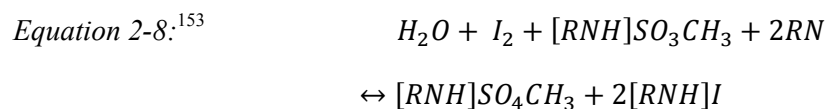
2.6 Brunauer-Emmett-Teller (BET) Analysis

Brunauer-Emmett-Teller (BET) analysis is the primary characterization technique for measuring the surface area and pore size distribution of a bulk material. BET operates by manipulating the adsorption of an inert gas on a sample’s surface. N₂ is the most commonly used “inert” gas but other materials such as Ar, and Kr can be substituted. Regardless, of which gas is used the operating mechanism is unchanged. A sample is placed in a sealed glass vessel and heated to sufficiently high temperatures under a vacuum to remove any adsorbed or absorbed species. Once the sample’s surface is removed of all adsorbed species, the glass vessel is filled with N₂ gas, which adsorbs on the sample’s surface. The process of evacuating the glass tube and filling with N₂ gas is subsequently repeated at different temperatures and pressures. During each cycle the equilibrium and saturation pressures of the N₂ on the sample is measured at the specific

temperature of adsorption. Since the amount of N_2 that adsorbs on to the samples is related to the magnitude of sample's surface, a quantitative value for the sample's surface area can be calculated from the pressure and temperature measurements.

2.7 Karl Fischer (KF) Coulometric Titration

Karl Fischer coulometric titration is an accurate way to measure the water content of a solid or liquid sample. During testing, an electrolyte comprised of a methanolic solution of iodine, sulfur dioxide, and a base is continuously stirred in the titration cell's main chamber.¹⁵³ When water is added to the electrolyte, it reacts with the sulfur dioxide and iodine and generates a charge that is detected by two Pt electrodes which are submersed in the electrolyte. The amount of charge passed between the two electrodes is directly related to the iodine in the solution and thus the amount of moisture in the sample can be calculated from the charge transferred during the experiment. The titration is concluded when an induced alternating current between the two electrodes remains constant, indicating that the amount of iodine in the electrolyte is unchanged. The reaction equation taking place during KF coulometry analysis is given in Equation 2-8.



In order to extract the moisture from solid samples, they need to be heated to high temperatures (~150-250°C) and an inert flow gas is used to transport the vaporized moisture to the titration chamber. A small volume of a liquid sample can be added directly to electrolyte solution assuming that the sample's solvent is compatible with the KF electrolyte. KF coulometric titration is a simple characterization technique that excels at providing accurate measurements of the moisture content, especially at more dilute concentrations. While it is a destructive characterization technique, only a small amount of sample is necessary unless the moisture content is extremely low.

2.8 Inductively Coupled Plasma – Optical Emission Spectroscopy (ICP-OES)

Precise chemical analysis of various materials was completed by inductively coupled plasma – optical emission spectroscopy (ICP-OES). ICP-OES is a destructive technique that uses a plasma created by introducing Ar gas into an intense electromagnetic field to ionize a liquid solution. Prior to interacting with the Ar plasma, the liquid solution is changed to a fine mist by an analytical nebulizer which disperses the sample and ensures that the entire sample is ionized. As the sample collides with the plasma, it is immediately decomposed to individual atoms, which are then stripped of some electrons and made into ions. As the atoms are ionized they emit a radiation that is characteristic of their atomic number. The emitted radiation is subsequently measured and permits the identification and quantification of the exact chemical makeup of the initial sample. Since the sample needs to be in the liquid state prior to testing, solid materials are dissolved in highly acidic solutions. When preparing a solid sample for ICP-OES analysis by dissolving it in an acidic solution, it is critically important to ensure that the acidic solution does not contain any impurity ions that may alter the measurements results.

2.9 Fourier Transform Infrared Spectroscopy (FTIR)

While XRD, TGA, and ICP-OES each give insight into the chemical identity of the entire sample, Fourier transform infrared spectroscopy (FTIR) provides information on chemical bonds present mainly on the sample's surface. FTIR is a form of infrared spectroscopy, which illuminates the sample with infrared radiation and measures the resulting signal. The sample can be in the solid, liquid, or gaseous phase, although only solid materials were analyzed as a part of this work. The wavelength of the incident infrared radiation is varied within a predetermined range by adjusting the position of a mirror in the instrument's apparatus. Because repositioning the mirror and taking individual measurements at every wavelength over a desired range is intensive and time consuming, measurements are taken at periodic intervals, and a Fourier

transform function is utilized to create a continuous spectrum over the entire range of wavelengths measured.

The resulting spectrum shows the absorbance of the sample as a function of wavenumber (inverse wavelength). Peaks in the spectrum signify the wavelengths that were particularly well absorbed by the sample and give critical information about the chemical bonding within the sample. The sample absorbs the incident infrared radiation by inducing rotations or vibrations in the material's chemical bonds, and is therefore a measure of the internal energy states of the sample material. Because the bonding energies between atoms are discrete and dependent upon the electronic configurations of the atoms and upon the bonding type (single, double, etc), analysis of the FTIR spectrum provides details of the chemical species in the sample. As the concentration of each unique bond increases, so will the material's absorption of the wavenumbers corresponding to that energy.

FTIR is mainly operated in two distinct modes: attenuated total reflection (ATR) and transmission. The fundamental principles are the same for both modes but the different instrument geometries provide each method with some significant advantages. Testing in the ATR mode is simple, fast, and accurate provided that there is good physical contact between the sample and the crystal, through which the infrared radiation is emitted. In ATR, the incident beam is transmitted through a low absorption crystal to the sample and then bounced between the sample and the crystal multiple times before being measured by a detector. However, the transmission mode, which measures the infrared radiation transmitted through the sample, is sometimes preferred because it has better sensitivity, especially for quantitative analysis. The percentage of the infrared radiation that is absorbed by the sample in transmission mode is proportional to the material's absorbance, thickness, and concentration. Since the sample thickness and concentration are often known properties, it is easy to calculate the intrinsic absorptivity of the sample material.

While it is not always possible to physically measure the thickness of the target material, quantitative analysis through FTIR can also be achieved by mixing the sample with a known quantity of a reference material. As long as the relevant absorption features of the sample and reference materials are distinct and the amount of reference material is known, a comparison of the magnitude of the sample peaks to the reference peaks will give quantitative information on the concentration of the sample. This method is shown to be particularly useful when analyzing the surface species that develop on positive electrode materials. Since FTIR measures the absorbance of the sample it is not well suited to investigating a material's bulk, especially for ATR mode which relies on reflection of the incident radiation off of the sample's surface.

2.10 Electrochemical Analysis

Several electrochemical characterization techniques were utilized throughout this work. Of which, galvanostatic cycling, potentiostatic intermittent titration technique (PITT), and electrochemical impedance spectroscopy (EIS) were the most important. Galvanostatic cycling is the process of applying a known current to an electrochemical cell while continuously measuring the cell's voltage. As explained in section 1.2, the applied charge is directly associated with the movement of the Li ions within the cell. By alternating the direction of the current, the cell can be charged or discharged in a controlled fashion. Potential limitations are generally imposed to dictate the beginning and end of the charging and discharging segments, although the total accumulated charge (i.e. lithiation) can also be used.

In contrast to galvanostatic cycling, where a current is applied and the voltage is measured, potentiostatic techniques control the voltage and measure the resulting charge passed. PITT is a potentiostatic technique that utilizes small potential steps followed by long relaxation times. By incrementally increasing (or decreasing) the potential and then measuring the subsequent current response for a long time or until it becomes negligible, the near equilibrium reaction dynamics can be measured. Unlike galvanostatic cycling where sizeable currents are

applied and an overpotential is expected, PITT uses small steps and the polarization effects are reduced as much as possible.

Important information about the electrochemical reactions in the cell can be determined from the results of either technique. The voltage profile gives insight into the energies at which the electrochemical reactions take place and into whether the reaction proceeds by a single phase or two phase mechanism. Furthermore, repeated cycling can show whether reactions are reversible or whether they differ as a function of time or cycle number. The accumulated charge is related to the magnitude of the reaction and is critically important for understanding the capacity of the cell. In PITT, the current response at each potential step is useful for discerning whether a reaction is single or two phase and can be used to calculate the Li^+ diffusivity and reaction kinetics. The main advantage of PITT is that it provides an electrochemical analysis of the cell near the cell's equilibrium conditions, which is particularly useful for understanding the fundamental mechanisms driving the reactions during cycling. Since the C-rates for galvanostatic cycling are generally much higher than an equivalent rate for PITT, galvanostatic cycling mimics more practical scenarios and enables substantially more rapid analysis.

EIS is a commonly used method for investigating the magnitude and source of impedance in an electrochemical cell. During EIS, a small alternating current potential is applied to the electrochemical cell at different frequencies and the resulting current signal is measured. Analysis of the current signal's magnitude at each frequency and the phase changes of the measured signal relative to the input potential, reveals a complex relationship that can be carefully deconstructed to identify and quantify various sources of impedance within the cell. Since EIS is non-destructive, relatively fast, and only requires the leads already used to cycle the cell, it is often used in conjunction with cycling. This enables the periodic measurement of impedance as a function of state of charge, or from any type of ageing (e.g. electrochemical, thermal, or time), and is useful for understanding how the different factors affect the internal resistance and electrochemical performance of the cell. Moreover, the use of a wide range of frequencies often

permits the assignment of impedances to specific parts of the cell. For example, the impedance attributed to the electrical contacts, is often distinct from the impedance due to the negative or positive electrodes, or from that associated with the long range diffusion of Li ions.

2.11 X-ray Photoelectron and Absorption Spectroscopies

X-ray photoelectron spectroscopy (XPS) and x-ray absorption spectroscopy (XAS) are two sophisticated surface characterization techniques that can provide detailed information about the chemical bonding on a sample's surface and sub-surface regions. While both XPS and XAS illuminate the sample with a high energy monochromatic x-ray beam, and measure the subsequent photons or electrons emitted by the sample, they differ based on the mechanism in which the electrons are emitted. When the incident x-rays interact with the sample, core electrons can be ejected directly to the vacuum, and can be measured by either XPS or XAS. XAS can additionally measure the signatures of electrons excited to higher unoccupied energy states or of the fluorescent radiation that is emitted during recombination of the core hole created by the incident x-ray beam. As the energy of the incident x-rays is scanned over a relevant range, the number and energy of the electrons emitted are measured by a detector. Since the energy necessary to excite an electron from a core state is known for each material, the electrons emitted can be correlated to specific electronic transitions. With this information both techniques can determine the bonding energy between atoms, and thus determine the type of elements present and their bonding environments.

As a result of using high energy photons, the wavelengths of the photons are small ($\sim 1 \text{ \AA}$) and thus the penetration depth of the x-rays is relatively short. For this reason, both techniques are surface sensitive and not as effective at measuring beyond the material's sub-surface. Due to the need for higher incident x-ray energy resolution and increased photon flux, XAS experiments are usually performed at synchrotron radiation sources, whereas XPS is more suitable in a conventional laboratory setting. Typically, the XAS spectrum is partitioned into two regions,

named: *i*) x-ray absorption near edge spectroscopy (XANES) and *ii*) extended x-ray absorption fine structure (EXAFS). XANES includes the region including and around the x-ray absorption edge, while EXAFS consists of the region beyond the absorption edge. Because the two regions each target different energy levels they measure different but complementary interactions in the sample. Analysis of the entire XAS spectrum permits a robust determination of the chemical and bonding environments within the sample.

2.12 Electron Microscopy and Associated Techniques

Compared to light microscopy, electron microscopy is advantageous because it has much better spatial resolution. The high energy electron beam used in either scanning electron microscopy (SEM) or transmission electron microscopy (TEM) has a small de Broglie wavelength, which enables the spatial resolution to be well below 1 Å. While both of these electron microscopy techniques use a highly focused electron beam, the characterization methods differ substantially. In SEM, an electron beam with a small diameter is methodically scanned over the sample and the secondary and backscattered electrons are measured. The beam is repeatedly scanned over the material and because of its small probing area, produces detailed images. Due to the nature of secondary and backscattered electrons, which will recombine quickly if not in a vacuum, SEM is good at collecting data from the surface of the sample, and not from the interior. Because of its flexibility, ease of use and the ability to take high quality images, this technique is advantageous for understanding a material's morphology and uniformity. The electron beam used in SEM can also eject a core electron from an atom, causing an electron from a higher energy to drop down to the lower energy state and releasing an x-ray in the process. This x-ray can be detected inside the SEM and is particularly useful because the identity of the atom can be determined based off of the energy of the emitted x-ray. The x-ray excitation and detection process is called energy dispersive x-ray spectroscopy (EDS). By counting the x-rays released

and correlating each x-ray to a specific element, EDS is often used to provide chemical analysis of materials, particularly with respect to their homogeneity.

In contrast to SEM, TEM measures the electron beam that was transmitted and diffracted through the sample. As a result, it measures both the surface and center of the material. Although, because transmission of the electron beam is difficult for all but thin materials, TEM is often limited to a particle's edge and thus mainly investigates a material's surface. The coherent diffraction measured by TEM and the small beam size makes the technique ideal for discerning information about the crystal structure and lattice properties on a localized scale. Selected area electron diffraction (SAED) is the formal name of the characterization technique that uses diffraction in TEM to investigate a material's structure. While TEM can perform EDS, it is also capable of another technique for chemical analysis called energy electron loss spectroscopy (EELS). In this method, the energy of the transmitted electrons is measured and their number counted. Since the initial energy of the electrons is known, the amount of energy that each electron lost can be calculated, and associated to a specific inelastic interaction with a particular element or ion. Similar to EDS, EELS can provide an approximate chemical distribution on a small area, and can be used to investigate the elemental homogeneity within a material..

3 ELECTROLYTE INDUCED SURFACE TRANSFORMATION AND TRANSITION METAL DISSOLUTION OF FULLY DELITHIATED $\text{LiNi}_{0.8}\text{Co}_{0.15}\text{Al}_{0.05}\text{O}_2$

3.1 Abstract

Enabling practical utilization of layered $\text{R}\bar{3}\text{m}$ positive electrodes near full delithiation requires an enhanced understanding of the complex electrode-electrolyte interactions that often induce failure. Using $\text{Li}[\text{Ni}_{0.8}\text{Co}_{0.15}\text{Al}_{0.05}]\text{O}_2$ (NCA) as a model layered compound, the chemical and structural stability in a strenuous thermal and electrochemical environment was explored. *Operando* microcalorimetry and electrochemical impedance spectroscopy identified a fingerprint for a structural decomposition and transition metal dissolution reaction that occurs on the positive electrode at full delithiation. Surface sensitive characterization techniques, including X-ray absorption spectroscopy and high resolution transmission electron microscopy, measured a structural and morphological transformation of the surface and subsurface regions of NCA. Despite the bulk structural integrity being maintained, NCA surface degradation at a high state of charge induces excessive transition metal dissolution and significant positive electrode impedance development, resulting in a rapid decrease of electrochemical performance. Additionally, the impact of electrolyte salt, positive electrode surface area, and surface Li_2CO_3 content on the magnitude and character of the dissolution reaction was studied.

3.2 Introduction

Meeting the power requirements of the next generation of portable electronics and electric vehicles will depend on significant advancements in the energy density of secondary Li-ion batteries. Layered ($\text{R}\bar{3}\text{m}$) oxide cathodes materials, such as LiCoO_2 (LCO) and $\text{LiNi}_{0.8}\text{Co}_{0.15}\text{Al}_{0.05}\text{O}_2$ (NCA), are presently incapable of practically achieving their theoretical capacities because of an intricate and not yet fully understood combination of structural degradation and adverse cathode-electrolyte interactions that occur when approaching full

delithiation. Stabilizing these materials at or near full delithiation would enable additional capacity while having a negligible impact on the cell weight and volume, resulting in increased specific and volumetric energy densities.

The initial theories for failure of layered compounds pointed to the exfoliation of the transition metal oxide layers of $R\bar{3}m$ compounds due to coulombic repulsions from opposing oxygens as a result of the removal of the Li^+ ions which act as a coulombic screen. This theory was disproved approximately 20 years ago by the realization of the CdI_2 structure of fully delithiated CoO_2 and the reinsertion of over 96% of the lithium in the subsequent discharge.¹⁷ Similar investigations revealed a degree of structural stability of NiO_2 and other layered compounds.¹⁵⁴ However, achieving practical reversibility of the fully delithiated structures has remained an elusive but important goal for many in the field. The challenge is complicated by the aggregate of failure modes present to various degrees amongst the entire $R\bar{3}m$ family. These range from electronic and/or ionic isolation induced by large lattice parameter changes resulting in electromechanical grinding, possibilities of bulk movement of the transition metal ions, and undesired surface reactions.^{104,155,156} Surface reactions represent a primary obstacle to overcome as they are represented by a complex symbiotic interaction between the positive electrode surface and electrolyte decomposition.

Multiple studies have explored the complex interactions that these materials have with alkyl carbonate solvents and commonly used Li salts. Particularly important – and easiest to comprehend – are the acid-base reactions that occur as a result of the trace levels of HF found in solutions containing LiPF_6 salt.^{27,157} These reactions lead to the formation of electronically and ionically insulating LiF on the cathode's surface as well as causing transition metal dissolution.^{27,128,157} The acid induced decomposition reaction produces H_2O as a byproduct, making the dissolution mechanism autocatalytic.¹²⁰ Elevated temperatures encourage the propagation of this reaction, leading to rapid structural degradation and transition metal

dissolution.^{27,120,128,157} Furthermore, catalytic transition metal oxides, especially when delithiated, can polymerize various solvents and salts, resulting in the development of a complex cathode-electrolyte interface (CEI).^{84,85,121,158} X-ray photoelectron spectroscopy (XPS) and Fourier transform infra-red spectroscopy (FTIR) measurements of cathode materials aged in ethylene carbonate (EC): dimethyl carbonate (DMC) solutions containing LiPF₆ salt have observed a host of decomposition products including: LiF, Li₂CO₃, transition metal fluorides, polycarbonates, P-O-F compounds, and reduced metal oxides.^{84,121,158} For each cathode material, the composition of the CEI is dependent upon the type of salt and solvent^{159,160}, the presence of additives^{159,161}, temperature^{159,160,162,163}, and state of charge (SOC).^{162,163} The magnitude and chemical makeup of the CEI significantly impacts the charge transfer impedance at the cathode and can be detrimental to the cell's overall performance.^{121,159,161,163}

At high states of charge, layered oxide cathode materials experience substantial structural changes in the surface and subsurface regions. When these electrodes are extensively delithiated, loss of oxygen can occur, thereby reducing transition metal ions from the 3b sites and allowing them to diffuse to some of the vacant 3a sites resulting in a structural transition to a disordered spinel-like (Fd3m) phase.^{29,164} Further delithiation results in complete interlayer mixing, continued reduction of the transition metals to the bivalent state, and the release of oxygen to form a more stable rocksalt-like (Fm3m) structure. Because oxygen loss can be difficult in the bulk, rocksalt-like phases are generally observed on the edges of the particles.^{89,95} The resulting lithium deficient phases are responsible for increased electrical and chemical impedance on the positive electrode, which has a profound impact on the material's electrochemical performance.⁹¹ The development of spinel and rocksalt type phases are commonly found on or near the surface of NCA particles when subjected to extended cycling or elevated temperatures.^{91,165,166} After only 10 cycles, NCA particles exhibit micro-cracking which is attributed to the volume changes during cycling, inducing greater surface exposure and subsequent reaction with the electrolyte.¹⁶⁷ Recently, Sallis *et al* observed a large rise in impedance on NCA particles that were held at 4.5 V

or 4.75 V. Using TEM and XAS, they correlated the rise in impedance to the development and growth of a disordered spinel phase on the particles' surface and subsurface.¹⁴⁰

During the formation of the disordered spinel and rocksalt decomposition phases, the transition metal ions are reduced to their bivalent states.^{91,140} In their lower valance state, transition metals ions are prone to dissolution, resulting in poisoning of the negative electrode, a reduced amount of electrochemically active lithium, and increased cathode impedance. During the reduction of the transition metals, extensive oxidation of the electrolyte can occur.^{128,157,168} As a result of these mechanisms, a significant decline in cell performance is well documented.^{169–171} Transition metal dissolution has been shown to be highly dependent upon the electrode structure, thermal environment, and electrolyte composition.^{104,120,157} Additionally, it has been suggested that the electromechanical grinding that occurs in LCO during charging above 4.2 V is partly responsible for increased levels of Co dissolution.¹⁰⁴ Watanabe *et al* observed extensive micro-cracking in $\text{LiAl}_{0.10}\text{Ni}_{0.76}\text{Co}_{0.14}\text{O}_2$ particles after cycling, and the growth of a NiO-like layer on the new surfaces.⁹¹ While not directly measured, these observations support the theory that electromechanical grinding accelerates transition metal dissolution by the creation of additional electrode interfacial area with the electrolyte. However, other mechanisms for dissolution from $R\bar{3}m$ compounds may exist and need further investigation.

Isothermal microcalorimetry has been used to measure the heat flux from electrode materials as a function of thermal¹⁷², electrochemical^{173–175}, and compositional^{146,176,177} conditions. In secondary lithium batteries, the heat flux during cycling is generally attributed to five sources: entropy, resistive heating, heat capacity, heat of mixing, and the heat from parasitic reactions. Newman *et al* developed a thorough model for heat generation sources in an insertion battery^{178,179}, and then later published extensive work on the heats of mixing and entropic heating.^{180,181} Other literature has focused on the multiple sources of irreversible heating¹⁸² and the heat production as a function of the state of charge.^{173–176,183,184} The heat generation during

charge and discharge has been measured for a variety of positive electrode chemistries including: LiCoO_2 ^{173,175,185}, LiFePO_4 ^{145,172}, $\text{LiNi}_{0.8}\text{Co}_{0.15}\text{Al}_{0.05}\text{O}_2$ ^{173,186}, and $\text{Li}[\text{Ni}_x\text{Mn}_y\text{Co}_z]\text{O}_2$ ^{146,176,187} type materials. While much of the published battery research utilizing isothermal microcalorimetry is focused on the entropic and resistive heating during cycling, publications by Dahn *et al* have isolated the thermal contribution from parasitic reactions, and provided a quantitative measurement of the cathode-electrolyte reactions that occur at high states of charge.^{28,146,188–192} By exploiting the different relationships between sources of heat and the current, Dahn *et al* were able to attribute the heat flow to entropy, polarization, or parasitic side reactions. Their work focused on the heat flow over small potential windows at potentials above 4.2 V and investigated the role that different electrolytes and electrolyte additives have on the parasitic reactions.^{28,146,188,189,192}

The focus of this work is the stability of NCA at full delithiation, under constant potential (4.75 V) and at elevated temperature (60°C), to investigate the relationship between the electrode and electrolyte as well as the modifications of the surface and subsurface structures of NCA. This protocol was performed without cycling to prevent extensive micro-cracking which may induce a significant increase in electrode-electrolyte interfacial area. These conditions represent the most stressful, practical environment to evaluate such materials in order to understand the driving force towards failure at full delithiation without going to such extremes which would activate new failure modes. Although such conditions seem extreme for carbonate electrolytes, especially using LiPF_6 , it has been shown that carbonate electrolytes enable excellent reversibility for 500 cycles in high voltage spinels at 60°C with charge cutoff of 4.99 V.^{65,193} The high degree of reversibility is stable as long as the electrode material does not induce a significant decomposition reaction with the electrolyte.

Continuous measurement of the parasitic reactions on NCA cathodes was achieved through *operando* isothermal microcalorimetry and electrochemical impedance spectroscopy (EIS). These techniques enabled the determination of the magnitude and character of the parasitic

reactions as a function of voltage, temperature, and electrolyte salt. Surface sensitive characterization methods, such as high resolution transmission electron microscopy (HRTEM) and X-ray absorption spectroscopy (XAS), were employed to observe the structural and compositional changes occurring at the material's surface. Coupling these techniques with dissolution measurements obtained by energy dispersive spectroscopy (EDS) and inductively coupled plasma – optical emission spectroscopy (ICP-OES), facilitated a deeper understanding of the impact that parasitic reactions have on the structural stability of NCA and the overall performance of the cell.

3.3 Experimental

3.3.1 Materials Preparation

LiCoO₂ (Seimi) and LiNi_{0.8}Co_{0.15}Al_{0.05}O₂ (NAT1050, TODA America) were mainly used as received and electrodes were made using the Bellcore method.¹⁹⁴ Electrode tapes were cast in a dry room (<1% relative humidity) to minimize exposure to moisture. Casting slurries were a mixture of poly(vinylidene fluoride-co-hexafluoropropylene) (PVDF-HFP, Kynar 2801, Elf Atochem), carbon black (Super P (SP), MMM), propylene carbonate (Aldrich), and acetone (Aldrich). Homogenous slurries were cast and allowed to air dry. Then, the propylene carbonate plasticizer was extracted by soaking the tape in 99.8% anhydrous diethyl ether (Aldrich). Electrodes with a composition of 88.81 wt% active material, 3.91 wt% SP, and 7.28 wt% PVDF-HFP were used unless otherwise specified. To accommodate the higher surface area and Li₂CO₃ samples, an electrode composition of 79.87 wt% active, 7.03 wt% SP, and 13.10 wt% PVDF-HFP was utilized. The free standing tapes were subsequently dried at 120°C under vacuum for a minimum of 10 hours and then stored in an Ar-filled glovebox to avoid atmospheric exposure. High surface area NCA was achieved by high energy milling the pristine material for 15 minutes at 400 rpm (Retsch PM100). Milling samples were prepared in an Ar-filled glovebox, where the dried powder was sealed in a zirconium oxide-lined milling cell. After milling the cell was

returned to the glovebox, so the sample could be retrieved with no exposure to the ambient atmosphere. To prepare NCA samples with increased Li_2CO_3 content, samples were deliberately exposed to ambient air for two weeks by resting in a hood with constant air flow.

3.3.2 Electrochemical Characterization

Coin cells (2032, Hohsen) and three electrode cells (in-house) were assembled in an Ar atmosphere glovebox using Whatman GF/D glass fiber separators saturated with either a 1M LiPF_6 or 1M LiBF_4 ethylene carbonate, dimethyl carbonate (EC:DMC) (1:1 volume ratio) solution (BASF) (<20 ppm H_2O), and a lithium metal (FMC) negative electrode. To eliminate the signal interference and possible interactions caused by the PVDF-HFP binder, powder cells comprised of 97.5 wt% active material and 2.5 wt% carbon black were used for all XAS, XPS and HRTEM measurements. Powder cell fabrication was identical to cells with tape electrodes except that in addition to the glass fiber separator, PVdF-HFP based and polyolefin (Celgard) separators were used. Potentiostatic and galvanostatic electrochemical testing was controlled by a VMP3 (Biologic) or Maccor battery cycling system at either 24°C or 60°C. Cells were galvanostatically charged at 25 mA/g of active material ($\sim\text{C}/11$) to V_{max} (4.1, 4.5, or 4.75 V), held under potentiostatic conditions for varying amounts of time, and then discharged at 5 mA/g ($\sim\text{C}/55$) to 2.7 V. Electrochemical impedance spectroscopy (EIS) scans were carried out using the VMP3, with a frequency range of 400 kHz to 15 mHz, and a 20 mV sinusoidal amplitude. EIS scans were performed under open circuit conditions unless the cell was in a potentiostatic hold, in which case the sinusoidal amplitude was added on top of the potentiostatic potential.

3.3.3 Physical Characterization

Thermogravimetric analyses (TGA) were performed utilizing Pt pans in a TA instruments TGA 2050. Experiments were performed by heating at 5°C/min to 600°C, and then holding at 600°C for 5 hours. Flowing dry air was used throughout the entire test. Multipoint Brunauer-Emmett-Teller (BET) surface area experiments were conducted on a Micromeritics ASAP 2020

analyzer using N₂ gas. Samples were degassed under vacuum at 120°C for at least 20 hours prior to evaluation.

ICP-OES analysis was completed by Galbraith Laboratories, Inc (Knoxville, TN). ICP-OES samples were prepared by dissolving Li negative electrodes in 37 vol% HCl, and adding DI water until the total volume was 7 mL. All cells for ICP-OES testing were assembled using additional Cu current collectors to prevent transition metal contamination from the stainless steel cell body. The average sample mass was 7.444 g, with all samples having a mass within 1.55% of the mean. Total amounts of Co and Ni dissolution were calculated by extrapolating the measured concentration to the entire sample mass. The percentage of dissolved Co and Ni was determined by dividing the mass of the measured dissolution products by the initial amount of Co and Ni present in each sample. Field emission scanning electron microscopy (FESEM) results were obtained on a Zeiss microscope and energy dispersive x-ray spectroscopy (EDS) data was measured with a INCAPenta FETx3 detector (Oxford Instruments). Samples were exposed to the ambient atmosphere for about 1 minute during sample transfer into the microscope.

The transmission electron microscopy experiments were performed using a JEOL 2010F microscope operated at 197 kV. The spatial resolution of the microscope in the high resolution (HRTEM) mode is ~ 1.4 Å. The fast Fourier transform (FFT) of the HRTEM images generates spots which correspond to crystallographic periodic arrangements of atomic planes. These spots were also used as filters to remove background noise from the high resolution images. The filtered HRTEM images provide crystallographic information from an approximate area of 16 nm². The smallest selected area aperture was used to obtain diffraction from an area within first 100 nm from the edge of the particle. All HRTEM and selected area electron diffraction (SAED) patterns were analyzed using Gatan Digital MicrographTM. In addition, the experimental SAED patterns were indexed using JEMS® software.

A Bruker D8 Advance diffractometer (Cu K α , $\lambda=1.5406$ Å) was used for all X-ray diffraction (XRD) characterization. XRD analysis of cycled electrodes was conducted by

disassembling and retrieving the sample electrode in an Ar-filled glovebox. The electrode was then washed with DMC to remove any residual electrolyte, and allowed to dry in the glovebox. To minimize atmospheric exposure, the dried samples were sealed onto glass slides using Kapton film and x-ray transparent grease, prior to leaving the glovebox. XRD scans were conducted over a two theta range of 15-70° at a scan rate of about 0.6°/min.

For all XPS spectroscopy measurements, disassembled NCA powder electrodes were mounted on conductive tape and transferred using vacuum suitcase set-ups between the glovebox and vacuum chamber to avoid any exposure to air. XPS measurements were performed using a Phi VersaProbe 5000 system at the Analytical and Diagnostics Laboratory (ADL), Binghamton University. A flood gun was used to charge compensate insulating samples, and the carbon black C 1s peak was aligned to 284.5 eV to account for possible charging effects.

Soft XAS was performed at beamline I09 at Diamond Light Source Ltd. (DLS) and beamline 8.0.1 at the Advanced Light Source (ALS) at the Lawrence Berkeley National Laboratory (LBNL). At both facilities, a vacuum suitcase set-up was employed to avoid any surface contamination. X-ray absorption spectroscopy in the surface-sensitive total electron yield (TEY) was conducted at both beamlines. Additional bulk-sensitive partial fluorescent yield (PFY) modes were performed at beamline 8.0.1 at the ALS. Measurements were repeated at both facilities whenever possible and were highly reproducible. All spectra were normalized to the current from a reference Au-coated mesh in the incident photon beam. The energy resolution was close to 0.1 eV (I09) and 0.2 eV (8.0.1) at the O K-edge. For the O K-edge, TiO₂ was used to calibrate the photon energy axis. Ni metal was used to calibrate the photon energy axis for the Ni L-edge.

3.3.4 Operando Microcalorimetry

A MMC 274 Nexus multi-mode calorimeter with a with high temperature coin cell module (Netzsch) was utilized to perform isothermal microcalorimetry and differential scanning

calorimetry experiments in parallel with electrochemistry. Samples were standard 2032 coin cells (previously described) oriented with the positive electrode flush against the sample heat flux sensor. To eliminate the thermal contribution from heat sources other than the electrodes, a reference cell consisting of all stainless steel cell parts, a separator, and an electrolyte was used. The reference cell was placed on the reference heat sensor, which is located directly opposite the sample sensor. The measured heat flux is the difference in the heat flux between the sample and reference sensors. For all microcalorimetry experiments the thermal protocol is as follows: heat to 30°C at 0.5°C/min, isothermal at 30°C for 20 hours, heat to 45°C at 0.5°C/min, isothermal at 45°C for 20 hours, heat to 60°C at 0.5°C/min, and a final isothermal step at 60°C until the end of the experiment.

3.4 Results

3.4.1 Reaction Identification

NCA half-cells were charged at 25 mA/g to 4.1, 4.5, or 4.75 V at 60°C and then held at constant voltage, as shown in Figure 3-1. After charging at constant current, cells with a 4.1 or 4.5 V cutoff showed a current decay to near 0 mA/g within 20 h or 30 h, respectively, as a result of the delithiation reaction reaching equilibrium. This current eventually relaxes into a steady state leakage current, which remains constant for the remainder of the experiment. The NCA cell with a 4.75 V cutoff also has relaxation current at the beginning of the potentiostatic segment related to the completion of the delithiation reaction. Afterwards the current plateaus to a much higher corrosion current than the analogous 4.5 V cell (1.495 mA/g vs 0.100 mA/g). In contrast to the cells at 4.1 V or 4.5 V, the current of the 4.75 V cell begins to increase after approximately 30 h at constant voltage and ultimately reaches a peak of around 10 mA/g. After peaking, a large decay in current is observed, and the current plateaus into a steady state rate. Since the potential of the negative electrode is independent of the cell's SOC and the parasitic reactions were only observed at 4.75 V, the measured peak in current is not due to a thermally induced reduction of

the electrolyte at the Li negative electrode. Any negative electrode interaction with electrolyte would be independent of the charge voltage. The elevated current is only observed at 4.75 V, so highly delithiated NCA must be necessary for the reaction to occur.

All NCA electrodes shown in Figure 3-1 consist of 3.91 wt% SP to improve the electrical conductivity. To identify any interactions between the SP and the electrolyte in this aggressive electrochemical and thermal environment, an electrode composed of only SP (20 wt%) and PVdF-HFP was tested under identical conditions. Since the SP/PVdF-HFP cell has no active material a 20 μ A charging current was used, and the mass normalized current data presented in Figure 3-1 (green) is based on the amount of SP. The SP/PVdF-HFP positive electrode has no peak in current, signifying that the peak in current experienced in the 4.75 V NCA cell, is a result of cathode-electrolyte interactions and not simply oxidation of the electrolyte. Additionally, despite having nearly 1.81X the absolute amount of SP as the 4.75 V NCA electrode, the SP/PVdF-HFP electrode did not show an increased leakage current at 4.75 V, indicating that the SP is not a catalyst for the increased current.

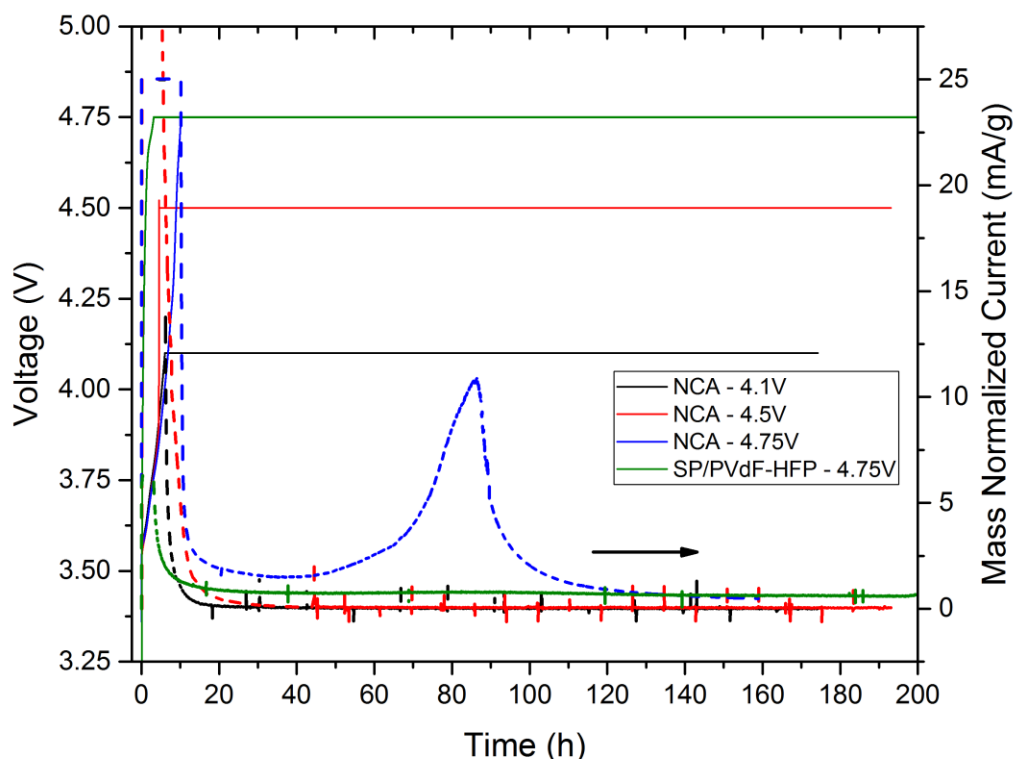


Figure 3-1: Voltage and current profiles as a function of time for NCA and SP/PVdF-HFP half-cells that were charged to and held at the upper cutoff potential while at 60°C. The upper cutoff potential was either 4.1, 4.5, or 4.75 V. Voltage and current data is scaled according to the left and right axes, respectively.

Operando microcalorimetry enables continuous monitoring of the heat flux and current, as well as intermittent impedance measurements, while providing control of the cell's electrochemical and thermal conditions. To validate our microcalorimetry set up and also provide a contrast to NCA, LCO electrodes were initially characterized. Figure 3-2 presents the heat flux (black), voltage (green), and current (blue) data from an *operando* microcalorimetry experiment of an LCO positive electrode as it was charged to 4.75 V and held potentiostatically, while under isothermal 30°C conditions. After the 4 h open circuit voltage (OCV) period, which allows the chamber temperature and heat flux signal to fully stabilize, the half-cell was charged at a constant current of 25 mA/g (~C/11). Relative to the stable background heat flux taken at the end of the OCV period, the initial delithiation reaction is endothermic and remains endothermic until the cell

potential is slightly greater than 4 V. Between ~ 4.08 - 4.28 V a significant exothermic peak is observed, which correlates to the hexagonal to monoclinic Li ordering phase transition. Immediately following this peak is a second less intense peak, which starts at about 9.25 h and is associated with the structural transition back to the hexagonal phase. As the LCO electrode approaches full delithiation, the delithiation reaction becomes very exothermic. The heat flux profiles for the LCO electrode during charging are consistent with the results from Saito *et al*¹⁷³, Kobayashi *et al*¹⁹⁵ and Miyashiro *et al*¹⁸⁵ and validate our experimental setup. Once within the 4.75 V constant voltage hold, the current and exothermic heat flux relax as the electrode approaches the equilibrium Li^+ concentration.

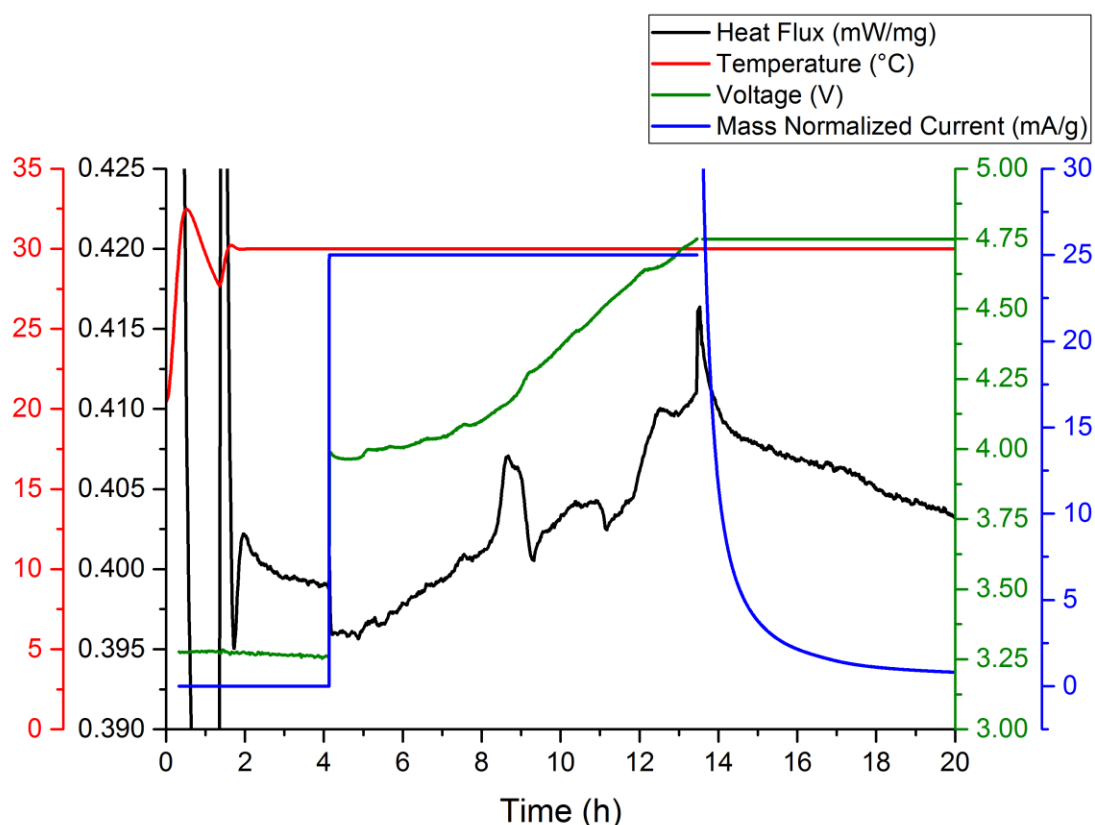


Figure 3-2: Heat flux and electrochemical measurements from an operando microcalorimetry experiment of an LCO half-cell as it was charged to and held at 4.75 V, while isothermal at 30°C. The heat flux (black), temperature (red), voltage (green), and current (blue) data are each scaled according to an individual axis.

To investigate the interesting peak in corrosion current shown in Figure 3-1 and contrast the results with LCO, LCO and NCA half-cells were charged to 4.75 V and held under potentiostatic conditions in the microcalorimeter. Additionally, the effect of temperature was explored by changing the thermal environment throughout the experiment. The thermal profile for all microcalorimetry experiments was as follows: after 20 h at 30°C the temperature was increased to 45°C, held isothermally for an additional 20 h, and then increased to 60°C, where it remained until the conclusion of the experiment. While at 4.75 V and 60°C, the duplicate *operando* microcalorimetry cells, in Figure 3-3 and Figure 3-5, show a peak in the current data nearly identical to the current response shown for the non microcalorimetry NCA cell at 4.75 V in Figure 3-1. A large peak in the heat flux mirrors the current indicating that the parasitic reactions are highly exothermic. The data in Figure 3-4 is of an LCO half-cell and the results in Figure 3-3 and Figure 3-5 are of duplicate NCA half-cells. All of the cells were tested under identical conditions, which demonstrates that the measurement of parasitic reactions is highly reproducible, as is the duality between the heat flux and current profiles. The exothermic reactions shown in Figure 3-3, Figure 3-4 and Figure 3-5 are either self-passivating or become exhausted, since the magnitude of both the heat flux and current at the end of the test are similar to their values at the beginning of the 60°C phase. The measurement of the parasitic exotherm in LCO and NCA is significant because it discredits the notion that the reactions are intrinsic to either material, and instead indicates that the parasitic reactions are correlated to the R $\bar{3}$ m structure or possibly the transition metals themselves.

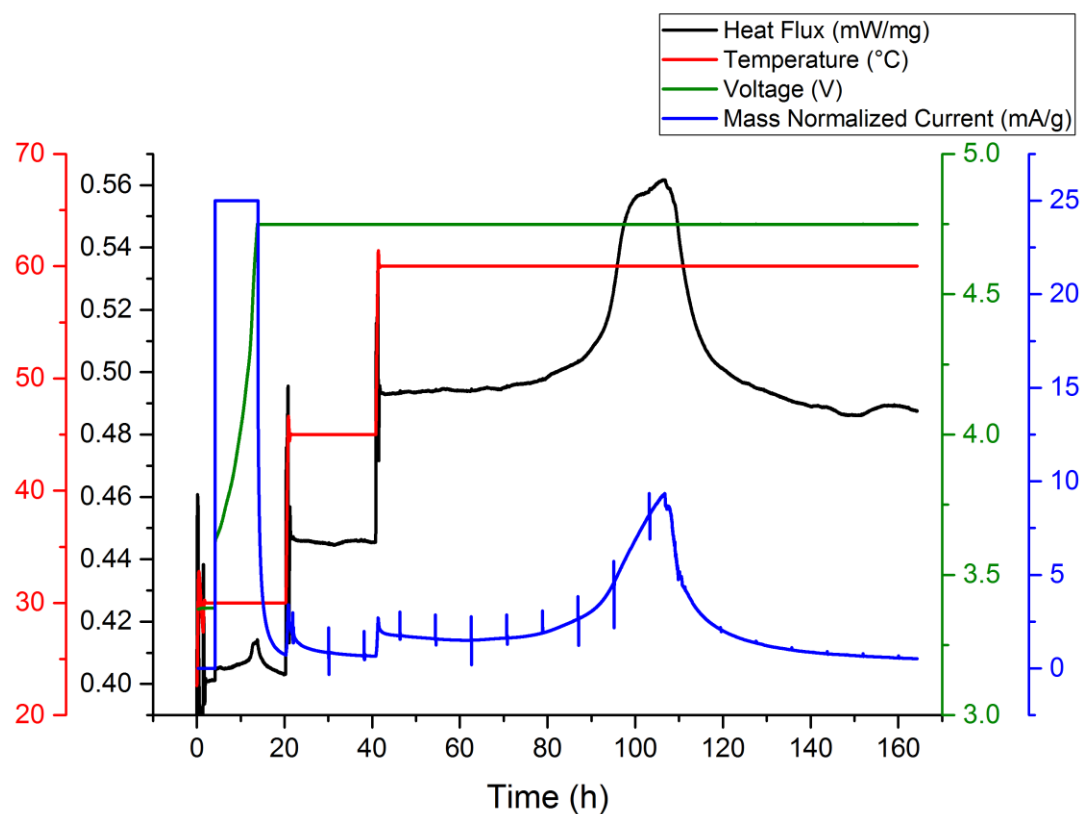


Figure 3-3: Heat flux (black) and electrochemical (blue and green) measurements from an operando microcalorimetry experiment of an NCA half-cell as it was charged to and held at 4.75 V. The NCA cell was charged to 4.75 V, and held at constant potential while the temperature (red) was incrementally stepped up from 30°C to 45°C to 60°C.

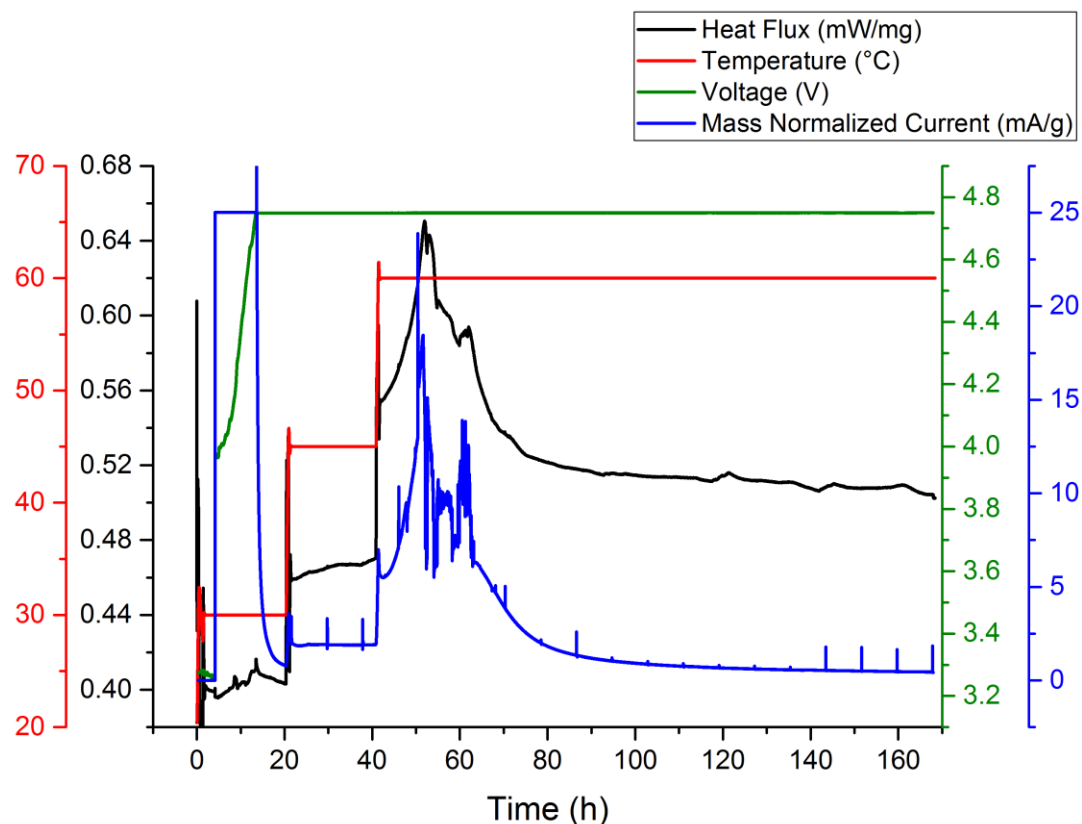


Figure 3-4: LCO microcalorimetry cell charged to 4.75 V, and held at constant potential while the temperature was incrementally stepped up from 30°C to 45°C to 60°C. The heat flux (black), temperature (red), voltage (green), and current (blue) data are each scaled according to an individual axis.

Clearly, the LCO half-cell initiates the current rise much earlier than NCA. Parasitic reactions were induced as soon as the LCO half-cell was raised to 60°C, while NCA required nearly 30 h at 60°C before the onset of the current peak. Using the final heat flux as a baseline, at 60°C the LCO cell in Figure 3-4 had a cumulative heat of 11,487.8 joules per gram of active material (J/g). Similar analysis of the NCA cells in Figure 3-3 and Figure 3-5 determined that the cumulative heats were 6527.7 and 7004.9 J/g, respectively, about half of the heat produced by the LCO cell. The higher instability of LCO relative to NCA is in agreement with other thermal studies.^{162,196} A corresponding microcalorimetry evaluation using an electrode without the R $\bar{3}$ m positive electrode material, but with all other components (SP, PVDF-HFP, etc), did not show an

evolution in current or an exotherm at 4.75 V and 60°C consistent with the response in current already shown in Figure 3-1.

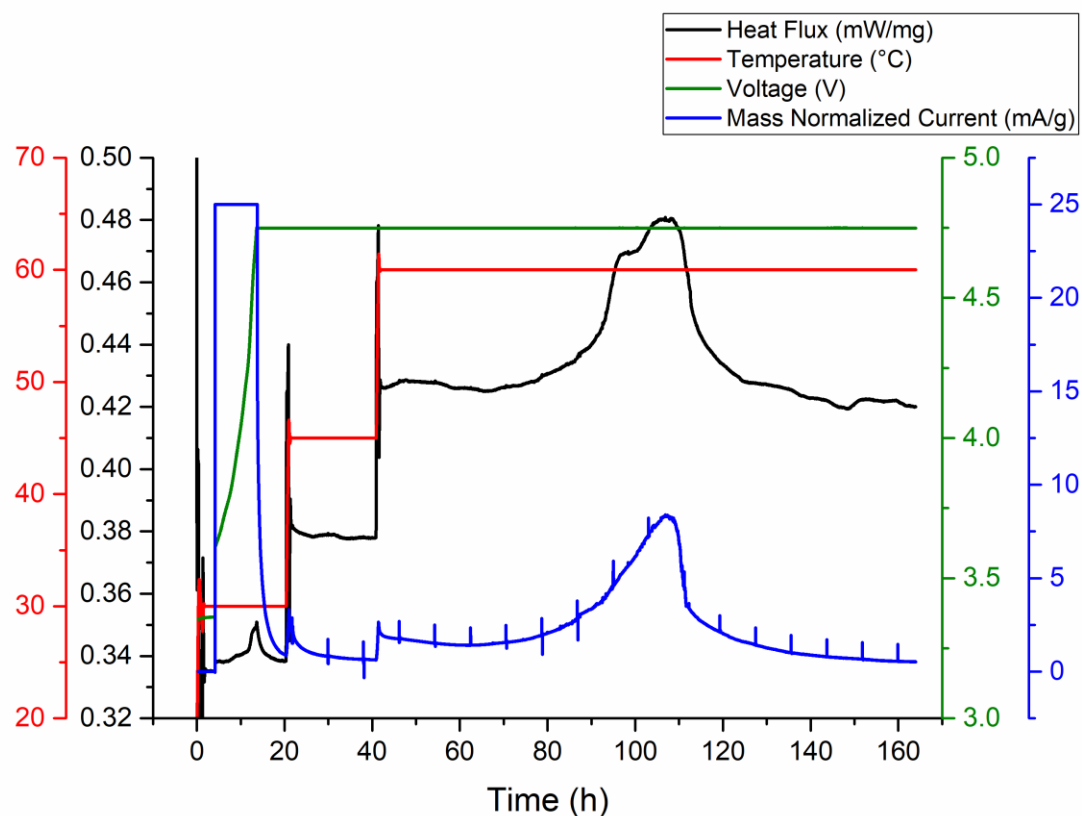


Figure 3-5: Heat flux (black) and electrochemical (blue and green) measurements from an operando microcalorimetry experiment of an NCA half-cell as it was charged to and held at 4.75 V. The NCA cell was charged to 4.75 V, and held at constant potential while the temperature (red) was incrementally stepped up from 30°C to 45°C to 60°C.

Selected impedance scans extracted from the NCA microcalorimetry test shown in Figure 3-3 are presented in Figure 3-6 (a) and (b). Figure 3-6 (a) shows the holistic view encompassing all of the Nyquist data, while Figure 3-6 (b) portrays the same data but focusing on the lower impedance region. The initial impedance scan at 4.75 V (black data), taken at 14 h, has a two semi-circle shape with a total impedance below 70 ohms. As the NCA electrode continues to delithiate during the 30°C and 45°C segments, the semi-circle associated to the charge transfer impedance increases. The impedance scan taken at 62 h (blue data), shows that prior to the exothermic reactions the total cell impedance is relatively small, but has still

increased by almost 1300 ohms. As the parasitic reactions begin to occur, the impedance growth is rapidly accelerated. Total impedance of the EIS scan taken near the peak of the exotherm (110 h, green data) is around two orders of magnitude larger than the pre-exotherm scan (62 h, blue data), as a result of impedance growth. While the parasitic reactions fade out, the large increase in charge transfer impedance continues, such that at the end of the test the total impedance is about three orders of magnitude greater than the pre-exotherm levels.

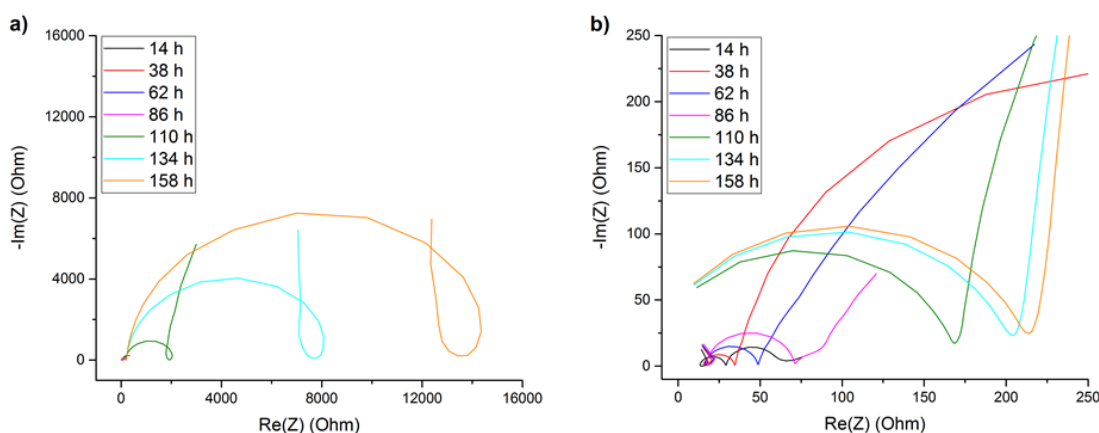


Figure 3-6: (a) General and (b) enhanced view of selected impedance scans from the 4.75 V potentiostatic segment of the microcalorimetry test shown in Figure 3-3.

Besides the parallel evolution of a heat exotherm and a peak in the current, two other characteristics are of specific importance: (i) the massive increase of cell impedance and (ii) the low OCV of approximately 2.5-3V of the post-exotherm cells. Considering that the NCA is near full delithiation, the low OCV could have been a result of the complete decomposition of the layered oxide into a spinel or rocksalt type structure. At first glance this seems to be the likely scenario. To investigate the plausibility of this reaction mechanism, after the microcalorimetry experiment the coin cell was disassembled in a glovebox and evaluated by *ex-situ* XRD. The XRD scans displayed in Figure 3-7 show that the initial rhombohedral layered structure (referred to as O3) is retained in the pre-exotherm and post-exotherm NCA samples, and exhibits good preservation of the (003):(104) ratio, and (108):(110) peak splitting. These results are indicative of little transition metal movement to the Li 3a sites, which would have been observed in a bulk

transformation to spinel/rocksalt structures. Minor shifts are associated with variations in Li content. While the relative intensity of the post-exotherm NCA sample is lower than the pristine or pre-exotherm samples, close evaluation of the data shows no new peaks or phases suggesting no significant amount of oxygen loss. In contrast to NCA, post-exotherm LCO, presented in Figure 3-8, shows a structural transformation of the rhombohedral layered phase to a hybrid phase of the initial rhombohedral and a hexagonal CoO_2 structure (referred to as H1-3). This is the expected layered phase to develop at high degrees of delithiation for LCO and again represents no significant oxygen loss or bulk decomposition.¹⁹⁷ The transformation and retention of the crystalline O1 CoO_2 phase is highly dependent upon the removal of all Li^+ ions. In summary, no evidence of bulk oxygen loss and subsequent decomposition of either the NCA or LCO phase can be attributed to the exotherm or the low OCV after reaction.

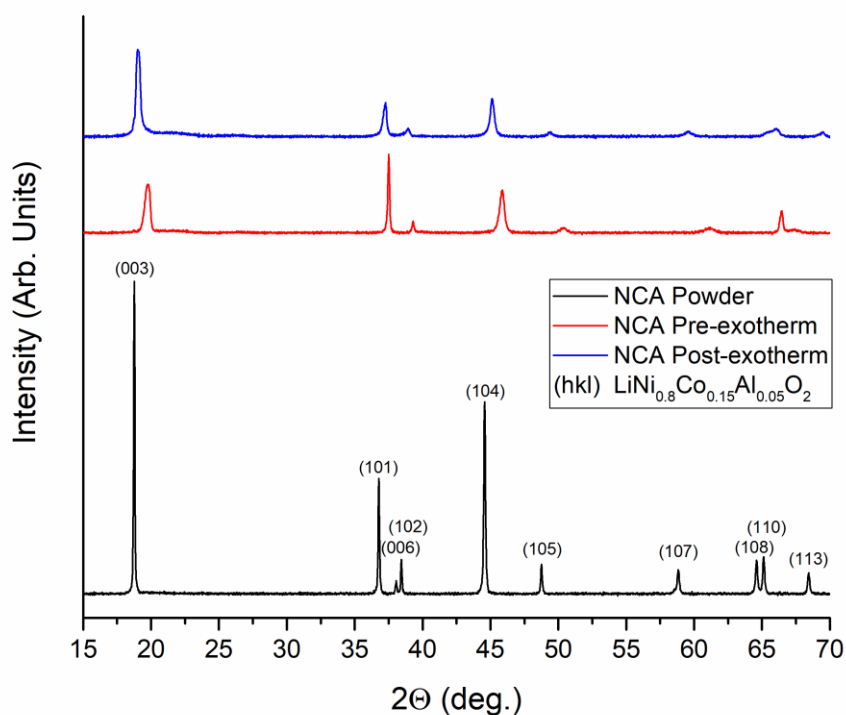


Figure 3-7: Comparison of XRD results of the pristine powder (black) and the positive electrodes before (red) and after (blue) exothermic reactions at 4.75 V and 60°C for NCA. The peaks associated with the layered ($R\bar{3}m$) structure are indexed for the pristine material.

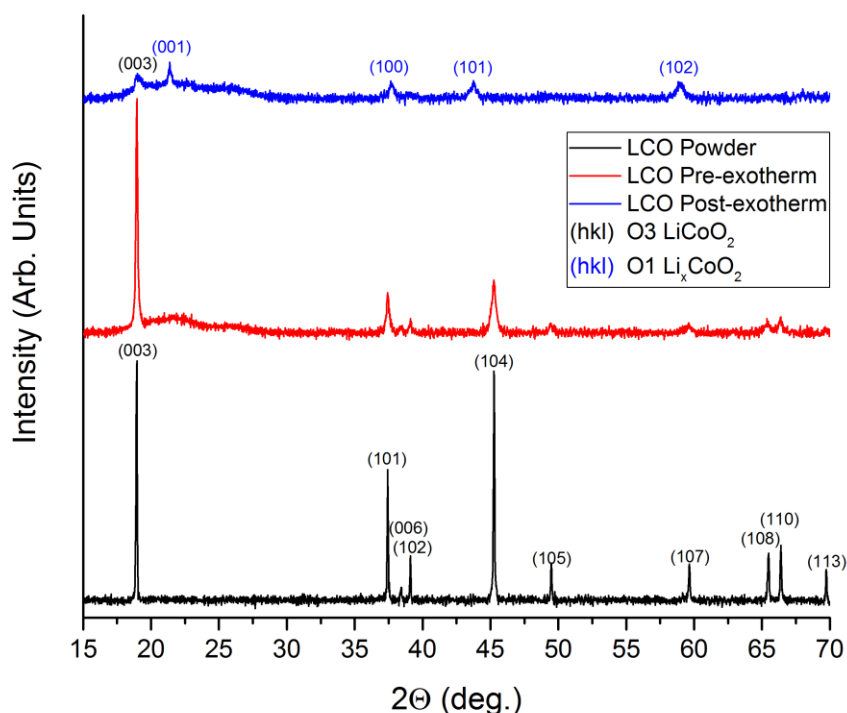


Figure 3-8: Comparison of XRD results of pristine powder (black) and positive electrodes before (red) and after (blue) exothermic reactions at 4.75 V and 60°C for LCO. The O3 and O1 structures are indexed when appropriate. The peaks associated with the layered ($R\bar{3}m$) structure are indexed for the pristine material.

During the disassembly of the microcalorimetry cells, visual observation noted the extreme deposition of transition metal dissolution products on the negative electrode. EDS was utilized to detect the presence and determine the relative magnitude of the transition metal plating on the Li negative electrodes. Figure 3-9 shows FESEM and EDS mapping images of Li negative electrodes extracted from NCA coin cells, before and after exothermic reactions. Ni and Co EDS measurement results are shown in Figure 3-9 (b-c) for the pre-exotherm sample, and (e-f) for the post-exotherm sample. In each sample, the left side of the negative electrode was thoroughly scraped to remove any products that either formed or deposited on the surface. Since the long-range diffusion of Ni or Co into the Li metal is assumed to be negligible, removing all surface products creates an internal reference which can be used to estimate the magnitude of

transition metal deposition. The Li negative electrodes are on stainless steel substrates, so there are trace amounts of detectable Ni and Co even in the absence of any dissolution products. The pre-exotherm sample shows that prior to the exothermic peak there is definitely some Ni and Co deposition on the untouched negative electrode relative to the scraped area. In contrast, after exothermic reactions high concentrations of Ni and Co metal are measured. Normalized to the cleaned areas, the post-exotherm negative electrode has between a 5-7X increase in both the Ni and Co concentrations.

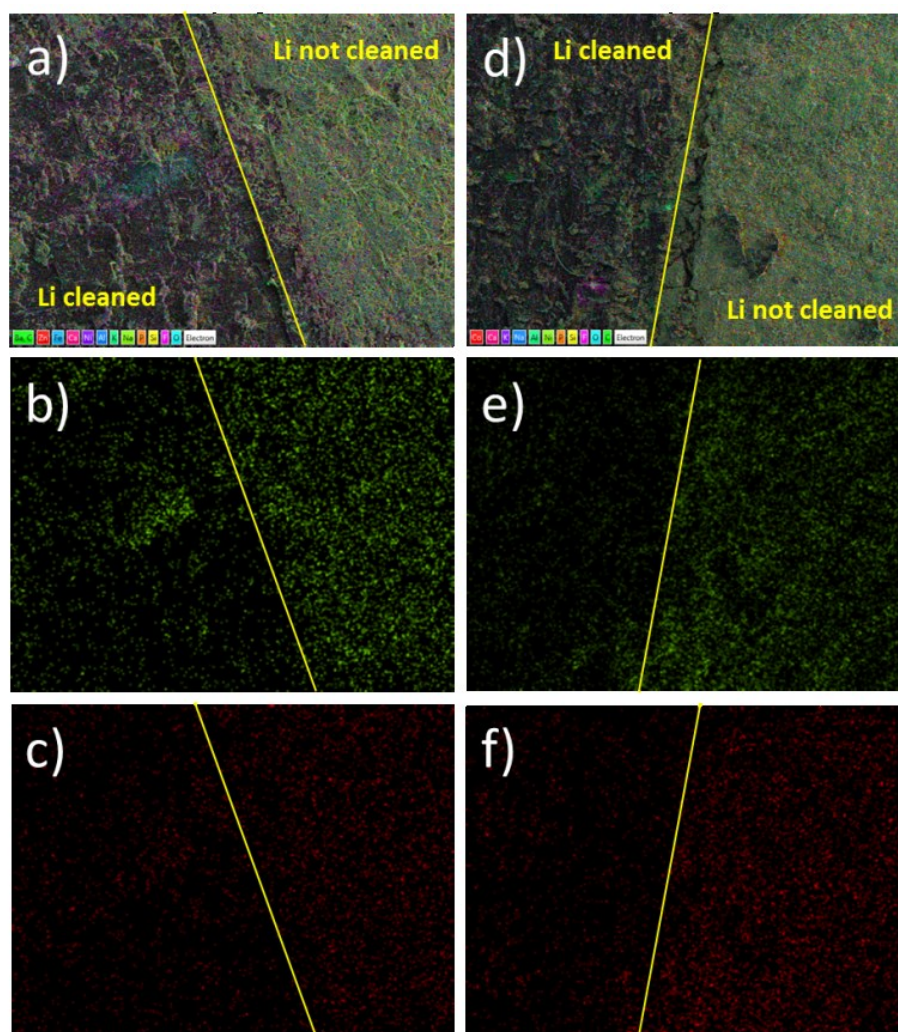


Figure 3-9: SEM images of Li negative electrodes (a) before and (d) after exothermic reactions. Corresponding Ni (b,e) and Co (c,f) EDS measurements taken from the (b-c) pre-exotherm and (e-f) post-exotherm Li negative electrodes. Noted areas of the negative electrodes were scraped to remove any products deposited on the surface, thereby creating an internal standard for baseline Ni and Co concentrations.

XRD (Figure 3-10) of a Li negative electrode after a microcalorimetry experiment revealed that at least a portion of the Ni and Co deposition products are fully reduced to their metallic structures. In Figure 3-10, the Li, Ni and Co metal Bragg reflections are denoted by black circles, red diamonds, and blue asterisks, respectively. As expected from using a Li foil negative electrode, the Li metal peaks are strong and narrow, while the Ni and Co peaks are broad due to their likely nano-sized domains.

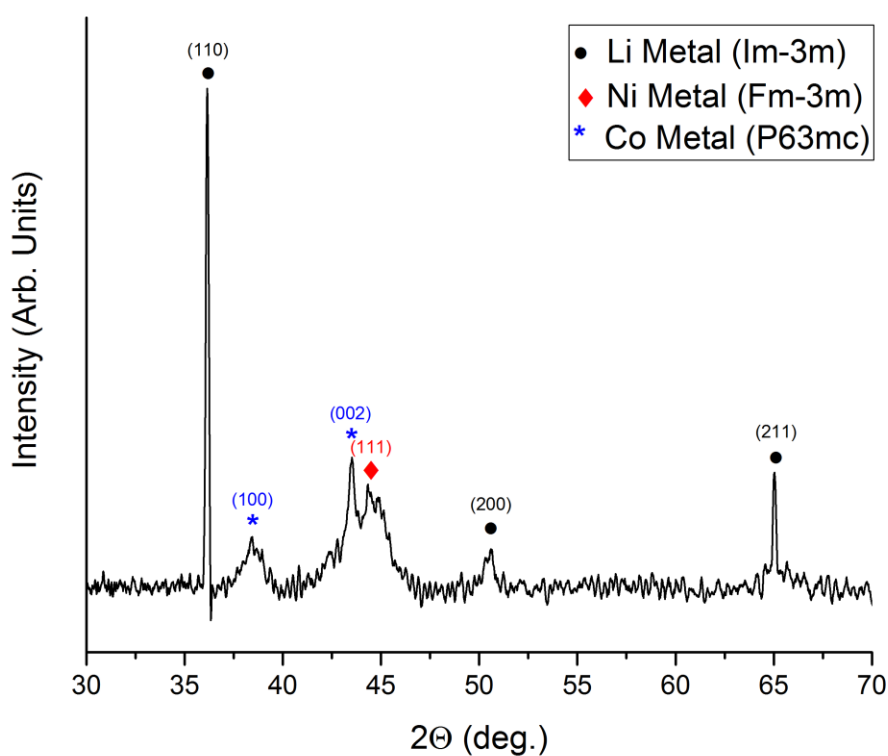


Figure 3-10: XRD plot of a Li foil negative electrode retrieved from an NCA microcalorimetry cell after testing at 4.75 V and 60°C. The main Li, Ni and Co metal peak locations are marked by a black circle, red diamond, and blue asterisk, respectively. For each phase the main peaks are indexed according to the listed space groups.

Reassembly of multiple post exotherm cells with fresh negative electrodes and electrolyte reveals that the OCV of the positive electrode is reproducibly between 4.1-4.3 V, indicative of a delithiated positive electrode. This suggests that the low OCV voltage of 2.5-3 V observed in the initial cell was a result of a potential shift induced at the negative electrode, possibly due to the

dissolution products from the positive electrode. The reassembled cells also showed a total impedance orders of magnitude less than the post exotherm cell, proving that the negative electrode was the origin of such increase. However, it should be noted that the post-exotherm cells still exhibited a positive electrode impedance of approximately an order of magnitude greater than the original cell. This suggests that some degree of degradation of the positive electrode did occur which could not be rectified with immersion in fresh electrolyte and a new negative electrode. Such surface transformations will be discussed in a later section of this paper. Subsequent discharge of the reassembled cells revealed that a specific capacity in the range of 119-145 mAh/g could be achieved as opposed to no specific discharge capacity before the cell was reassembled.

3.4.2 Three-Electrode Electrochemical Analysis

Particularly peculiar was the observation that the dissolution products induced a significant shift in the post exotherm cell OCV to the low voltage of 2.5-3 V, as noted above. In order to distinguish between the changes occurring on the positive and the negative electrodes *during* the exothermic reaction, a three-electrode cell was constructed and tested under similar electrochemical and thermal conditions to those present in the microcalorimetry characterization. The three-electrode cell, shown in Figure 3-11 (a), is comprised of an NCA positive, Li metal negative, and Ag metal quasi-reference electrodes. Reference electrode materials were chosen so that they would not reduce the transition metal dissolution products present in the electrolyte. Obviously, a Li reference electrode would not be effective, and results (not shown) using $\text{Li}_4\text{Ti}_5\text{O}_{12}$ as the reference electrode also showed reaction with the dissolution products. Thus, Ag and V_2O_5 were chosen as suitable quasi-reference and reference electrode materials, respectively.

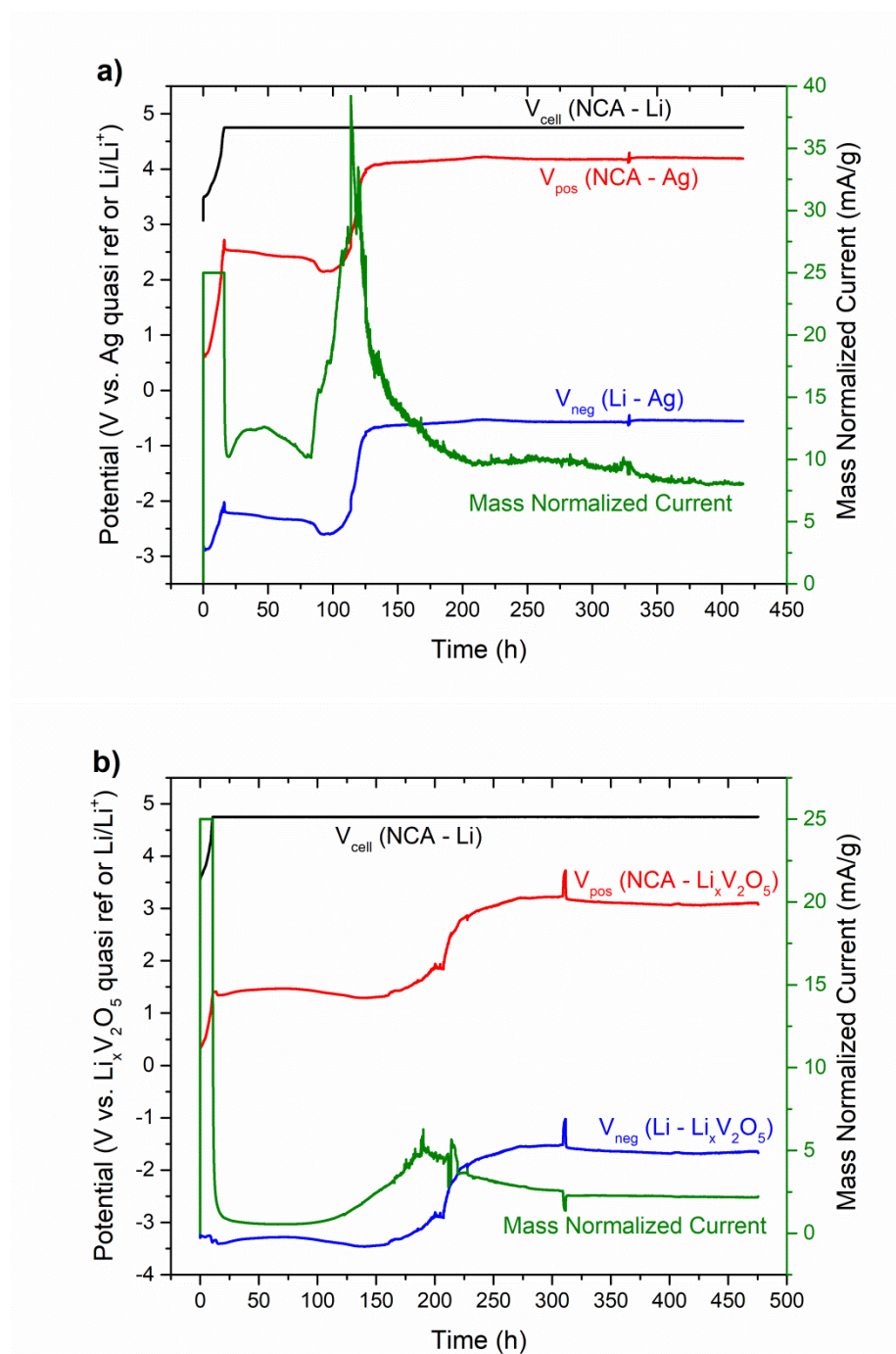


Figure 3-11: Three-electrode electrochemical cells with an NCA positive, Li metal negative, and a (a) Ag metal quasi-reference or a (b) Li_xV₂O₅ reference electrode. The cell potential was charged to 4.75 V (vs. Li negative electrode) at 25mA/g and then held at 4.75 V at 60°C. The positive and negative electrode potentials are each relative to the reference electrode, while the cell potential is the difference between the positive and negative electrodes. The cell (black), positive (red) and negative (blue) potentials are scaled according to the left axis, while the current (green) is correlated to the right axis. The three-electrode cells in figures (a) and (b) were identically made, except for the reference electrode used.

Analogous to the microcalorimetry tests displayed in Figure 3-3 and Figure 3-5, the results of a three-electrode experiment are shown in Figure 3-11 (a). Unlike the microcalorimetry experiments which had a varying temperature profile, the three electrode cells were in a 60°C incubator for the entirety of the test. In contrast to the two-electrode arrangement of the microcalorimetry cell, the three-electrode cell also includes a Ag metal quasi-reference electrode which enables simultaneous and objective measurement of the positive and negative electrode potentials. The two-electrode output voltage of $V_{\text{pos}} - V_{\text{neg}}$ represented by “ V_{cell} ” is similar to the microcalorimetry cell of Figure 3-5. The cell voltage is raised to 4.75 V vs. Li/Li^+ during the complete delithiation of NCA followed by a featureless constant voltage hold at 4.75 V vs. V_{neg} for approximately 400 h. The evolution of the current is also in agreement with the two-electrode microcalorimetry experiments. Specifically, after approximately 83 h at 4.75 V a large increase in current is observed which peaks and then dissipates. In the microcalorimetry evaluation, this peak in current parallels the evolution of the exotherm. What is surprising is the evolution of the positive and negative electrode potentials relative to the reference electrode. Approximately 20 h after the initiation of the parasitic current spike, a significant rise in the potentials of the negative and positive electrodes was observed, paralleling a rapid increase in current. Within the next 50 h, the potentials of the positive and negative electrodes increase by ~ 2 V relative to the reference electrode and the parasitic current starts to decline as the reactions appear to be nearing completion. The adjusted potential of the negative electrode is consistent with the redox potential of Ni and Co. For the remainder of the potentiostatic phase, the parasitic current continues to taper off, and the electrode potentials stabilize.

The evidence presented within the three-electrode analysis suggests that after a period of time at 4.75 V vs. V_{neg} , a corrosion reaction commences resulting in the rapid dissolution of the positive electrode surface into the electrolyte. The dissolution reaction products migrate and deposit on the negative electrode, inducing a large potential shift of the negative electrode due to the formation of a mixed potential of Li with deposited transition metals. Since the experiment is

run at constant potential (4.75 V vs. Li negative electrode), the positive electrode potential is raised to maintain the delta of 4.75 V between the positive and negative electrodes. This translates to the NCA electrode rising above 6 V vs. Li/Li^+ (likely greater than 7 V) undoubtedly further accelerating the dissolution of the positive electrode. As the mixed potential of the negative electrode becomes weighted towards the metal products, the potential shift continues to increase. One can envision this entire experiment as an accelerating rate study of an electrode material's tendency to form dissolution products. The reaction eventually ceases and the current is lowered to a constant corrosion state when either the positive electrode becomes passivated or the impedance at the negative electrode becomes so large that it cannot support the electrochemical oxidation reaction at the positive electrode.

As quasi reference electrodes can be prone to a shift in potential, the three-electrode results were validated by cross checking these interesting observations with a three-electrode configuration consisting of a more stable intercalation-based reference electrode. In addition to being stable, the redox potential of $\text{Li}_x\text{V}_2\text{O}_5$ is also higher than the standard reduction potentials of both Ni and Co, thus preventing Ni and Co dissolution products from poisoning the $\text{Li}_x\text{V}_2\text{O}_5$ reference electrode. Figure 3-11 (b) displays the electrode potentials and the mass normalized current for this cell, as it was tested identically to the first three-electrode cell. As with the Ag metal reference, the potential of the $\text{Li}_x\text{V}_2\text{O}_5$ electrode drifts slightly during charging, and its equilibrium potential was assumed to be 3.46 V vs. Li/Li^+ , which corresponds to the potential of the V_{neg} at around 140 h. At the beginning of the potentiostatic phase, the gradual current relaxation is due the extraction of the remaining Li ions from the cathode. With time, the relaxation current transitions into a stable leakage current, and the potentials of both electrodes are little changed. Starting around the 100 h mark, the current rises in accordance with the beginning of the parasitic reactions. Similar to the three-electrode cell in Figure 3-11 (a), there is a delay before an increase in the potentials of the positive and negative electrodes vs. the $\text{Li}_x\text{V}_2\text{O}_5$ reference. Once the electrodes' potentials do begin to change, they quickly experience a ~ 2 V

adjustment vs. the reference electrode, comparable to the potential shift shown in Figure 3-11 (a). While the working and counter electrode potentials are adjusting, the parasitic current reduces in intensity and eventually plateaus as the electrodes' potentials steady. Figure 3-12 displays the corresponding impedance data taken at the beginning (solid lines) and the end (dashed lines) of the experiment. Initial scans show little impedance between the positive and reference electrodes, negative and reference electrodes, or positive and negative electrodes. EIS data taken at the conclusion of the test measures little change in the positive electrode impedance, but an order of magnitude increase on the negative electrode.

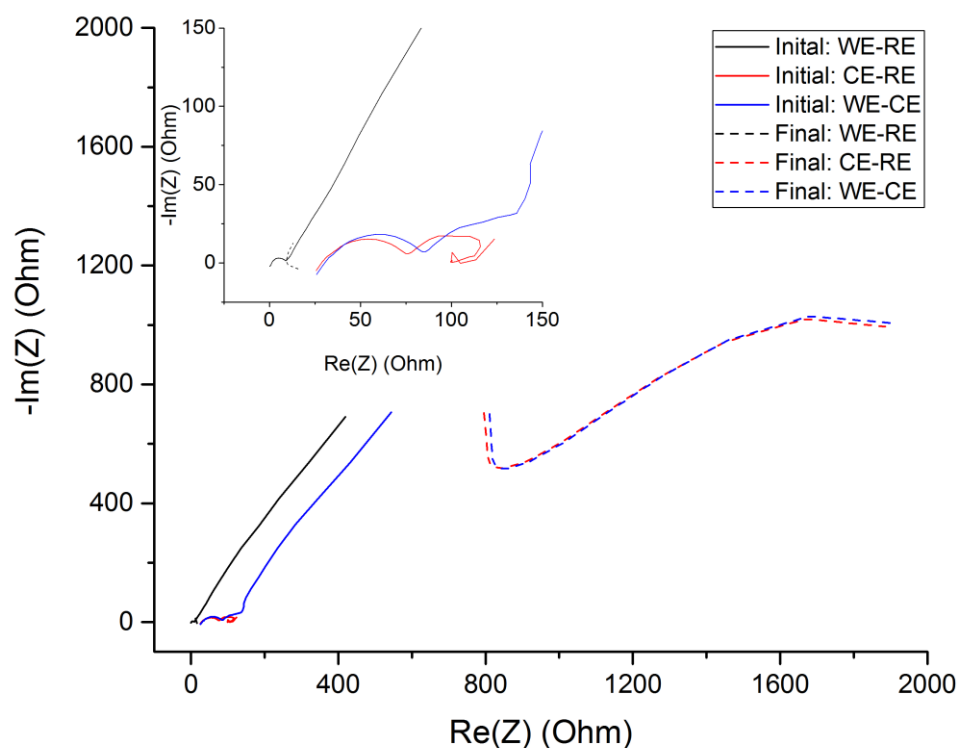


Figure 3-12: Nyquist plots taken at the beginning (solid lines) and end (dotted lines) of the three-electrode experiments. Scans were taken between the working – reference (black), counter – reference (red), and working – counter (blue) electrodes. All scans were taken at 60°C. The final working – reference scan (black dotted line) is only partially visible in the inset graph. This scan intersects the x-axis at approximately 8 ohms higher than the initial scan, suggesting a slight increase in the electronic impedance. The final working –reference scan reaches the Warburg impedance at roughly the same impedance as the initial scan.

The potential, current and impedance data for a third three-electrode cell, made similarly to the one presented in Figure 3-11 (b), is shown in Figure 3-13 and Figure 3-14. Despite being tested identically to the other three electrode cells, this cell doesn't show a large peak in the parasitic current or a shift in the counter electrode potential. This is undoubtedly due to the fact that the dissolution products did not diffuse to the negative electrode and react in such excess which would result in a potential shift, thereby initiating the accelerating rate dissolution reaction. It should be noted that the physical architecture of the three-electrode cell is different and much more tortuous than the coin cell, the latter of which has and will be further shown to offer very reproducible results. However, the initial development of the parasitic current is indistinguishable from the other three-electrode cells, suggesting that the transition metals entered the electrolyte via this pre-reaction but were never deposited on the negative electrode resulting in a potential shift. We have observed this result in a fourth three-electrode cell with construction similar to that of the cell in Figure 3-11 (a). This result is important as it shows the intrinsic current development from the parasitic reactions initially induces the transition metal dissolution at the NCA surface. It does so without having any artifacts in the current response directly associated to the current needed to raise the cell potential or the current evolved from the positive electrode at potentials in excess of 4.75 V vs Li/Li^+ . This mirrors behavior in a shoulder identified in the exotherm of Figure 3-3. Figure 3-14 displays the EIS data taken at the beginning and the end of the experiment. In contrast to the previous cells, there is little impedance growth on the negative electrode but a two order of magnitude increase on the positive electrode. The lack of significant impedance development on the negative electrode supports the conclusion that the majority of the transition metal ions in electrolyte weren't able to deposit on the negative electrode. It is possible that the metal ions were incapable of migrating to the negative electrode, and instead deposited on the separator and positive electrode. This would explain the extreme growth in positive electrode impedance as well as the absence of a shift in the negative electrode potential.

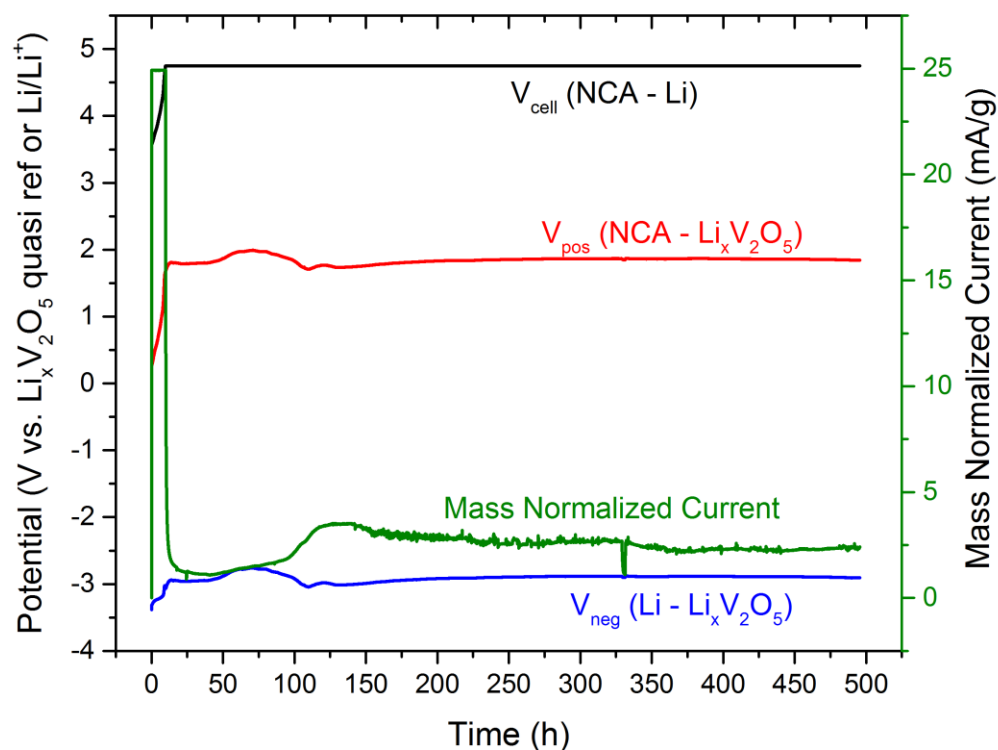


Figure 3-13: A three-electrode electrochemical cell with an NCA positive, Li metal negative, and a $\text{Li}_x\text{V}_2\text{O}_5$ reference electrode. The cell potential was charged to 4.75 V (vs. Li negative electrode) at 25mA/g and then held at 4.75 V at 60°C. The positive and negative electrode potentials are each relative to the reference electrode, while the cell potential is the difference between the positive and negative electrodes. The cell (black), positive (red) and negative (blue) potentials are scaled according to the left axis, while the current (green) is correlated to the right axis.

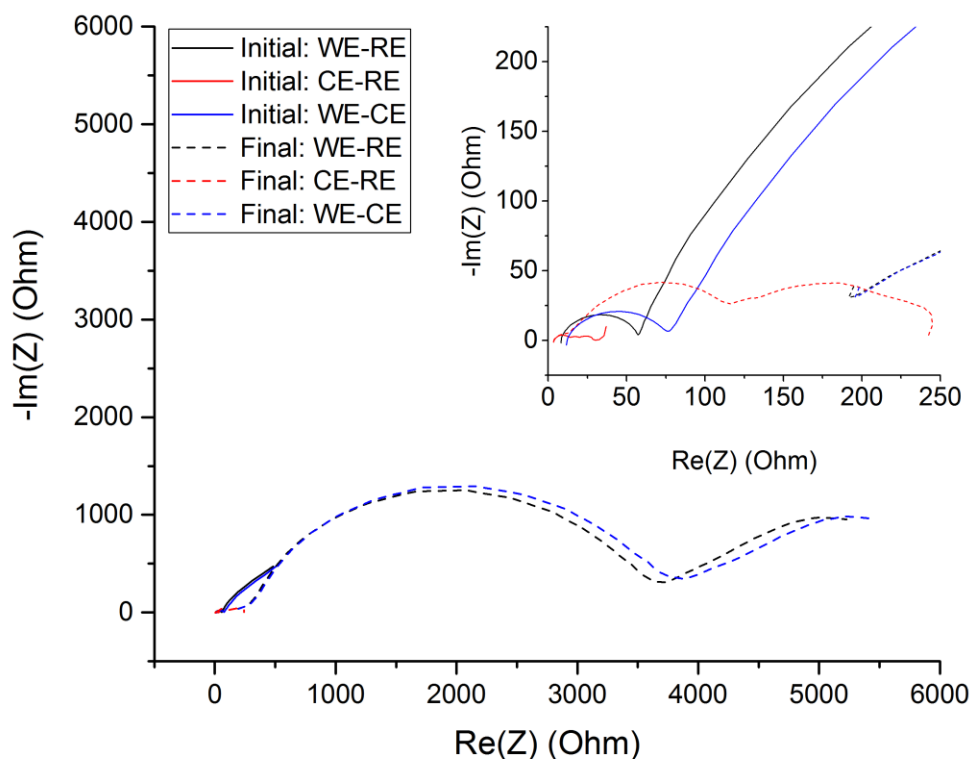


Figure 3-14: Nyquist plots taken at the beginning (solid lines) and end (dotted lines) of the three-electrode experiments. Scans were taken between the working – reference (black), counter – reference (red), and working – counter (blue) electrodes. All scans were taken at 60°C.

3.4.3 Impact of Electrolyte Salt on Heat Flux and Impedance

The impact of the electrolyte salt composition on the exothermic reactions was studied by performing identical microcalorimetry experiments on NCA electrodes using 1M LiPF₆ EC:DMC (1:1) and 1M LiBF₄ EC:DMC (1:1). The comparison of the heat flux and current profiles for the two electrolytes are shown in Figure 3-15 (a) and (b), respectively. Both electrolytes show nearly identical heat flux and current profiles during the 30°C, 45°C, and pre-exotherm 60°C segments. This indicates that little differences in corrosion behavior beyond the effects of the solvent are active in these regions. In contrast to the exothermic reactions that occur with LiPF₆ salt at 4.75 V and 60°C, samples with LiBF₄ have a moderate increase in both heat flux and current, and maintain this elevated state until the cell vents without the formation of a sharp exotherm.

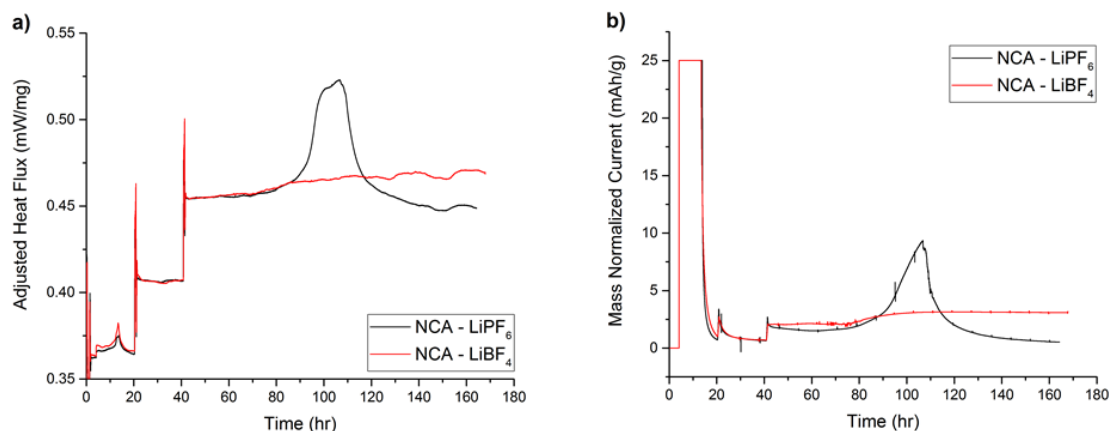


Figure 3-15: (a) Heat flux and (b) current profiles for microcalorimetry experiments of NCA half-cells made with 1M LiPF_6 (black) and 1M LiBF_4 (red) salt in EC:DMC (1:1) solvent. Cells were charged to 4.75 V at 25mA/g and held potentiostatically, while the temperature of the microcalorimeter was changed from 30°C to 45°C to 60°C.

Selected scans from the corresponding *operando* impedance measurements for the LiPF_6 and LiBF_4 microcalorimetry samples are displayed in Figure 3-16 (a) and (b), accordingly. As previously mentioned, the exothermic reaction enabled by LiPF_6 salt causes a drastic impedance development, however, samples utilizing LiBF_4 have only a modest impedance rise that directly correlates to the growth of the current. From each EIS scan, three key impedance values were extracted. The electrical resistance of the cell (mainly from electrolyte) is denoted as R1. While the impedance of the solid-electrolyte interface on the negative electrode is represented by R2, and the impedance of the cathode and cathode-electrolyte interface is recorded as R3. For clarity, Figure 3-16 (b) has a visual example of the three fitted impedance values for the 229 h Nyquist plot. A direct comparison of all the impedance values obtained from the EIS data sets shown in Figure 3-16 (a) and (b) are presented in Figure 3-17 (a-c). When interpreting the data it is important to be cognizant of the temperature change from 30°C to 45°C after 20 h, and the increase from 45°C to 60°C at around 40 h. For both salts, the R1 impedance (Figure 3-17 (a)) is relatively small and stable throughout the experiment. As expected due to the increase in the conductivity of the electrolyte, the R1 impedance drops as the cells are heated from 45°C to 60°C, followed by a slow gradual increase as the cells are held at 4.75 V and 60°C.

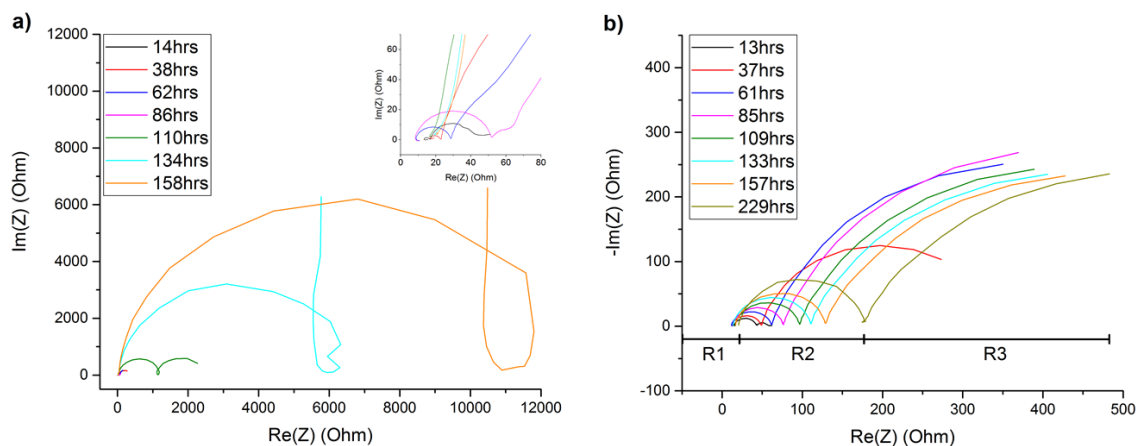


Figure 3-16: Selected scans from Nyquist plots of NCA microcalorimetry electrodes at 4.75 V, 60°C with either 1M (a) LiPF_6 or (b) LiBF_4 salt in EC:DMC (1:1). A visual representation of the R1, R2, and R3 values measured for the 229 h Nyquist plot of the LiBF_4 sample is shown in (b).

Unlike the R1 data which shows little difference between the two salts, the impedance of the solid-electrolyte interface of the negative electrode (R2) presented in Figure 3-17 (b) has a stark distinction. For the LiPF_6 sample, the R2 impedance slowly begins to increase after the scan taken at 38 h. The rate of impedance growth accelerates after the 70 h scan, which correlates to the development of parasitic heat and current shown in Figure 3-15 (a) and (b), respectively. Following the 102 h scan a large impedance development is observed, and results in the R2 impedance increasing by over two orders of magnitude. The exponential rise in impedance begins as the parasitic current peaks, which has been previously demonstrated to be associated with the beginning of the potential shift of the negative electrode. As a result of the lack of dissolution inducing parasitic reactions, the LiBF_4 sample has only a moderate, steady R2 impedance growth. This impedance development is due to the continuous solid-electrolyte interface formation from the reduction of the electrolyte at the negative electrode.

Importantly, Figure 3-17 (c) shows that, regardless of the salt used, both samples have similar R3 impedance evolution. This is attributed to the positive electrodes' impedance development as the materials approached full delithiation. Initially, R3 impedance was measured

as 28.49 Ω for LiPF_6 and 13.98 Ω for LiBF_4 . After 40 h in the potentiostatic segment, the impedances grew to 708.5 and 351.8 Ω for LiPF_6 and LiBF_4 , respectively. The two R3 impedances started similar to each other, and gradually began to deviate with time in the 4.75 V hold, but both had a $\sim 25\times$ increase in R3 impedance associated with the delithiation reaction. Around the time when the parasitic current begins for the LiPF_6 sample, it becomes impossible to ascertain the R3 impedance because the impedance data correlating to the positive electrode is overshadowed by the extremely large R2 and Warburg impedances. As a result of the significantly lower cell impedance, NCA cells with LiBF_4 are able to be discharged with near full capacity, whereas no relithiation capacity was capable for cells using LiPF_6 . Visual analysis of opened cells after testing shows that cells using LiBF_4 have significantly less transition metal deposition on the lithium negative electrode than their LiPF_6 counterparts. The reduced transition metal deposition on the anode (Table 3-II), is likely the origin of the 1-2 order of magnitude lower impedance observed in cells with LiBF_4 .

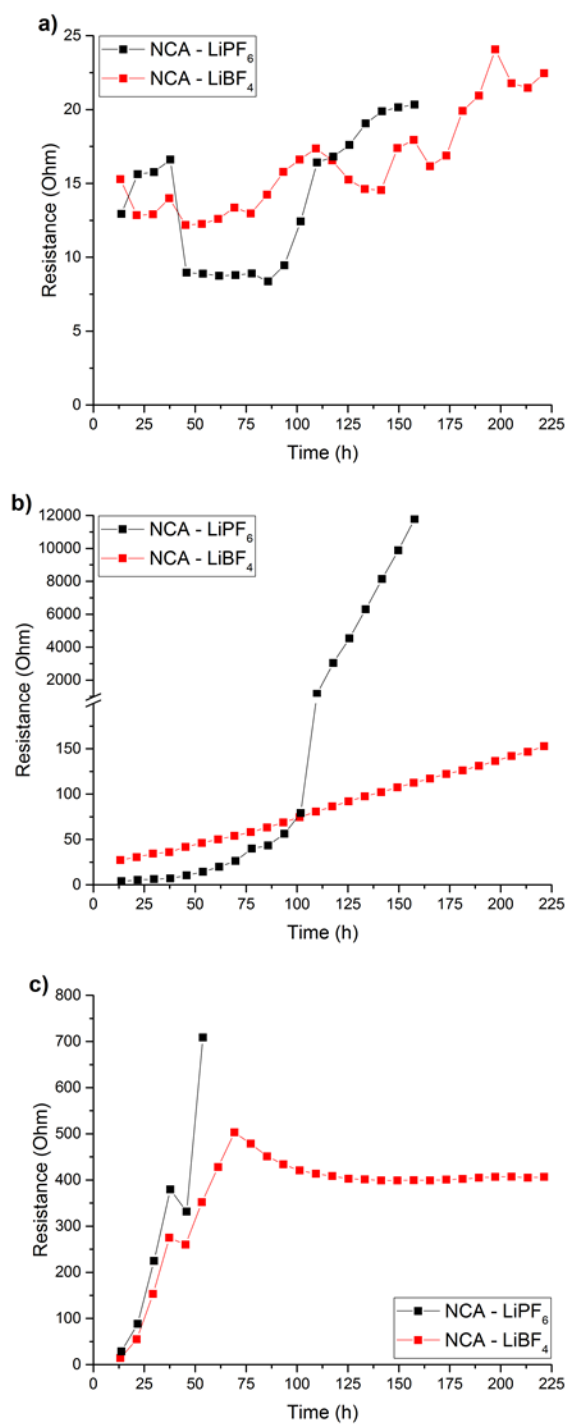


Figure 3-17: R_1 , R_2 , and R_3 impedance values extracted from the LiPF₆ (black) and LiBF₄ (red) impedance spectra in Figure 3-16 are plotted versus time in figures (a), (b), and (c), respectively. Note the differences in the scale of the y axis.

3.4.4 Evolution of the Surface

To study the influence of Li_2CO_3 , native to the $\text{R}\bar{3}\text{m}$ materials' surfaces, towards the deleterious reactions, NCA powder was exposed to ambient air for two weeks to accentuate the growth of Li_2CO_3 .¹⁹⁸ TEY mode XAS O K-edge results shown in Figure 3-18 (a) compare spectra of pristine NCA (solid lines) and NCA powder that was exposed to air for two weeks (dashed lines). Both the pristine and air exposed samples show a peak at 534 eV indicative of Li_2CO_3 on the NCA's surface. However, the magnitude of the peak for the air exposed sample is much larger than for the pristine material, signifying that exposure to air developed ample additional Li_2CO_3 . Quantitative TGA experiments measured 0.12 wt% and 0.82 wt% Li_2CO_3 for the pristine and air exposed materials, respectively. The increase in Li_2CO_3 content, as measured by TGA, is supported by the significantly larger peak in O K-edge spectra. Both the air exposed and pristine NCA powders were charged to 4.75 V, held for 10 h at 4.75 V, and then slowly discharged to 2.7 V, all while at 60°C. The resulting O K-edge spectra is displayed in Figure 3-18 (b), which shows that the O K-edge features related to the surface Li_2CO_3 have disappeared for both samples even after discharging. Other than the slightly higher intensity around 534 eV, little difference is observed between the exposed and non-exposed materials. Even when Li_2CO_3 was intentionally grown on the NCA's surface, negligible amounts of Li_2CO_3 are measured after charging the powder to 4.75 V and holding at constant voltage. The disappearance of Li_2CO_3 may be related to the oxidation decomposition reaction that occurs at high potentials.

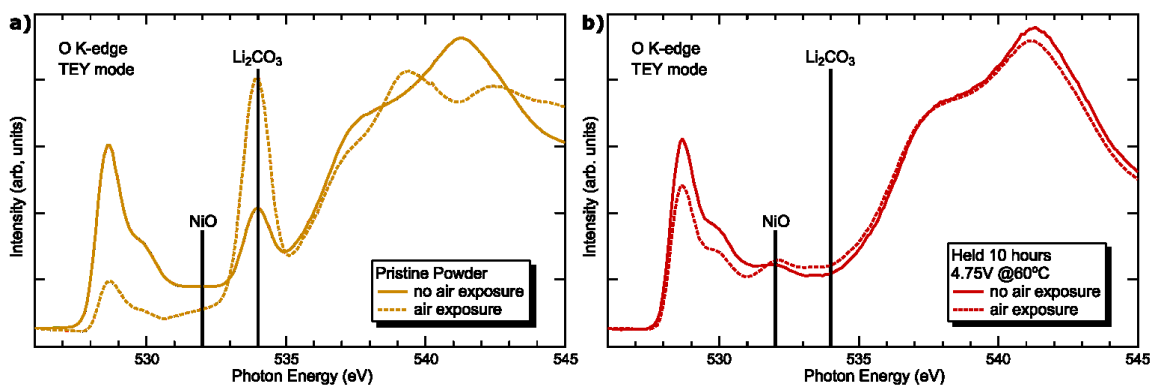


Figure 3-18: (a) TEY O K-edge spectra of 2 week exposed (dashed lines) and pristine (solid lines) NCA powder. (b) TEY O K-edge spectra of powder electrodes of pristine and 2 week exposed NCA that were charged to and held at 4.75 V, and then discharged to 2.7 V while in a 60°C incubator. All measurements were taken on beamline I09 at DLS.

TEY XAS O K-edge and Ni L₃-edge results on NCA samples before and after parasitic reactions are displayed in Figure 3-19. Figure 3-19 (a) and (b) are for samples utilizing LiPF₆ salt, while samples in Figure 3-19 (c) and (d) use LiBF₄. To maintain the surface oxidation state, all samples were prepared from electrodes that were disassembled in the charged state (no discharge phase). The surface sensitive O K-edge (a) and Ni L₃-edge (b) spectra for NCA in LiPF₆ electrolyte show a clear transformation of the transition metal oxidation state with the length of the potentiostatic hold. NCA charged to 4.75 V at room temperature with no potentiostatic segment (blue data) shows a line shape consistent with little Ni²⁺. Pre-exotherm samples that were charged to 4.75 V and held for 10 h at 60°C (red data), have spectra that suggests an average Ni oxidation state of ~2.5, matching a significant growth in a surface Ni²⁺ containing oxide, and is consistent with transition metal reduction at the surface before the exponential rise in the current and heat. This suggests that the surface decomposition precludes the potential shift in the negative electrode. These results are in agreement with the observed increase of the parasitic current prior to the potential shift of the negative electrode as detailed by the previously discussed three-electrode measurements. The line shape of the post-exotherm NCA sample (green data) reveals much more character related to the Ni²⁺ reference material, particularly the O K-edge XAS shows evidence of a feature at 532 eV consistent with the “NiO” reference. This signified that lengthening the potentiostatic hold time allows a further extension of the surface transition metal

reduction to an oxidation state of ~ 2 , but cannot be used as conclusive proof of the presence of rocksalt “NiO” phase. LiBF_4 samples show the same general trend of surface metal reduction but to a lesser degree. With no potentiostatic segment, a highly oxidized Ni environment is observed. Relative to the no hold sample, the Ni^{2+} environment associated with “NiO” increases with the 10 h hold, but not to the same magnitude of the LiPF_6 sample. Further potentiostatic hold up to 295 h reveals little additional growth of the “NiO.” For all samples, the lack of a peak around 534 eV in the O K-edge spectra suggests that negligible Li_2CO_3 was present on the surface. This observation is critical because it eliminates Li_2CO_3 as the *direct* source of the parasitic reactions.

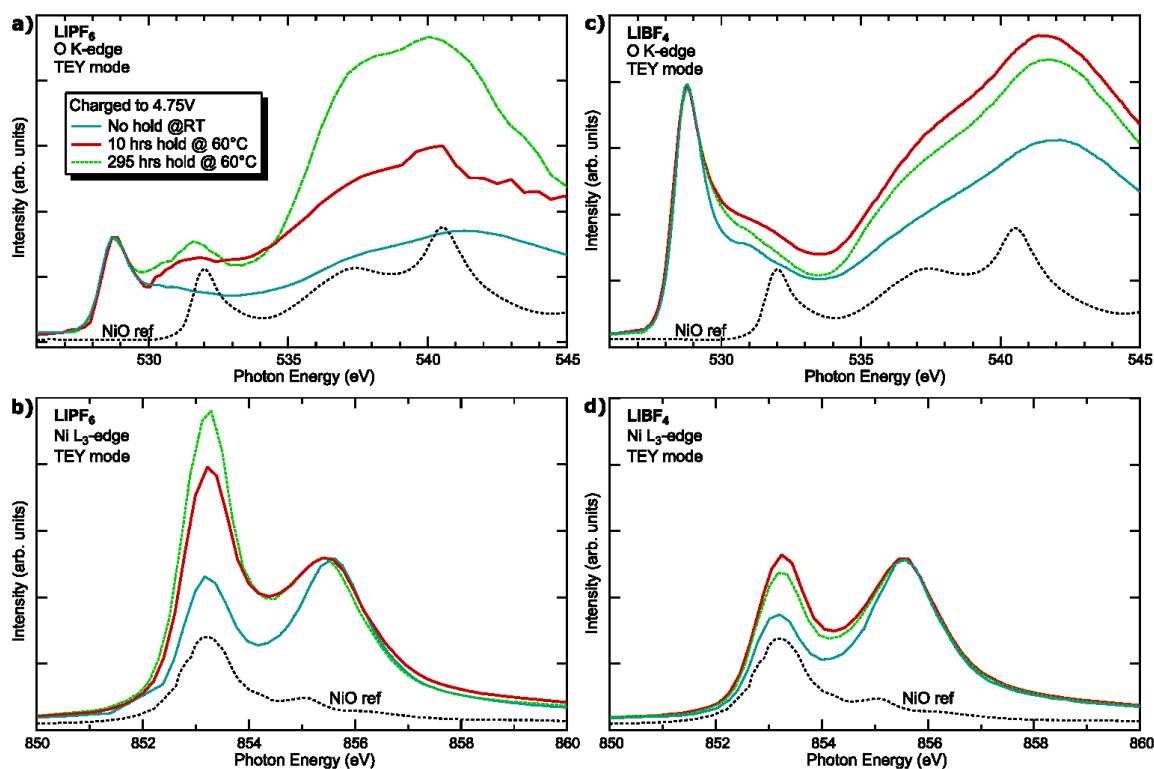


Figure 3-19: (a,c) TEY O K-edge and (b,d) Ni L_{3} -edge XAS spectra taken at ALS for NCA samples before (red) and after (green) exothermic reactions. Samples with electrolyte containing LiPF_6 are shown in (a-b) and those with LiBF_4 are presented in (c-d). All figures show reference spectra of “NiO” (black) and of NCA charged to 4.75 V at room temperature (blue).

To contrast with the surface sensitive TEY O K-edge and Ni L-edge data for all samples introduced in Figure 3-19, the bulk-sensitive PFY spectra are displayed in Figure 3-20. As opposed to the surface sensitive measurements, no significant changes were observed in the O K-

edge PFY spectra regardless of time at the 4.75 V hold or composition of the electrolyte salt. However, there is a small reduction in the average oxidation state of Ni for LiPF_6 samples with increasing time at 4.75 V, but no change in the LiBF_4 samples. Since PFY mode XAS preferentially measures the bulk of the material, it is concluded that the majority of the changes in the transition metal oxidation state and all of the growth of new phases is limited to surface of the samples. This finding confirms the XRD results discussed above, which demonstrated that the structural changes on the particles' surface don't propagate into the material's bulk.

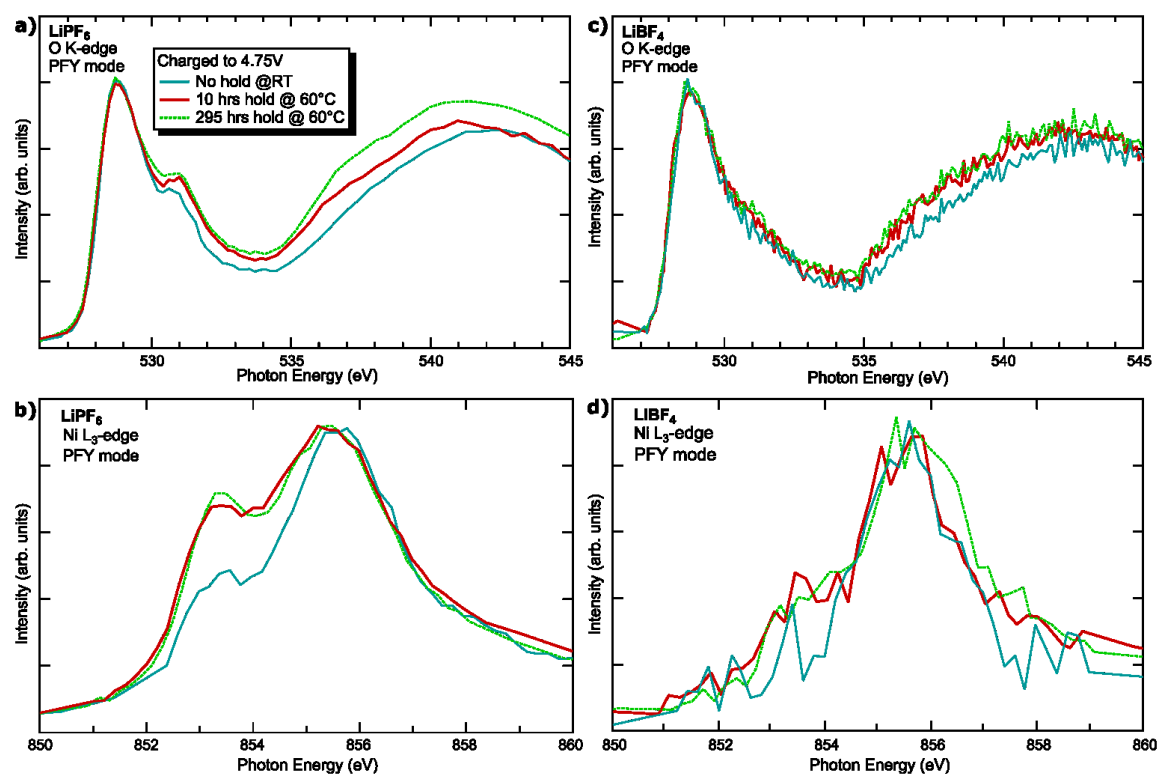


Figure 3-20: O K-edge (a,c) and Ni L-edge (b,d) PFY measurements taken at ALS of NCA charged to 4.75 V at room temperature (blue), pre-exotherm (red), and post-exotherm NCA (green) with either LiPF_6 (a-b) or LiBF_4 (c-d) salts.

To determine if there was a presence of LiPF_6 salt or its decomposition products on the samples' surface, the P 2p region was also probed, and is shown in Figure 3-21 (a). The P 2p results provide clear evidence of the formation of a peak centered around 135 eV, which increases in intensity with a longer potentiostatic hold. The post-exotherm sample (green data) shows a much stronger peak than the pre-exotherm (red data) signifying that the exothermic reactions

were the main cause of this surface species. Based on the P 2p and F 1s (not shown) XPS spectra, this new species was determined to be a P-O-F type material. A likely peak position for the P-O-F material is denoted in Figure 3-21 (a). The P-O-F signal is also supported by the broad intensity development in the O K edge spectra in the region of 535-540 eV in Figure 3-19 (a). Unlike LiPF_6 , the B 1s (Figure 3-21 (b)) spectra did not present an analogous B-O-F species or even signs of deposition of the LiBF_4 salt. In fact, the B 1s spectra showed no significant difference between samples, regardless of the length of the potentiostatic hold, and the O K-edge XAS for LiBF_4 (Figure 3-19 (c)) presented no evidence of any B-O-F material. The expected location for a material similar to the LiBF_4 salt is shown in Figure 3-21 (b).

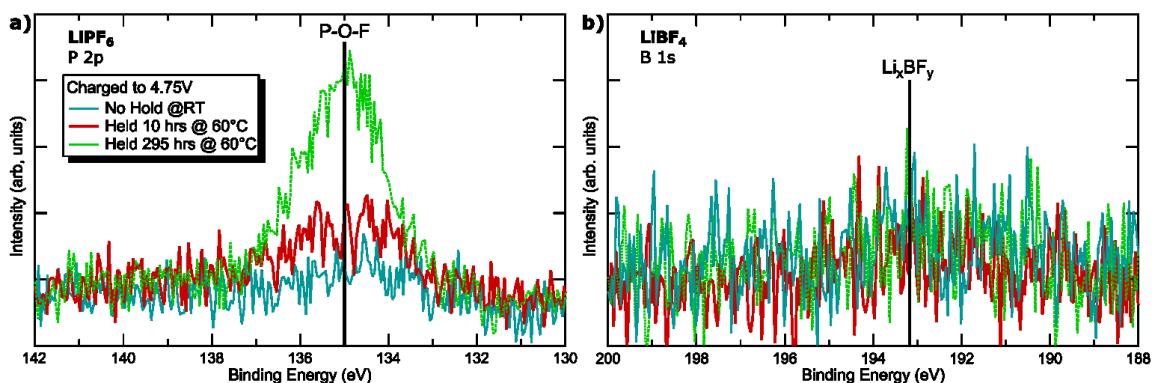


Figure 3-21: (a) P 2p XPS spectra for NCA electrodes with LiPF_6 and (b) B 1s spectra for identical samples with LiBF_4 salt. NCA electrodes charged to 4.75 V at room temperature are shown in blue, while pre-exotherm (10 h hold) and post-exotherm (295 h hold) samples are displayed in red and green, respectively.

Multiple particles of NCA aged for 10 h in LiPF_6 or LiBF_4 at 60°C and 4.75 V were analyzed by HRTEM. As demonstrated by the HRTEM and FFT images in Figure 3-22, the native NCA material exhibited an $\text{R}\bar{3}\text{m}$ phase in the subsurface and surface regions. The pristine material was sometimes observed to be capped by an extremely thin (1 nm) rocksalt-like phase at the surface. In contrast, all LiPF_6 aged surface and subsurface regions showed a transformation to a spinel-like structure.

Figure 3-23 (a) shows a HRTEM image of the surface and subsurface areas of a LiPF_6 aged sample, and

Figure 3-23 (b) provides an enlarged image of the particle's surface. The phase identification is supported by FFT and SAED analyses of approximately 5 nm from the surface

Figure 3-23 (c) and (d), respectively. The SAED data shows a much better match to the simulated SAED pattern intensities of $\text{Fd}3\text{m}$ spinel (

Figure 3-23 f) than to the $\text{R}\bar{3}\text{m}$ layered phase (

Figure 3-23 e). The structural transformation to a spinel-like phase within at least the first 5 nm of the NCA surface was complete and consistent from surface to surface and particle to particle. It was often observed that the structural degradation continued well into the subsurface region. The structural transformation supports transition metal migration to the 16d octahedral sites of the spinel structure concomitant with the oxygen loss and Ni reduction as evidenced by XPS and XAS. It should be noted that one cannot conclusively state that it is of the $\text{Fd}3\text{m}$ structure as partial occupation of the former Li 3a layer by transition metal ions are noted but the developed intensities seem to suggest ordering analogous to a spinel-like structure versus a disordered rocksalt within that layer. Despite XAS results showing the evolution of Ni^{2+} , no significant reflections associated with $\text{Fd}3\text{m}$ 8a tetrahedral sites could be identified.

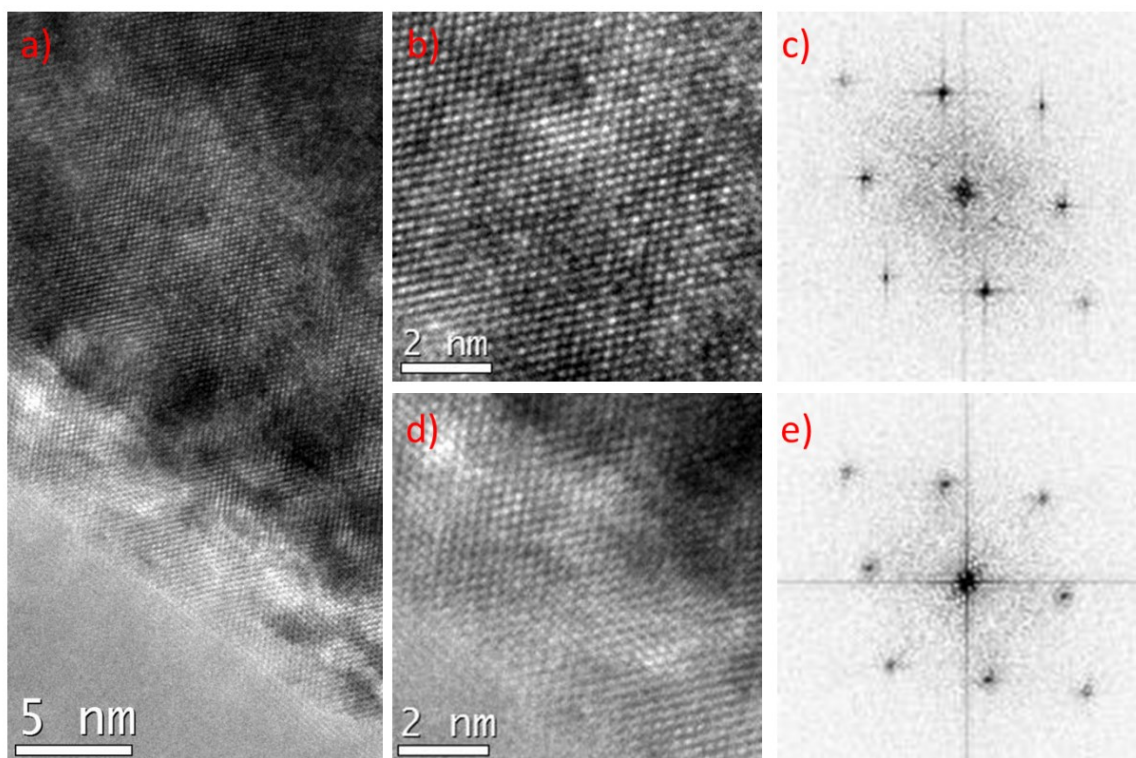


Figure 3-22: A HRTEM image of the (a) pristine, uncycled NCA material, and enhanced HRTEM images of the (b) sub-surface and (d) surface structure are provided. FFT images taken along the $[241]_{\text{Trigonal}}$ zone axis corresponding to figures (b) and (d), are shown in (c) and (e), respectively. Both of the surface and sub-surface have a layered ($R\bar{3}m$) structure.

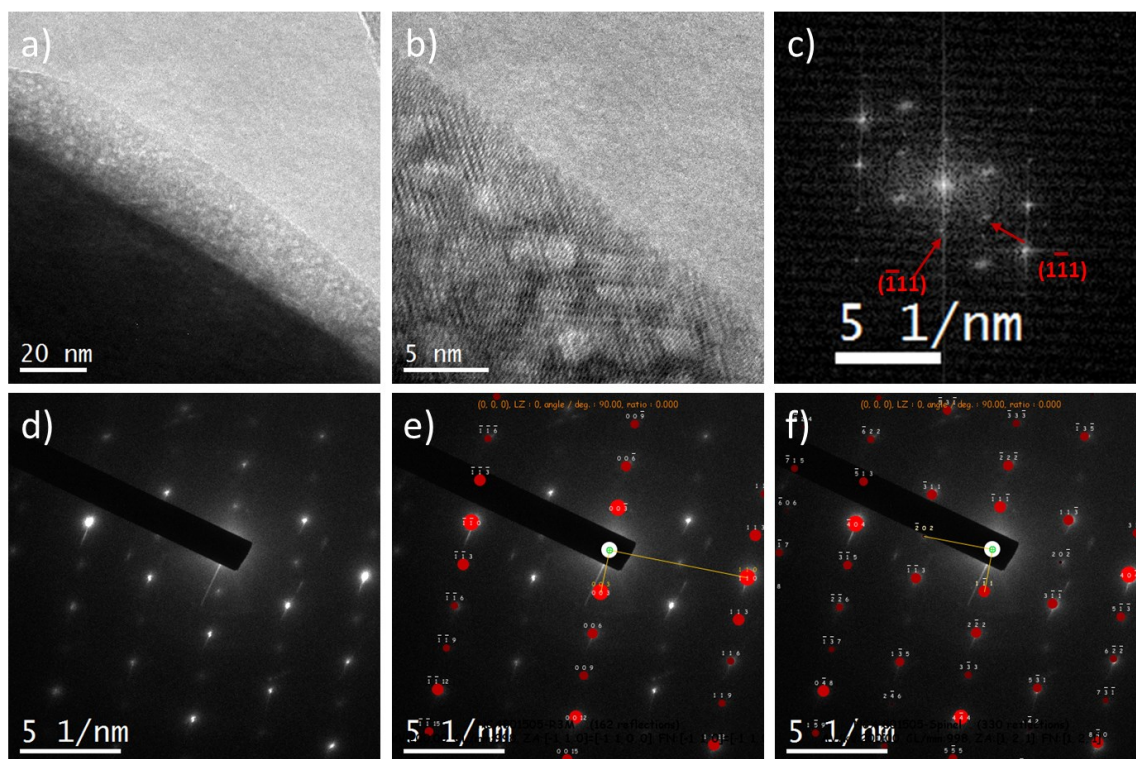


Figure 3-23: (a-b) HRTEM images of the surface and subsurface regions of NCA aged in LiPF_6 at 4.75 V, 60°C for 10 h. The surface region in (a) is enhanced and shown in (b). (c) FFT and (d) SAED of the surface layer are also provided. The SAED image (d) is indexed with a zone axes of either $[-110]_{\text{layered}}$ or $[121]_{\text{spinel}}$ in images (e) and (f), respectively.

For HRTEM images of LiBF_4 aged samples (Figure 3-24 (a-b)) the surface transformation to “spinel-like” occurred throughout at least the first 5 nm, but it was not consistent or deeply penetrated, as was observed with the LiPF_6 aged materials.

Figure 3-24 (b) demonstrates that surfaces, even within the same particle, contained a mixture of spinel, residual $R\bar{3}m$ and a very small amount of true rocksalt phase. The rocksalt phase may be from the native 1 nm film of rocksalt initially present on the NCA. The corresponding SAED patterns for the three surfaces in Figure 3-24 (b) are presented in Figure 3-24 (c-e), respectively. All three surfaces had mainly layered structures with varying

spinel reflection intensities. The spinel reflections were weak on surface 1, very weak on surface 2, and non-existent on surface 3. In short, a transformation similar to the LiPF_6 case seems to be initiating but the degree of the transformation is far less in intensity and consistency.

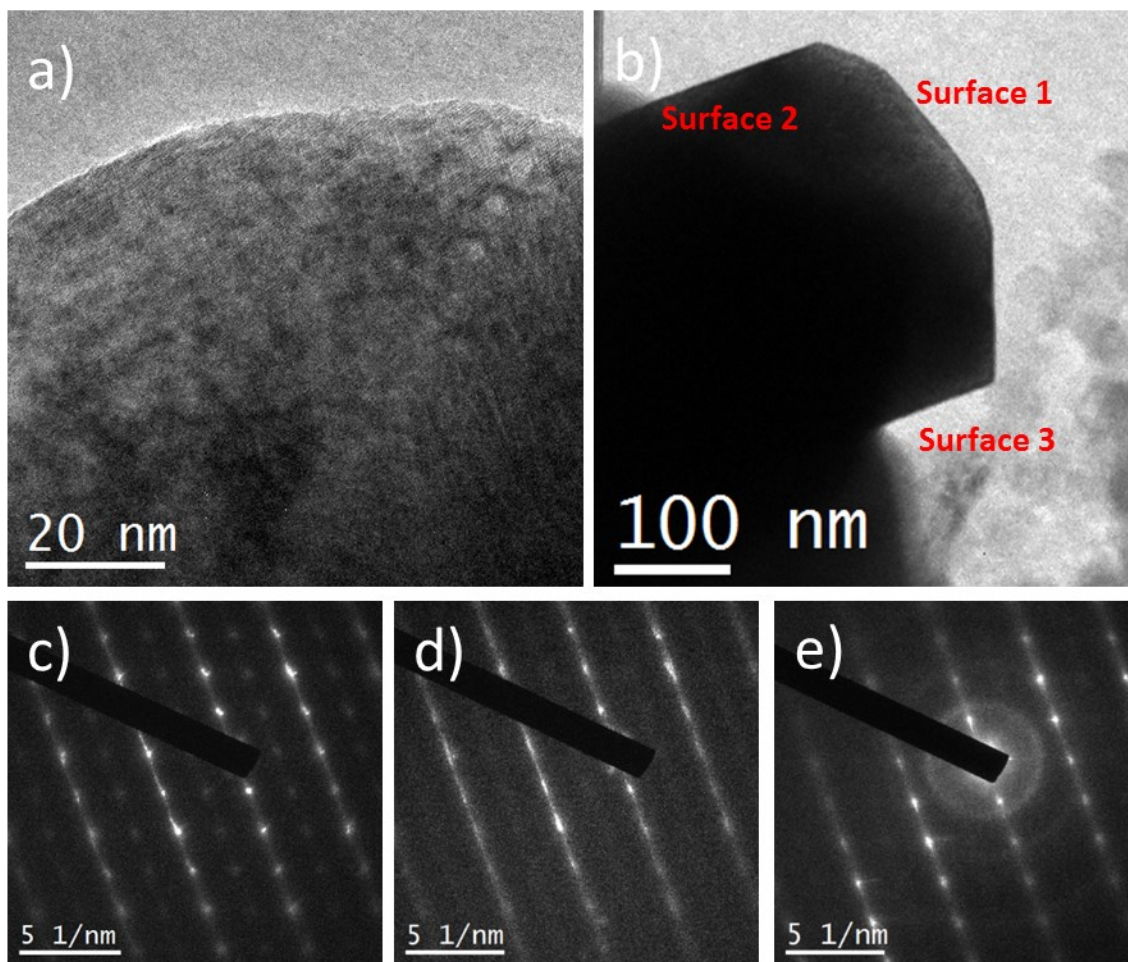


Figure 3-24: (a-b) HRTEM images of NCA particles aged in LiBF_4 at 4.75 V, 60°C for 10 h. SAED figures corresponding to surfaces (c) 1, (d) 2, and (e) 3 in image (b) are provided. Additional rows of weak reflections in (c) are indicative of the formation of the spinel phase.

Interestingly, the sharp difference in contrast between the bright 20 nm surface layer and the bulk (

Figure 3-23 (a)) in the LiPF_6 sample, is attributed to the significant amount of porosity observed in the surface layer. This porosity is a result of the observed transition metal dissolution and

reduces the absorption of the transmitted beam significantly. In contrast, the surface of LiBF_4 exposed particles (Figure 3-24 (a-b)) did not show this line of contrast demarcation consistent with the reduced dissolution products. While powder XRD experiments show that there are no structural changes to NCA throughout the bulk material (Figure 3-7), HRTEM results provide evidence of large structural and morphological transformations in the surface and subsurface regions. It was also observed that the LiPF_6 aged particles had significant surface roughening relative to the pristine material. Some surface texturing was also apparent in LiBF_4 samples, but at a much lesser degree than what was observed for LiPF_6 , consistent with the reduced dissolution for LiBF_4 aged samples.

3.4.5 Additional Studies

To facilitate faster analysis of new samples, coin cells were tested in a 60°C incubator, which mimics the thermal environment required for the exothermic reactions. Incubator cells were subjected to an identical electrochemical testing procedure as microcalorimetry cells, but in a 60°C isothermal environment instead of the dynamic profile used for microcalorimetry experiments. Figure 3-25 compares the current and accumulated capacity for duplicate microcalorimetry cells (black) and incubator cells (red). Both sets of cells show nearly indistinguishable exothermic reaction profiles during the 4.75 V, 60°C hold. The earlier onset of parasitic reactions and slightly higher measured capacity for the incubator cells can be attributed to the isothermal conditions at 60°C . Lower temperature phases (30°C and 45°C) for the microcalorimetry cells cause periods of reduced leakage currents and result in a lower measured capacity. The reproducibility of the parasitic reactions between the microcalorimetry and incubator cells enables a higher throughput approach to studying these particular cathode-electrolyte interactions by just measuring the current response as a test for the propensity of transition metal dissolution.

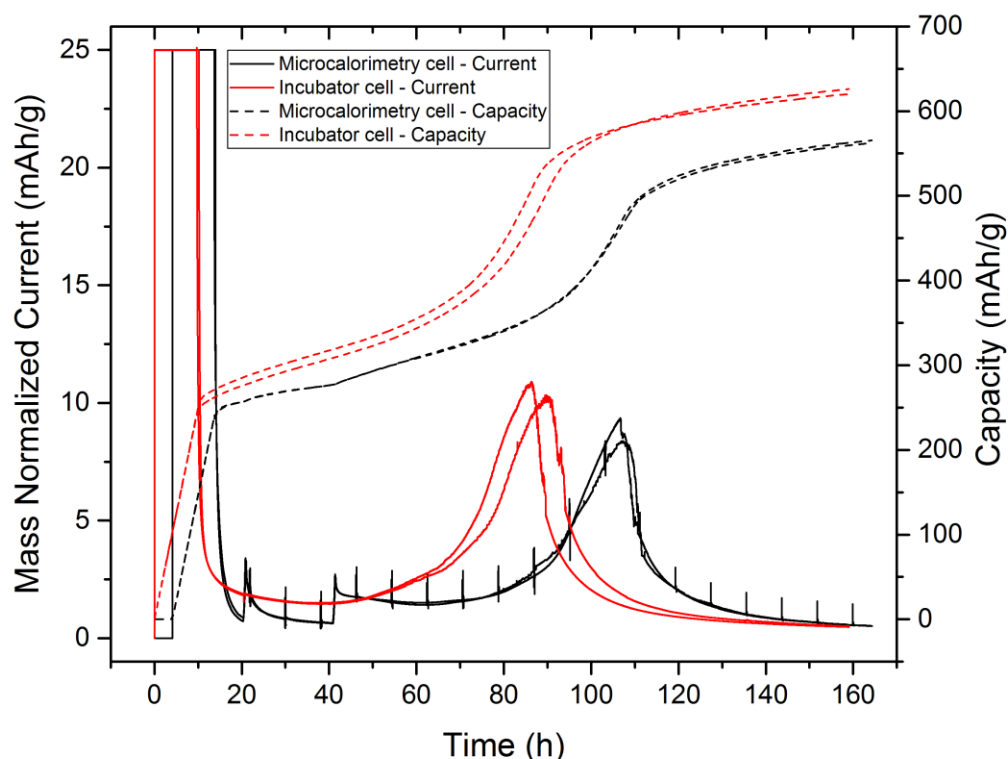


Figure 3-25: Current (solid lines) and accumulated capacity (dotted lines) comparison for NCA microcalorimetry coin cells (black) and incubator (red) coin cells. All cells were charged to 4.75 V at 25mA/g, and then held at 4.75 V under potentiostatic conditions. As previously described, the microcalorimetry cells were subjected to dynamic and isothermal conditions, while the coin cells in the incubator were isothermal at 60°C for the entirety of the test.

If such reactions are surface induced, the magnitude and/or kinetics of the dissolution should be increased with higher surface area NCA. High surface area (SA) NCA was developed by ball milling pristine NCA powder at 400 rpm for 15 minutes in an Ar atmosphere. XRD results (not included) showed no evidence of new phase development or structural degradation of the pristine material as a result of milling. In order to investigate the effect of native Li_2CO_3 on the surface of NCA, which can develop with ambient exposure during processing, portions of both the pristine and high surface area samples were exposed to ambient atmosphere to develop Li_2CO_3 on the particles' surface as discussed in the preceding section. It is important to note that the two samples were not exposed to ambient air at the same time, resulting in exposure to

potentially different degrees of humidity, temperature, and air composition. Regardless of when the samples were exposed, two weeks was observed to be ample time for the Li_2CO_3 growth. Other experiments show that additional exposure beyond two weeks resulted in minimal increases of Li_2CO_3 content, signifying that the reaction rate has been reduced to incremental levels.

For all samples, surface area was measured using BET analysis, while an estimate of the Li_2CO_3 content was determined by TGA.¹⁹⁹ Results of the BET and TGA experiments are shown in Table 3-I. Milled NCA was found to have a surface area of $7.40 \text{ m}^2/\text{g}$, around 16 times larger than the pristine sample ($0.46 \text{ m}^2/\text{g}$). The high surface area NCA had only minimal Li_2CO_3 development relative to the original material: 0.24 vs 0.12 wt%, respectively. 2 week exposed NCA and 2 week exposed, high surface area NCA samples had Li_2CO_3 contents around 0.82 and 1.74 wt%, each a roughly 7-fold increase compared to the non-exposed precursors. The surface areas of the exposed samples were assumed to be little changed as a result of exposure, based on BET measurements of similar NCA samples that were exposed to the ambient atmosphere.

Table 3-I: Surface area, Li_2CO_3 content, and average discharge capacities for four variations of NCA. Measured surface area, and Li_2CO_3 content for the four NCA variations are provided. After the constant voltage phase, cells were discharged at 5 mA/g to 2.7 V. The average discharge capacities after testing with either 1M LiPF_6 or 1M LiBF_4 in EC:DMC (1:1) are included.

Sample	Surface Area (m^2/g)	Li_2CO_3 Content (wt%)	Discharge Capacity in LiPF_6 (mAh/g)	Discharge Capacity in LiBF_4 (mAh/g)
Pristine NCA	0.46	0.12	0	165.5
High SA NCA	7.40	0.24	0	140.1
2 Week Exposed NCA	-	0.82	0	173.5
2 Week Exposed High SA NCA	-	1.74	0	137.7

Parasitic reactions for incubator cells made of pristine NCA, the $7.40 \text{ m}^2/\text{g}$ NCA and their exposed analogs are shown in Figure 3-26 (a) and Figure 3-26 (b) for cells with LiPF_6 and LiBF_4 salt, respectively. To accommodate the higher surface area NCA samples, a modified electrode

composition with additional binder and carbon black was used, as described in the experimental section. All active electrodes in Figure 3-26 (a) and (b) use this new composition to enable direct comparisons between samples. The parasitic peak shape is similar for all cells in Figure 3-26 (a), and despite the change in electrode composition, is comparable to the structure of exothermic reactions previously presented.

Comparison of the higher surface area, $7.40 \text{ m}^2/\text{g}$ NCA (red) to the lower surface area, $0.46 \text{ m}^2/\text{g}$ NCA (black) in Figure 3-26 (a) clearly demonstrates an earlier onset for parasitic reactions related to dissolution, however there is no significant change in the measured corrosion capacity. Since the observed reactions take place on the surface of the NCA particles, it is expected that increasing the number of potential sites for reaction would result in increased dissolution which manifests itself as an accelerated reaction. The 0.82 wt% Li_2CO_3 NCA sample (blue) also had a quicker initiation of the exotherm relative to the initial 0.12 wt% Li_2CO_3 NCA, although not as rapid as the 0.24 wt% Li_2CO_3 , $7.40 \text{ m}^2/\text{g}$ material. As with the increase in surface area, increasing Li_2CO_3 content did not result in additional total capacity. The critical indicator is the time it takes for the peak current to develop as it is a direct indication of both the quantity and kinetics of the dissolution products. The total corrosion capacity is relatively meaningless as all cells will shut down once the impedance of the negative increases to a critical value. Of all samples, the 1.74 wt% Li_2CO_3 , $7.40 \text{ m}^2/\text{g}$ material (green), representing the highest Li_2CO_3 content and surface area, has the shortest time to the peak in exothermic reactions. The combination of high surface area and increased Li_2CO_3 content causes the parasitic current to develop within a couple hours of reaching 4.75 V, around 10 h quicker than the next sample, $7.40 \text{ m}^2/\text{g}$ NCA. In summary, a trend towards faster initiation of the dissolution reaction is observed with both increasing surface area, and additional Li_2CO_3 wt%.

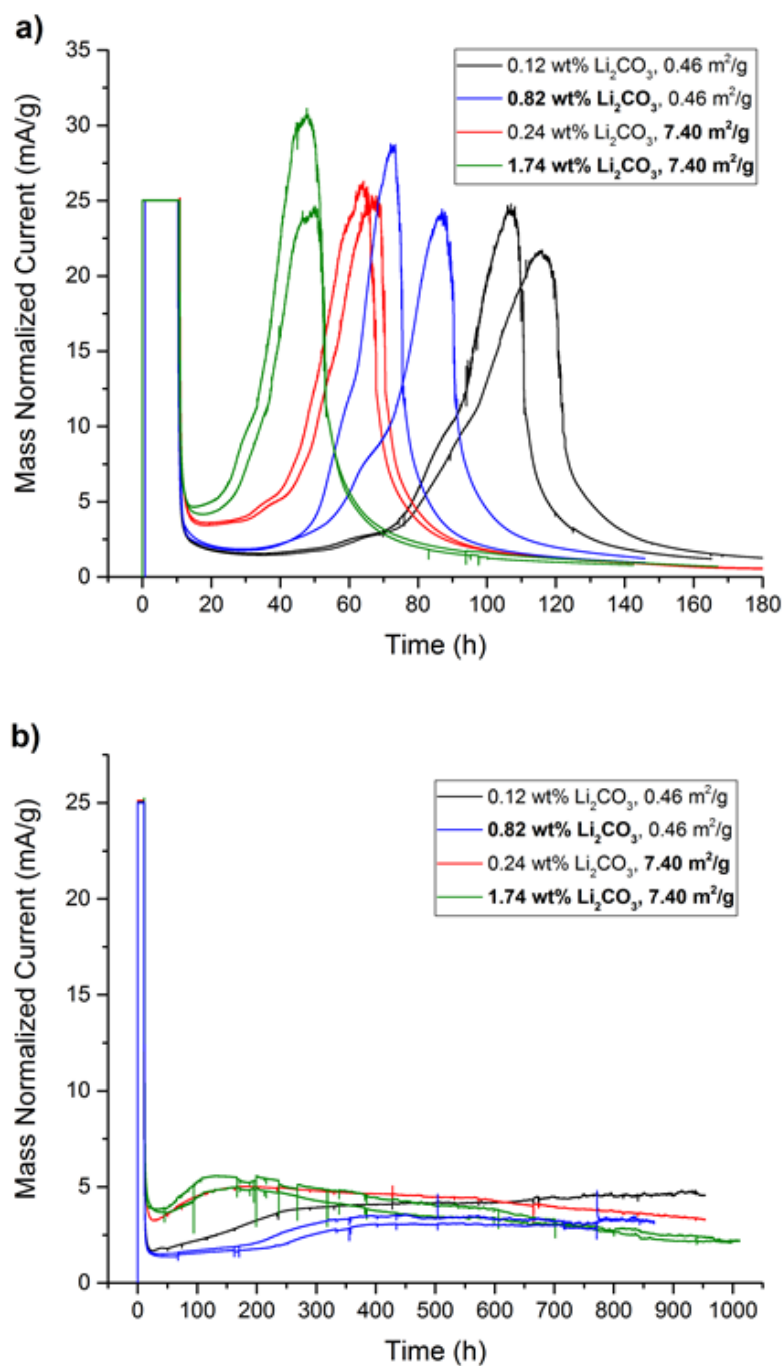


Figure 3-26: Comparison of the current from the parasitic reactions for 0.12 wt% Li_2CO_3 , $0.46 \text{ m}^2/\text{g}$ (black), 0.82 wt% Li_2CO_3 (blue), 0.24 wt% Li_2CO_3 , $7.40 \text{ m}^2/\text{g}$ (red), and 1.74 wt% Li_2CO_3 , $7.40 \text{ m}^2/\text{g}$ (green) NCA materials when using (a) LiPF_6 or (b) LiBF_4 salt in a EC:DMC (1:1) solvent. All samples were charged at 25 mA/g to 4.75 V , and then held potentiostatically at 4.75 V in a 60°C incubator.

The impact of surface area and Li_2CO_3 content on the parasitic reactions of NCA with 1M LiBF_4 EC:DMC (1:1) electrolyte is presented in Figure 3-26 (b). As shown in Figure 3-15, the degradation reactions for NCA with LiBF_4 salt have a fundamentally different profile than with LiPF_6 salt. The current profiles shown in Figure 3-26 (b) are similar to those for the LiBF_4 microcalorimetry cells; a small increase in current plateaus into a prolonged phase of elevated current. However unlike the microcalorimetry cells, the LiBF_4 incubator cells were held under potentiostatic conditions for nearly 1,000 h before being discharged. All samples maintained significant current throughout the entire test indicating that no passivation of the decomposition reaction occurred. The 0.24 wt% Li_2CO_3 , 7.40 m^2/g (red), and 1.74 wt% Li_2CO_3 , 7.40 m^2/g (green) NCA samples rapidly show an increase in current, after being charged to 4.75 V, correlated to the quick development of degradation reactions. However, the rise in current for 0.12 wt% Li_2CO_3 , 0.46 m^2/g (black) and 0.82 wt% Li_2CO_3 , 0.46 m^2/g NCA (blue) was much more gradual. As with the LiPF_6 sample set, the faster kinetics for the higher surface area materials can be attributed to the larger electrode-electrolyte interfacial area.

After the constant voltage segment, cells were discharged to 2.7 V at 5 mA/g at 60°C. Average discharge capacities for all cells in Figure 3-26 (a) and (b) are presented in Table 3-I. When tested with LiPF_6 salt, all cell variations demonstrated no discharge capacity. However, all of these cells had an OCV below 3 V prior to discharge, and half had an OCV below the 2.7 V threshold. As previously shown, the low OCV is a result of the excessive transition metal deposition on the negative electrode. Separate experiments show that when the negative electrode is replaced with a new piece of Li foil and fresh electrolyte, the post-exotherm NCA can be relithiated with a capacity of up to 150 mAh/g. As described earlier, for post-exotherm cells using LiPF_6 drastic impedance buildup on the negative electrode is observed, which makes removing Li ions during discharge exceedingly difficult. LiBF_4 cells fared much better, showing OCV values greater than 4.54 V and average discharge capacities between 140-175 mAh/g after 850-1000 h at 60°C and 4.75 V. Visual observations show that negative electrodes from LiBF_4 samples have

significantly less transition metal plating, even after much longer times at 4.75 V, and 60°C. Impedance scans of other LiBF₄ samples measure only moderate levels of impedance on the negative electrode, supporting our visual observations.

*Table 3-II: Co and Ni dissolution measurements from NCA determined by ICP-OES. * denotes that the minimum detection limit was reached, and that the listed value is the maximum possible.*

Sample Description	1M LiPF ₆ :EC:DMC (1:1)				1M LiBF ₄ :EC:DMC (1:1)			
	Total Co Dissolution (ug)	Total Ni Dissolution (ug)	% Co Dissolved	% Ni Dissolved	Total Co Dissolution (ug)	Total Ni Dissolution (ug)	% Co Dissolved	% Ni Dissolved
Baseline cell	1.116*	3.497	0.095*	0.056	7.444*	7.444*	0.495*	0.093*
4.5V-10hr	1.265*	2.530	0.091*	0.034	7.301*	7.301*	0.558*	0.105*
4.5V-10hr	1.265*	3.274	0.082*	0.040	7.370	32.012	0.534	0.436
4.5V-25hr	1.339*	8.928	0.080*	0.100	7.560*	7.560*	0.409*	0.077*
4.5V-25hr	1.116*	11.904	0.064*	0.128	7.430*	14.860	0.450*	0.169
4.75V-10hr	8.928	57.288	0.591	0.713	7.356*	27.492	0.455*	0.320
4.75V-10hr	13.392	89.280	0.769	0.966	7.220*	36.100	0.384*	0.362
4.75V-25hr	37.944	223.200	2.115	2.342	9.613	56.940	0.560	0.625
4.75V-25hr	40.920	238.080	2.226	2.438	10.263	68.176	0.561	0.701
4.75V-175hr	194.483	1054.694	10.349	10.566	53.820	299.000	3.167	3.312
4.75V-175hr	187.748	1006.327	10.994	11.095	47.852	276.645	2.914	3.171

Quantitative dissolution data was obtained from an additional set of 60°C cells which were specially prepared and tested using ICP-OES analysis. The ICP-OES samples were pristine NCA materials and used one of two different max potentials (4.5 or 4.75 V), a 10, 25 or 175 h CV period, and either LiPF₆ or LiBF₄ salt in EC:DMC (1:1). The left column of Table 3-II contains the sample description which provides information on the max charging potential and duration of the constant voltage segment. All samples were tested with both LiPF₆ and LiBF₄ salts to enable direct comparisons of the voltage and time in the potentiostatic hold as a function of salt. ICP-OES samples were prepared by disassembling charged cells, extracting the negative electrode and adjacent separator, and then dissolving the electrode in an HCl solution. The amount of total transition metal dissolution was calculated by extrapolating the detected concentrations of Co and Ni to the entire sample volume, while the % dissolution value was obtained by normalizing the magnitude of transition metal dissolution to the amount of metal originally present in the positive electrode sample. Samples with total dissolution data denoted by * indicated that the minimum detection limit for ICP-OES was reached, and the maximum possible value is listed.

Baseline cells, comprised of all cell parts and active materials but having no electrochemical or thermal testing, were made using each electrolyte salt. These samples established baseline Co and Ni dissolution levels, from native acids that may be present in the electrolyte. Since the ICP-OES measurements only measure the Co and Ni deposited on the negative electrode, and trapped within one of the two separators, the technique will always provide results slightly below the true degree of dissolution. Comparison of the NCA – LiPF₆ samples charged to 4.5 V, shows that regardless of whether a 10 or 25 h constant voltage segment (CV) was used, no significant Co dissolution was measured. While absolute amounts of Ni were measured in all of these samples, the degree of dissolution was still minimal, with ~0.04% and ~0.12% for the 10 and 25 h potentiostatic holds, respectively. In contrast, NCA – LiPF₆ samples charged to 4.75 V have markedly higher levels of both Co and Ni dissolution. % Co and % Ni dissolution results for the 10 h CV samples were ~0.68 and ~0.84, while the analogous 25 h CV samples had extremely high values of ~2.17% and ~2.39%. Clearly, the magnitude of dissolution increases rapidly with higher potentials and with extended time in the potentiostatic hold. In fact, below 4.75 V the measured dissolution products were either indistinguishable or insignificant compared to the baseline sample.

NCA – LiBF₄ samples, although showing much less dissolution, provide supporting evidence of increased transition metal dissolution with higher potentials and a longer potentiostatic hold. Compared to the LiBF₄ baseline sample, both the 10 and 25 h, 4.5 V LiBF₄ samples had negligible levels of Co dissolution. Only one of the duplicate cells for each the 4.5 V 10 h and 4.5 V 25 h samples had a significant degree of Ni dissolution: 0.436% and 0.169%, respectively. For the LiBF₄ samples at 4.75 V, ~0.34 % for 10 h CV, and ~0.66 % for 25 h CV were measured reproducibly for both cells. Although enhanced relative to 4.5 V, these values are approximately 300% less than analogous the LiPF₆ samples. For both LiPF₆ and LiBF₄ salts, NCA samples were held at 4.75 V until parasitic reactions were completed (175 h potentiostatic phase) to quantitatively determine the amount of Co and Ni dissolution in an extreme scenario. In

LiPF₆, the 4.75 V 175 h samples had ~10.67% Co and ~10.83% Ni dissolution, while in LiBF₄ ~3.04 % Co and ~3.24 % Ni dissolution was observed. Samples using LiPF₆ again exhibit approximately 3X the Co and Ni dissolution rates compared to the LiBF₄ samples, which supports the conclusions determined previously by electrochemistry, XAS, and HRTEM. Importantly, the analysis of the % Co and % Ni dissolution results from the ICP-OES data shows that the dissolution rate for Co and Ni is nearly identical for every sample, suggesting that there is no preferential etching of Co or Ni from the positive electrode.

3.5 Discussion

A number of studies have explored the surface and sub-surface evolution of R $\bar{3}$ m compounds including NCA, but most of these have been performed at voltages <4.4 V and very few at full delithiation. On one hand, this study could be taken as an extrapolation of the failure modes observed at lower potentials and elevated temperature. On the other hand, voltages above 4.4 or 4.5 V can activate new decomposition processes, particularly related to carbonates as many commence anodic decomposition at such potentials. The goal of this particular research was to explore the role of the electrolyte in inducing failure modes, especially dissolution, at the surface of the fully delithiated R $\bar{3}$ m materials without the mechanochemical related failure modes induced by cycling. Clearly there is an intimate relationship between the electrolyte and the stability of the positive electrode at high potentials.

Based on the surface characterization of NCA by XPS, TEY mode XAS, FFT via HRTEM and SAED, one could conclude that exposure to LiPF₆ and LiBF₄ electrolytes induces a structural transformation to a phase comprised of a Ni²⁺ environment consistent with a spinel-like structure and that the transformation is much more pronounced in the LiPF₆ electrolyte. The reaction seems to passivate or proceed slowly in LiBF₄, vs. a more intense evolution when using LiPF₆. One should not infer from this statement that the diffusion of O out of the structure or back diffusion of Ni²⁺ is enhanced when LiPF₆ is present leading to a thicker transformation at the

surface. Inspection of the HRTEM images suggests that the etching induced by dissolution when LiPF_6 is used allows a porous surface to develop. This porous surface enables electrolyte penetration into the pores and results in a “deeper” transformation of the surface to the spinel-like phase. Therefore, the thicker surface phase is not necessarily a result of enhanced oxygen and Ni^{2+} diffusion, but rather enhanced access to the sub-surface structures via etched porosity. As such, if dissolution induced porosity could be limited; the depth of the spinel-like surface transformation could be limited also.

The surface transformation which induces the impedance increase is classified as “spinel-like” within this manuscript due to the fact that there is a degree of transition metal occupation developing in the octahedral 3a Li sites in $R\bar{3}m$, not due to significant tetrahedral site (8a in $Fd\bar{3}m$) occupation. This leads to an important question of what a partially occupied 3a site (16d in $Fd\bar{3}m$) is called crystallographically, especially in the context to the spectrum of the spinel to rocksalt transformation where the rocksalt would signify full transition metal occupation of the 3a site (vs. 25% for spinel). In this paper we refer to it as “spinel-like” as the electron diffraction suggests a degree of transition metal ordering within the octahedral sites has developed. It is likely that the 3a occupation may have exceeded the 25% required for spinel on the path towards rocksalt. Such defects would also enable proper charge balancing such that bivalent Ni could be observed in a “spinel-like” structure. This is the subject of a following paper and is too detailed to be discussed herein. A takeaway relative to the electrochemistry is that the surface transformation can be protective and passivating by limiting further back diffusion of Ni or forward diffusion of oxygen, but if a porous structure develops the extension of the transformation layer can be extended significantly. This extension does not necessarily increase the impedance significantly as the electrolyte penetrates this porous layer and allows effective transport of Li^+ deeper through the surface transformed regions. Indeed both LiPF_6 and LiBF_4 electrolytes increase the positive

electrode impedance about 10X due to the surface transformation after about 10 h at 4.75 V and 60°C even though the thickness of the transformed layer is drastically different.

The quantitative dissolution data via ICP was revealing in its reproducibility and its systematic correlation to the onset of the peak in current and exotherm observed in the potentiostatic electrochemical data. The latter suggests such studies can be used in lieu of the ICP analysis to extract qualitative comparisons as long as the structure of the electrochemical cell and subsequent tortuosity of the electrolyte through the cell is kept consistent. The quantitative analysis tied with the electrochemical data revealed these conclusions regarding dissolution in LiPF_6 EC:DMC electrolytes:

- i. Dissolution correlates with an increase of surface area
- ii. Dissolution correlates with an increase of surface Li_2CO_3
- iii. Dissolution correlates with the cell voltage
- iv. Dissolution correlates with potentiostatic time

The dissolution products are intimately tied to the presence of LiPF_6 as 300% less dissolution is observed for samples containing LiBF_4 . This dissolution is not a result of hydrolysis from the HF native to LiPF_6 solutions, as the dissolution products trend significantly with the state of charge, time at elevated voltages, and subsequent reduction of the NCA surface. The voltage dependency of the dissolution product is consistent with results shown earlier for LiCoO_2 and other materials.^{40,104} These results, combined with the fact that the magnitude and intensity of the dissolution is correlated with the material (NCA vs. LCO), the surface area, and the surface chemistry (especially Li_2CO_3 content), clearly cements the symbiotic relationship between the surface, surface chemistry and the decomposition of the LiPF_6 based electrolyte. A few mechanisms have been published on the interaction of LiPF_6 leading to the catalytic decomposition of LiPF_6 at high potentials which creates an oxidized PF_6 “radical” and HF. This is despite the fact that LiPF_6 is in theory a stable electrolyte salt at high voltage.

The impact of dissolution on the mixed potential of the negative electrode was very significant. The potential shift occurring at the positive and negative electrodes is undetectable under constant voltage charge, but three electrode studies revealed that the Li negative electrode gradually developed a mixed potential approximately equivalent to that of the redox potential of Ni/Ni^{2+} , resulting in a greater than 2 V shift. Even a < 0.05 V shift in the positive electrode potential induced by the increase of the negative electrode potential would be detrimental to the long term performance of an electrochemical cell. The effective potential of the positive electrode will rise thus launching the positive electrode into an accelerated continuous cycle of dissolution and potential increase, all while the two-electrode voltage is invariant. Even small potential shifts in a non-fully delithiated positive electrode could induce such a cycle to occur over a long period of time. The main importance of transition metal dissolution to Li-ion batteries is the metal deposition on the negative electrode, which even in small amounts induces catalytic reactions and modification of the SEI formed on graphite and alloy negative electrodes. While most studies have not shown that the deposition product is a metallic species, our data herein shows the presence of metallic Ni and probable identification of metallic Co, present on the Li metal negative electrode. In a research scenario, tracking the propensity of a material to induce dissolution within an electrolyte, beyond simple HF acid attack from the native HF in equilibrium with LiPF_6 , has been problematic. Using this accelerated cycle of dissolution, the potential shifts while held at constant two-electrode potential show a surprisingly reproducible methodology for studying the degree for which positive electrode surfaces and electrolytes induce dissolution. No doubt, refined three-electrode cells tracking small potential changes will make the resolution of the technique even more effective.

Both the baseline exothermic heat generation and corrosion current was observed to increase systematically with voltage and temperature. The background current at 4.75 V and 60°C is likely due to the anodic decomposition of the carbonate solvent as the current and heat generated were virtually identical for the LiBF_4 and LiPF_6 EC:DMC electrolytes before the

dissolution induced voltage shift in LiPF_6 electrolytes. A few model reactions based on electrolyte characterization have been proposed by others, when factoring in the catalytic NCA, the most obvious case of NCA surface and salt independent solvent interactions rests in a simplified reaction of Equation 3-1 and Equation 3-2 which are intimately tied.



This is based on the over-oxidation reactions proposed by Kumai *et al* for CoO_2 ($\text{Li}_{1-x}\text{CoO}_2$) leading to Co_3O_4 . The generation of water was confirmed by their analysis.²⁰⁰ Both our XPS and HRTEM results support the reduction of Ni^{3+} to Ni^{2+} and the formation of a surface layer composed of a Ni^{2+} rich oxide “spinel,” which provides evidence that these reactions are likely accelerated by the oxidation of the solvent. However, in the LiBF_4 case the Ni^{2+} and “NiO” surface content is much lower suggesting effective passivation. This leads us to the second question of why would “NiO” be effective in passivation in LiBF_4 electrolyte but not as much with LiPF_6 . As discussed above, much relates to the propensity of LiPF_6 to aggressively etch the surface. This promotes curiosity as to what the exact decomposition reactions of the salt are and their influence on the NCA surface as we have discussed above with respect to dissolution.

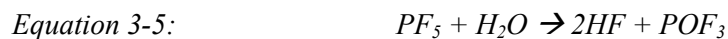
LiBF_4 is quite oxidation resistant



in contrast, LiPF_6 itself decomposes easily⁶⁷:



In traces of water a further decomposition also develops:



or



In both reactions, the presence of even minute amounts of H_2O , either native or byproduct, rapidly shifts the mechanisms towards the production of POF_x products and HF.²⁰¹

Clearly the presence of LiPF_6 resulted in the decomposition products of Li-P-O-F present based on our XPS results. The HF will then proceed to attack the NCA surface regardless of if it has transformed to “NiO” already or not. The fact that all characterization shows the presence of “NiO” “spinel” suggests that the solvent decomposition reaction precedes any HF attack. Assuming a simplified surface of “NiO,” the reaction would then be expected to proceed by way of:

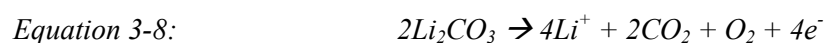


The water produced will further react with LiPF_6 and also cause H_2 production at the negative electrode, either by reduction of H_2O or HF. NiF_2 could also be produced by interaction with the HF, but there is little evidence of NiF_2 on the surface of the NCA reacted at 4.75 V. The reason likely rests in the fact that NiF_2 is relatively soluble in carbonates especially if nickel oxyfluoride species are produced. An important question remains as to what complexes allow the diffusion of the transition metals through the electrolyte and deposit on the negative electrode. This could be by way of simple solvated divalent cations charged balanced by PF_6^- anions. A comprehensive analysis of 4.7 V $\text{LiNi}_{0.5}\text{Mn}_{1.5}\text{O}_4$ spinel, which also has transition metal dissolution challenges¹⁹³, revealed the formation of a variety of $\text{Mn}^{2/3+}$ and Ni^{2+} complexes with β -diketonate ligands when linear and cyclic carbonates were anodically decomposed in the presence of the spinel.¹²⁶ These partially polymerized films dissolved in the electrolyte solution and migrated to the negative electrode.

Devoid of the carbonate solvent oxidation, and the O_2 contribution given by the reduction of the NCA, we must also be cognizant of the following reactions that may be generated at the surface of the non-oxide positive electrode components. Density functional theory suggests the formation of molecular HF from the proton abstraction from the carbonate species at high voltages (>4.5 V) for DMC/ PF_6^- and DMC/ BF_4^- scenarios.²⁰² Indeed, this reaction may proceed to a degree as we observe a small, but systematic increase in voltage induced dissolution products even when utilizing LiBF_4 . It has been theorized in studies based on LiMn_2O_4 that the PF_6^- anion

is oxidized by the positive electrode leading to PF_6^0 which then reacts with carbonate electrolytes to form insoluble oxyfluorophosphate compounds.²⁰³ Another model has been presented by Aoshima *et al* in their work based on delithiated LiMn_2O_4 . They propose the decarboxylation of the carbonate solvent resulting in the formation of $\text{EtOH} + \text{CO}_2 + \text{C}_2\text{H}_2$.¹²⁸ They then propose the EtOH reduces MnO_2 to MnO resulting in the formation of AcOEt and H_2O . NCA could follow a similar reaction pathway where the water produced will then interact with LiPF_6 per Equation 3-5 and Equation 3-6.

The impact of Li_2CO_3 which we observed to accelerate dissolution deserves particular attention. It is clear from the surface characterization that Li_2CO_3 is consumed from the surface of the NCA. Excess Li_2CO_3 has long been known to be highly detrimental to the stability of LiCoO_2 ¹⁹⁹ and NMC.²⁰⁴ Li_2CO_3 is a particular nemesis of NCA as even brief exposures of NCA to an ambient processing environment will induce a thin coating of Li_2CO_3 . In addition, Li_2CO_3 is known to oxidize from the surface of NCA (Equation 3-8) resulting in the formation of CO_2 and O_2 .⁹³



The O_2 can then react with carbonates as per (Equation 3-2) thus leading to additional water generation. Once water is generated, the traditional LiPF_6 hydrolysis reaction (Equation 3-4, Equation 3-5, and Equation 3-6) will become prevalent. In addition, at 4.75 V and elevated temperature, we would expect the thermodynamically favored reaction (Equation 3-9) to be accelerated.²⁰⁵ However, it should also be noted that the process leading to the formation of Li_2CO_3 on the positive electrode surface has some complexity and the intermediate states leading to the identifiable Li_2CO_3 may have their own contribution to the observed impact on the electrochemical properties.



Once POF_3 species are generated, these react with cyclic carbonates to form CO_2 and oligoethylene oxides containing fluorophosphates end groups and capped with alkyl fluoride $[\text{OPF}_2(\text{OCH}_2\text{CH}_2)_n\text{F}]$.²⁰⁶

This presents an unfortunate scenario for Li-ion batteries as LiPF_6 offers outstanding conductivity and Al current collector passivation. Recent reports for stability of electrolytes at high voltages have trended away from LiPF_6 towards LiBF_4 .^{64,207} Our results herein support this direction as significantly less dissolution was identified for electrolytes containing LiBF_4 as the electrolyte salt. However, this should not be taken as a quick fix to the voltage window issue with catalytic surfaces. The downside is apparent in that little passivation of the surface occurs and we observe much corrosion current and heat generation. This is undoubtedly due to the surface of the NCA acting as a catalyst to the constant generation of CO_2 gas through the anodic oxidation of the carbonate electrolyte as per Equation 3-1 and Equation 3-2.²⁰⁸ The gas generation was so great that LiBF_4 coin cells held at 4.75 V, and 60°C, physically ruptured due to high pressure. Obviously, such issues can be addressed by appropriate selection of surface coatings/chemistry¹³⁷ and also additives to decompose and passivate the surface.

Serendipitously, we have performed a de facto investigation of the stability of NCA at voltages in excess of 6 V. Surprisingly, the bulk structure of the NCA and LCO survived such excursions with little phase transformation or transition metal migration from the 3b to 3a layer. Densifications to 3D oxides of reduced oxidation state require considerable oxygen diffusion from the bulk to the surface or back diffusion of the transition metals into the core of the structure. Under much less extreme conditions, but after storage for over 2 years, Watanabe *et al* showed reduced performance of LiCoO_2 vs. NCA positive electrodes and that the surface decomposition towards densified oxides progressed deeper in the case of LiCoO_2 .¹⁹⁶ A mechanism which disrupts the diffusion of the oxygen or back diffusion of the transition metal is established in these layered compounds.

Although much focus is on the surface and sub-surface reactions and their critical role in achieving practical cycling of layered compounds at full delithiation, it is only one of a series of failure modes. However, many of the failure modes attributed to the bulk may in fact be surface related. Such an example can be found in the transition metal movement to the 3a site in the bulk. In most, but not all, layered oxides this movement requires divalent cation diffusion through the tetrahedral sites to the 3a octahedral sites. The reduction of the transition metal occurs by oxygen loss at the surface of the material, most likely catalyzed by the electrolyte reactions. During complete delithiation there is a strong anisotropic collapse in the c lattice parameter which places considerable strain within the structure. In one case this can lead to dislocation effects and blocking of diffusion pathways, as well as micro-cracking. Micro-cracking and increased surface area, as long as they do not lead to electrochemical isolation, can be a good thing if the increased surface area does not induce additional access points for surface decomposition. As such, much attention to bulk transformations and their role in failure modes needs to be explored. However, all of these are addressable challenges and there is no reason not to be optimistic about full utilization of the theoretical capacity of $R\bar{3}m$ materials in the future. Indeed, “Ni⁴⁺” rich 4.7 V transition metal oxides of spinel structure cycled to 4.99 V has seen stability for over 500 cycles when cycled at 50-60°C in LiPF₆ or LiBF₄ EC:DMC.^{64,65} As such, the transition metal oxide structure plays an important role in the initiation of the decomposition reactions, and it may be no coincidence that “spinel-like” transformation of the layered surface seems to passivate the layered compound from excessive electrode decomposition. However the detrimental role of gassing still remains a factor in many of these scenarios.

3.6 Conclusion

The characterization of NCA after long periods of potentiostatic analysis near full delithiation reveals little bulk degradation but significant transformations of the surface and subsurface structure. Surface degradation to Ni²⁺-rich, spinel-like regions seems to be initiated by

the oxidation of the electrolyte solvent through the release of oxygen by the metastable delithiated $\text{R}\bar{3}\text{m}$ NCA. Evidence suggests that the surface reduction reaction would be largely passivated if etching induced by the decomposition of the fluoride salt did not exist, especially for LiPF_6 which is known to readily form HF. Such etching led to a porous surface layer which enabled electrolyte access to further propagate the reaction. Extensive dissolution studies revealed a consistent 300% increase in transition metal dissolution induced by LiPF_6 relative to LiBF_4 . Such dissolution is activated by the cell voltage, and likely tied into the water producing oxidation reaction of the carbonate solvents. Dissolution of Co and Ni occurred in stoichiometric ratios consistent with the original stoichiometry of the NCA parent material. Fine analysis by *operando* microcalorimetry and potentiostatic studies reveal that dissolution can be extensive enough to induce a large potential shift of the negative electrode, which was confirmed by three-electrode electrochemical analysis. A detailed dissolution study using the aforementioned method and/or ICP analysis revealed increased transition metal dissolution with the use of LiPF_6 vs. LiBF_4 , with increased surface area, and with increased quantities of Li_2CO_3 degradation products present on the surface of NCA after atmospheric exposure.

3.7 Acknowledgement

This work was supported as part of NECCES, an Energy Frontier Research Center funded by the U.S. Department of Energy, Office of Science, Office of Basic Energy Sciences under Award No. DE-SC0012583. XAS experiments were performed at beamline 8.0.1 at the ALS and beamline I09 at Diamond Light Source. The work at ALS was supported by the Office of Basic Energy Sciences, of the U.S. Department of Energy under Contract No. DE-AC02-05CH11231. We thank Diamond Light Source for access to beamline I09 (SI 12764) that contributed to the results presented here. We would also like to thank the beamline scientists, Wanli Yang at ALS and Tien-Lin Lee at Diamond Light Source, for their assistance.

3.8 Next Steps

The results presented in Table 3-I and Figure 3-26 made evident the deleterious impact that Li_2CO_3 has on the structural and chemical stability of NCA at high states of charge. The reaction mechanisms supporting the increased parasitic currents and material degradation of the exposed NCA samples were proposed in Equation 3-8 and Equation 3-9. While the negative consequences of ambient exposure of layered oxides were clear from the results, the specific mechanisms in which the surface impurity species are developed are relatively unknown. Furthermore, the impact of Li_2CO_3 could not be conclusively determined because a comprehensive analysis of all the surface impurity species present on the exposed material was not performed. To gain better insight into relationship between the electrode's surface species and the electrochemical capabilities of the layered oxide material a thorough investigation into the growth mechanisms for surface impurity species was completed. These species were rigorously identified and quantified, and then methodically removed such that the individual impact that each specie had on the electrode's electrochemical performance could be understood. Chapter 4 details and discusses the study of the growth mechanisms and impact of the surface impurity species on layered oxide materials.

4 GROWTH OF AMBIENT INDUCED SURFACE IMPURITY SPECIES ON LAYERED POSITIVE ELECTRODE MATERIALS AND IMPACT ON ELECTROCHEMICAL PERFORMANCE

4.1 Abstract

Surface impurity species, most notably Li_2CO_3 , that develop on layered oxide positive electrode materials with atmospheric aging have been reported to be highly detrimental to the subsequent electrochemical performance. $\text{LiNi}_{0.8}\text{Co}_{0.15}\text{Al}_{0.05}\text{O}_2$ (NCA) was used as a model layered oxide compound to evaluate the growth and subsequent electrochemical impact of H_2O , LiHCO_3 , LiOH and Li_2CO_3 . Methodical high temperature annealing enabled the systematic removal of each impurity specie, thus permitting the determination of each specie's individual effect on the host material's electrochemical performance. Extensive cycling of exposed and annealed materials emphasized the cycle life degradation and capacity loss induced by each impurity, while rate capability measurements correlated the electrode impedance to the impurity species present. Based on these characterization results, this work attempts to clarify decades of ambiguity over the growth mechanisms and the electrochemical impact of the specific surface impurity species formed during powder storage in various environments.

4.2 Introduction

The initial surface chemistry of Li-ion electrode materials plays a critical role in the development of in-situ derived interphases with the electrolyte and on the subsequent electrochemical performance. The surface chemistry can have a beneficial or destructive impact on performance relative to the bulk material. The principal challenge is controlling the variable surface chemistries which are induced by impurities during processing or material instability in an ambient atmosphere. Impurity species on the surface of the electrochemically active materials have been shown to decrease both the electronic and ionic conductivities as well as reduce the amount of electrochemically viable lithium.^{122,209} These consequences have a profound negative impact on the materials' cycle life and energy density, resulting in significantly reduced cell

performance.^{94,130,147} The higher impedance has been proposed to create localized heating, which is known to increase the risk of catastrophically destroying the cell or igniting a liquid electrolyte.^{27,95,210,211} As a result, understanding the impact and controlling the surface impurities on positive electrode materials is of utmost importance to improve the functionality and safety of secondary lithium-ion batteries.

The primary surface impurity species that develop when layered positive electrode materials are exposed to the ambient atmosphere include adsorbed H_2O , LiHCO_3 , LiOH , and Li_2CO_3 .^{94,100,212–215} Since the impurity species are limited to the surface of the host particles, surface sensitive characterization techniques such as Fourier transform infrared (FTIR) spectroscopy^{94,121,147,209,212,216}, and X-ray photoelectron spectroscopy (XPS)^{100,121,122,147,214,217}, are frequently used to study these materials. These techniques in conjunction with thermogravimetric analysis (TGA)^{122,213}, X-ray diffraction (XRD)^{94,100,122,213–215,218} and Karl-Fisher titration (KF)²¹² have enabled the identification and quantification of these impurity species.

Transition metal reduction in the surface and subsurface regions of these positive electrode materials, which cause the structural transition from the layered phase to spinel or rocksalt-type phases, has been observed upon exposure in air.^{89,91,95,140,164} It has been proposed that the transition metal reduction from a valence state of +3 to +2 produces active oxygen species which concurrently catalyzes the formation of the surface impurity species.^{100,122} Adsorbed H_2O and CO_2 react with the highly active oxygen species to produce hydroxyl, bicarbonate, and carbonate species. Then lithium from the host structure and the newly formed surface products, react to create LiOH , LiHCO_3 and Li_2CO_3 .¹²² The instability of Ni^{3+} and the propensity for Ni^{3+} to be reduced to Ni^{2+} encourages the development of impurity species on the surfaces of Ni-rich layered oxides, by easily forming active oxygen sites.^{122,214,218} In isostructural materials with higher amounts of Co, less LiOH and Li_2CO_3 are observed because the increased stability of Co^{3+} minimizes the creation of active oxygen species on the surface.²¹⁸ Similarly, when layered oxide materials contain some Mn atoms, lower concentrations of surface impurities

are measured because of the preference for Mn^{3+} to be oxidized to Mn^{4+} , which simultaneously reduces another transition metal to the +2 valence state and prevents additional transition metal reduction that would create the active oxygen sites.^{215,219}

A systematic inverse relationship between a material's redox potential and air stability is known.²²⁰ For example, the trend of increasing redox potential during the delithiation process of $\text{LiNi}_{0.8}\text{Co}_{0.15}\text{Al}_{0.05}\text{O}_2$ (NCA) < LiCoO_2 < LiMn_2O_4 leads to the instability of nickelates, such as NCA, in air relative to the increased stability of LiCoO_2 and the excellent stability of LiMn_2O_4 . While some Li_2CO_3 has been observed to form on LiCoO_2 with long exposures, it is mostly a byproduct of excess Li utilized in the initial fabrication of the electrode.³⁷ Similarly, little Li_2CO_3 is observed on air exposed LiMn_2O_4 because of the material's high redox potential.²²⁰

The detrimental impact that the chemical and structural changes on the layered oxide's surface have on the material's electrochemical performance is well documented. Lower discharge capacities and reduced rate capability for NCA electrodes were correlated to carbonate species for cells with both solid and liquid electrolytes by *Visbal et al.*¹⁴⁷ and *Zhuang et al.*⁹⁴, respectively. The increased interfacial resistance caused by the development of the surface impurity layer impedes the lithium-ion transport across the electrode-electrolyte barrier resulting in increased deviation from the thermodynamic potential when cycling, especially at higher rates.^{94,100,122,139} Additionally, the newly formed divalent transition metals migrate from the 3b to the 3a sites in the $R\bar{3}m$ structure. This causes the transformations from layered to spinel and rocksalt-type phases on the material's surface, which obstructs both the electronic conductivity and lithium-ion diffusivity.^{89,91,94,164} These structural changes further increase the positive electrode's electronic and charge transfer impedances.¹⁴⁰ The presence of Li_2CO_3 on the surface of LiCoO_2 was shown to be highly detrimental to the electrochemical performance and that such performance was renewed with the high temperature removal of the Li_2CO_3 .^{199,221} The development of impurity species also influences the reversible capacity by trapping lithium from the host structure in the newly formed surface layer. These trapped lithium ions can be at least partially restored by

charging the electrode to sufficient potentials to deintercalate the lithium from the impurity species.^{209,216} However, charging to the high potentials necessary to retrieve the lithium atoms from the impurity species may generate adverse consequences such as electrolyte oxidation, or reactions between the deintercalated impurity species and the electrolyte.^{124,156,163,222} Furthermore, it has been proposed that growth of Li_2CO_3 can induce some positive electrode particle isolation by establishing either an electronic or ionic barrier around particles or by preventing electrolyte from accessing a sufficient number of pores.⁹⁴ While positive electrode particle isolation hasn't yet been conclusively attributed to other impurity species, the low electronic and lithium conductivities of LiOH or Li_2O are likely sufficient to duplicate the isolation mechanisms proposed for Li_2CO_3 .

The presence of impurity species at the electrode-electrolyte interface can also initiate adverse reactions between the electrolyte and either the impurity species or the reduced transition metals on the surface of the positive electrode.^{121,157,201,223} *Aurbach et al.* observed that the initial layer of Li_2CO_3 on their pristine LiNiO_2 samples is lost during storage in electrolyte solutions containing Li salts, and replaced by an assortment of surface species including organic and inorganic carbonates, alkoxides, and salt decomposition products.¹²¹ Their FTIR and XPS measurements show that when submersed in an LiPF_6 solution the Li_2CO_3 layer is replaced by LiF , which is a product of the HF present in the electrolyte, and that this new surface layer significantly raises the electrode impedance.¹²¹ Similar results were obtained for LiMn_2O_4 ¹²¹, and NCA ^{216,224} positive electrodes. Our previous work demonstrates that layered oxide materials with higher contents of surface impurities have an amplified propensity for transition metal dissolution, likely caused by the increase of reduced transition metals that are present at the material's surface.²²³ Impurity species other than Li_2CO_3 can also have adverse effects on a cell's performance. For example, it is well known that adsorbed and absorbed H_2O will react with fluorinated electrolyte salts to produce HF , which then degrades the positive electrode.^{157,201}

Furthermore, the reactions between HF and the positive electrode are autocatalytic, leading to significant destruction of the electrode's surface.^{157,225}

While the formation of Li_2CO_3 and other impurity species on the surface of layered oxide materials is frequently documented, the exact growth mechanisms are not well understood. As previously mentioned, many publications support the conclusion that adsorbed H_2O and CO_2 react with the positive electrode because reduction of the transition metal atoms creates active oxygen sites. However, there is uncertainty in the literature over whether Li_2CO_3 can form by a direct reaction between CO_2 and the layered oxide material or if intermediary phases, such as LiHCO_3 or LiOH , are necessary. *Matsumoto et al.* suggest that NCA readily reacts with CO_2 to form Li_2CO_3 , but acknowledge that moisture promotes the carbonate formation at low temperatures.²¹³ Both *Liu et al.* and *Zhang et al.* proposed reaction mechanisms that require intermediary impurity phases before the development of Li_2CO_3 .^{122,215} The topic is further complicated by the temperature dependence of these reactions. Li_2CO_3 has been shown to form on NCA when exposed to dried 100% CO_2 at 400°C , but the authors did not demonstrate that this reaction could take place at lower temperatures.²¹⁴

In order to elucidate the mechanisms for the formation of impurity species on the surface of layered oxide materials and to clarify the understanding of the atmospheric environments necessary for growth, a comprehensive analysis of the changes to the surface of NCA as a function of atmosphere has been investigated. As noted above, a number of studies, including those from our own group, have documented evidence of distinct performance improvements, mostly in reduced impedance and improved cycling stability, once surface Li_2CO_3 is removed. The ultimate goal of the present investigation is to identify if Li_2CO_3 is the main surface species leading to poor performance or whether it is one of the other species that are present and integral to the formation of Li_2CO_3 .

In this investigation NCA electrodes were exposed to ambient atmosphere, the resulting surface species were identified, and these species were systematically removed one by one by

way of careful thermal annealing. The annealed materials were then electrochemically characterized and benchmarked with unexposed NCA to identify each species' role in the electrochemical degradation of NCA. By exploring how the impurity species develop on positive electrode materials and by correlating individual species to changes in the electrochemical performance, this work attempts to clarify decades of ambiguity over the growth mechanisms and impact of different surface impurity species. The results presented here outline the optimal atmospheric conditions to store and process layered positive electrode materials for lithium-ion batteries.

4.3 Experimental

4.3.1 Materials Preparation

Samples were fabricated by exposing $\text{LiNi}_{0.8}\text{Co}_{0.15}\text{Al}_{0.05}\text{O}_2$ (NAT1050, TODA America) for two weeks in either an Ar-filled glovebox, a dryroom (dew point of -35 to -40°C), a sealed bag of dry CO_2 (<10 ppm H_2O , Airgas), or by exposing to ambient air in a hood with constant air flow. All anneals were performed using a box furnace (48000 Furnace, Barnstead Thermolyne) in the dryroom. Electrode tapes were made using the Bellcore method and were cast in the dryroom to minimize exposure to moisture.¹⁹⁴ Casting slurries were a mixture of poly(vinylidene fluoride-co-hexafluoropropylene) (PVDF-HFP, Kynar 2801, Elf Atochem), carbon black (Super P (SP), MMM), propylene carbonate (Aldrich), and acetone (Aldrich). Homogenous slurries were cast, allowed to air dry, and then the propylene carbonate plasticizer was extracted by soaking the electrode in 99.8% anhydrous diethyl ether (Aldrich). All electrodes had a composition of 79.87 wt% active material, 7.03 wt% SP, and 13.10 wt% PVDF-HFP. Free standing electrodes were subsequently dried at 120°C under vacuum for a minimum of 10 hours, and stored in an Ar atmosphere glovebox to avoid atmospheric exposure.

4.3.2 Electrochemical Characterization

Coin cells (2032, Hohsen) were assembled in an Ar-filled glovebox using Whatman GF/D glass fiber separators saturated with a 1M LiPF₆ ethylene carbonate: dimethyl carbonate (EC:DMC) (1:1 volume ratio) electrolyte (BASF) (<20 ppm of H₂O), and a Li metal (FMC) negative electrode. Potentiostatic and galvanostatic electrochemical testing was controlled by a VMP3 (Biologic) or Maccor battery cycling system at 24°C. Cells were galvanostatically charged at 20 mA/g (per g of active material) to V_{\max} (4.2 or 4.5 V), held under potentiostatic conditions until the current dropped below 10 mA/g, and then discharged at 15 mA/g to 2.75 V. Starting on the 6th cycle, and every 19 cycles afterwards, the cells were discharged at 150 mA/g to 2.75 V.

4.3.3 Physical Characterization

Thermogravimetric analysis (TGA) experiments were performed in a TA instruments TGA 2050, with Pt pans and a flowing dry air atmosphere. Tests consisted of constant heating rate and isothermal segments. All heating was at 5°C/min and isothermal segments were at 150°C, 350°C, 500°C, and 750°C. The first three isotherms each had durations of two hours and the 750°C isothermal segment was held for four hours. The samples presented in Figure 4-5 were also cooled at 5°C/min to 30°C. As described in the text, experiments shown in Figure 4-12 use slightly adjusted profiles, and a dry air with <0.1 ppm of CO₂. KF titration (831 Coulometer and 860 Thermoprep, Metrohm) was used to measure the moisture content in all samples and in relevant standard materials. Samples were sealed in KF coulometry vials while inside the Ar-filled glovebox to eliminate any exposure to the ambient or dryroom atmospheres. KF tests were run at 250°C with flowing N₂ gas to ensure that all moisture was desorbed. Successive KF experiments were performed on each sample until the measured moisture content was below 10 ppm.

Attenuated Total Reflectance (ATR) Fourier Transform InfraRed (FTIR) experiments were run in the MidIR range using a Smart Orbit accessory with a TypeIIa diamond crystal

(Nicolet 6700 FTIR Spectrometer, Thermo). All experiments used a background scan performed the same day as the sample test. Tests consisted of 250 scans with a resolution of 4 cm^{-1} , unless otherwise noted. Exposed materials were mixed with $26 \pm 1\text{ wt\%}$ polyethylene (PE) powder (Sigma) and ground using a mortar and pestle. The mixtures were then sealed on the ATR stage with an adhesive backed lead tape while inside the Ar-filled glovebox. However, the sampling area was free of lead tape adhesive in order to prevent any contamination. To support surface impurity identification, Li_2CO_3 (Johnson Matthey), LiOH (Sigma), $\text{LiOH}\cdot\text{H}_2\text{O}$ (Sigma) and Li_2O (Alfa Aesar) standards were also examined. After TGA analysis, exposed materials were held in a closed chamber with flowing dry air to prevent the adsorption of moisture. Samples were then quickly transferred to the ATR stage and sealed with lead tape. Ambient exposure was less than 30 seconds during transfer.

A Bruker D8 Advance diffractometer ($\text{Cu K}\alpha$, $\lambda=1.5406\text{ \AA}$) was used for all X-ray diffraction (XRD) characterization. XRD samples of exposed materials were assembled in an Ar-filled glovebox, by sealing the powder onto a glass slide with Kapton film and grease to prevent ambient exposure during testing. XRD scans were conducted over a two-theta range of $15\text{-}70^\circ$ at a scan rate of $0.6^\circ/\text{min}$. TOPAS software (version 5, Bruker AXS) was used for all Rietveld refinement. XPS measurements were performed using a Phi VersaProbe 5000 system at the Analytical and Diagnostics Laboratory (ADL), Binghamton University on powders mixed with carbon black. A flood gun was used to charge compensate insulating samples, and the carbon black C 1s peak was aligned to 284.5 eV to account for possible charging effects. Exposed materials were deposited on conductive tape and transferred into the XPS chamber in under 30 seconds. Similar surface species were observed when select samples were transferred using vacuum a suitcase set-up between the glovebox and vacuum chamber.

4.4 Results

4.4.1 Effect of Atmosphere Exposure

NCA powder was exposed to four different atmospheric environments; an Ar-filled glovebox (Pristine), ambient air (Ambient), a dryroom (Dryroom), and dry CO₂ gas (CO₂). Each sample was exposed continuously for two weeks, and intermittent recordings of the temperature and humidity are presented in Figure 4-1 (a) and (b), respectively. While all of the environments were at room temperature, the relatively humidity (RH) varied substantially. The Pristine and CO₂ environments should only have trace amounts of moisture since they were in sealed enclosures filled with very dry gasses. Although the dryroom was measured to have a dew point of -35 to -40°C, the moisture content is slightly higher than the Pristine (dew point of glovebox is < -80°C) or CO₂ environments. In contrast, the average dew point of the ambient laboratory was +8.0°C (45.8% RH).

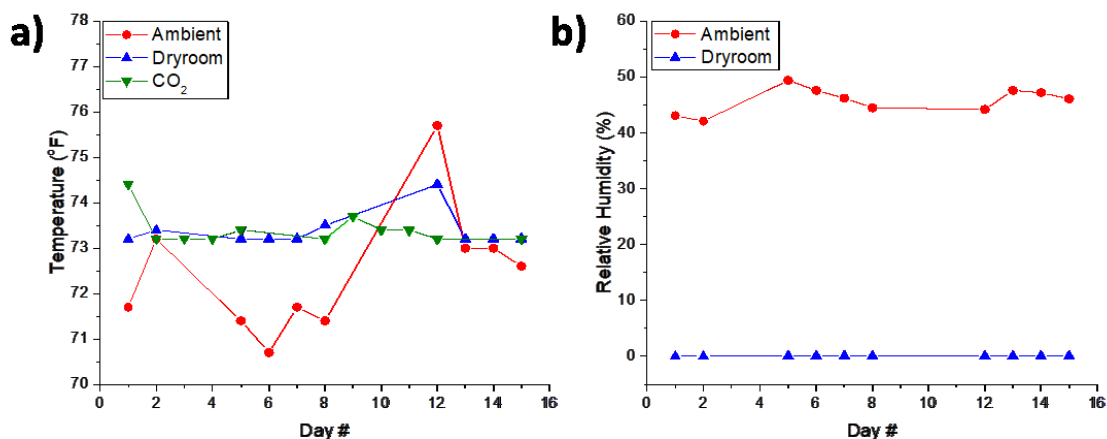


Figure 4-1: Intermittent (a) temperature and (b) relative humidity measurements collected during baseline NCA exposure to various atmospheres. Pristine NCA was stored in an Ar-filled glovebox in our laboratory, as such, the temperature history should be similar to that of Ambient NCA. Additionally, since Pristine and CO₂ NCA were stored in exceedingly dry gases the relative humidity for both materials is assumed to be negligible.

XRD scans of the four baseline samples and of the initial commercial NCA material are shown in Figure 4-2 (a-e). There was no evidence for the development of impurity phases or of structural degradation to the initial material within the detection limitations for powder XRD. Rietveld refinement of the diffraction profiles (Table 4-I) revealed little evidence of significant bulk lattice parameter or transition metal occupancy changes as a function of exposure.

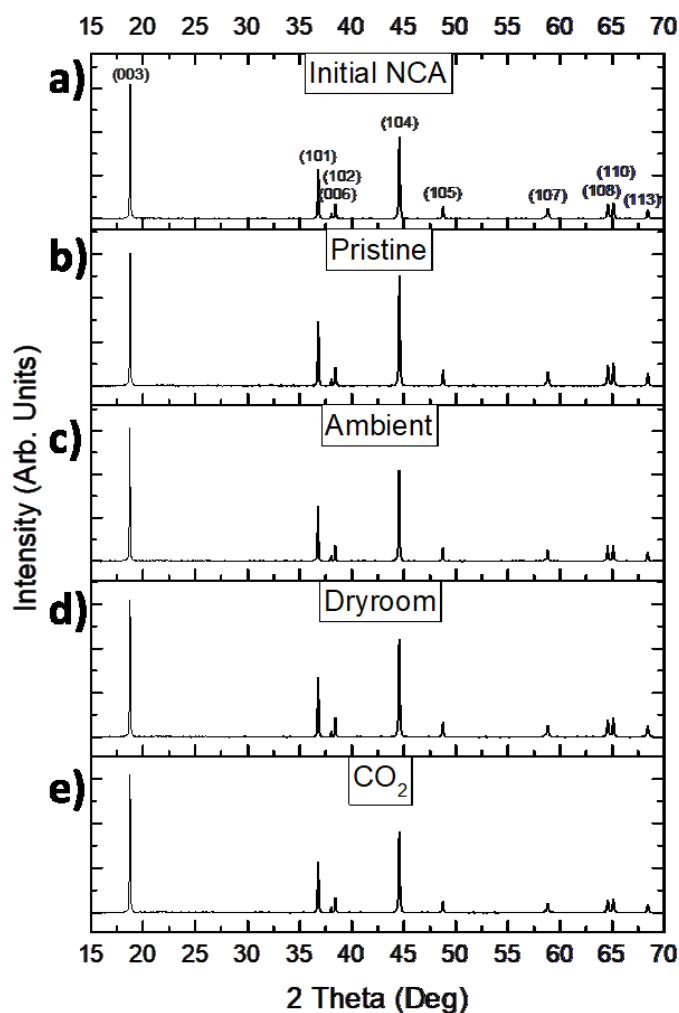


Figure 4-2: XRD scans of (a) the initial NCA material, as well as (b) Pristine, (c) Ambient, (d) Dryroom, and (e) CO₂ NCA. Each scan was performed on a powder sample that was sealed in an Ar-filled glovebox to prevent subsequent atmospheric exposure. The $R\bar{3}m$ layered oxide peaks are indexed for the initial NCA material.

Table 4-I: Provides the results for the working profile (R_{wp}), goodness of fit (GOF), calculated lattice parameters, and transition metal occupancies from Rietveld simulations on XRD scans of the initial NCA material as well as all baseline and annealed samples. The refined occupancy of Ni atoms in the Li layer is listed as “Ni (3a),” while those in the transition metal layer are denoted as “Ni (3b).”

Sample	R_{wp}	GOF	a (Å)	c (Å)	Cell Volume (Å ³)	Occupancies			
						Ni (3a)	Ni (3b)	Co (3b)	Al (3b)
Initial NCA	2.42	1.27	2.863	14.179	100.630	0.019	0.800	0.150	0.048
Pristine NCA	1.65	1.50	2.863	14.175	100.608	0.015	0.803	0.153	0.053
150C - Pristine	1.64	1.49	2.863	14.176	100.618	0.015	0.801	0.151	0.050
350C - Pristine	1.85	1.61	2.863	14.179	100.630	0.020	0.804	0.154	0.043
500C - Pristine	1.77	1.53	2.863	14.181	100.660	0.019	0.802	0.153	0.051
750C - Pristine	1.74	1.53	2.864	14.183	100.741	0.027	0.802	0.152	0.043
Ambient NCA	1.84	1.65	2.862	14.178	100.600	0.016	0.800	0.150	0.038
150C - Ambient	1.83	1.61	2.863	14.182	100.643	0.017	0.801	0.151	0.051
350C - Ambient	1.76	1.60	2.863	14.181	100.654	0.022	0.804	0.153	0.046
500C - Ambient	1.68	1.49	2.863	14.181	100.692	0.022	0.802	0.152	0.049
750C - Ambient	1.72	1.52	2.864	14.184	100.742	0.026	0.801	0.151	0.043
Dryroom NCA	1.83	1.67	2.863	14.177	100.599	0.019	0.802	0.152	0.051
150C - Dryroom	2.01	1.82	2.862	14.177	100.595	0.016	0.800	0.150	0.047
350C - Dryroom	1.67	1.52	2.863	14.180	100.639	0.017	0.803	0.154	0.052
500C - Dryroom	1.63	1.48	2.863	14.181	100.654	0.020	0.801	0.151	0.049
750C - Dryroom	2.03	1.65	2.864	14.183	100.717	0.029	0.812	0.162	0.046
CO₂ NCA	2.01	1.69	2.862	14.178	100.587	0.016	0.798	0.148	0.038
150C - CO ₂	1.83	1.58	2.863	14.179	100.619	0.021	0.811	0.163	0.044
350C - CO ₂	1.76	1.68	2.863	14.180	100.618	0.018	0.799	0.149	0.037
500C - CO ₂	1.72	1.60	2.862	14.178	100.598	0.015	0.800	0.150	0.049
750C - CO ₂	1.68	1.49	2.864	14.183	100.760	0.025	0.803	0.153	0.464

FTIR spectra on the baseline materials in Figure 4-3 (a-d) revealed the presence of $\text{LiOH} \cdot x\text{H}_2\text{O}$ (x denotes an unknown constant), H_2O and Li_2CO_3 . Ambient, Dryroom, and CO_2 NCA samples showed broad peaks centered at $\sim 3700\text{--}3745\text{ cm}^{-1}$ which are from the hydroxyl stretching mode of a $\text{LiOH} \cdot x\text{H}_2\text{O}$ -type material.^{226–229} The CO_3 group bending, asymmetric and symmetric C-O stretching modes associated with Li_2CO_3 were clearly present at 870 cm^{-1} , 1419 cm^{-1} , and 1471 cm^{-1} , respectively.^{94,216,230} Ambient and CO_2 NCA also showed a broad peak between 1576 cm^{-1} and 1714 cm^{-1} , which coincides with the expected location for the H_2O bending mode.^{226–228} Figure 4-3 (g-h) shows a decline in the magnitude of the $1576\text{--}1714\text{ cm}^{-1}$ peak after annealing at 150°C supporting that the peak is from water. The surfaces of the baseline materials may have also contained LiHCO_3 , but because of the similarities to the Li_2CO_3 spectra, the presence of LiHCO_3 could not be conclusively determined.

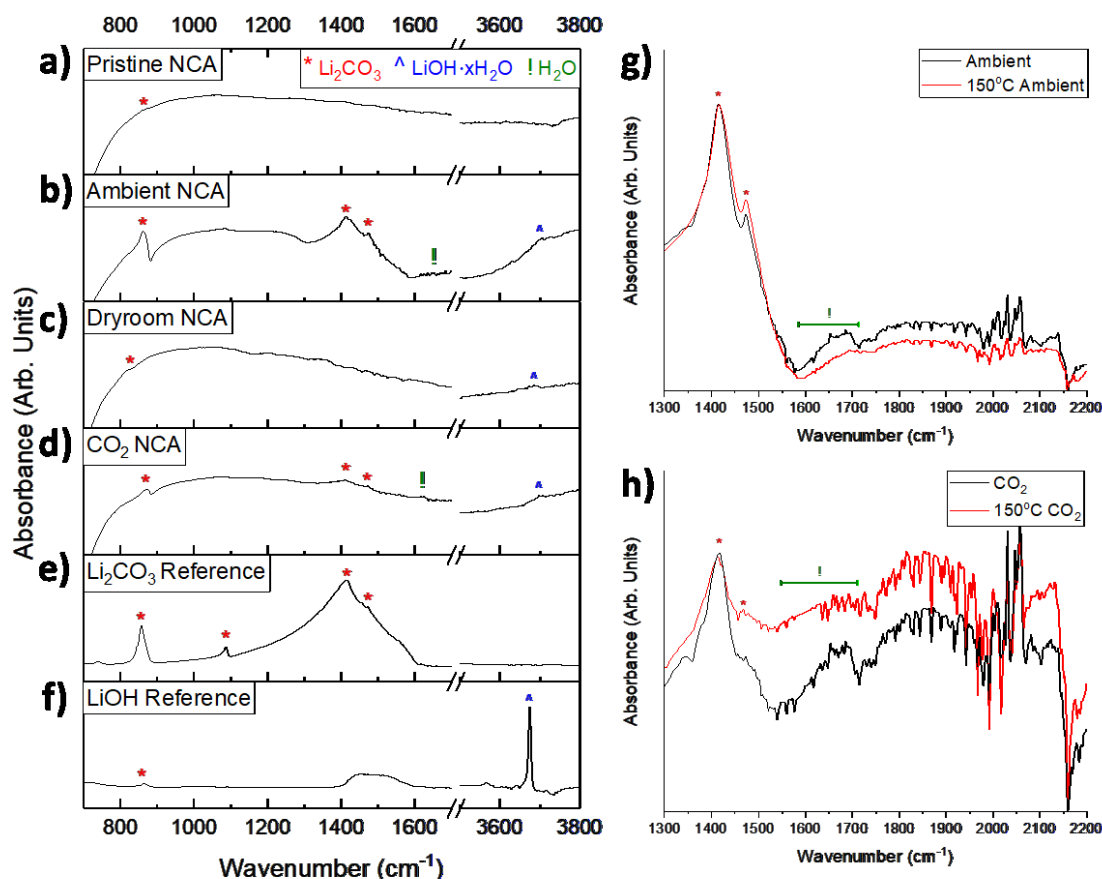


Figure 4-3: FTIR spectra of the (a) Pristine, (b) Ambient, (c) dryroom, and (d) CO₂ baseline materials as well as (e) Li₂CO₃ and (f) LiOH reference materials. A break in the x-axis was included to emphasize the regions with relevant peaks. In contrast to the samples presented in Figure 4-4, none of these materials were mixed with PE. Additional spectra, taken with 1,000 scans instead of 250, show the effect of annealing at 150°C on (g) Ambient and (h) CO₂ NCA. In all spectra the Li₂CO₃, LiOH·xH₂O and H₂O peaks are denoted by red stars, blue carets, and green exclamation points, respectively. The exact composition of LiOH·xH₂O cannot be determined because the visible peak is very broad and has low intensity.

In an Ar-filled glovebox, each of the four baseline materials were mixed with approximately 26 wt% PE and ground together by a mortar and pestle. Extra precautions were taken to ensure that no additional moisture was added to the sample during creation of the PE mixtures. PE was used as an internal standard to normalize the peak heights between samples and enable relative quantitative comparisons between materials. The FTIR spectra of these mixtures are shown in Figure 4-4 (a-d). Peaks corresponding to PE, Li₂CO₃, and LiOH·xH₂O are denoted

with black, red, and blue symbols, respectively. To enable direct visual comparison, the y-axes of Figure 4-4 (a-d) are normalized to the area of each scan's 2912 cm^{-1} PE peak (not shown). The bending mode $\text{LiHCO}_3/\text{Li}_2\text{CO}_3$ (870 cm^{-1}) peak was used for quantitative analysis because it is clearly distinct from any PE peaks. It is evident from Figure 4-4 (a-d) that little $\text{LiHCO}_3/\text{Li}_2\text{CO}_3$ is present on either the Pristine or Dryroom samples, only slightly more on CO_2 NCA, but that the Ambient material has an appreciable amount. Relative to Pristine NCA, the carbonate peak areas were around 23% and 617% larger for CO_2 and Ambient materials, respectively. While LiOH and H_2O peaks were observed by FTIR in the baseline materials, they were obscured by the PE and too small for a conclusive quantitative analysis.

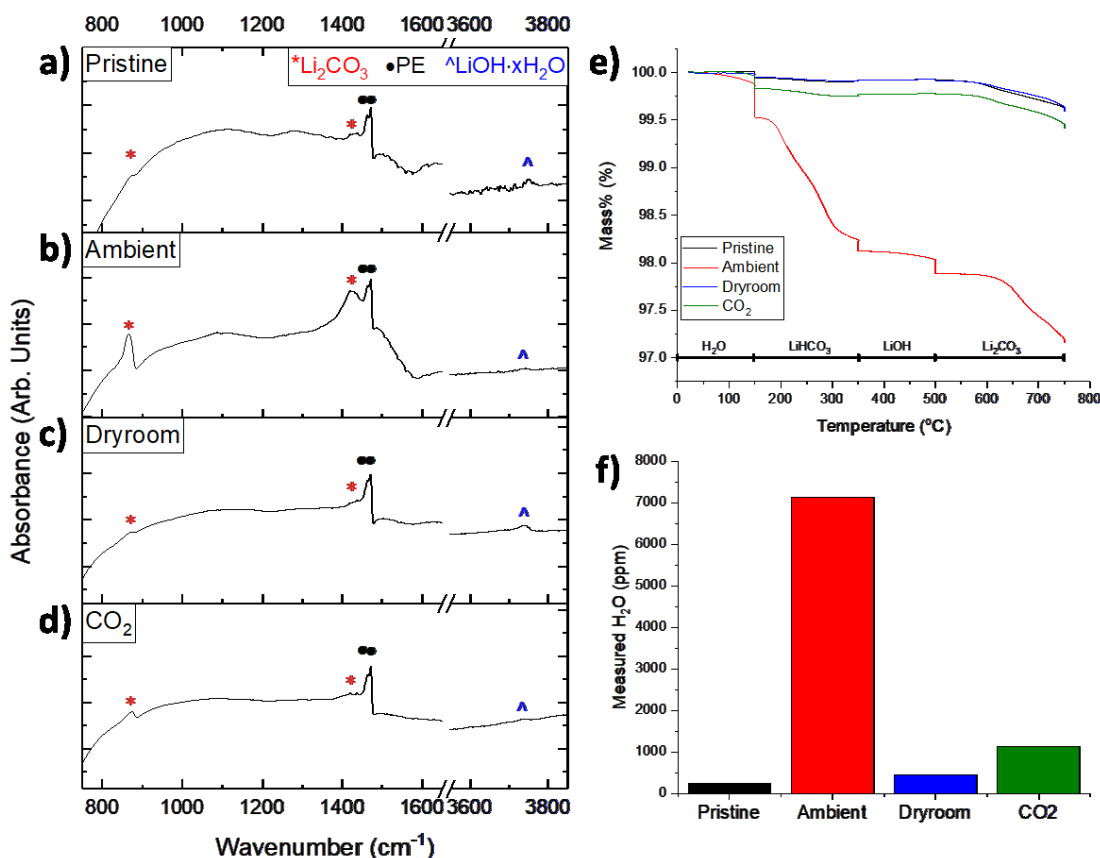
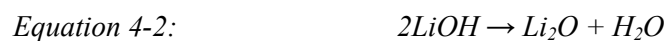
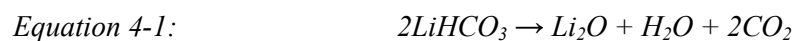


Figure 4-4: FTIR measurements of the (a) Pristine, (b) Ambient, (c) Dryroom and (d) CO₂ baseline materials mixed with 26 wt% PE. The spectra focus on the Li_2CO_3 (red star), PE (black dot), and hydroxyl (blue caret) peaks in the ranges of 750 to 1650 cm^{-1} , and 3550-3850 cm^{-1} . Both absorbance ranges for the FTIR spectra are normalized to the size of each spectrum's 2912 cm^{-1} PE peak. Mass loss curves from (e) TGA and the moisture content from cumulative (f) KF experiments on Pristine (black), Ambient (red), Dryroom (blue) and CO₂ (green) NCA baseline materials are also presented. TGA experiments had 2 h isothermal holds at 150 $^{\circ}\text{C}$, 350 $^{\circ}\text{C}$, and 500 $^{\circ}\text{C}$ to systematically remove H_2O , LiHCO_3 , and LiOH , respectively. The fourth and final isotherm, at 750 $^{\circ}\text{C}$, lasted 4 h and measured the mass loss from Li_2CO_3 decomposition.

Figure 4-4 (e) presents the results of TGA experiments for each baseline material. During these experiments, samples were heated at 5 $^{\circ}\text{C}/\text{min}$ to 750 $^{\circ}\text{C}$ with 2 h isothermal segments at 150 $^{\circ}\text{C}$, 350 $^{\circ}\text{C}$ and 500 $^{\circ}\text{C}$, and a 4 h isothermal hold at 750 $^{\circ}\text{C}$. Throughout the tests, dry air was flowed through the sample chamber to carry away any evolved gases. Dry air was utilized not only because the lack of moisture prevents the adsorption of additional H_2O or the formation of LiHCO_3 or LiOH impurities, but also because the atmosphere doesn't induce

transition metal reduction and oxygen gas evolution at higher temperatures. The temperatures of the isothermal segments were selected to isolate the mass loss from each impurity specie and the duration of the isothermal holds provided significant time to remove the majority of the particular specie. The 150°C, 350°C, 500°C, and 750°C isothermal segments were designed to remove the adsorbed and absorbed H₂O, LiHCO₃, LiOH, and Li₂CO₃ species, respectively.

Adsorbed water should be highly unstable at 150°C and is expected to evaporate from the sample relatively quickly. Using temperature programmed desorption-mass spectroscopy to measure the evolved H₂O, O₂ and CO₂ while heating LiNi_{0.8}Co_{0.2}O₂, *Liu et al.* showed that lithium bicarbonate and adsorbed carbonate species on positive electrode materials will decompose at 270°C and 350°C.¹²² Other studies have demonstrated that LiOH is thermally degraded at 410°C, and Li₂CO₃ is evolved at 710°C.^{37,38} The thermal decompositions of LiHCO₃, LiOH and Li₂CO₃ are expected to follow equations Equation 4-1, Equation 4-2, and Equation 4-3, respectively.



To maximize the mass loss while still isolating a particular impurity specie, the isothermal temperatures were chosen to be slightly higher than the previously measured degradation temperatures. The duration of each isotherm was determined by multiple tests and represents the amount of time necessary for the mass loss to plateau at the isotherm temperature. To ensure that the mass loss at high temperatures is due to the loss of Li₂CO₃ and not from oxygen loss associated with Ni reduction, additional TGA tests with a cooling segment were performed on Pristine and Ambient NCA, and are presented in Figure 4-5. During cooling there is negligible mass gain indicating that the high temperature mass loss is not from a reversible Ni redox transition.

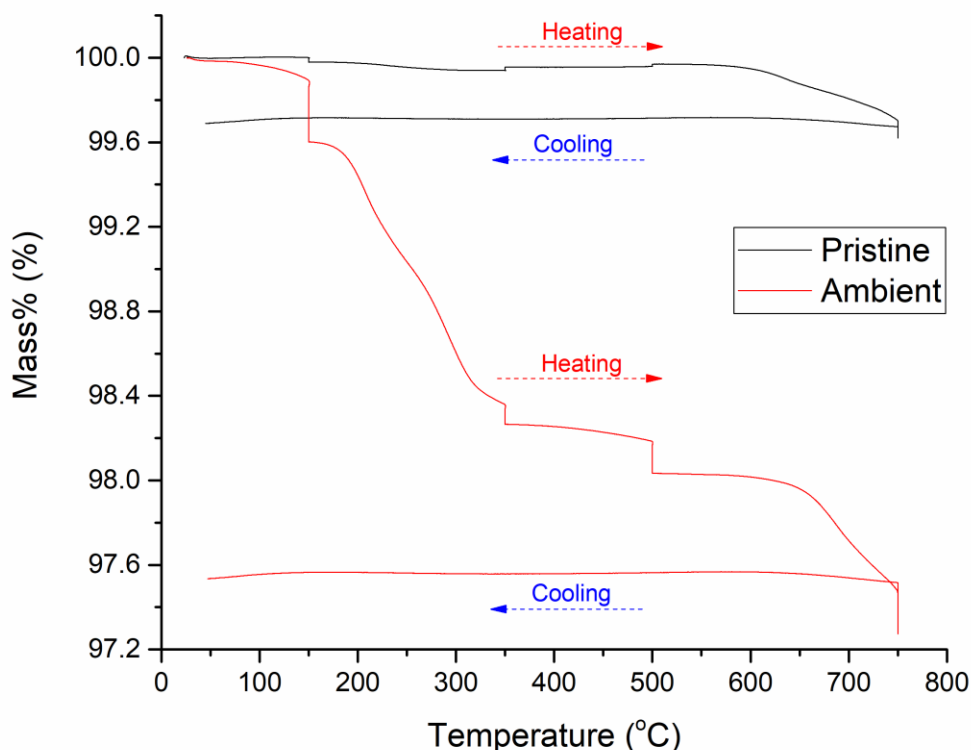


Figure 4-5: TGA mass loss curves during heating, isothermal, and cooling segments in dry air for Pristine (black) and Ambient (red) NCA. Samples were tested identically to previously described TGA experiments, except that they were also cooled to 30°C at 5°C/min after completing the heating and isothermal segments. The part of each mass loss curve that correlates to heating or cooling is labeled for clarity.

The loss curves in Figure 4-4 (e) show that Pristine and Dryroom NCA are virtually indistinguishable by TGA. This indicates that the two materials have similar amounts of each impurity, and that exposure to the dryroom atmosphere did not result in significant formation of surface species. On the contrary, Ambient NCA lost over 7 times as much mass as the Pristine sample. While the Ambient material lost more mass than Pristine at every isotherm, the largest differences in mass loss corresponded to H₂O, LiHCO₃ and Li₂CO₃. CO₂ NCA also lost more mass than the Pristine or Dryroom samples, but the majority of the additional mass lost was evolved during the 150°C isotherm, indicating that it was H₂O.

KF coulometry results presented in Figure 4-4 (f) perfectly supports the water desorption measurements from TGA. Pristine (253.3 ppm) and Dryroom (461.3 ppm) samples have small moisture contents, while CO₂ NCA (1125.7 ppm) has marginally more, and the Ambient material (7125.4 ppm) has over 28 times as much moisture as Pristine. The incrementally higher moisture content on CO₂ NCA relative to the Pristine material is believed to be from contamination by the plastic container and/or the interior surface of the bag used to enclose the material during storage. Quantitative results from FTIR, TGA, KF and electrochemistry experiments on all baseline and annealed materials are presented in Table 4-II.

Table 4-II: Quantitative results from KF, TGA, FTIR and electrochemistry experiments on all baseline and annealed materials. KF results are the cumulative ppm of H₂O, while the FTIR results are listed as an approximation of the peak area relative to the area of that scan's main PE peak. Some materials had insufficiently sized LiOH·xH₂O peaks to determine the relative peak area, and are labeled as "N/A." The % capacity loss results were calculated by using the maximum discharge capacity and the discharge capacity of the 50th cycle. The % capacity loss for Ambient NCA was "N/A" when cycled to 4.2 V because the discharge capacity was negligible for all cycles, and the % capacity loss was 0.00 when charged to 4.5 V since the 50th cycle also had the largest discharge capacity of the first 50 cycles. The discharge rate capacity retention data was obtained by dividing the discharge capacity of the 25th cycle (150 mA/g) by the discharge capacity of the 24th cycle (15 mA/g). Since Ambient NCA had no discharge capacity when cycled to 4.2 V, the capacity retention is listed as "N/A." The average OCV values for all electrodes are listed in the rightmost column.

Technique:	KF	TGA	TGA	TGA	FTIR	TGA	FTIR	Electrochemistry				
Material	H ₂ O [ppm]	H ₂ O loss [wt%]	LiHCO ₃ loss [wt%]	LiOH loss [wt%]	LiOH·xH ₂ O [Relative to PE]	Li ₂ CO ₃ loss [wt%]	LiHCO ₃ /Li ₂ CO ₃ [Relative to PE]	% Capacity loss after 50 cycles to 4.2V [%]	% Capacity loss after 50 cycles to 4.5V [%]	4.2V Cells, Discharge Rate Capacity Retention [%]	4.5V Cells, Discharge Rate Capacity Retention [%]	Average OCV vs Li/Li ⁺ [V]
Pristine NCA	253.3	0.06	0.02	0.00	0.098	0.32	0.044	3.26	8.31	89.42	89.98	3.391
150C - Pristine	131.2	0.01	0.00	0.00	0.181	0.30	0.200	4.12	8.37	89.15	89.43	3.407
350C - Pristine	97.4	0.02	0.05	-0.01	0.221	0.58	0.209	5.61	9.75	87.81	88.17	3.410
500C - Pristine	86.4	-0.01	0.04	0.07	N/A	0.79	0.154	3.87	9.50	86.91	88.40	3.368
750C - Pristine	178.4	0.02	0.04	-0.01	N/A	0.77	0.066	2.56	10.91	87.90	88.83	3.380
Ambient NCA	7125.4	0.47	1.41	0.24	0.032	0.72	0.271	N/A	0.00	N/A	N/A	3.441
150C - Ambient	407.3	0.16	0.78	0.22	0.088	0.89	0.272	25.69	28.29	79.73	77.76	3.489
350C - Ambient	103.6	0.03	0.07	0.13	0.044	0.98	0.192	9.26	15.46	87.47	87.17	3.395
500C - Ambient	88.7	0.00	0.05	0.07	N/A	0.99	0.252	3.38	9.61	86.87	87.91	3.368
750C - Ambient	175.4	0.01	0.05	0.06	N/A	0.44	0.095	10.13	10.16	89.06	89.06	3.393
Dryroom NCA	461.3	0.05	0.02	0.01	0.089	0.32	0.039	2.91	8.25	89.42	89.73	3.405
150C - Dryroom	96.4	0.02	0.00	-0.01	0.044	0.31	0.068					
350C - Dryroom	66.2	0.01	0.04	0.04	N/A	0.72	0.140					
500C - Dryroom	107.7	0.03	0.05	0.06	N/A	0.86	0.135					
750C - Dryroom	117.5	0.00	0.04	-0.01	N/A	0.69	0.079					
CO ₂ NCA	1125.7	0.17	0.06	0.00	N/A	0.37	0.054	0.39	3.42	88.21	89.96	3.434
150C - CO ₂	509.9	0.09	0.07	0.00	N/A	0.44	0.114					
350C - CO ₂	45.0	-0.01	0.04	0.00	N/A	0.51	0.089					
500C - CO ₂	103.4	0.01	0.05	0.04	N/A	0.76	0.109					
750C - CO ₂	112.9	0.01	0.03	-0.01	N/A	0.62	0.092					

Electrodes fabricated from each of the baseline positive electrode materials were dried overnight at 120°C under vacuum prior to storage in an Ar-filled glovebox. Coin cells containing these positive electrodes were charged at 20 mA/g to V_{max} (4.2 V or 4.5 V), held under

potentiostatic conditions until the current dropped below 10 mA/g and then discharged to 2.75 V at -15 mA/g, all at 24°C. To investigate the capacity retention as a function of rate for each material, cells were discharged at -150 mA/g starting on the 6th cycle, and every 19 cycles afterwards. The discharge capacity results for each material are presented in Figure 4-6. Duplicate cells were made to ensure reproducibility.

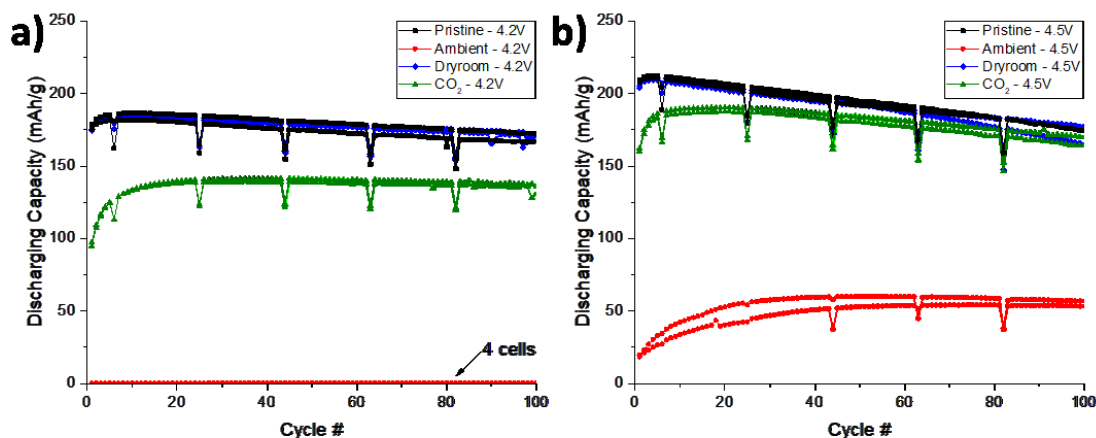


Figure 4-6: Comparison of the discharge capacities as a function of cycle number for all four baseline materials. Electrodes were charged to an upper cutoff potential of either (a) 4.2 V or (b) 4.5 V. Cells were charged at 20 mA/g to V_{max} (4.2 V or 4.5 V), held under potentiostatic conditions until the current dropped below 10 mA/g and then discharged to 2.75 V at -15 mA/g. Starting on the 6th cycle, and every 19 cycles afterwards, the cells were discharged at -150 mA/g instead of -15 mA/g. All of the cycling was done in a temperature controlled chamber set at 24°C.

Pristine NCA demonstrated good initial specific capacities to both 4.2 (Figure 4-6 (a)) and 4.5 V (Figure 4-6 (b)), and maintained robust capacity retention over many cycles. As expected, there is small capacity fade when charging to 4.2 V, and a slightly faster degradation rate when charging to 4.5 V. The cycling stability of Dryroom NCA was nearly identical to that of the Pristine material, which is expected because there was negligible differences in the surface impurity species between the samples. When charged with a cutoff potential of 4.2 V, Ambient NCA had negligible discharge capacity and was functionally useless. When the upper potential was increased to 4.5 V, the positive electrode became capable of reproducibly delivering some capacity, but the discharge capacity was still only about a fourth of the Pristine material. The

initial discharge capacities of the CO₂ NCA cells were significantly lower than the Pristine samples, and even though the capacity of the 4.2 V cells rose steadily over the first 45 cycles, the material still well underperformed the Pristine NCA cells. The dependence of the discharge capacity on the upper cutoff potential was much larger for CO₂ NCA, than it was for Pristine or Dryroom NCA.

Figure 4-7 displays the first cycle voltage profile of a cell with a 4.5 V cutoff for each baseline material. The degree of polarization varies significantly between materials, with Ambient and CO₂ NCA electrodes showing substantial polarization when current is applied while Dryroom and Pristine NCA showed little to none. The initial polarization is only temporary for Dryroom NCA, which quickly regained a voltage profile similar to the Pristine material. However, the over-potentials for Ambient and CO₂ NCA only partially relaxed during charging, and both materials reach the cutoff potential well before being sufficiently delithiated. The discharge capacity retention of the 25th cycle (150 mA/g) vs. the 24th cycle (15 mA/g) was calculated for each material when electrodes were charged up to either 4.2 or 4.5 V. The resulting data is listed in Table 4-II. The rate dependent capacity retention for 4.2 V cells was best for Pristine and Dryroom NCA, only slightly diminished for CO₂ NCA, and immeasurable for Ambient NCA since there was no discharge capacity at either rate.

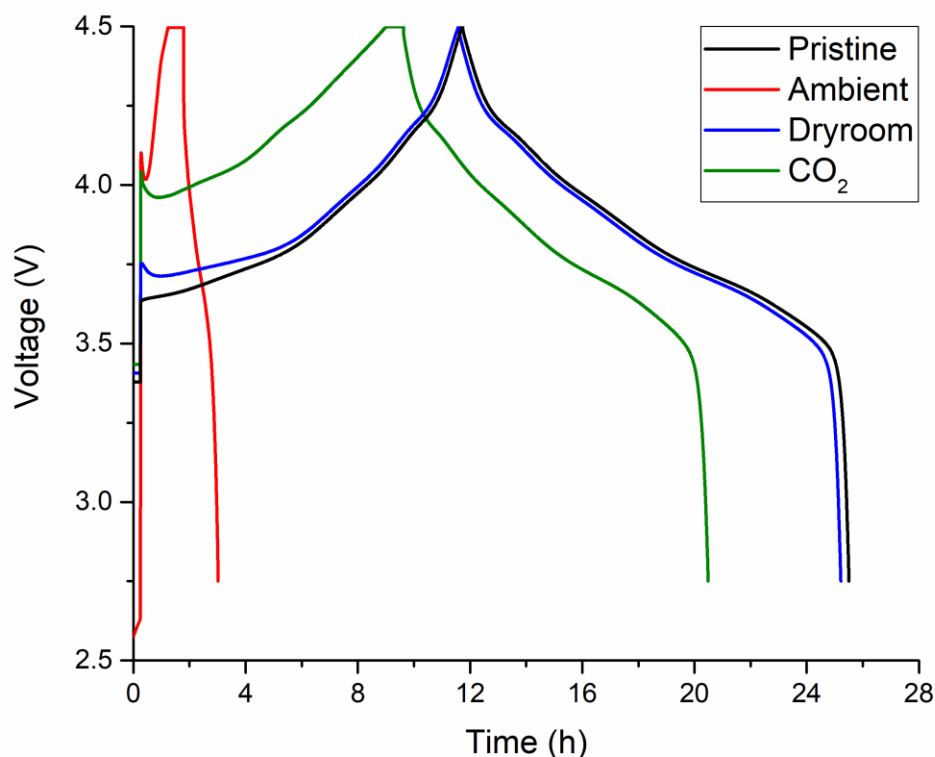


Figure 4-7: First cycle voltage profiles for Pristine (black), Ambient (red), Dryroom (blue), and CO₂ (green) NCA electrodes cycled with an upper cutoff potential of 4.5 V. Electrodes were charged at 20 mA/g to 4.5 V, and then held at 4.5 V until the current dropped below 10 mA/g before being discharged at 15 mA/g to 2.75 V.

4.4.2 Isolation and Analysis of Impurity Species

To further investigate the growth mechanisms for the surface impurity species and isolate the impact that each specie has on electrochemical performance, all materials were separately annealed in the dryroom at 150°C, 350°C, or 500°C for 2 h, or at 750°C for 4 h. Similar to the TGA experiments, the temperature and duration of the anneals were designed to remove species one at a time. Rietveld analysis was performed on the XRD scans of each annealed sample, and the *a* and *c* lattice parameters as well as the calculated cell volume are presented in Figure 4-8. The Rietveld calculated lattice parameters and transition metal occupancies are listed in Table 4-I. While none of the XRD scans showed any signs of impurity phases, the *a* (Figure 4-8 (a)) and *c*

(Figure 4-8 (b)) lattice parameters and the cell volume (Figure 4-8 (c)) increased steadily by annealing at higher temperatures for all samples. Starting with the baseline materials, which are represented as the samples annealed at 24°C, to the 750°C annealed samples the *a* and *c* lattice parameters each increased by ~0.05%, causing the cell volume to grow by ~0.15%. Even though the change in the lattice parameters is near the margin of error, the clear trends support the results' validity. Coincident with the development of the lattice parameters, Rietveld analysis calculated a rough trend of increasing amounts of Ni in the Li 3a site. This, along with the increased cell volume may be associated to the formation of divalent Ni or Co which subsequently migrated to the 3a layer.

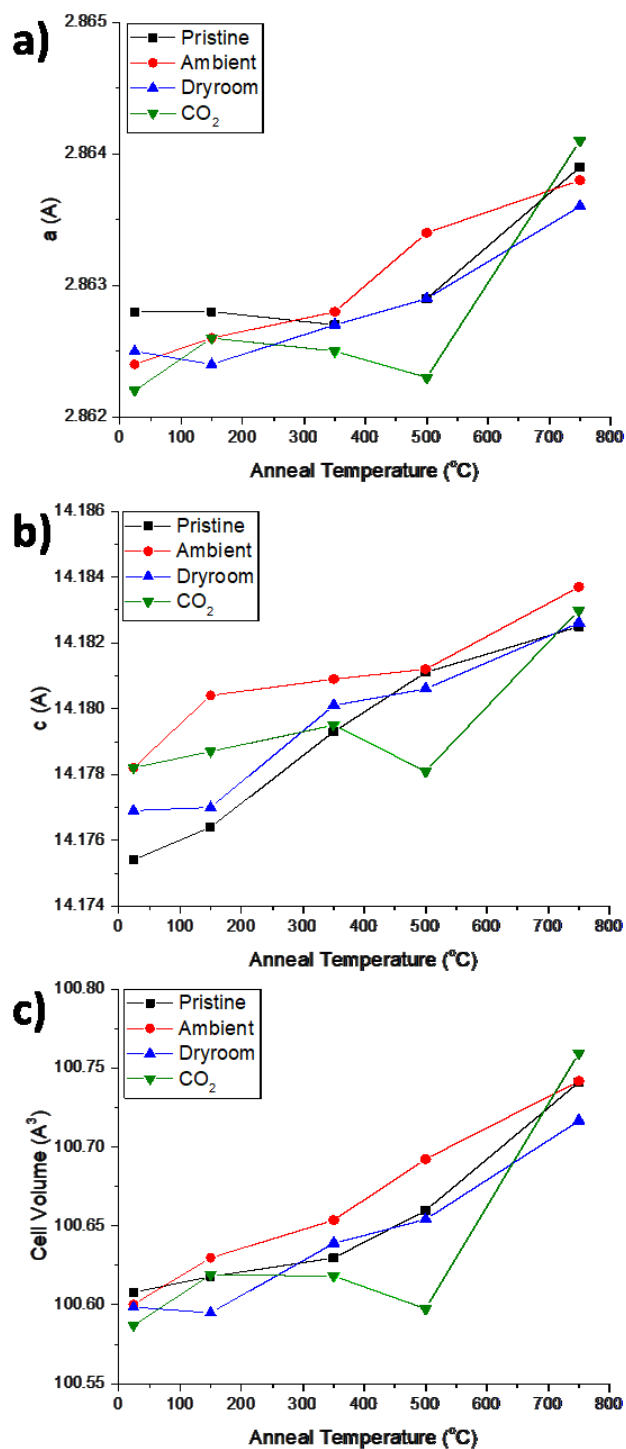


Figure 4-8: Plots of the (a) a and (b) c lattice parameters, and (c) cell volume as determined by Rietveld analysis of XRD scans of each annealed sample. The calculated parameters for the baseline materials are shown as having an anneal temperature of 24°C.

While Li_2CO_3 was imperceptible by XRD, FTIR easily detected Li_2CO_3 peaks on all of the annealed materials. Figure 4-9 compares the PE normalized magnitudes of the 870 cm^{-1} peak as a function of baseline material and annealing conditions. Since this peak corresponds to the CO_3 group bending mode and is relatively broad, it can arise from the presence of either LiHCO_3 or Li_2CO_3 . After being annealed at 150°C and 350°C , the carbonate content on Pristine and Dryroom NCA increased steadily, but slowly began to decline on the 500°C annealed materials, and rapidly decreased after being annealed at 750°C . The carbonate peak on Ambient NCA, which is initially very high, showed little change after annealing at 150°C , but otherwise steadily decreased with increasing annealing temperature. Similar to Pristine and Dryroom NCA, the CO_2 material had an increase in the size of the Li_2CO_3 peak after annealing at 150°C , but then the Li_2CO_3 content remained relatively consistent until it declined slightly after the 750°C anneal. For all materials, regardless of exposing atmosphere, annealing at 750°C caused a reduction of the Li_2CO_3 content relative to the 500°C annealed samples. While Ambient and CO_2 NCA do show incrementally more Li_2CO_3 after being annealed at 750°C than the 750°C Pristine or Dryroom samples, these materials started with higher amounts of Li_2CO_3 and this excess Li_2CO_3 could likely be fully removed with a longer anneal at 750°C .

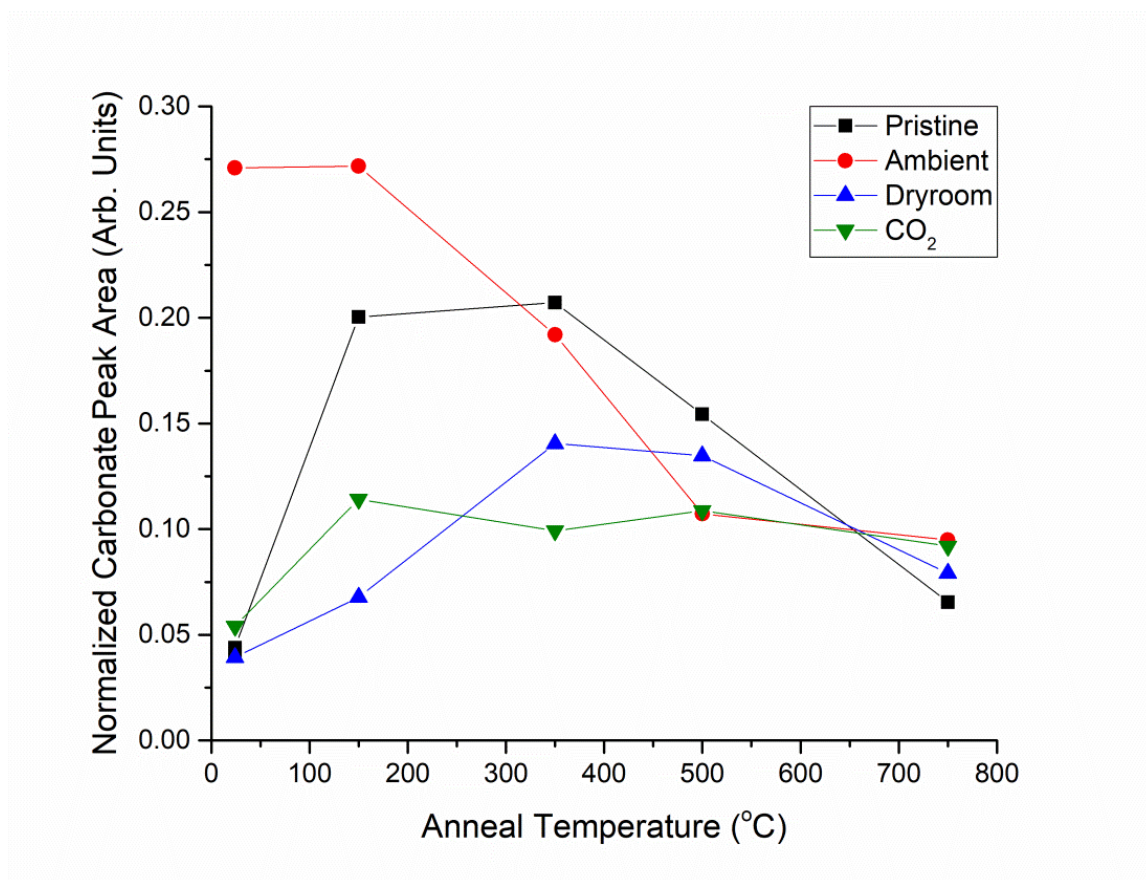


Figure 4-9: FTIR data showing the normalized 870 cm^{-1} carbonate peak area as a function of the baseline material and annealing conditions. Carbonate peak intensities are normalized to the area of the 2912 cm^{-1} PE peak in each scan, and show the changes in the $\text{LiHCO}_3/\text{Li}_2\text{CO}_3$ content as a result of annealing.

Table 4-II shows the average OCV (open circuit voltage) for electrodes comprised of each baseline material and every annealed sample of Pristine and Ambient NCA. Of the baseline materials, Pristine NCA had the lowest OCV (3.391 V), followed by Dryroom (3.405 V), CO_2 (3.434 V) and Ambient NCA (3.441 V). The OCV values are intimately related to the LiHCO_3 and Li_2CO_3 results listed in Table 4-II and shown in Figure 4-9. Careful analysis of the OCVs for annealed Pristine and Ambient electrodes shows the same trend as the normalized carbonate peak area results in Figure 4-9. Samples with higher (bi)carbonate contents have increased OCVs, which may be associated with the partial delithiation of the NCA. OCV results for the four baseline materials may help explain the discrepancies in the c lattice parameters determined by XRD, since materials with higher OCVs have less Li in the interlayer, which is known to cause

expansion of the c -axis for mostly lithiated layered oxides.¹⁷ There is a clear correlation between the OCV and c lattice parameter for each baseline material. Changes to the c lattice parameter as a function of annealing can be explained by a combination of changes in the OCV and increased degrees of transition metal mixing.

To provide a more rigorous quantitative analysis of the impurity species present, and to distinguish between the evolution of LiHCO_3 and Li_2CO_3 , TGA experiments identical to those previously described were run on all annealed samples. Mass loss results for each of the main impurity species is plotted as a function of annealing temperature for each baseline material in Figure 4-10 (a-d) and listed in Table 4-II. From Figure 4-10 (a), which shows the impurity mass loss for all variations of Pristine NCA, it is clear that there is very little moisture, LiHCO_3 , or LiOH on the baseline material, and that there are minimal changes in the quantity of these species for the annealed samples. 0.31 wt% of Li_2CO_3 was observed on Pristine NCA, and the quantity of Li_2CO_3 grew with higher temperature anneals until it reached a maximum of 0.79 wt% on the 500°C annealed material. The 750°C annealed sample had a slightly lower Li_2CO_3 content than the 500°C material, but had a smaller decline in the amount of Li_2CO_3 than was suggested by the FTIR results.

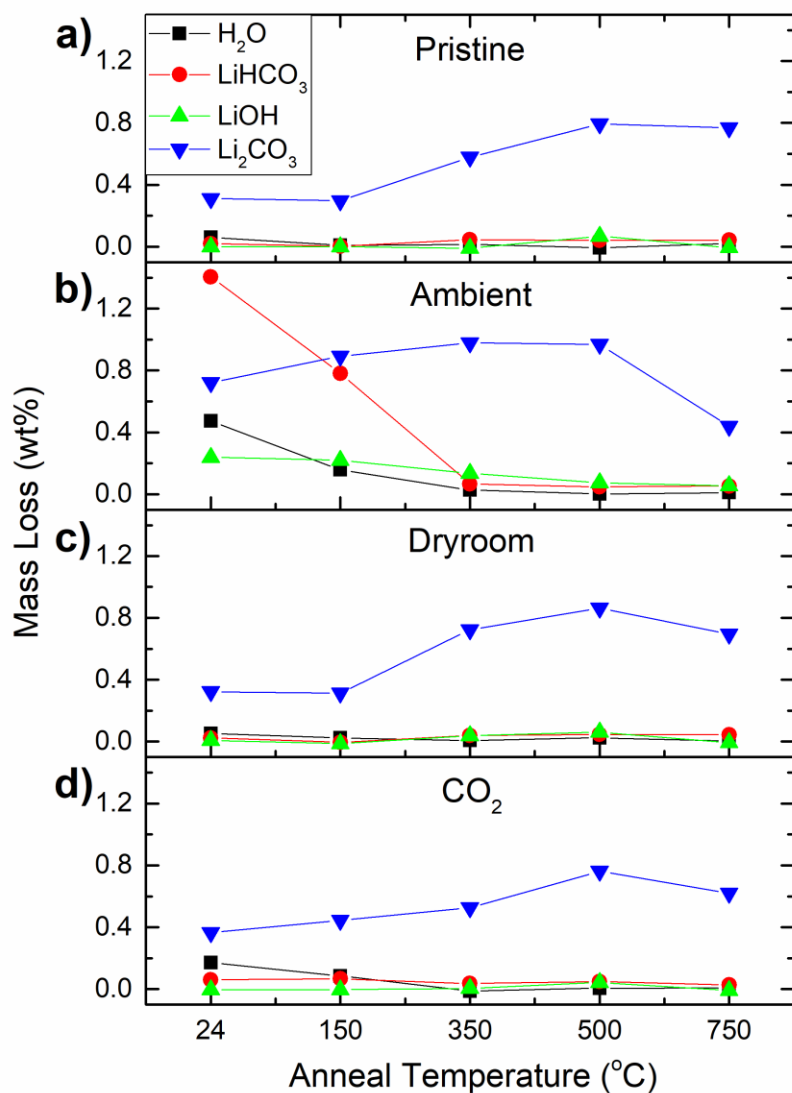


Figure 4-10: Quantification of H₂O, LiHCO₃, LiOH, and Li₂CO₃ contents as determined by TGA. The surface impurity mass loss results of the baseline and annealed samples for Pristine, Ambient, Dryroom, and CO₂ NCA materials are displayed in panels (a-d), respectively. The magnitude of the H₂O (black square), LiHCO₃ (red circle), LiOH (green upward triangle), and Li₂CO₃ (blue inverted triangle) contents were determined by the mass loss from the 20-150°C, 150-350°C, 350-500°C, and 500-750°C regions, respectively.

In contrast to the Pristine material, Ambient NCA (Figure 4-10 (b)) had large quantities of every impurity specie. 0.47 wt% H₂O was measured on the Ambient baseline sample, however after annealing at 150°C and 350°C the amount of water dropped to 0.16 and 0.03 wt%,

respectively. Similar trends were observed for the LiHCO_3 and LiOH contents on Ambient NCA, which initially had 1.41 and 0.24 wt% of LiHCO_3 and LiOH . The LiHCO_3 content was negligible after annealing Ambient NCA at 350°C and a 500°C anneal proved sufficient to eliminate the vast majority of the LiOH . Supporting the FTIR results, the amount of Li_2CO_3 on baseline Ambient NCA was 0.72 wt%, much higher than what was observed on Pristine NCA (0.31 wt%). The measured Li_2CO_3 content on Ambient materials increased with higher temperature annealing, reaching a maximum after the 500°C anneal, comparable to the development seen on the TGA experiments of Pristine NCA. After the 750°C anneal, much less Li_2CO_3 was observed on Ambient NCA (0.44 wt%) than what was on either the baseline Ambient (0.72 wt%) or 500°C Ambient (0.97 wt%) materials, confirming that annealing at such high temperatures causes a reduction in the Li_2CO_3 content. FTIR results from post-TGA Pristine and Ambient baseline materials are displayed in Figure 4-11. The absence of the 870 cm^{-1} peak and the peaks in the range of $1419\text{--}1480\text{ cm}^{-1}$ or $1576\text{--}1714\text{ cm}^{-1}$, signify the complete removal of the Li_2CO_3 , LiHCO_3 and H_2O species. Similar FTIR experiments were run on all post-TGA materials, none of which had signs of any remaining moisture, hydroxide or carbonate species.

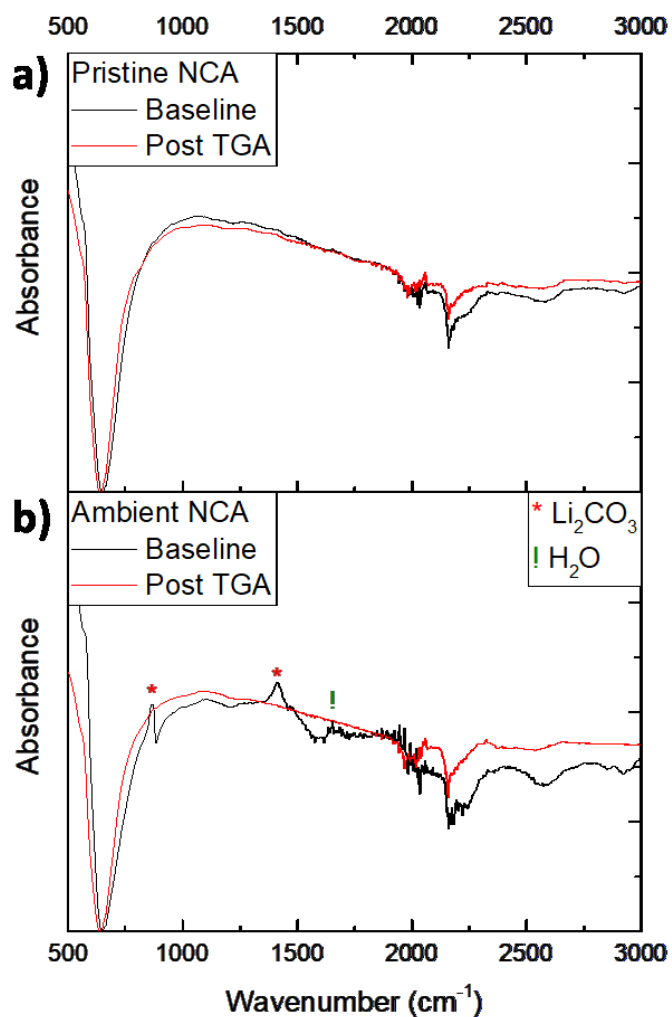


Figure 4-11: Comparison of the FTIR spectra from baseline and post-TGA versions of (a) Pristine and (b) Ambient NCA. The post-TGA scans show no carbonate (red star), hydroxide or moisture peaks (green exclamation point), indicating their complete removal during the TGA experiment. None of the samples were mixed with PE.

Dryroom NCA (Figure 4-10 (c)) was nearly identical to the Pristine material. Very little H_2O , LiHCO_3 or LiOH was observed and with a Li_2CO_3 content of 0.32 wt% Dryroom NCA had essentially the same amount of Li_2CO_3 as the Pristine baseline (0.31 wt%). Analogous to the annealed Pristine NCA samples, Li_2CO_3 continued to develop after the 150°C, 350°C, and 500°C anneals, but decreased after being annealed at 750°C. The quantity of the other impurity species was little changed as a result of annealing, similar to what was observed on the Pristine NCA

samples. While difficult to see, CO₂ NCA, shown in Figure 4-10 (d), had about 3 times as much moisture and lithium bicarbonate than either the Pristine or Dryroom baseline materials. Additionally, the Li₂CO₃ content of 0.37 wt% found on CO₂ NCA is slightly (19%) higher than the analogous Pristine sample, supporting the relative increase that was measured by FTIR. From the TGA results, CO₂ NCA had lower concentrations of Li₂CO₃ on the 500°C and 750°C samples than either of the corresponding Pristine or Dryroom NCA materials did.

The insight provided by TGA helps explain the FTIR results shown in Figure 4-9. Ambient NCA was the only material not to have a large increase in the carbonate peak after annealing, which is attributed to a saturation of LiHCO₃ and Li₂CO₃ by previous exposure. The reduction of the carbonate peak on the 350°C annealed Ambient material can be explained by the loss of LiHCO₃, which was more than enough to offset any increase in Li₂CO₃. However, annealing at 350°C caused an increase in the carbonate peak for Pristine and Dryroom NCA because there was an insignificant amount of LiHCO₃ to lose.

Discrepancies in the observed Li₂CO₃ content between FTIR and TGA can be partially attributed to how each technique was performed. For FTIR, the samples were only exposed to an Ar atmosphere, and were kept at room temperature during testing. However, in the TGA experiments all samples were heated to temperatures as high as 750°C and were continually exposed to dry air. As a result, the samples were essentially annealed a second time, allowing for additional Li₂CO₃ to develop or reform on the surface at temperatures below 710°C, and causing the Li₂CO₃ mass loss to be inflated from what was originally on the sample. To confirm that Li₂CO₃ was developing on these materials as a result of the TGA experimental setup, additional TGA tests where individual isotherms were systematically removed were performed on 750°C Pristine NCA. Figure 4-12 compares the measured Li₂CO₃ mass loss when using the standard TGA protocol, and when removing each isotherm one by one. In the absence of the 500°C isotherm the Li₂CO₃ content on 750°C Pristine NCA decreased by 23%, but when the 350°C or 150°C isotherms were also removed the quantity of Li₂CO₃ was little changed. These results

suggest that Li_2CO_3 readily develops on the material's surface at higher temperatures, but the growth rate is insignificant at lower temperatures ($\leq 350^\circ\text{C}$). Figure 4-12 also shows that when using a specialty dry air gas that is devoid of CO_2 (<0.1 ppm) the Li_2CO_3 mass loss from 750°C Pristine NCA is considerably reduced. The Li_2CO_3 mass loss was comparable between samples that used the dry air with no CO_2 (patterned bar) and ones that used standard dry air but had no 500°C isotherm (solid bars), confirming that Li_2CO_3 growth is prevalent only at higher temperatures when in the presence of a dry atmosphere with CO_2 . *Matsumoto et al.* measured the growth of Li_2CO_3 on $\text{LiNi}_{0.81}\text{Co}_{0.16}\text{Al}_{0.03}\text{O}_2$ during heating to 800°C in air by in-situ XRD. Their results show that Li_2CO_3 began to develop around 525°C , and reached a maximum concentration at 675°C before decomposing.²¹³ In their study of Li_2CO_3 growth on Li_2O , *Mosqueda et al.* proposed that the formation of Li_2CO_3 was limited at lower temperatures because of the inability for Li atoms to diffuse through the thin Li_2CO_3 shell. When their samples were heated to 530°C and higher, they observed rapid Li_2CO_3 development due to the temperature promoted increase in diffusion through the Li_2CO_3 layer.²³¹

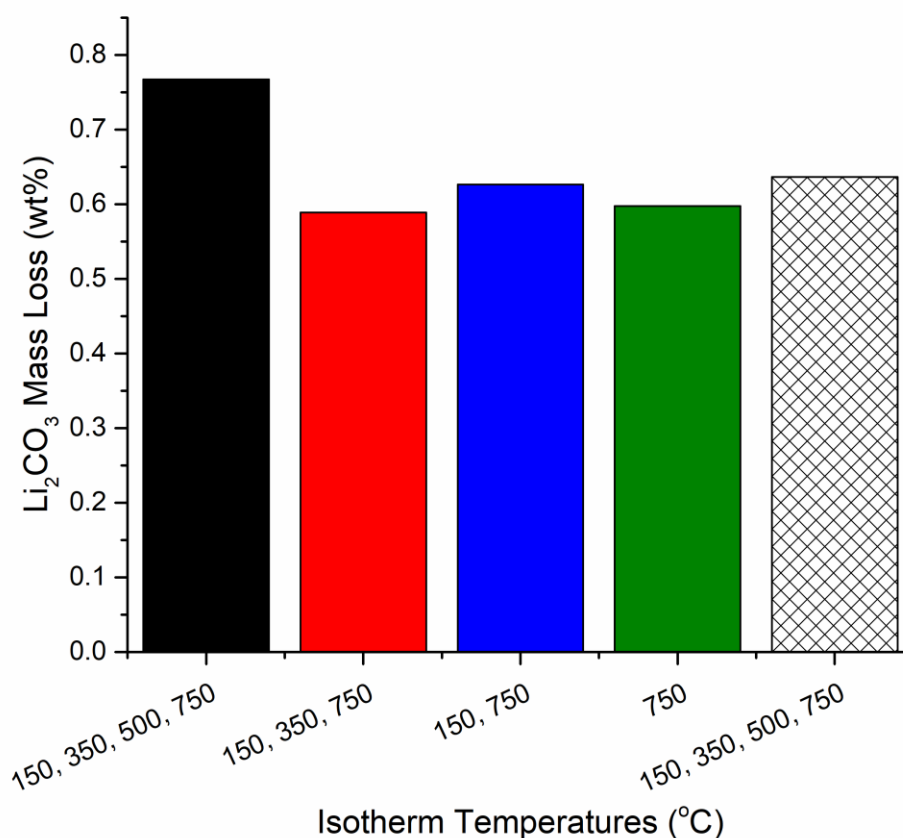


Figure 4-12: Li_2CO_3 mass loss determined by TGA measurements on 750°C annealed Pristine NCA. The solid bars show experiments where the 150°C, 350°C, and 500°C isothermal temperature segments were systematically removed to isolate the temperature range where Li_2CO_3 develops. All TGA experiments used heating rates of 5°C/min and were run with flowing dry air. The white and black patterned bar shows the Li_2CO_3 mass loss from an experiment using a specialty dry air gas with no CO_2 (<0.1 ppm), and was tested according to the standard TGA procedure (black bar).

The moisture content of every annealed and baseline sample was measured by KF coulometry and the results are shown in Figure 4-13. For each sample the moisture determined by the first KF test (black bars) and the cumulative result from successive tests (red bars) are provided. For all four baseline materials, the amount of moisture decreased significantly by annealing at 150°C, and decreased further by annealing at 350°C. Annealing at 500°C and 750°C was not effective in continuing to reduce the moisture content, likely because longer cool down times enabled more moisture to re-adsorb onto the surface.

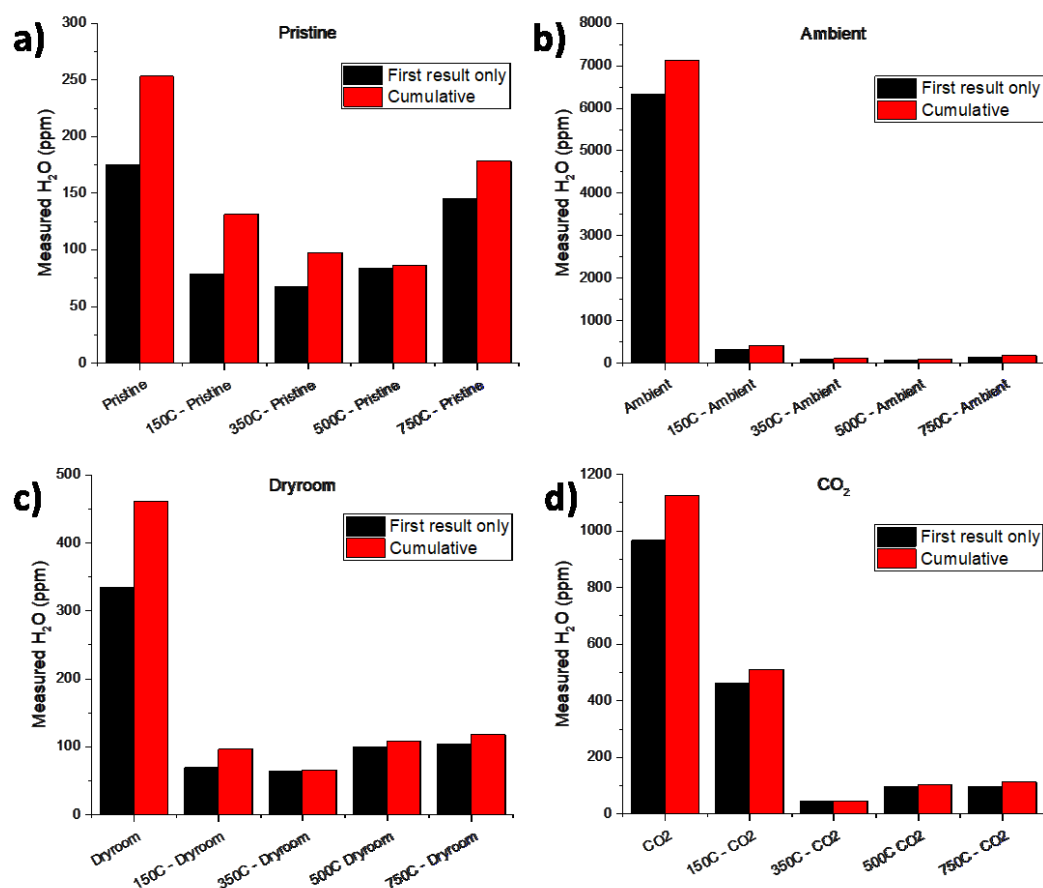


Figure 4-13: KF coulometry results for all anneals of (a) Pristine, (b) Ambient, (c) Dryroom, and (d) CO_2 NCA. Results from the measured moisture content of the first test (black) and the cumulative result from successive experiments (red) are provided. Note that the scale of the measured H_2O axis varies significantly between samples. All KF samples were prepared and sealed in an Ar-filled glovebox to prevent atmospheric exposure.

When comparing samples from different exposures it is critical to take note of the scale, which for clarity was made different for each baseline sample. Not surprisingly, the Pristine material had the lowest moisture content and Ambient NCA had the most. The cumulative ppm of H_2O for Ambient NCA was over 28 times the Pristine measurement, and well above either the Dryroom or CO_2 baseline samples. The slight (~200 ppm) increase in H_2O that Dryroom NCA had compared to the Pristine material is a result of the 2 week exposure to the dryroom atmosphere, which contains a minute amount of moisture. KF measurements show that CO_2 NCA had a moisture content about 4 times that of Pristine NCA, which supports the TGA experiments

that observed around 3 times higher wt% loss from water. For all samples the moisture measured from the first test was a good indicator of the cumulative quantity, and the two bars always moved in lock-step with one another.

XPS measurements on baseline Pristine, Ambient exposed, and annealed Ambient NCA samples are presented in Figure 4-14. The O 1s region (Figure 4-14 (a) and

Figure 4-15 (a)) shows peaks centered at 531-532 eV, and at 529 eV. The 531-532 eV peak location and breadth for Ambient and 150°C Ambient NCA corresponds well to a Li_2CO_3 reference material as shown in

Figure 4-15 (b). For our reference Li_2CO_3 , the main O 1s lattice peak around 531.5 eV is slightly lower in energy than previously reported for *in-situ* measurements of 531.9 eV, which may indicate the presence of a thin bicarbonate surface layer on the Li_2CO_3 reference.²³² The peak at 529 eV is from the lattice oxygen in NCA and is used to normalize the O 1s spectra intensities, with the exception of Ambient NCA whose surface impurity layer was thick enough to obscure the lattice oxygen signal. Results of the peak intensity ratios between surface (from impurity species) and lattice oxygen are presented in Figure 4-14 (b), and exhibit a trend that closely mirrors the FTIR results presented in Figure 4-9. After annealing at 150°C the percent composition of surface oxygen decreases slightly, mainly because the impurity layer is now not completely obscuring the lattice oxygen signal. Annealing at 350°C, which removes LiHCO_3 , causes a large decline in the normalized surface oxygen peak, while annealing at 500°C has little impact on the surface to lattice oxygen ratio. As expected the 750°C anneal, which removes Li_2CO_3 , induced another substantial drop in the surface oxygen signal. With each anneal the degree of change to the surface to lattice oxygen ratio closely resembles the magnitude of impurity species lost as determined by TGA. It was also observed that as H_2O , LiHCO_3 , LiOH and Li_2CO_3 are subsequently removed from the Ambient exposed materials, the O1s 531-532 eV peak is consequentially shifted to higher energies. The peak position at around 531.9 eV is

consistent with primarily Li_2CO_3 remaining on the 500°C and 750°C annealed samples, supporting the TGA results presented earlier.

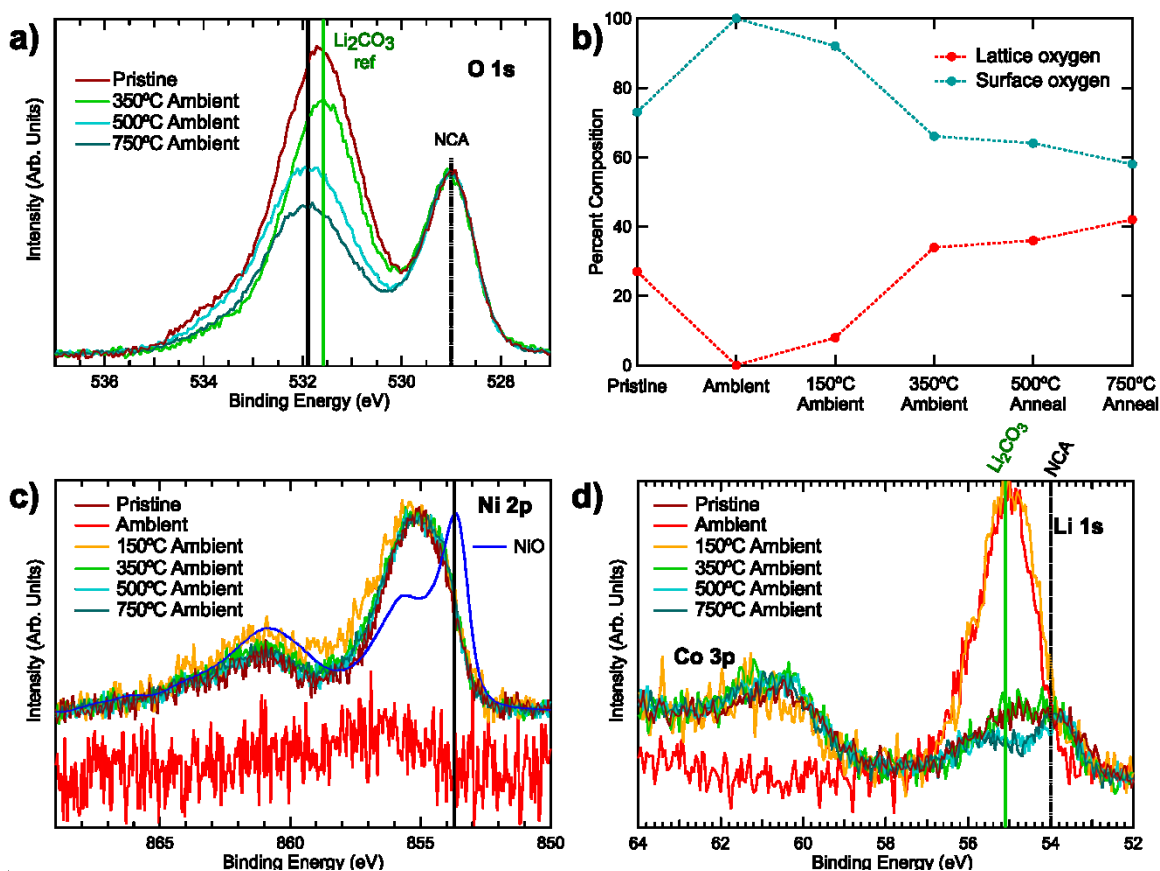


Figure 4-14: XPS spectra of the (a) O 1s region for select samples and (b) the percent composition of surface and lattice oxygen for Pristine NCA and all Ambient materials. The amount of surface and lattice oxygen were determined by the relative intensities of the higher binding energy peaks (530-533 eV) and NCA (529 eV) peaks. Peak intensities of the spectra in the (a) are normalized to the size of the NCA peak. The peak locations from a Li_2CO_3 reference and NCA are denoted by vertical bars. (c-d) show the Ni 2p, Co 3p, and Li 1s regions for the same samples shown in (a). For reference, the Ni 2p region of a NiO reference material is displayed in (c).

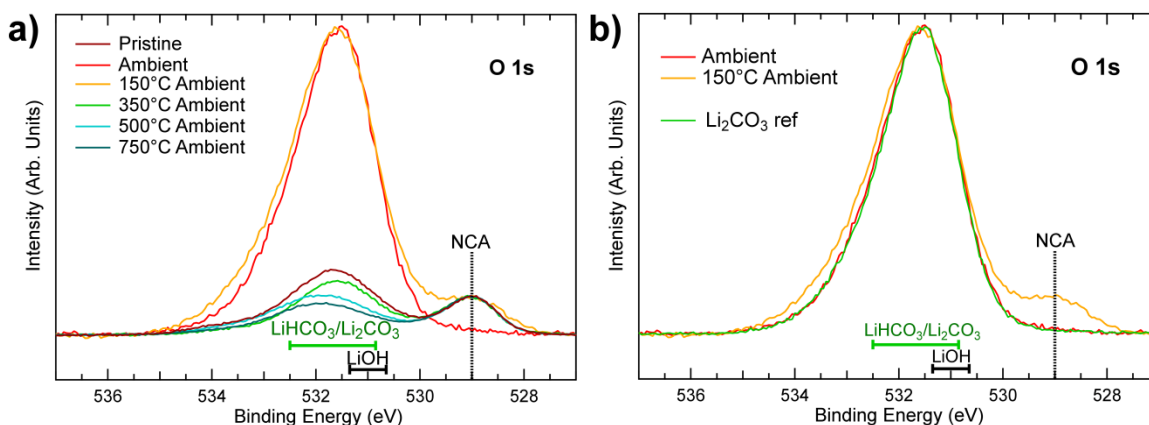


Figure 4-15: (a) The XPS O 1s spectra of Pristine NCA and all Ambient exposed materials. The approximate $\text{LiHCO}_3/\text{Li}_2\text{CO}_3$ and LiOH regions are shown by the horizontal green and black brackets, respectively. The LiOH peak position is based on previous work by Dupin et. al.²¹⁷ (b) A comparison of the O 1s region for Ambient NCA, 150°C annealed Ambient NCA, and a Li_2CO_3 reference material is provided. The expected peak locations for Li_2CO_3 and NCA are denoted by vertical bars, while the approximate location for LiOH is indicated by a horizontal bracket.

Figure 4-14 (c) and (d) display the XPS spectra in the Ni 2p, Co 3p, and Li 1s regions. Other than Ambient NCA, whose surface layer was too thick to clearly see the lattice signal, there are no significant differences in the Ni or Co signals between samples, suggesting no change in the redox state of the transition metals. The samples spectra clearly differ from the NiO reference, which seems to suggest that the average valence state of the Ni is closer to +3. This is in contrast to other studies which have observed an increase in Ni^{2+} on the surface after ambient exposure. Importantly, it should be noted that the Ni 2p line shapes for materials such as Ni^{3+}OOH and $\text{Ni}^{2+}(\text{OH})_2$, which could form upon proton exchange or insertion, are shifted to higher energies compared to NiO, and are similar to Ni^{3+} in layered oxides.²³³ While the Ni 2p lineshape for samples annealed at temperatures $\geq 350^\circ\text{C}$ compare well with the Pristine NCA, the similarity of NiOOH and $\text{Ni}(\text{OH})_2$ peak positions, makes conclusive determination of the nickel redox state exceedingly difficult.²³⁴ The steady decrease of the Li 1s Li_2CO_3 peak with higher temperature annealing confirms the loss of the carbonate signal observed in the O 1s spectra.

To complement the electrochemistry results of the baseline materials (Figure 4-6), electrodes were fabricated from all of the annealed analogs of the Pristine and Ambient NCA

materials. The discharge capacities versus cycle number for coin cells using these materials are plotted in Figure 4-16 (a-d). Each material was cycled using the same procedure as the previously shown cells. Figure 4-16 (a) shows that 150°C annealed (H₂O removed) Ambient NCA performs drastically better than the Ambient baseline material, but still underperforms 150°C annealed and baseline Pristine NCA samples. Annealing at 150°C had minimal impact on the cycling capabilities of Pristine NCA relative to the baseline material, and only a slight reduction in discharge capacity (<2%) was observed. As a result of the 150°C anneal, 150°C Ambient NCA has discharge capacities as high as 152 and 168 mAh/g when charged to 4.2 and 4.5 V. However, there is a rapid capacity fade that quickly degrades the electrochemical performance, and causes the discharge capacity to drop below 100 mAh/g after only 69 and 86 cycles. While the discharge capacity of 150°C Ambient NCA is higher when the cutoff potential is 4.5 V versus 4.2 V, the capacity increase is relatively minor compared to the increase in capacity between 4.5 and 4.2 V for 150°C Pristine NCA.

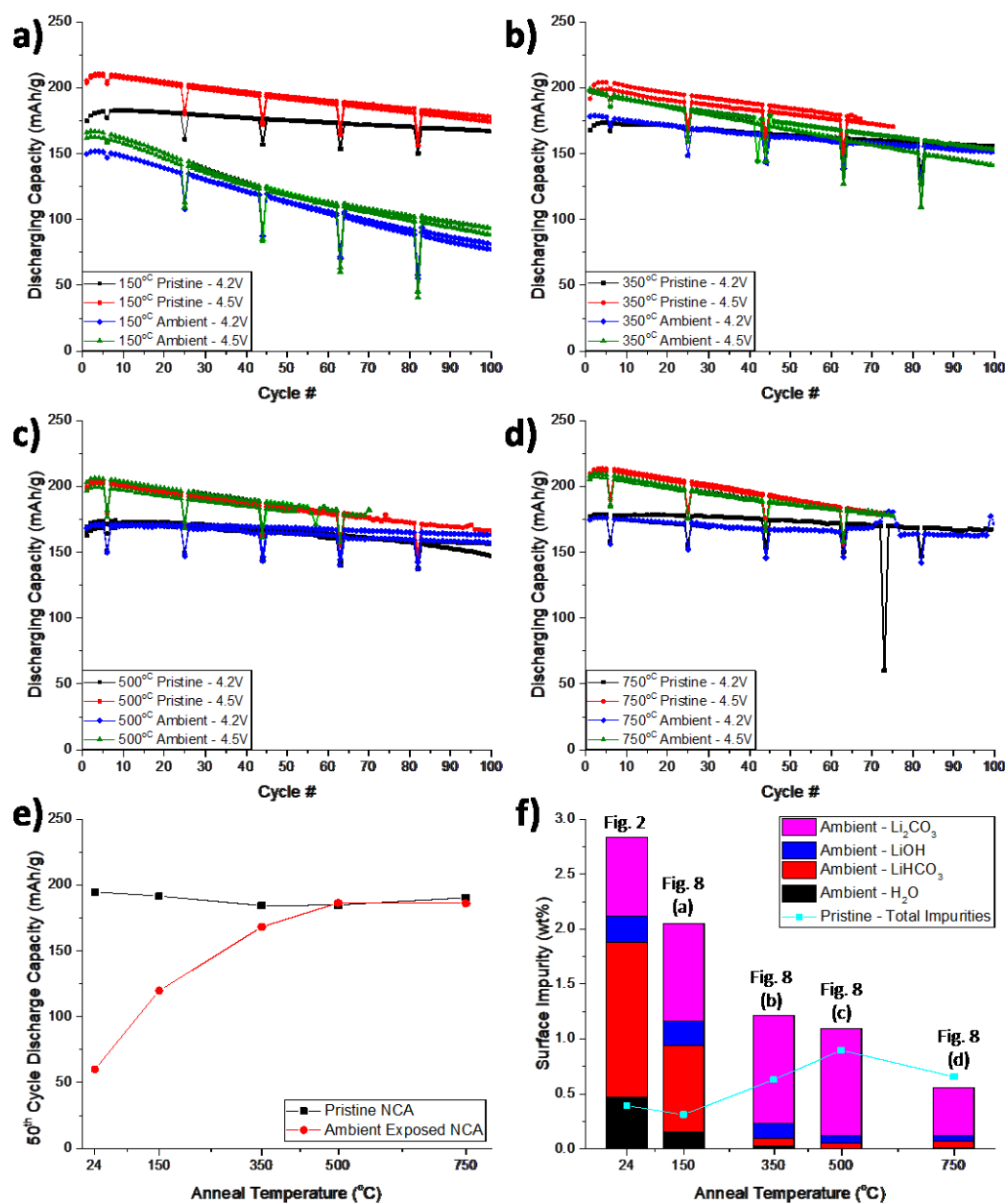


Figure 4-16: Discharge capacity vs. cycle number for cells made with positive electrodes of (a) 150°C, (b) 350°C, (c) 500°C, and (d) 750°C annealed Pristine and Ambient NCA materials. All cells were cycled at 24°C by charging to V_{max} (4.2 or 4.5 V) at 20 mA/g, holding at constant voltage until the current fell below 10 mA/g, and then discharging at 15 mA/g to 2.75 V. Starting on the 6th cycle and every 19 cycles afterwards, the cells were discharged at 150 mA/g instead of 15 mA/g. (e) The 50th cycle discharge capacity as a function on annealing temperature for all Pristine and Ambient materials is provided. A breakdown of the surface impurity species on Ambient exposed materials as a function of anneal, and the total impurity species on Pristine materials is shown in part f.

As shown in Figure 4-16 (b), annealing at 350°C (LiHCO_3 removed) had a profound impact on the electrochemical performance of Ambient NCA. When cycled to 4.2 V, the cycling stability of the 350°C Pristine and 350°C Ambient are indistinguishable, and even when charged to 4.5 V the discharge capacity of 350°C Ambient is only marginally worse than the Pristine counterpart. Not only are the initial discharge capacities similar between the two materials, but so is the capacity retention performance. These results are mimicked when comparing the 500°C (Figure 4-16 (c)) and 750°C (Figure 4-16 (d)) annealed materials. While the discharge capacities of the 350°C Pristine material were a bit lower than what was measured for the 150°C Pristine cells, they had a nearly identical performance as the 500°C Pristine samples. The 750°C Pristine cells had higher capacities than any of the other annealed Pristine materials, since the 750°C anneal removed most of the Li_2CO_3 that developed at lower temperatures. As a result of the Li_2CO_3 decomposition, the 750°C Pristine electrodes had similar capacities as the baseline Pristine NCA.

The change in the discharge capacity of the Pristine NCA samples as a result of annealing follows the inverse trend of the Li_2CO_3 content identified from the FTIR and TGA measurements (Figure 4-9 and Figure 4-10). As the Li_2CO_3 content increases the discharge capacity is reduced, and after annealing at 750°C, when the Li_2CO_3 is mostly decomposed, the discharge capacity increases. As shown by the percent capacity loss after 50 cycles for all Pristine and Ambient materials in Figure 4-16 (e) (and in Table 4-II), there are significant increases in the capacity retention of Ambient NCA as H_2O , LiHCO_3 , and LiOH are removed. The % capacity loss for Pristine electrodes are relatively invariant because of the minimal surface species present on the material. Comparison of the 500°C annealed Pristine and Ambient materials (H_2O , LiHCO_3 , and LiOH removed) shows that there is a negligible difference in the capacity retention after 50 cycles. Figure 4-16 (f), which depicts a breakdown of the surface impurity species on each Ambient exposed sample (bars) and the cumulative impurity content on the annealed Pristine

materials (line), is a useful visual for understanding the relationships between each impurity specie and the impact on the material's cycle performance.

The voltage profiles of the 1st and 50th cycles from cells charged to 4.5 V for all baseline and annealed versions of Pristine and Ambient NCA are presented in Figure 4-17. The 50th cycle voltage profiles in Figure 4-17 (a) show little difference between Pristine, Dryroom, and CO₂ NCA materials. This suggests that the impurity species on CO₂, which caused the initial overpotential, are lost during cycling and didn't cause significant damage to the positive electrode. However, even on the 50th cycle the Ambient material still shows significant polarization, which results from its excess of impurity species. 1st cycle voltage profiles for the annealed Pristine NCA samples, shown in Figure 4-17 (b), display a strong correlation between the initial overpotential and the carbonate content presented in Figure 4-9. By the 50th cycle, there are minimal differences in polarization between samples, confirming the loss of the carbonate species with cycling. The Ambient materials annealed at $\geq 350^{\circ}\text{C}$ (Figure 4-17 (c)) have substantially reduced polarization on their 50th cycle relative to the 1st cycle. Yet, due to the exceedingly large amount of impurity species still on 150^{°C} annealed Ambient NCA significant polarization even on the 50th cycle was observed.

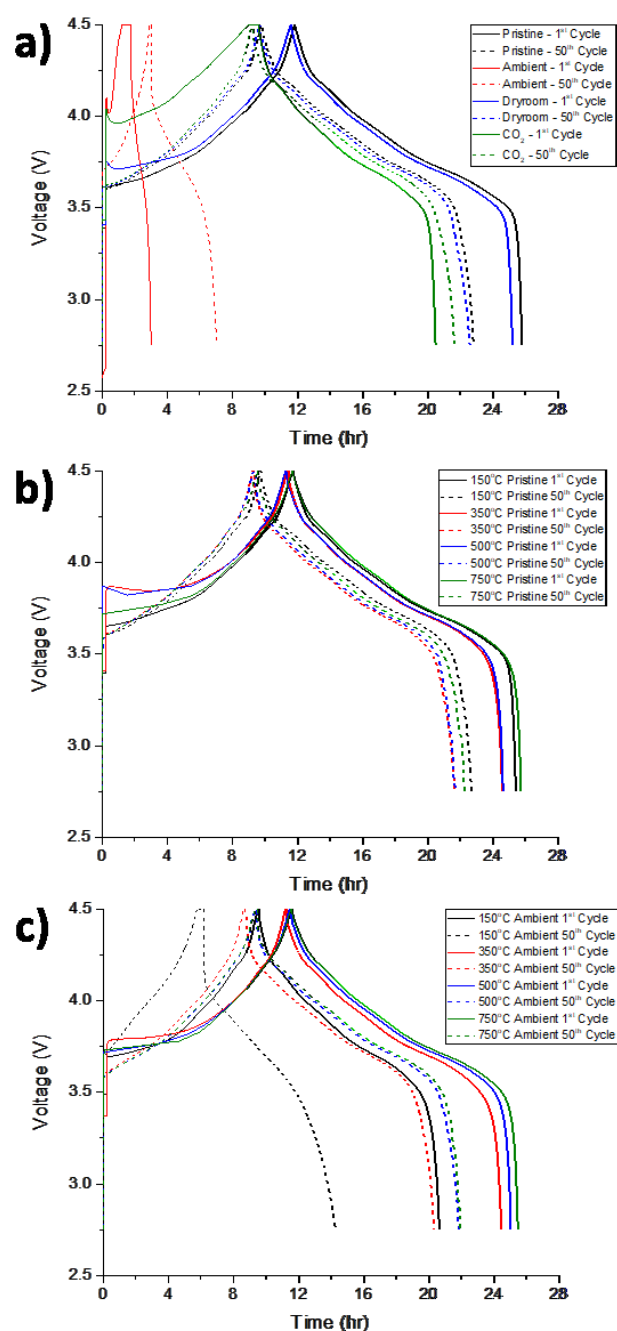


Figure 4-17: The voltage profiles of the 1st and 50th cycles from cells cycled to 4.5 V for (a) all baseline materials, and annealed (b) Pristine and (c) Ambient materials. All cells were charged at 20 mA/g to 4.5 V, held at constant voltage until the current dropped below 10 mA/g, and then discharged at 15 mA/g to 2.75 V. Starting on the 6th cycle and every 19 cycles afterwards the cells were discharged at 150 mA/g. All of the cells shown here were discharged at 15 mA/g.

When charged to either 4.2 or 4.5 V, the rate dependent capacity retention (Table 4-II) for Pristine NCA decreases substantially after being annealed at 350°C, and subsequently increases after being annealed at 750°C. The decline in high rate performance after the 350°C anneal may be attributed to the formation of Li_2CO_3 or Li_2O by the degradation of LiHCO_3 whereas the increase in rate capability after annealing at 750°C is likely associated to the reduced Li_2CO_3 content. In contrast, the high discharge rate performance of Ambient NCA increased significantly after annealing at 150°C, 350°C, and 750°C. The large increases in rate capability after the 150°C and 350°C anneals is likely because Ambient NCA originally had so much excess moisture and bicarbonate species which formed an exceedingly thick cathode-electrolyte interface upon reaction with the electrolyte. Even though Li_2CO_3 and Li_2O likely formed from LiHCO_3 decomposition, the cumulative interface impedance was still reduced. The improvement in rate capability after annealing at 750°C is associated with the loss of Li_2CO_3 , similar to the Pristine materials. Baseline, 150°C and 350°C annealed Ambient NCA electrodes had steady impedance growth with extended cycling, as measured by the high discharge rate capacity retention, while the rate capabilities of all other samples only decreased slightly. The large quantities of surface impurities on baseline, 150°C and 350°C annealed Ambient materials likely created an excess of HF which continually degraded the positive electrode's surface.

4.5 Discussion

Comparison of the four baseline materials offers valuable insight into the formation mechanisms of surface impurity species on layered oxide materials and their impact on the host materials' cycle stability. Exposure to the dryroom atmosphere (CO_2 and O_2 sans H_2O) had negligible impact on the quantity of the impurity species or the electrochemical performance relative to the Pristine material. While storage in a pure CO_2 atmosphere induced the development of some additional moisture and Li_2CO_3 and hindered the material's capacity retention, the magnitude of degradation was far less than what was observed in the Ambient

sample. The ambient atmosphere caused a nearly 30-fold increase in the moisture content, as well as ample LiHCO_3 , LiOH and Li_2CO_3 development. As a result of the extreme increase in the surface impurity species concentrations, Ambient NCA was incapable of cycling with a cutoff potential of 4.2 V, and performed terribly when charged to 4.5 V.

While it is intuitive that storage of NCA in the dryroom only caused a marginal increase in the moisture content, it was surprising to find that the CO_2 exposed sample had nearly 3 times the amount of H_2O as Pristine NCA, despite using dry CO_2 gas and storing the sealed container in the dryroom. The CO_2 NCA material also had slightly higher Li_2CO_3 and LiHCO_3 contents than Pristine NCA, and it is believed that the slight increases of these impurities are all related. Adsorbed moisture already present on the initial material, or trace H_2O from the CO_2 gas could have caused the formation of some LiHCO_3 and LiOH . Once bicarbonate or hydroxide species are created, they could interact with either the CO_2 gas (Equation 4-4 and Equation 4-5) or other impurity species (Equation 4-6 and Equation 4-7) to produce new LiHCO_3 , Li_2CO_3 and H_2O .



Since many of the reactions between surface impurities (Equation 4-5, Equation 4-6, and Equation 4-7) produce water as byproduct, these mechanisms of surface impurity development would likely be autocatalytic and would continue until the source of Li or CO_2 is impeded. Even though the LiHCO_3 and Li_2CO_3 contents did increase from exposure to 100% CO_2 the degree of formation was minor relative to the Ambient samples, which were exposed to an atmosphere with only had a few hundred ppm of CO_2 . These results, in conjunction with the Dryroom NCA results, strongly suggest that the formation of surface species at room temperature requires both moisture and CO_2 , and that Li_2CO_3 is mainly created through intermediary species and not, as suggested by some in the past, by direct reaction between CO_2 and the layered oxide

material.^{201,213,237} Thus dry atmospheres, especially ones with low CO₂ concentrations, have a negligible impact on the growth of impurity species and are safe for handling layered oxide electrode materials.

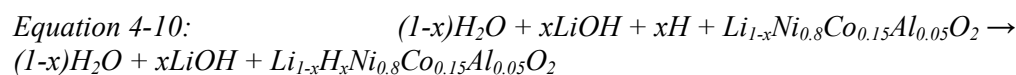
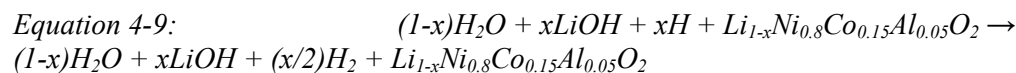
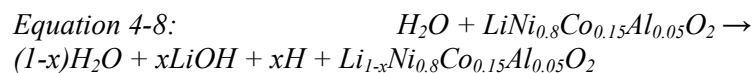
As shown in Figure 4-13, annealing at 150°C for 2 h significantly reduces the moisture content of the baseline materials, and by 350°C there is only a negligible amount remaining. TGA results demonstrate that the vast majority of LiHCO₃ and LiOH can be eliminated by annealing at 350°C and 500°C, respectively. While annealing in dry air had the unintended consequence of promoting Li₂CO₃ growth, especially at high temperatures, annealing above 710°C is known to cause the degradation of Li₂CO₃ and all of our 750°C annealed materials had a reduction in the Li₂CO₃ content. Eliminating all of the Li₂CO₃ could have been achieved by using either a higher temperature or longer anneal. By choosing the right annealing temperature and duration, one can selectively remove impurity species. However, it was observed that when annealing at higher temperatures the material's lattice parameters increased, and the resulting impact on the electrode's stability and transport properties needs to be taken into account.

Defining the mechanism of Li₂CO₃ formation on the surface of layered compounds has been widely investigated and the main conclusions are summarized in the introduction of this paper. While it was not our primary goal to define the specific details of this mechanism within this paper, we have accumulated a body of evidence that can be useful to further advance the collective understanding. As noted above, the fact that exposure to dry CO₂ does not enhance the formation of Li₂CO₃ by a great degree clearly shows that at room temperature direct reaction of CO₂ with NCA to extract Li and form Li₂CO₃ is not the active mechanism as proposed by others. Undoubtedly, moisture is required and is the catalyst for Li₂CO₃ growth.

It is evident that the OCV increases systematically with Li₂CO₃ formation at the surface of the NCA. This in itself can be utilized as a valuable quality check for layered oxide materials without any advanced characterization to examine the degree of contamination of the material's surface with ambient induced impurity species. With respect to the Li₂CO₃ formation mechanism,

there are two likely and relevant scenarios that can lead to the increase of the OCV and the production of $\text{LiHCO}_3/\text{LiOH}$, which is the necessary precursor for Li_2CO_3 . One scenario is the deintercalation of Li^+ and subsequent oxidation of the NCA, the other is the formation of surface protonated NCA with no change in oxidation state of the transition metals. It is known that NiOOH and CoOOH both have higher OCV vs. Li/Li^+ than the lithiated analogues of LiNiO_2 and LiCoO_2 .^{17,238} In the first scenario, based on redox of the transition metal atom (Equation 4-8), H_2O is reduced at the surface of NCA producing LiOH , H and a partially oxidized NCA. This is quickly followed by either the loss of H_2 gas (Equation 4-9) or subsequent oxidation of the H to reduce NCA back to its original state and partially intercalate a proton (Equation 4-10). The transition metal redox scenario is attractive because it is known that the propensity to form Li_2CO_3 inversely scales with the initial redox potential of the intercalation compound.

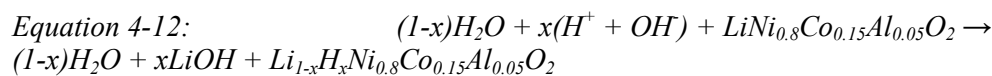
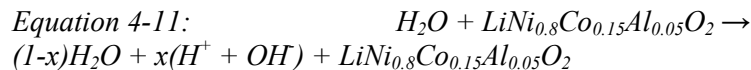
Scenario 1 (redox):



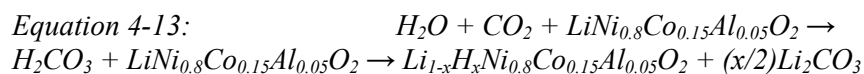
The second explanation relies on ion exchange. In this case (Equation 4-11), OH^- is strongly adsorbed to the surface of NCA via coordination with either Li or a transition metal charge density. This in turn enables a local ion exchange between a proton and Li atom, concomitant with the formation of LiOH (Equation 4-12). An advantage of this model is that such ion exchange is very likely to occur. Indeed, the reverse reaction, $\text{LiOH} + \text{CoOOH}$ or NiOOH has been used to form both LiCoO_2 and LiNiO_2 at low temperatures.²³⁹ An alternative model (Equation 4-13), which bypasses the formation of LiOH completely, relies on the formation of carbonic acid and a direct exchange between H^+ and Li^+ . Regardless of the ion exchange scenario,

the question remains as to why the lower voltage nickelates more frequently induce this reaction compared to the higher voltage LiCoO_2 or LiMn_2O_4 .

Scenario 2 (ion exchange):

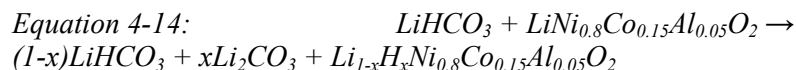


or



From either the redox (Equation 4-8, Equation 4-9, and Equation 4-10) or 1st ion exchange scenario (Equation 4-12) the subsequent reactions to form Li_2CO_3 can be envisioned to be straight forward. LiOH will react with ambient CO_2 to either directly form Li_2CO_3 (Equation 4-5) or create LiHCO_3 (Equation 4-4). The proton from LiHCO_3 can ion exchange with the Li in NCA to form Li_2CO_3 (Equation 4-14) or simply decompose along a pathway explained by either Equation 4-6 or Equation 4-7. Both degradation scenarios, laid out in Equation 4-8 to Equation 4-14, are not limited to NCA and the basic mechanisms can be applied to other $\text{R}\bar{3}\text{m}$ layered oxide materials. However, the propensity for redox is unique to each type of transition metal and this will have a large effect on the driving force for the proposed redox mechanism.

Subsequent Reaction:



The primary motivation for investigating the surface impurity species is to understand the impact that each specie has on the electrochemical performance of the electrode. The cycling results for the baseline (Figure 4-6) and annealed materials (Figure 4-16) highlight the impact that surface impurities have on the stability and capacities of layered oxide materials. Analysis of the improvement in capacity retention when Ambient NCA was annealed at 150°C demonstrates the importance of ensuring that the electrodes are completely dry. Even trace amounts of water can

react with the fluorinated electrolyte, forming HF and leading to the decomposition of the positive electrode surface structure.^{67,121,201} The increase in capacity retention that occurred when Ambient NCA was annealed at 350°C is from further reduction in the material's moisture content and, more importantly, the removal of LiHCO₃, which besides increasing impedance is also expected to react with fluorinated salts, producing HF. After annealing at 500°C, all of the surface species other than Li₂CO₃ were removed and the Ambient material performs identically to the 500°C annealed Pristine samples. However, annealing below 750°C was shown to have caused the formation of Li₂CO₃, and this Li₂CO₃ layer is responsible for the reduced (~5%) discharge capacity of the 500°C annealed materials compared to the baseline Pristine NCA cells. When annealed at 750°C, the Li₂CO₃ layer was mostly removed and the discharge capacities for both Pristine and Ambient cells improved slightly. An important takeaway is that with respect to cycling stability and capacity, Li₂CO₃ has a minimal impact. Previous observations of improved performance of layered electrodes when Li₂CO₃ was removed are more likely attributed to the simultaneous removal of LiHCO₃, LiOH, and possibly moisture (which was not removed during the standard electrode processing before cell fabrication) and not from Li₂CO₃. Chen and Dahn demonstrated that a similar performance increase of LiCoO₂ can be obtained by annealing at 550°C instead of 800°C, supporting our results that surface species other than Li₂CO₃ induce the majority electrochemical stability and capacity degradation.²²¹

4.6 Conclusion

Counter to some reports, Li₂CO₃ on the surface of layered oxides is not formed by direct reaction with ambient CO₂ at room temperature. Moisture is a definitive entity required to trigger the formation of Li₂CO₃ at room temperature. In contrast to almost all previous reports, including those from our group, Li₂CO₃ on the surface of layered compounds, such as NCA, is not detrimental to the material's cycle life. The previously observed degradation can now be attributed to the species integral to the formation of Li₂CO₃. Specifically H₂O, LiHCO₃ and likely

LiOH each have their own contribution to the significant degradation of capacity and cycle stability. Removal of these species while retaining Li_2CO_3 resulted in excellent cycling stability, comparable to the initial pristine NCA. It should be noted that the presence of Li_2CO_3 may have other impacts, both positive and negative, beyond cycling stability which was not addressed here. Regardless of impact, it is necessary for battery manufacturers to gauge the degree of exposure and formation of Li_2CO_3 on as received and stored powders. It is imperative to the material's electrochemical performance that the magnitude of surface impurities are measured and controlled. The most quantitative of all the characterization methods is TGA, while a more sensitive and practical approach to measure the degree of surface impurities is simply monitoring the initial OCV of the as fabricated battery, since the OCV was found to rise with ambient exposure and subsequent surface impurity development.

4.7 Acknowledgements

The authors would like to acknowledge Frederic Cosandey, Pinaki Mukherjee, and Gerbrand Ceder for useful discussions. This work was supported as part of NECCES, an Energy Frontier Research Center funded by the U.S. Department of Energy, Office of Science, Office of Basic Energy Sciences under Award No. DE-SC0012583.

4.8 Next Steps

As demonstrated by the results shown in Chapter 3, the electrode-electrolyte reactions that occur on layered oxide electrodes at high states of charge will cause substantial degradation of the electrode material and lead to significant impedance development. The ample transition metal dissolution and structural decomposition of the material's surface and sub-surface generates this impedance growth and reduces the electrochemical performance of the electrode. This chemically induced degradation of the positive electrode material was made worse by the presence of surface impurity species. Chapter 4 proved that Li_2CO_3 was not detrimental to the electrode material, and

that the other surface impurity species, mainly H_2O and LiHCO_3 , were markedly more harmful. While these results provide tremendous insight into understanding the poor performance of layered oxide electrodes at such high states of charge, they ignore the intrinsic structural stability of the electrode material. By synthesizing a wide range of layered oxide materials with varying transition metal chemistries and then extensively characterizing these materials a thorough analysis of how the intrinsic structural stability of the electrode affects the electrochemical performance at high states of charge. The results from this investigation are introduced and described in the following chapter.

5 STRUCTURAL EFFECTS ON THE ELECTROCHEMICAL PERFORMANCE OF HIGHLY DELITHIATED LAYERED OXIDE MATERIALS

5.1 Abstract

Obtaining energy densities near the theoretical limit for layered oxide positive electrode materials is dependent on improving the stability of the electrochemical performance of these materials at or near full delithiation. In order to develop new materials and novel approaches to increasing the electrochemical performance of these materials at such high states of charge, a robust understanding of the failure mechanisms limiting current materials is necessary. Thorough analysis of $\text{Li}_x\text{Co}_{1-y}\text{Al}_y\text{O}_2$ and $\text{Li}_x\text{Ni}_{1-y}\text{Al}_y\text{O}_2$ ($1 \geq x \geq 0$ and $0.2 \geq y \geq 0$) as well as $\text{Li}_x\text{Ni}_{0.8}\text{Co}_{0.2}\text{O}_2$ and $\text{Li}_x\text{Ni}_{0.8}\text{Co}_{0.15}\text{Al}_{0.05}\text{O}_2$ enabled the identification of key relationships between an electrode's transition metal chemistry, structural stability, and cycling characteristics. Extensive characterization of these materials was achieved by a multitude of electrochemical techniques, *in-situ* and *ex-situ* X-ray diffraction, *operando* microcalorimetry, and inductively coupled plasma – atomic emission spectroscopy. The resulting insights derived from these analyses highlight the importance of an electrode's intrinsic structural stability when highly delithiated and indicate guidelines for identifying positive electrode materials with improved high state of charge performance.

5.2 Introduction

To enhance the energy density of lithium-ion batteries and reduce the gap between the theoretical and practically obtained capacities for layered oxide ($R\bar{3}m$) positive electrodes, the upper limit of the operating potential window needs to be increased.⁵ Presently, commercial layered oxide electrode materials are limited to ~ 4.2 V, but full delithiation often occurs at potentials greater than 4.7 V.^{5,14,17,18,240} This results in only $\sim 60\%$ utilization of the stored energy, which is insufficient to meet the future energy demands of electric vehicles and portable devices.^{5,131} While an abundance of work focused on increasing the potential of positive

electrodes has been completed, there are still numerous obstacles preventing the application of these materials at or near full delithiation. Amongst the main issues restricting the use of layered oxide materials at the highest states of charge is the structural instability of these materials,^{170,240,241} which can catalyze parasitic reactions with the electrolyte,^{66,85,211} evolve oxygen from the host structure,^{124,211,222,242} lead to significant transition metal dissolution^{66,104,120,128,157} and cause thermal stability issues.^{135,242} Furthermore, degradation of the layered structure can result in significantly reduced electrochemical capacity and increased capacity fading.^{141,171,243,244}

LiCoO₂ was not only the first layered oxide material to be commercially used as a positive electrode in lithium-ion batteries, but also established the foundation from which current layered positive electrodes are based.⁵ The structural transitions in LiCoO₂ and in the isostructural corollary, LiNiO₂, during delithiation are well documented, and are thoroughly described elsewhere.^{14,17,18,105,170,197,240,241} Both LiCoO₂ and LiNiO₂ have very similar phase transitions as a function of delithiation, although the specific lithiation values at which these transitions occur differ because of the different electronic states of Ni and Co.^{18,103} The main structural differences between LiCoO₂ and LiNiO₂, especially when highly delithiated, occur because of the Jahn-Teller distortion of nickel octahedra, and from the propensity for Ni to be reduced from Ni³⁺ to Ni²⁺ and subsequently migrate to the Li layer.^{105,133,241} Fully delithiated LiCoO₂ has been shown to form a stable CoO₂ compound, having an O1 structure in the hexagonal lattice. This structure arises from the shifting of the basal planes as the Li separating these planes is completely removed.^{17,197} Formation of the O1 structure with AB oxygen packing and face sharing octahedra has been experimentally and theoretically shown to be more stable than the O3 structure with AB CA BC oxygen packing and edge sharing octahedra for both completely delithiated LiCoO₂ and LiNiO₂.^{17,105,197,241} However, as demonstrated by *Croguennec et al.* it can be experimentally

difficult to observe the O1 phase for LiNiO₂ because an excess of nickel ions in the Li layer is sufficient to prevent the sliding of basal planes.²⁴¹

The higher energy density, reduced cost and lower toxicity of Ni relative to Co, has made LiNiO₂ a highly desirable positive electrode material.^{11,131,187} Unfortunately, the poor cycle stability and capacity retention of LiNiO₂ has prevented its commercial utilization.^{134,141,245,246} As a result, there has been much effort to enhance the structural stability and electrochemical properties of LiNiO₂ through partial substitution of Co or Al ions for Ni. Both Co and Al dopants are effective in limiting the Ni ions present in the Li layer, which causes a significant improvement in the electrochemical performance.^{98,102,132–136,138,141,142,247–249} *Rougier et al.* demonstrated that when Co partially replaces Ni in LiNiO₂, the smaller ionic radii of Co³⁺ ($r_{Co}^{III} = 0.53 \text{ \AA}$) relative to Ni³⁺ ($r_{Ni}^{III} = 0.56 \text{ \AA}$) contracts the transition metal slab. The tighter slab substantially reduces the stability of divalent Ni ($r_{Ni}^{II} = 0.68 \text{ \AA}$) within the transition metal-oxygen layer, and subsequently limits the amount of Ni²⁺ on the Li sites. This mechanism occurs because of the necessity to maintain charge neutrality in synthesized materials, which requires a divalent Ni ion the transition metal slab for every divalent Ni ion in the Li layer.¹³² A similar mechanism has been shown for Al-substituted nickelates, except with amplified efficacy because of the increased ionicity of Al-O bonds.^{98,142} However, Al-substituted materials often still have transition metal mixing because of phase segregation into Al-rich and Al-deficient regions, and because of the tendency for Al to reside in the tetrahedral site.^{98,246,247,249} A recent computational study suggests that the reduced transition metal mixing and increased structural stability of Co or Al-substituted LiNiO₂ may also be attributed to the partial elimination of the 180° Ni-O-Ni “superexchange interaction” energy benefit that occurs when Ni ions reside in the Li sites.⁹⁸

In addition to reduced transition metal mixing, Co and Al substitution in LiNiO₂ increases the voltage profile during lithium insertion and extraction and smooths voltage plateaus from phase transitions.^{132,134,141,142} The degree of changes to the voltage profile scales with the

amount of transition metal additive incorporated into the host material.^{132,142} Furthermore, metal substitution can have a profound impact on increasing the cycling stability and capacity retention of LiNiO₂. The enhanced cycling performance can be partially attributed to the reduction of transition metal mixing, which restricts lithium ion diffusivity, and to the smoothing of phase transitions, which alleviates some of the internal stresses on the host structure.^{141,142,246} It should be noted that Al is electrochemically inactive and can lower the obtained capacity, by limiting the amount of lithium available for extraction.^{134,142,246,248} Al substitution has also been experimentally observed and theoretically calculated to limit the Li⁺ diffusivity in layered transition metal oxides.^{245,250} Kang and Ceder suggested that Al substitution raises the activation barrier for Li hopping by lowering the electron density around the oxygen atoms, and thus minimizing the electron screening that reduces the electrostatic interactions between Li and the transition metals.²⁵⁰ As a result of the beneficial properties obtained by substituting low cost LiNiO₂ with Co and Al, and the performance limitations from adding large amounts of Al, LiNi_{0.8}Co_{0.15}Al_{0.05}O₂ (NCA) has emerged as a leading positive electrode material.^{5,102,131} By using a mixture of multiple metal ions, NCA has increased structural stability, and capacity retention relative to the baseline Ni and Co layered oxide materials.¹⁰³

While there is much published work on the structural and electrochemical properties of Al-substituted LiCoO₂ and LiNiO₂ materials in the conventional potential window, there is a dearth of results for these materials near full delithiation. Moreover, there is an inherent shortcoming in that these materials are often made in-house and generally only a few compositions are studied at once. As a result, there are large variations in material quality and characteristics between groups, which makes it difficult to draw broad conclusions about the effect of the metal chemistry on the material's properties. Here, we investigate the structural and chemical stability of a variety of highly delithiated Al-substituted LiCoO₂ and LiNiO₂ materials, as well as Co-substituted LiNiO₂ and NCA. When possible, we compare our samples to

commercially available materials to demonstrate sample quality. By correlating the phase transitions, Li^+ transport properties, and electrochemical performance to each material's metal chemistry, we elucidate key insights about the impact that the electrode's composition has on layered oxide materials near full delithiation.

5.3 Experimental

5.3.1 Materials Preparation

Commercially produced NCA (NAT1050, TODA America) and LiCoO_2 (Seimi) materials were used as received as references in all characterization and electrochemistry experiments. All materials synthesized in-house were fabricated as follows. Lithium acetate (Aldrich), aluminum acetate basic hydrate (Alfa Aesar), nickel (II) acetate tetrahydrate (Aldrich), and cobalt (II) acetate (Aldrich) were mixed in stoichiometric amounts based on the precursor's metal content and dissolved in deionized water. While continuously stirring, the water was boiled off and the resulting material was dried for at least 16 hours at 60°C in a dry room (dew point of -35 to -40°C), and then ground into a fine powder with a mortar and pestle. Mixtures were annealed at 750°C (for Ni-rich compositions) or 850°C (for Co-rich compositions) for 4 hours and cooled gradually to room temperature, all in a flowing O_2 gas environment. These temperatures were experimentally identified to produce the highest quality layered structures with respect to phase purity and cation ordering. Post-annealed materials were quickly transferred into the dry room, where they were ground well with a mortar and pestle, and then annealed a second time, using conditions identical to the first, before being ground again. To protect the phase purity and surface structure of these layered oxide materials, which has been shown to degrade upon exposure to ambient air, all materials were kept in a dryroom (dew point of -35 to -40°C) or Ar-filled glove box (< 0.1 ppm of H_2O and O_2).²⁴⁴

Free standing electrodes were cast in the dry room using the Bellcore method.¹⁹⁴ Casting slurries were a mixture of the active material, poly(vinylidene fluoride-co-hexafluoropropylene) (PVDF-HFP, Kynar 2801, Elf Atochem), carbon black (Super P (SP), MMM), propylene carbonate ($\geq 99.7\%$, Aldrich), and acetone ($\geq 99.9\%$, Aldrich). Homogenous slurries were cast, allowed to air dry, and then the propylene carbonate plasticizer was extracted by soaking the electrode in 99.8% anhydrous diethyl ether (Aldrich). All electrodes had a composition of 79.87 wt% active material, 7.03 wt% SP, and 13.10 wt% PVDF-HFP. Free standing electrodes were subsequently dried at 120°C under vacuum for a minimum of 10 hours, and stored in an Ar atmosphere glovebox to avoid atmospheric exposure.

5.3.2 Electrochemical Characterization

316 stainless steel coin cells with Al clad positive electrodes (2032, Hohsen) were assembled in an Ar-filled glovebox (< 0.1 ppm of H_2O and O_2) using a Li metal (FMC) negative electrode and Whatman GF/D glass fiber separators saturated with a 1M LiPF_6 ethylene carbonate: dimethyl carbonate (EC:DMC) (1:1 volume ratio) electrolyte (BASF) (< 20 ppm H_2O). Electrochemical characterization was controlled by a VMP3 (Biologic), Maccor, or MacPile battery cycling system in either a 24°C or 60°C incubator. All cells were made in duplicates to ensure reproducibility. Cycling cells were galvanostatically charged at room temperature at 20 mA/g (per g of active material) to V_{max} (4.5 or 4.75 V), held under potentiostatic conditions until the current was below 10 mA/g, and then discharged at 10 mA/g to 2.75 V. Differential charge cells, used to extract dQ/dV data, were charged and discharged at 5 mA/g between 4.75 – 2.75 V at room temperature, while samples to study dissolution by inductively coupled plasma – optical emission spectroscopy (ICP-OES) were charged at 25 mA/g to 4.75 V, and held at a constant potential of 4.75 V for 10 hours, all at 60°C. A potentiostatic intermittent titration technique (PITT) electrochemical profile was used for a multitude of applications. In all cases, a 10 mV step with a current cutoff of 1 mA/g was employed at room

temperature. All Li^+ diffusivity calculations were based on the methodology used by Xia et al, where the Li^+ diffusivity (D_{Li}) can be calculated from the linear portion of a single phase region in a PITT experiment using Equation 5-1.¹⁷⁰

$$\text{Equation 5-1:} \quad D_{\text{Li}} = -\frac{d \ln(I)}{dt} \frac{4L^2}{\pi^2}$$

The Li^+ diffusivity is dependent only on the change in the natural log of current (I) with time and the diffusivity length (L). Confirmation that the current response was linear at each calculated Li^+ diffusivity point was completed by plotting $\ln(I)$ and individually analyzing the results at each potential. To provide a comprehensive approximation of the Li^+ diffusivity over the entire lithiation range studied, both single and two phase reactions were considered. In the case of two phase reactions, the Li^+ diffusivity results were only taken from the data points after the non-Cottrellian region when the current response became linear. To easily associate the changes in the Li^+ diffusivity between materials to the differences in the material's chemistries and structures, L was assumed to be 100 nm for all materials. Since changes in the diffusivity length can cause shifts in the calculated Li^+ diffusivity by greater than an order of magnitude, the focus of the diffusivity calculations was on the variation in the Li^+ diffusivity as a function of material and lithiation rather than calculating the precise magnitude of the diffusivity. Reliable comparisons between all fabricated materials can be made since the synthesis procedure for all materials and the FESEM determined particle sizes were similar.

5.3.3 Physical Characterization

Field emission scanning electron microscopy (FESEM) images were obtained on a Zeiss microscope. Prior to being put under vacuum, samples were coated with approximately 20 nm of Au to prevent charging, and subsequently exposed to the ambient atmosphere for less than 1 minute. Nanometer resolution X-ray energy dispersive spectroscopy (EDS) mapping and scanning transmission electron microscopy (STEM) imaging were performed at Brookhaven

National Laboratory in a FEI Talos microscope and in a FEI Titan Themis at Michigan Technological University. Both microscopes were fitted with four super EDS Bruker detectors.

A Bruker D8 Advance diffractometer (Cu K α , $\lambda=1.5406$ Å) was used for all X-ray diffraction (XRD) characterization. XRD samples of positive electrode materials were assembled by carefully sprinkling the powder onto a glass slide with x-ray transparent grease in a manner to minimize preferential orientation. XRD scans of pristine powders for each material were conducted over a two-theta range of 15-70° 2 θ at a scan speed of 0.08° 2 θ /min. Analysis of cycled electrodes was conducted by disassembling and retrieving the sample electrode in an Ar-filled glovebox. The electrode was then washed with DMC to remove any residual electrolyte, and allowed to dry in the glovebox. To minimize atmospheric exposure, the dried samples were sealed onto glass slides using Kapton film and x-ray transparent grease, prior to leaving the glovebox. A scan speed of 2° 2 θ /min over a range of 15-70° 2 θ was employed to minimize reaction with ambient atmosphere as the sealed slides were not truly hermetic. A custom-made in-situ XRD cell with a Be window and a carbon coated Al mesh positive electrode current collector was used for all in-situ experiments.²⁵¹ The cell consisted of the same active components as the previously discussed coin cells. A Kapton film lining protected the Be window from oxidation at high potentials. During in-situ experiments, the cell was charged galvanostatically at C/50 to 4.75 V, and then held potentiostatically until full delithiation was achieved. Concurrent to charging, 1 hr (~1° 2 θ /min) XRD scans were continuously run, and the slow charging rate ensures that the change in the positive electrode lithiation during each scan will be $x \leq 0.02$ in Li_xMO₂. TOPAS software (version 5, Bruker AXS) was used for all Rietveld refinement.

A MMC 274 Nexus multi-mode calorimeter with a with high temperature coin cell module (Netzsch) was utilized to perform *operando* isothermal microcalorimetry experiments. Samples were 2032 coin cells (previously described) oriented with the positive electrode flush against the sample heat flux sensor. To eliminate the thermal contribution from heat sources other

than the electrodes, a reference cell consisting of all stainless steel cell parts, separator and the electrolyte was used. The reference cell was placed on the reference heat sensor, which is located directly opposite the sample sensor. The measured heat flux is the difference in the heat flux between the sample and reference sensors. A chamber temperature of 30°C was used for all isothermal microcalorimetry experiments and cells were cycled at a constant current (25 mA/g) between 4.75 V and 2.75 V. By using a low current for cycling the influence of the irreversible heat and the heat from Li concentration gradients should be minimal. Furthermore, the impact of the cell's heat capacity is negligible because the microcalorimeter is operated under isothermal conditions. Due to the absence of a prolonged time at very high potentials, little heat contribution is expected from parasitic electrode-electrolyte reactions. Thus, the entropic changes to the positive electrode material during cycling should be the main factor dictating the measured heat flux.

To characterize transition metal dissolution, ICP-OES analysis was completed by Galbraith Laboratories, Inc (Knoxville, TN). All ICP-OES coin cells were assembled identically as previously described except an additional Cu negative electrode current collector was added to prevent direct transition metal leaching from the stainless steel cell body. Cells were charged to 4.75 V at 25 mA/g, and held at 4.75 V for 10 h, while in a 60°C incubator. After charging, cells were quickly brought into the glovebox and the Li negative electrode and adjacent separator were removed, dissolved in an acidic (28 vol% HCl) solution and tested by ICP-OES. Total amounts of Co, and Ni dissolution were calculated by extrapolating the measured concentration to the entire sample volume. The percentage of dissolved Co, and Ni was determined by dividing the mass of the measured dissolution products by the initial amount of each metal present in the sample. To determine the precise stoichiometry of our in-house fabricated materials, select as-synthesized materials were also tested by ICP-OES. To account for any possible Ni or Co contamination from the stainless steel body or any of the cell's inactive components, two baseline cells which consisted of all cell components except for the positive electrode were fabricated and tested

identically to the other samples. In both of the baseline samples the amount of Ni and Co on the negative electrode was below the instrument's detection limit, signifying that the cell components have negligible contribution to the measured Ni and Co on the remaining samples.

5.4 Results

5.4.1 Overview of Materials

$\text{LiM}_{1-y}\text{Al}_y\text{O}_2$ ($\text{M} = \text{Co}, \text{Ni}$) layered oxide materials where $y = 0, 0.05, 0.1$, or 0.2 were synthesized in order to investigate the role that Al substitution has on the phase evolution and structural stability of LiCoO_2 and LiNiO_2 at high degrees of delithiation. As a result of poor transition metal mixing and increased phase segregation in the first $\text{LiNi}_{0.8}\text{Al}_{0.2}\text{O}_2$ material, a second sample with identical stoichiometry and good Ni/Al mixing was developed. The disordered $\text{LiNi}_{0.8}\text{Al}_{0.2}\text{O}_2$ material is denoted as $\text{LiNi}_{0.8}\text{Al}_{0.2}\text{O}_2$ (DO), while the well-ordered material is referred to as $\text{LiNi}_{0.8}\text{Al}_{0.2}\text{O}_2$ (O). Results from both $\text{LiNi}_{0.8}\text{Al}_{0.2}\text{O}_2$ materials are presented as their contrast highlights the impact of chemical homogeneity on the structural development and electrochemical performance of these materials. In addition to the Al-substituted LiCoO_2 and LiNiO_2 materials, $\text{LiNi}_{0.8}\text{Co}_{0.2}\text{O}_2$ and $\text{LiNi}_{0.8}\text{Co}_{0.15}\text{Al}_{0.05}\text{O}_2$ were also fabricated. To benchmark the quality of the materials synthesized in-house and also to demonstrate a contrasting particle size, commercially produced LiCoO_2 (cLCO) and $\text{LiNi}_{0.8}\text{Co}_{0.15}\text{Al}_{0.05}\text{O}_2$ (cNCA) were tested alongside the rest of the materials. Figure 5-1 compares representative FESEM images of cNCA and $\text{LiNi}_{0.85}\text{Co}_{0.15}\text{Al}_{0.05}\text{O}_2$ and shows that while both materials have similar particle shapes and form agglomerates, the synthesized $\text{LiNi}_{0.85}\text{Co}_{0.15}\text{Al}_{0.05}\text{O}_2$ has a much smaller average particle size relative to cNCA.

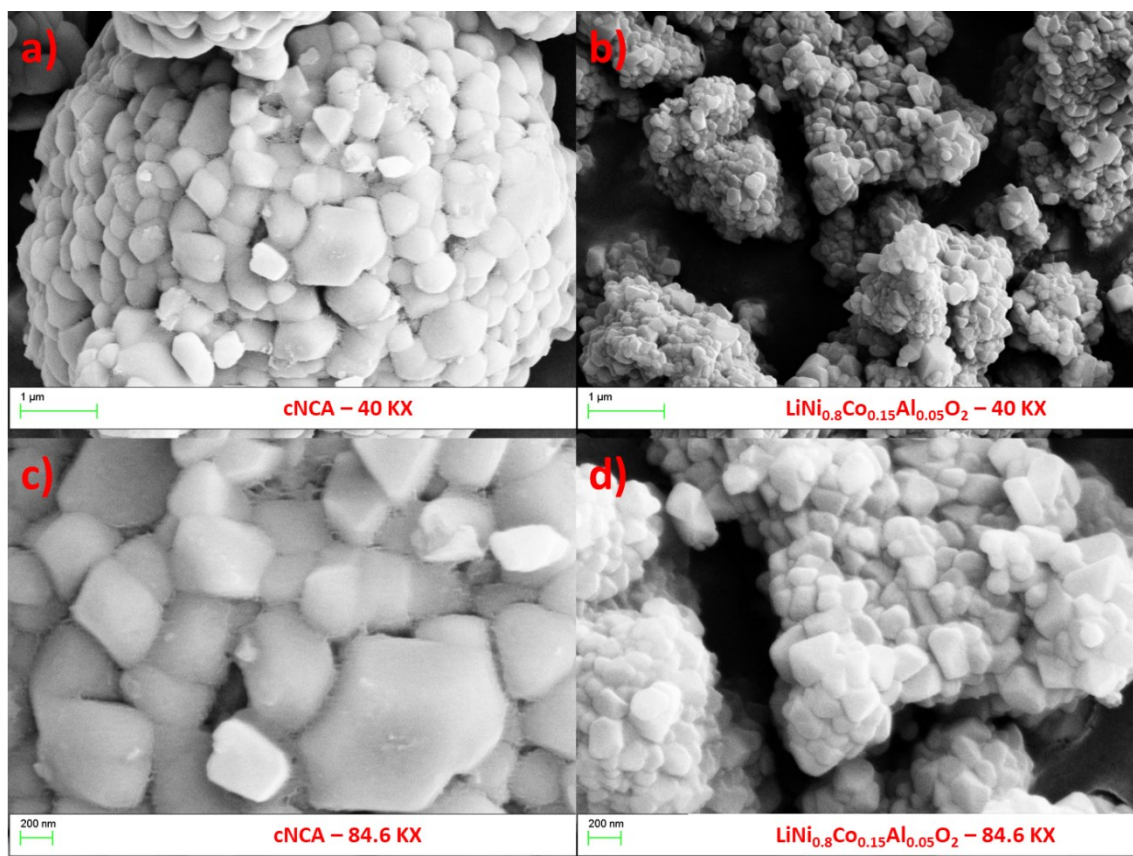


Figure 5-1: Representative FESEM images of cNCA and $\text{LiNi}_{0.8}\text{Co}_{0.15}\text{Al}_{0.05}\text{O}_2$ particles at a magnification of (a-b) 40 KX and (c-d) 84.6 KX. Both materials were coated with a thin Au layer to prevent charging by the electron beam.

The materials were separated into three groups based off of their transition metal chemistry. Group 1, which includes cLCO, LiCoO_2 , $\text{LiCo}_{0.95}\text{Al}_{0.05}\text{O}_2$, $\text{LiCo}_{0.9}\text{Al}_{0.1}\text{O}_2$, and $\text{LiCo}_{0.8}\text{Al}_{0.2}\text{O}_2$, addresses the impact of Al substitution on LiCoO_2 . Group 2 is similar to the first group but consists of LiNiO_2 -based materials (LiNiO_2 , $\text{LiNi}_{0.95}\text{Al}_{0.05}\text{O}_2$, $\text{LiNi}_{0.9}\text{Al}_{0.1}\text{O}_2$, $\text{LiNi}_{0.8}\text{Al}_{0.2}\text{O}_2$ (O), and $\text{LiNi}_{0.8}\text{Al}_{0.2}\text{O}_2$ (DO)). The third group is comprised of LiNiO_2 and the Ni-rich materials with 20% total metal substitution which equates to the total metal substitution for Ni in the ubiquitous NCA. This includes LiNiO_2 , $\text{LiNi}_{0.8}\text{Co}_{0.2}\text{O}_2$, $\text{LiNi}_{0.8}\text{Al}_{0.2}\text{O}_2$ (O), $\text{LiNi}_{0.8}\text{Co}_{0.15}\text{Al}_{0.05}\text{O}_2$, and cNCA. This latter group allows us to address the effect of the mixed impact of Ni and Co along with Al substitution.

XRD powder scans of the positive electrode materials from groups 1-3 are shown in Figure 5-2 (a-c), respectively. All materials were well crystallized, mainly phase pure ($R\bar{3}m$), and contained good (003)/(104) peak ratios. Table 5-I presents the Rietveld calculated % phase impurity and the transition metal occupancy in the Li 3a site. Most materials were > 98% phase pure and all of them > 96%. The synthesized Co-rich materials were found to contain some Co_3O_4 (~3.0-3.41%) but no other impurity phases, signifying that the materials were partially Li deficient.¹⁹⁹ All of the Co-rich materials had very low Co in the Li 3a site, which is typical of layered oxide materials with high Co contents. Of the Ni-rich materials, only $\text{LiNi}_{0.8}\text{Al}_{0.2}\text{O}_2$ (O and DO) had any impurity phases. These two samples had ~1.3-1.98% $\gamma\text{-LiAlO}_2$, which begins to form from $\alpha\text{-LiAlO}_2$ at temperatures around 750°C .²⁵² The $\gamma\text{-LiAlO}_2$ impurity phase is a byproduct of the phase segregation that is commonly observed when high Al dopant concentrations are used in Ni-rich materials.²⁴⁹

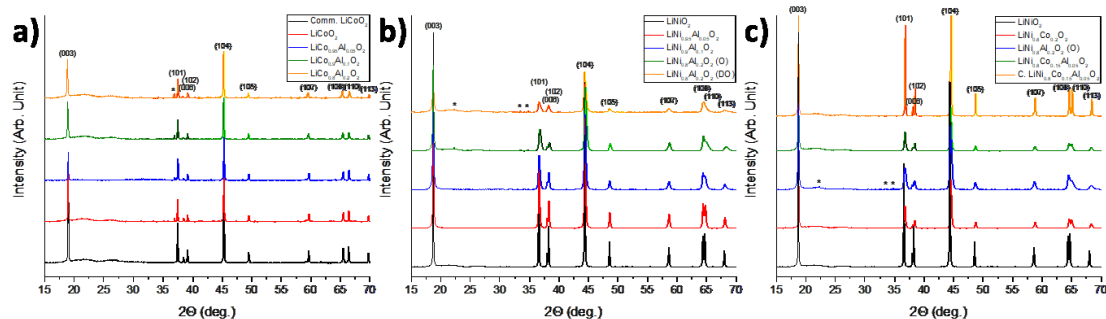


Figure 5-2: Overnight powder XRD scans of all fabricated and commercial materials are shown according to group number in (a-c), respectively. All XRD scans were measured over of a two theta range of $15\text{-}70^\circ$ at a scan rate of $0.08^\circ/\text{min}$ under ambient lab conditions. The peaks associated with the layered ($R\bar{3}m$) structure are indexed, while the peaks corresponding to the impurity phase are denoted by a *.

Table 5-I: Rietveld calculated unit cell lattice parameters, Ni/Co occupancy, volume and % phase impurity from the overnight XRD scans shown in Figure 1. For the group 1 materials (blue rows) Co_3O_4 is the impurity phase, while $\gamma\text{-LiAlO}_2$ is the impurity phase for the group 2 (red rows) and 3 (green rows) materials. For each Rietveld calculation the weighted profile residual (R_{wp}) and goodness-of-fit (GOF) are provided in the two rightmost columns.

Material	a (Å)	c (Å)	Volume (Å ³)	Ni/Co Occupancy on 3a Site	% Phase Impurity	Rwp	GOF
C. LiCoO_2	2.817	14.058	96.584	0.014	0.00	1.84	5.52
LiCoO_2	2.814	14.044	96.308	0.001	3.91	1.23	3.00
$\text{LiCo}_{0.95}\text{Al}_{0.05}\text{O}_2$	2.814	14.058	96.415	0.013	3.41	0.89	2.35
$\text{LiCo}_{0.9}\text{Al}_{0.1}\text{O}_2$	2.813	14.069	96.385	0.002	3.03	1.54	3.68
$\text{LiCo}_{0.8}\text{Al}_{0.2}\text{O}_2$	2.809	14.103	96.395	0.001	3.29	1.36	3.43
LiNiO_2	2.879	14.203	101.954	0.034	0.00	2.67	5.74
$\text{LiNi}_{0.95}\text{Al}_{0.05}\text{O}_2$	2.875	14.202	101.687	0.026	0.00	2.37	5.01
$\text{LiNi}_{0.9}\text{Al}_{0.1}\text{O}_2$	2.874	14.204	101.637	0.035	0.00	3.31	6.85
$\text{LiNi}_{0.8}\text{Al}_{0.2}\text{O}_2$ (O)	2.864	14.207	100.949	0.067	1.30	3.12	6.36
$\text{LiNi}_{0.8}\text{Al}_{0.2}\text{O}_2$ (DO)	2.873	14.200	101.489	0.089	1.98	3.18	5.80
LiNiO_2	2.879	14.203	101.954	0.034	0.00	2.67	5.74
$\text{LiNi}_{0.8}\text{Co}_{0.2}\text{O}_2$	2.868	14.175	100.936	0.051	0.00	2.24	4.81
$\text{LiNi}_{0.8}\text{Al}_{0.2}\text{O}_2$ (new)	2.864	14.207	100.949	0.067	1.30	3.12	6.36
$\text{LiNi}_{0.8}\text{Co}_{0.15}\text{Al}_{0.05}\text{O}_2$	2.866	14.180	100.881	0.025	0.00	1.89	4.01
C. $\text{LiNi}_{0.8}\text{Co}_{0.15}\text{Al}_{0.05}\text{O}_2$	2.863	14.177	100.598	0.013	0.00	1.72	4.52

The Rietveld calculated a and c lattice parameters and unit cell volume for all materials shown in Figure 5-2 are listed in Table 5-I. With increasing y in $\text{LiCo}_{1-y}\text{Al}_y\text{O}_2$, the in plane a lattice parameter systematically decreases consistent with Vegard's rule for the substitution of the smaller Al^{3+} for Co^{3+} , while the interlayer c parameter increases (Figure 5-3 (a)). Excluding $\text{LiNi}_{0.8}\text{Al}_{0.2}\text{O}_2$ (DO), which had poor transition metal mixing, these trends also hold true for the $\text{LiNi}_{1-y}\text{Al}_y\text{O}_2$ samples (Figure 5-3 (b)). The observed impact of Al substitution on the lattice parameters of the cobaltates and nickelates are well supported by the literature.^{134,142,243,246,249,253} The effect of Al-substitution on LiCoO_2 and LiNiO_2 is mainly associated with the difference in bond ionicity between Al-O and either Co-O or Ni-O.^{142,243,249} The smaller and more ionic Al^{3+} ions create shorter Al-O bonds, which contract the unit cell along the a axis, but enable an

expansion of the c axis by elongating the LiO_6 octahedra.^{142,249} The growth of the LiO_6 octahedra has been attributed to the Al dopants reducing the electron density around the oxygen atoms, causing an increase in the Li-O bond length.²⁵⁰ From comparison of the unit cell parameters for LiNiO_2 , $\text{LiNi}_{0.8}\text{Al}_{0.2}\text{O}_2$ (O), $\text{LiNi}_{0.8}\text{Co}_{0.2}\text{O}_2$, and $\text{LiNi}_{0.8}\text{Co}_{0.15}\text{Al}_{0.05}\text{O}_2$ it was observed that 20% Al substitution contracts the a parameter and elongates the c axis more than 20% Co substitution. Intuitively, the $\text{LiNi}_{0.8}\text{Co}_{0.15}\text{Al}_{0.05}\text{O}_2$ material which has both Co and Al substitution has unit cell parameters between $\text{LiNi}_{0.8}\text{Al}_{0.2}\text{O}_2$ (O) and $\text{LiNi}_{0.8}\text{Co}_{0.2}\text{O}_2$. These observations are expected because while both Co^{3+} ($r_f(\text{Co}^{3+}) = 0.525 \text{ \AA}$) and Al^{3+} ($r_f(\text{Al}^{3+}) = 0.53 \text{ \AA}$) have smaller effective ionic radii than Ni^{3+} ($r_f(\text{Ni}^{3+}) = 0.56 \text{ \AA}$) and will thus contract the transition metal octahedra, only Al^{3+} is significantly more ionic than Ni^{3+} .^{132,249}

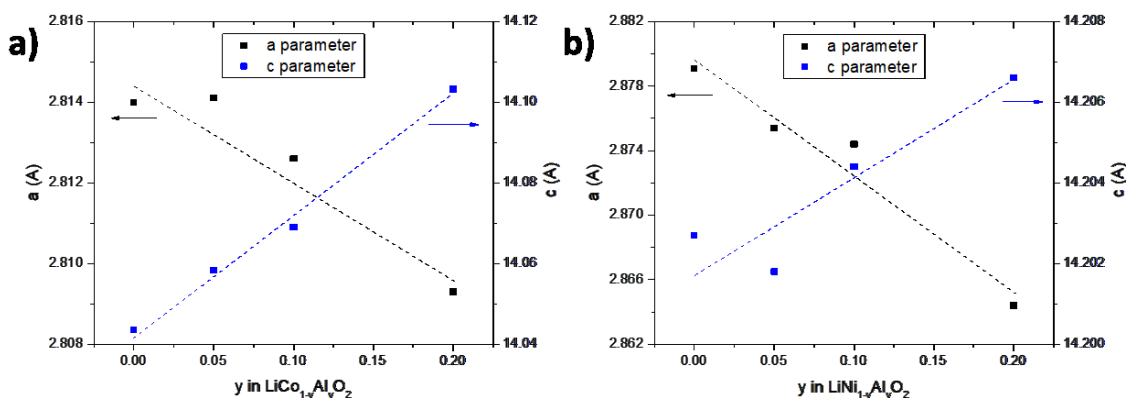


Figure 5-3: Reitveld calculated a (black) and c (blue) lattice parameters for the (a) the synthesized $\text{LiCo}_{1-y}\text{Al}_y\text{O}_2$ and (b) the $\text{LiNi}_{1-y}\text{Al}_y\text{O}_2$ materials from the XRD scans shown in Figure 1. $\text{LiNi}_{0.8}\text{Al}_{0.2}\text{O}_2$ (DO) is excluded because the disordered structure gave distorted lattice parameters. All lattice parameters were calculated based on an $R\bar{3}m$ unit cell.

While Ni-rich layered oxide materials are prone to having divalent Ni ions on the 3a site, the materials fabricated in-house had relatively low Ni concentrations on the 3a site. The Ni occupancy on the 3a site in $\text{LiNi}_{0.8}\text{Co}_{0.15}\text{Al}_{0.05}\text{O}_2$ (0.025) was similar to cNCA (0.013). In addition, LiNiO_2 , which typically has much more Ni/Li mixing, only had a Ni occupancy of 0.034 at the 3a site. However, both highly substituted $\text{LiNi}_{0.8}\text{Al}_{0.2}\text{O}_2$ materials had significantly

more Ni in the Li layer, and a clear trend was observed where Al-substitution above 5% in LiNiO_2 increased the amount of Ni in the 3a site. The slightly smaller c axis and reduced Ni occupation in the 3a site for $\text{LiNi}_{0.95}\text{Al}_{0.05}\text{O}_2$ relative to LiNiO_2 is supported by a steric driven process and previous findings by *Zhong* and *Sacken*.¹³⁴ Like the results presented here, their study documents the beneficial effects that some Al-substitution has on LiNiO_2 , while too much causes an increase in the transition metal-lithium mixing.¹³⁴

5.4.2 Group 1: $\text{LiCo}_{1-y}\text{Al}_y\text{O}_2$

5.4.2.1 Electrochemical Characterization: $\text{Li}_x\text{Co}_{1-y}\text{Al}_y\text{O}_2$

Coin cells consisting of $\text{LiCo}_{1-y}\text{Al}_y\text{O}_2$ positive electrodes vs. Li metal negative electrodes were slowly cycled between 4.75 V and 2.75 V at 5 mA/g (g of active material) at 24°C. The resulting voltage and differential charge (dQ/dV) profiles for the group 1 materials are shown in Figure 5-4 (a). Duplicate cells were cycled using a PITT profile with 10 mV steps and a 1 mA/g current cutoff in the same potential window. The first cycle of the voltage and current plots from these cells are shown in Figure 5-4 (b) and the calculated Li^+ diffusivities from the PITT data are presented in Figure 5-4 (c). The voltage and differential charge plots for the unsubstituted cLCO and LiCoO_2 , shown in panels 1 and 2 of Figure 5-4 (a), initially have a very flat voltage at ~3.92 V between lithiation values of 0.99 and 0.74 consistent with a two phase reaction. This two phase reaction is confirmed by the non-Cottrellian current response in the PITT experiments and consistent with the known semiconductor to metal transition.^{18,113} During this transition both materials have slow Li^+ diffusivities, in the range of $1\text{E-}15$ to $1\text{E-}16$ cm^2/s .

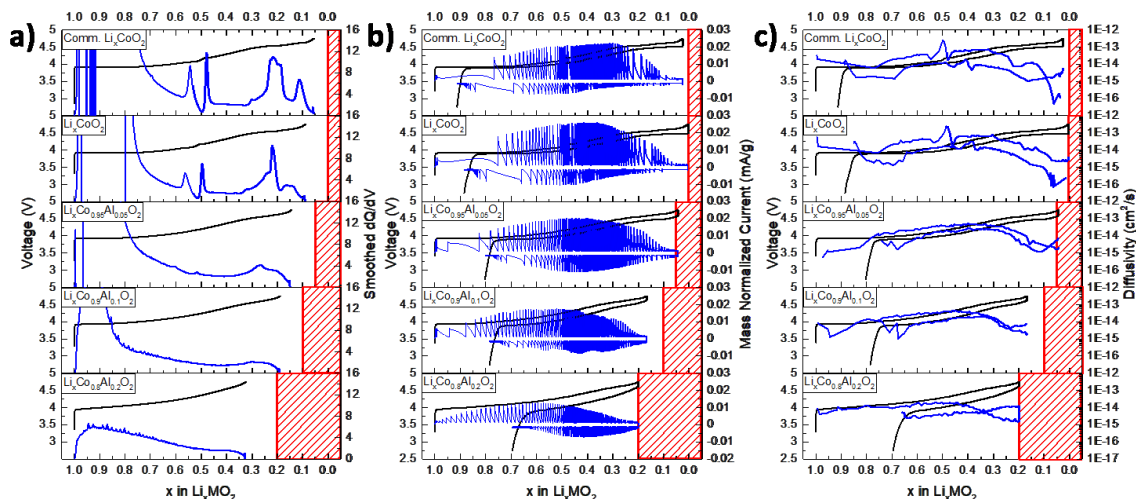


Figure 5-4: The (a) voltage (black) and differential charge (blue) profiles from the first charge of coin cells that were cycled at a constant current of 5 mA/g between 4.75 – 2.75 V are shown for all group 1 materials. Duplicate cells were cycled under PITT conditions (10 mV steps, 1 mA/g current cutoff) and the resulting first cycle (b) voltage (black) and current (blue) profiles, and (c) the voltage (black) and diffusivity (blue) plots of each material are also presented. The red boxes in the three graphs denote the theoretically inaccessible lithiation regions based on the amount of transition metals that can be electrochemically oxidized in each material.

As these materials continue to delithiate, the two phase reaction becomes single phase which is concurrent with an increase of the voltage and Li^+ diffusivity. At $0.55 \leq x \leq 0.45$, two peaks and a trough were observed in the differential charge profiles which originate from the hexagonal to monoclinic to hexagonal phase Li^+ ordering transitions.^{110,197} Similar to the previous two phase reaction, longer potentiostatic steps were observed during these phase transitions, and an order of magnitude increase in the Li^+ diffusivity is measured. The next feature, a small peak in the dQ/dV plot, was measured at $\sim x = 0.3$ (~ 4.465 V) and followed by a much larger peak centered at $\sim x = 0.2$ (~ 4.540 V). These signatures arise from the monoclinic/hexagonal distortions that are known to occur at $0.21 \leq x \leq 0.18$.¹⁷ A final peak, at $x < 0.2$ associated with the H1-3 staging transitions, was observed in both cLCO and LiCoO_2 . For the commercial material, this peak is sharper and positioned at $x = 0.11$ (4.616 V), while the in-house fabricated LiCoO_2 had a broader peak centered at $x = 0.15$ (4.610 V).

The substitution of even 5% Al for Co in LiCoO_2 has enormous ramifications on the material's structural changes during charging and discharging. While the initial two phase transition is still present, albeit with lower intensity, the addition of either 5% or 10% Al has nearly eliminated the differential charge peaks associated with the hexagonal to monoclinic to hexagonal ordering transitions. Furthermore, at higher states of charge, $\text{LiCo}_{0.95}\text{Al}_{0.05}\text{O}_2$ and $\text{LiCo}_{0.9}\text{Al}_{0.1}\text{O}_2$ had much broader and less intense differential charge peaks than LiCoO_2 , with $\text{LiCo}_{0.9}\text{Al}_{0.1}\text{O}_2$ being almost featureless. When 20% of the Co atoms are replaced with Al, all structural transitions become single phase reactions over the entire lithiation range. This is supported by the lack of clear peaks in the dQ/dV profiles and the typical Cottrellian response at each potential step for $\text{LiCo}_{0.8}\text{Al}_{0.2}\text{O}_2$. The two phase reaction observed in Li_xCoO_2 at approximately $0.95 > x > 0.74$ was concurrent with the semiconductor to metal transformation which was induced by the systematic shrinkage of the MO_2 a lattice parameter with Co^{4+} formation that eventually causes overlap of the transition metal orbitals. The smaller a lattice parameter from the substitution of Al^{3+} for Co^{3+} may induce transition metal orbital overlap and metallic behavior much sooner thereby resulting in the elimination of the two phase behavior during delithiation. Indeed the a lattice parameter of 2.809 Å for the $\text{LiCo}_{0.8}\text{Al}_{0.2}\text{O}_2$ was consistent with the approximately 2.81 Å lattice parameter of the metallic phase. The addition of Al also has a profound impact on the Li^+ diffusivity. As more Al was substituted into the structure, the Li^+ diffusivity becomes less dependent on the material's state of lithiation, and was more consistently in the $1\text{E-}14$ to $1\text{E-}15$ cm^2/s range. This is in sharp contrast to LiCoO_2 , whose Li^+ diffusivity systematically rose from $1\text{E-}16$ to $1\text{E-}13$ cm^2/s during charging to 4.15 V, and then decreased back to around $1\text{E-}16$ cm^2/s as it was further delithiated.

The voltage, current, and diffusivity profiles from the PITT experiments show that the structural transitions that occurred during delithiation are highly reversible upon subsequent discharge despite the near full delithiation state at 4.75 V. Little hysteresis was observed in the

PITT voltage profiles, and the difference in diffusivity between charge and discharge at each lithiation value is usually less than an order of magnitude. While some irreversible capacity is expected during the first cycle, especially when charging to near full delithiation at 4.75 V, the amount of irreversible capacity was small. The irreversible capacity was observed to increase significantly and systematically with Al content, especially when 20% Al was substituted for Co. Since there was little change in the average Li^+ diffusivity between materials, the increase in irreversible capacity with Al substitution is likely dependent on other factors which will be discussed later.

5.4.2.2 Structural Characterization: $\text{Li}_x\text{Co}_{1-y}\text{Al}_y\text{O}_2$

In-Situ XRD was utilized to provide structural data to complement the high resolution electrochemical data presented in the previous section. Figure 5-5 shows the *in-situ* XRD development of the (003) peak (in $R\bar{3}m$) as a function of lithiation, for each group 1 material. The (003) peak is influenced entirely by the interlayer spacing and is indicative of the evolution of the c lattice parameter. To the left of each *in-situ* XRD contour plot are the voltage and lithiation profiles. A red dashed line which corresponds to when 4.75 V was reached and a constant voltage segment commences is superimposed on each sub-figure to enable easy comparison between materials.

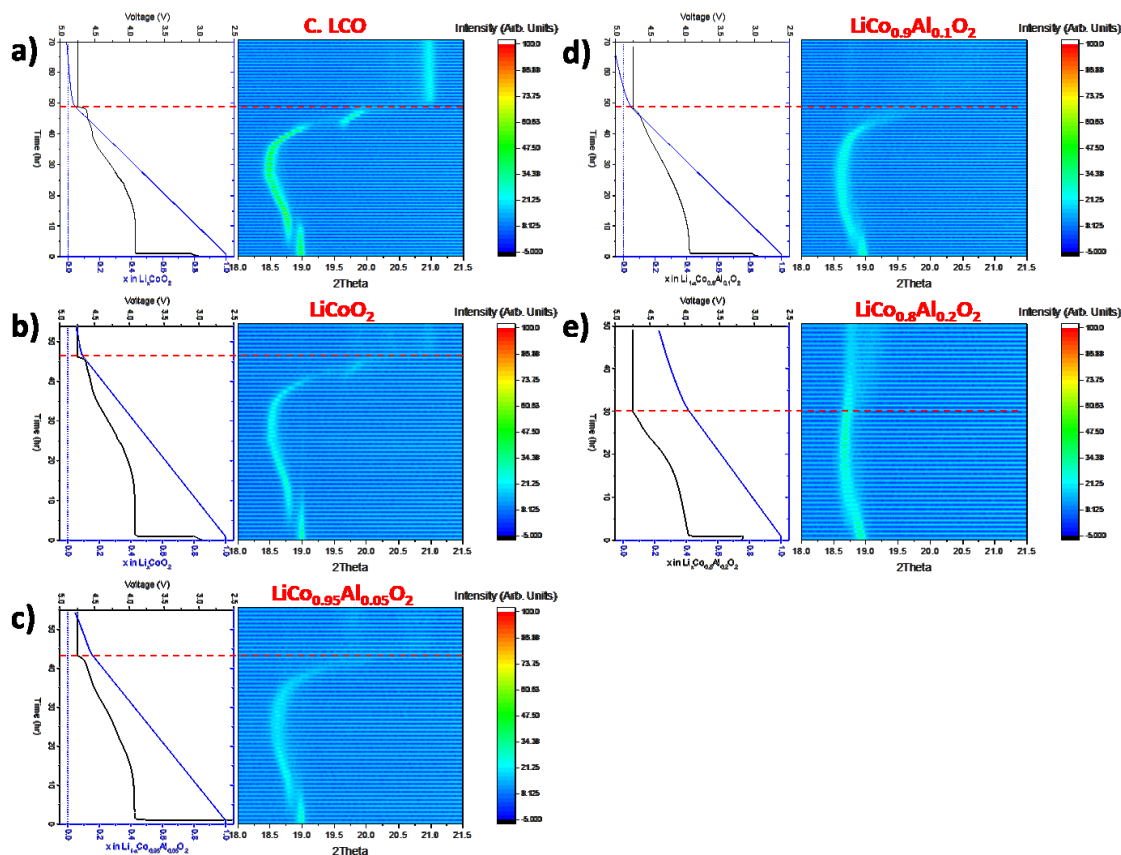


Figure 5-5: In-situ XRD contour plots of the (003) peak and corresponding electrochemical profiles for (a) cLCO, (b) LiCoO_2 , (c) $\text{LiCo}_{0.95}\text{Al}_{0.05}\text{O}_2$, (d) $\text{LiCo}_{0.9}\text{Al}_{0.1}\text{O}_2$, and (e) $\text{LiCo}_{0.8}\text{Al}_{0.2}\text{O}_2$. Cells were charged at a constant current of $C/50$ to 4.75 V, and then held at a constant potential indefinitely, all while 1 h XRD scans were continuously running. To avoid missing any features, the experimental parameters were chosen such that $\Delta x \leq 0.02$ for every scan. A red dashed line corresponding to when the potential reached 4.75 V is superimposed on each sub-figure to enable easy comparison between materials.

Comparison of cLCO (Figure 5-5 (a)) and LiCoO_2 (Figure 5-5 (b)) revealed nearly identical changes to the (003) peak during charging, consistent with previously published data and the high resolution electrochemistry discussed in the previous section. A two phase region clearly started at $\sim x = 0.95$ and continued until $\sim x = 0.74$, followed by a single phase reaction which persisted until the phase transformation to and from the monoclinic structure. The calculated c and a lattice parameters from the *in-situ* XRD experiment for each group 1 material, are shown in Figure 5-6 (a) and (b), respectively. To make visual analysis of the results easier, all lattice parameters were determined using an $R\bar{3}m$ structure, even though the presence of the

monoclinic phase was confirmed. The calculated lattice parameters confirmed the existence of the initial two phase region, and quantified the changes to the unit cell as a result of the hexagonal to monoclinic to hexagonal transformations. During charging to $\sim x = 0.45$ the (003) peak systematically moved toward lower angles, indicative of an expanding c axis. When delithiated beyond $\sim x = 0.45$ the c axis contracts, and at $x \leq 0.3$, the rate of contraction in the c axis increases rapidly. At very high states of charge ($x \leq 0.2$) a sudden shift of the (003) peak towards higher angles was observed. The stepwise shift in the (003) peak was attributed to staging reactions, where some of the Li layers of the $R\bar{3}m$ structure were completely emptied. Based on the peak positions at the end of charging, both cLCO and LiCoO_2 were fully delithiated and converted to the O1 phase (AB stacking). In agreement with previously reported results, during delithiation the a lattice parameter (Figure 5-6 (b)) of cLCO and Li_xCoO_2 contracts until $x \sim 0.5$ and then systematically expands.^{17,18,254} When highly delithiated but prior to the staging phase transitions, the a parameter for cLCO and LiCoO_2 was roughly the same as when the electrode was in the initial fully lithiated state. The structural changes observed by *in-situ* XRD results on cLCO and LiCoO_2 are in excellent agreement with our differential charge and PITT cells shown in Figure 5-4, as well as with previously published studies.^{17,18,254}

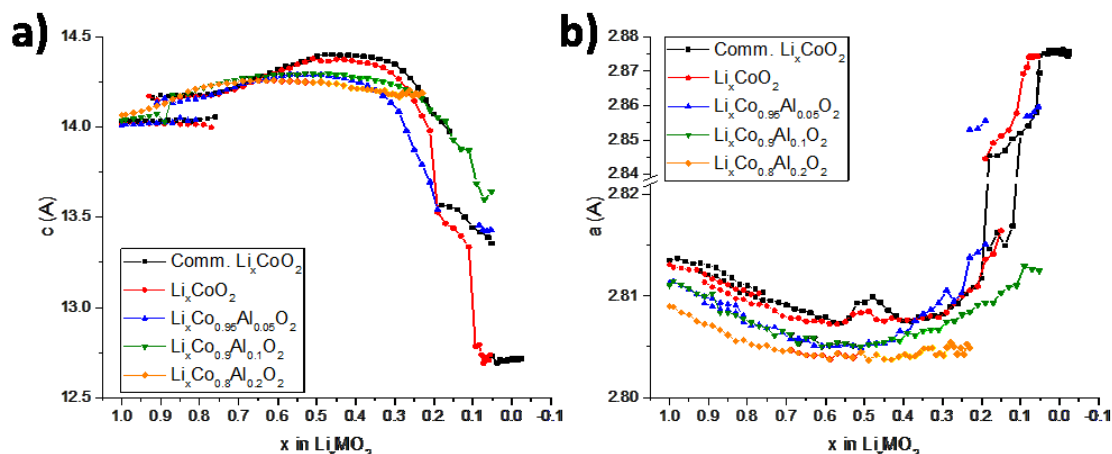


Figure 5-6: Calculated (a) c and (b) a lattice parameters as a function of delithiation for the *in-situ* XRD experiments of cLCO (black), LiCoO_2 (red), $\text{LiCo}_{0.95}\text{Al}_{0.05}\text{O}_2$ (blue), $\text{LiCo}_{0.9}\text{Al}_{0.1}\text{O}_2$ (green), and $\text{LiCo}_{0.8}\text{Al}_{0.2}\text{O}_2$ (orange) positive electrodes. Lattice parameters were calculated from a rhombohedral unit cell using the peak locations of the (003) and (101) peaks. Note that a break was included in the y-axis of (b).

Similar to the differential charge and PITT results, *in-situ* XRD shows that when Al was substituted into LiCoO_2 , the structural transitions throughout delithiation were significantly reduced. While the initial two phase transition was still present when 5% or 10% Al was substituted into LiCoO_2 , the two phases were less distinguishable in $\text{LiCo}_{0.95}\text{Al}_{0.05}\text{O}_2$ than in LiCoO_2 . When 20% Al was substituted into LiCoO_2 the initial delithiation reaction appeared to be single phase. The % change of the c and a lattice parameters for the group 1 materials, shown in Figure 5-7 (a, d), clearly demonstrates that as Al was added to the positive electrode material the lattice parameters changed less during delithiation and were especially apparent towards the end of delithiation. Even 5% Al was sufficient to prevent the stepwise shift in the (003) peak that was observed for LiCoO_2 near full delithiation. Thus, substituting 5% Al into LiCoO_2 was effective at preventing the formation of the O1 structure and in minimizing the staging reactions. The absence of these structural transitions will reduce the lattice strain when accessing such high states of charge. $\text{LiCo}_{0.9}\text{Al}_{0.1}\text{O}_2$ is a particularly important sample, since it showed that Al substitution can prevent the staging transitions even though the material was sufficiently delithiated. Comparison of the c lattice parameters (Figure 5-6 (a)) for $\text{LiCo}_{0.9}\text{Al}_{0.1}\text{O}_2$ and LiCoO_2 shows that 10% Al

substitution completely averted the staging reactions even though the materials were at similar states of delithiation. $\text{LiCo}_{0.8}\text{Al}_{0.2}\text{O}_2$ presents the clearest example of how significant Al substitution can be in suppressing the structural changes during delithiation. Because of the 20% Al and Li in fully charged $\text{LiCo}_{0.8}\text{Al}_{0.2}\text{O}_2$, all phase transitions during charging were gradual and single phase, and there was relatively little change in the lattice parameters compared to LiCoO_2 .

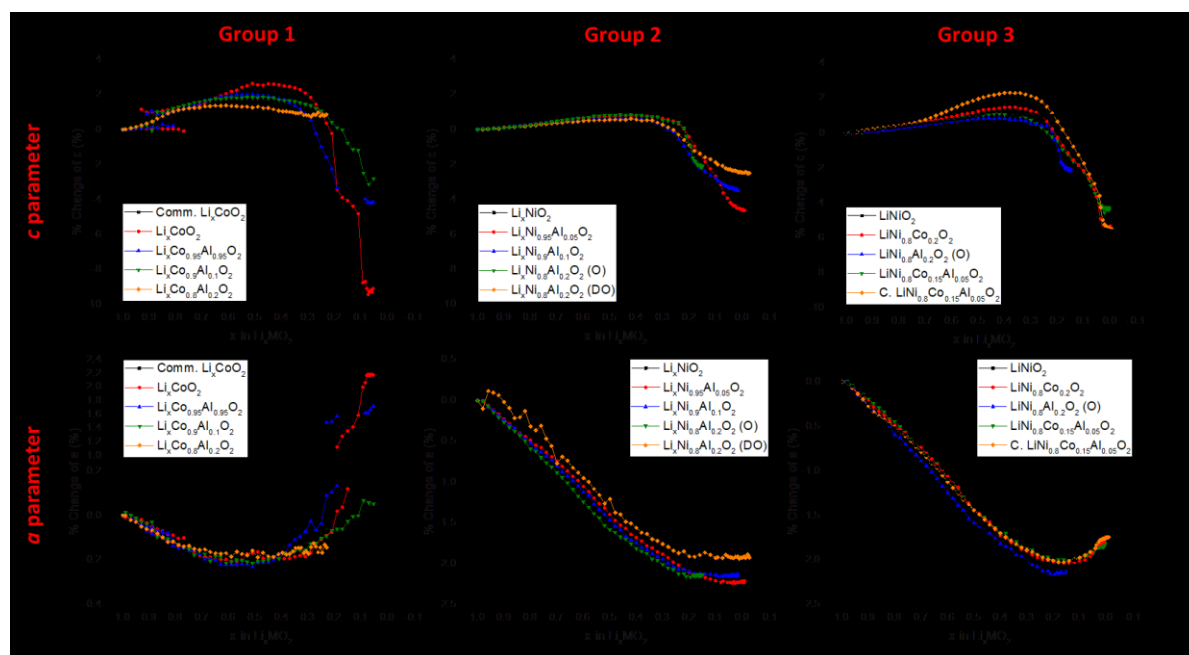


Figure 5-7: The % change of the c and a lattice parameters relative to the unit cell parameters of the material in OCV was calculated as a function of lithiation. The calculations are based on the c and a lattice parameters derived from the in-situ XRD experiments. (a-c) Shows the % change of the c parameter for the group 1-3 materials, while the % change of the a parameter are presented in (d-f).

Additional PITT cells, identical to those previously reported, were charged to 4.75 V and then disassembled in an Ar-filled glovebox. *Ex-situ* XRD samples were prepared from the positive electrodes retrieved from these cells, and are advantageous because they have much better signal to noise ratios than the *in-situ* experiments due to the absence of the Be window. Figure 5-8 shows the XRD results in the (003) (18-21.5°) and (104) (42-47°) peak regions for all group 1 materials charged to 4.75 V under PITT conditions, and the corresponding voltage profiles are presented in Figure 5-9 (a). From the peak locations in Figure 5-8, it is evident that

both cLCO and LiCoO_2 transformed to the O1 structure, and are in agreement with the *in-situ* XRD results. The *ex-situ* XRD patterns of the Al-substituted LiCoO_2 electrodes also support the *in-situ* experiments. Even 5% Al substitution was sufficient to prevent the O1 structure, and the final (003) peak position moved to lower angles (higher d-spacing) as more Al was substituted into the structure. Clearly, the Al concentration had a profound impact on the peak positions of the fully charged electrodes. Adding Al to LiCoO_2 proportionally reduced the maximum degree of delithiation (Figure 5-9), thus limiting the phase transitions that occur at the higher states of charge.

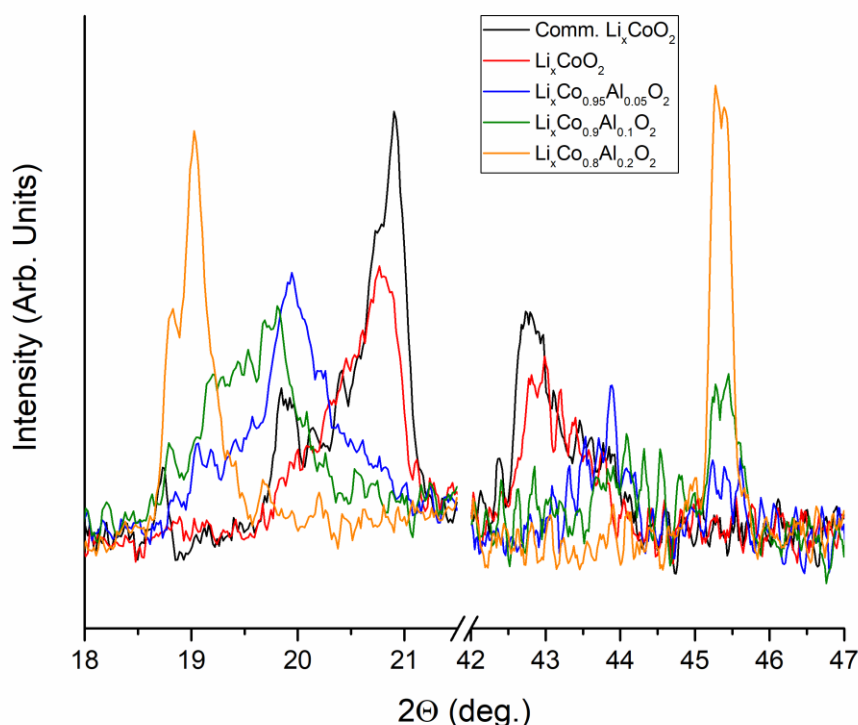


Figure 5-8: *Ex-situ* XRD scans of positive electrodes that were charged to 4.75 V under PITT conditions (10 mV step, 1 mA/g cutoff). Results are presented in the regions of the (003) (18–21.5°) and (104) (42–47°) peaks for cLCO (black), LiCoO_2 (red), $\text{LiCo}_{0.95}\text{Al}_{0.05}\text{O}_2$ (blue), $\text{LiCo}_{0.9}\text{Al}_{0.1}\text{O}_2$ (green), and $\text{LiCo}_{0.8}\text{Al}_{0.2}\text{O}_2$ (orange). All coin cells were disassembled in an Ar-filled glovebox and the XRD samples were sealed with a Kapton film to temporarily prevent hydrogen intercalation upon exposure to ambient atmosphere.

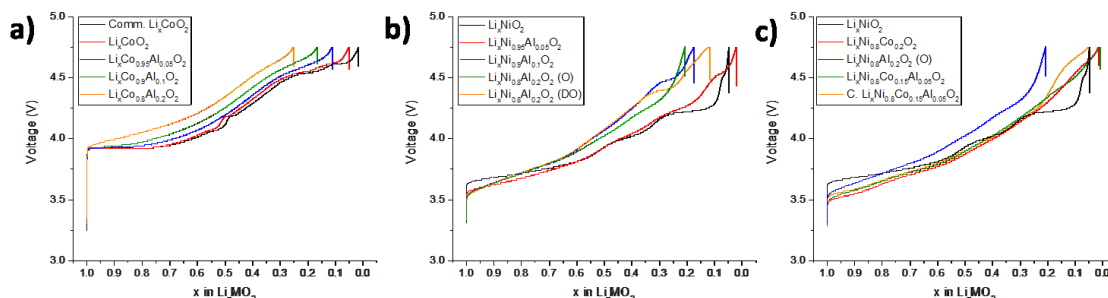


Figure 5-9: Voltage vs. lithiation profiles for coin cells made with each positive electrode material. Cells were charged under PITT conditions (10 mV step, 1 mA/g current cutoff) in a 24°C incubator. The charging profiles for group 1, 2, and 3 electrode materials are shown in (a), (b), and (c).

Table 5-II provides the open circuit voltage (OCV) after a 1 h rest, the final lithiation, and the percent of the Ni and Co (% Ni/Co) that were oxidized during charging of the 4.75 V *ex-situ* XRD cells for each positive electrode material. The OCV taken 1 h after charging gives insight into how the transition metal chemistry affects the quasi equilibrium voltage of each material. Increasing Al substitution is expected to systematically lower the maximum degree of delithiation due to the decrease of the amount of Co available for oxidation: however, it is important to note that Co is still fully oxidized. The % Co that was oxidized during charging to 4.75 V is a useful measure of the state of charge that the material was in. The % Co oxidation for the Al-substituted group 1 materials was similar to but slightly lower than LiCoO₂. Despite this, all of the Al-substituted samples showed a very significant increase in the OCV after relaxation, relative to LiCoO₂. This can be attributed to the reduced potential associated with reintercalation of Li into O1 (vs. O3)-type electrodes, and provides further evidence that the O1 structure did not form in any of the Al-substituted materials.¹⁷

Table 5-II: The OCV taken 1 h after charging finished, the final lithiation in the positive electrode and the % Ni/Co oxidation for each of the ex-situ XRD coin cells (Figure 5-9) are listed. The group 1 materials are shown in the blue rows, while the group 2 and 3 materials are shown in the red and green rows, respectively. The % Ni/Co oxidation was calculated from the measured charging capacity and the theoretical capacity assuming that Al is electrochemically inactive.

Material	OCV (V) After 1 h	Final Lithiation	% Ni/Co Oxidation
Comm. LiCoO ₂	4.592	0.016	98.368
LiCoO ₂	4.579	0.051	94.888
LiCo _{0.95} Al _{0.05} O ₂	4.648	0.111	93.553
LiCo _{0.9} Al _{0.1} O ₂	4.682	0.167	92.554
LiCo _{0.8} Al _{0.2} O ₂	4.654	0.252	93.481
LiNiO ₂	4.466	0.047	95.305
LiNi _{0.95} Al _{0.05} O ₂	4.501	0.020	103.120
LiNi _{0.9} Al _{0.1} O ₂	4.535	0.175	91.694
LiNi _{0.8} Al _{0.2} O ₂ (O)	4.613	0.207	99.114
LiNi _{0.8} Al _{0.2} O ₂ (DO)	4.588	0.116	110.538
LiNiO ₂	4.466	0.047	95.305
LiNi _{0.8} Co _{0.2} O ₂	4.646	0.015	98.455
LiNi _{0.8} Al _{0.2} O ₂ (O)	4.613	0.207	99.114
LiNi _{0.8} Co _{0.15} Al _{0.05} O ₂	4.637	0.009	104.317
C. LiNi _{0.8} Co _{0.15} Al _{0.05} O ₂	4.725	0.057	99.287

Operando isothermal microcalorimetry experiments enabled the measurement of the heat flux as a function of charge. Coin cells placed in the microcalorimeter were cycled between 4.75 V and 2.75 V at a constant current of 25 mA/g at 30°C. The resulting voltage and heat flux profiles for all group 1 materials are presented in Figure 5-10. As charging began cLCO and LiCoO₂ each had a small endothermic heat flux. Two exothermic peaks found at ~4.10 and 4.28 V were from the ordering transition from and to the hexagonal structure. With further delithiation, the topotactic reaction became gradually more exothermic. The heat flux profiles for cLCO and LiCoO₂ during delithiation are consistent with previously reported results.^{173,175,185,223}

Interestingly, as Li^+ was initially reinserted back into the fully charged cLCO and LiCoO_2 materials the heat flux remained exothermic, which could be a result of the heat generated by the sluggish Li^+ diffusivity at such high states of charge. When the lithiation of cLCO and Li_xCoO_2 was between 0.25 and ~ 0.5 , the heat flux became endothermic because of the entropic changes to the host material. Based on the heat flux peaks in the range of $\sim x = 0.45\text{--}0.6$, it is evident that the hexagonal to monoclinic to hexagonal phase transitions were reversible. As expected, at lower states of charge the Li^+ insertion reaction was exothermic and of approximately the same magnitude as the endothermic deintercalation reactions at equivalent states of charge. At the end of discharge, the heat flux became very exothermic as an abundance of irreversible heat was generated by the material's slow Li^+ diffusivity and high internal resistance.

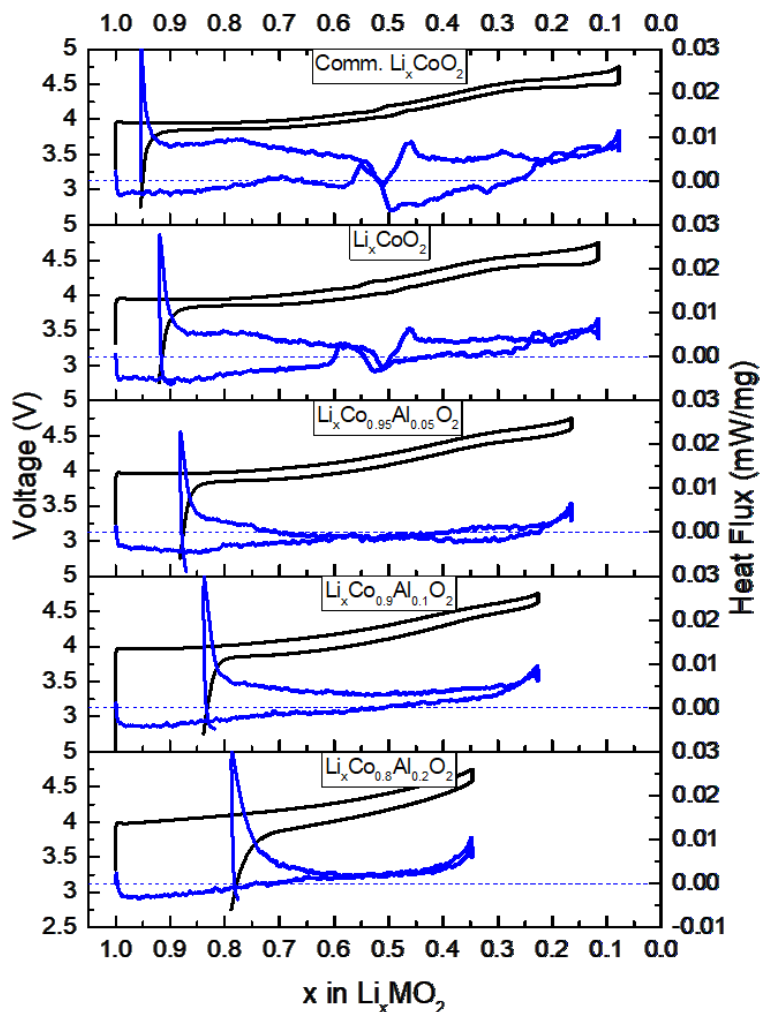


Figure 5-10: Operando isothermal microcalorimetry voltage (black) and heat flux (blue) measurements are presented during the first cycle for each group 1 material. Coin cells were cycled at a constant current (25 mA/g) between 4.75 V and 2.75 V, while the chamber was isothermal at 30°C.

Panels 3-5 of Figure 5-10 display the voltage and heat flux profiles for $\text{LiCo}_{0.95}\text{Al}_{0.05}\text{O}_2$, $\text{LiCo}_{0.9}\text{Al}_{0.1}\text{O}_2$, and $\text{LiCo}_{0.8}\text{Al}_{0.2}\text{O}_2$, respectively. Instead of showing distinct peaks related to the monoclinic phase, the heat fluxes for all Al-substituted LiCoO_2 materials gradually increased from endothermic to exothermic as the materials were delithiated. While the monoclinic phase changes that were observed in LiCoO_2 are removed, the Al-substituted materials became systematically more exothermic during charge just like LiCoO_2 . Operando microcalorimetry

confirmed the results previously shown by the differential charge, PITT, and *in-situ* XRD experiments that the substitution of even 5% Al into LiCoO_2 prevented the hexagonal to monoclinic transitions. Based on the heat fluxes during discharge, materials with higher Al concentrations were observed to be more exothermic, which was a sign that these materials have more irreversible heat generation possibly due to higher electronic resistance.

5.4.2.3 Cycling Performance: $\text{Li}_x\text{Co}_{1-y}\text{Al}_y\text{O}_2$

Of critical importance to the analysis of the structural stability of these positive electrode materials near full delithiation is the impact of the structural transitions on the materials' electrochemical performance. Coin cells made with each positive electrode material were cycled by charging at 20 mA/g to V_{max} (4.5 or 4.75 V), maintaining a constant potential until the current dropped below 10 mA/g, and then discharging at 10 mA/g to 2.75 V. The discharge capacities vs. cycle number plots for each group 1 positive electrode material are presented in Figure 5-11. When cycled with an upper cutoff potential of either 4.5 V (Figure 5-11 (a)) or 4.75 V (Figure 5-11 (b)) cLCO had a slightly higher discharge capacity than LiCoO_2 , which was likely associated to the additional electrode-electrolyte reactions that LiCoO_2 has because of its higher surface area. The increased electrode-electrolyte reactions on LiCoO_2 would also explain why the difference in discharge capacities between cLCO and LiCoO_2 increases when the cells were charged to 4.75 V, where electrolyte decomposition becomes accelerated. Table 5-III provides the first cycle charging and discharging capacity as well as the irreversible loss for each material in Figure 5-11.

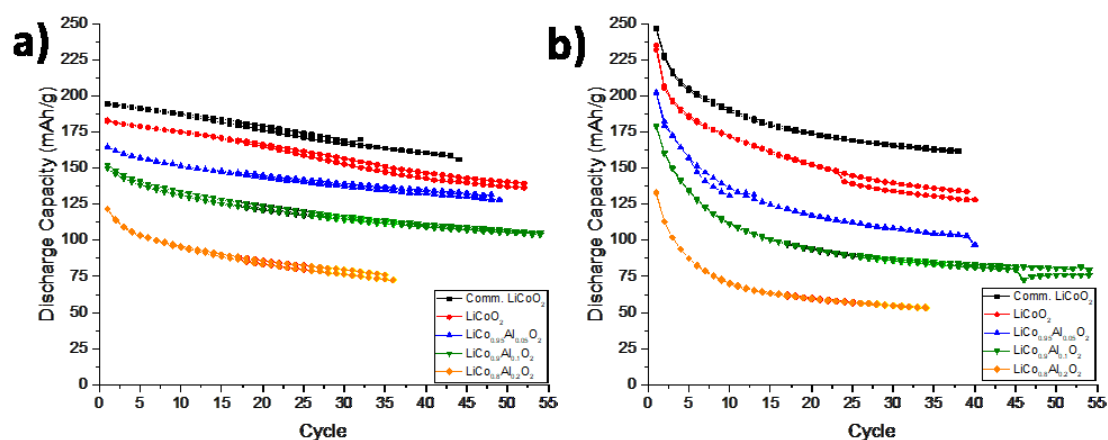


Figure 5-11: Discharge capacity vs. cycle results for coin cells charged to either (a) 4.5 V or (b) 4.75 V. Cells were charged at 20 mA/g to V_{max} (4.5 or 4.75 V), held at a constant potential until the current dropped below 10 mA/g, and were then discharged at 10 mA/g to 2.75 V, all at room temperature. Duplicate cells of each positive electrode material were made to ensure reproducibility.

Table 5-III: First cycle charge capacity, discharge capacity, and irreversible loss for each coin cell shown in Figure 5-11. The theoretical capacity (assuming Al is electrochemically active) is given for each material.

Active Material	Vmax	First Cycle Charge Capacity (mAh/g)	First Cycle Discharge Capacity (mAh/g)	Irreversible Loss (mAh/g)	Irreversible Loss (%)	Theoretical Capacity (mAh/g)
C. LiCoO ₂	4.5	199.06	194.69	4.37	2.20	273.85
C. LiCoO ₂	4.5	198.71	194.06	4.65	2.34	273.85
C. LiCoO ₂	4.75	257.01	246.38	10.63	4.14	273.85
C. LiCoO ₂	4.75	257.83	247.03	10.79	4.19	273.85
LiCoO ₂	4.5	191.81	183.43	8.38	4.37	273.85
LiCoO ₂	4.5	193.00	182.27	10.73	5.56	273.85
LiCoO ₂	4.75	252.02	235.07	16.96	6.73	273.85
LiCoO ₂	4.75	248.99	232.03	16.96	6.81	273.85
LiCo _{0.95} Al _{0.05} O ₂	4.5	187.63	164.84	22.79	12.14	278.39
LiCo _{0.95} Al _{0.05} O ₂	4.5	187.81	164.79	23.02	12.26	278.39
LiCo _{0.95} Al _{0.05} O ₂	4.75	237.31	202.12	35.19	14.83	278.39
LiCo _{0.95} Al _{0.05} O ₂	4.75	238.82	202.83	35.99	15.07	278.39
LiCo _{0.9} Al _{0.1} O ₂	4.75	179.99	149.74	30.25	16.81	283.09
LiCo _{0.9} Al _{0.1} O ₂	4.75	183.31	152.23	31.08	16.95	283.09
LiCo _{0.9} Al _{0.1} O ₂	4.5	224.52	179.60	44.92	20.01	283.09
LiCo _{0.9} Al _{0.1} O ₂	4.5	225.21	179.02	46.19	20.51	283.09
LiCo _{0.8} Al _{0.2} O ₂	4.5	168.88	121.43	47.44	28.09	292.98
LiCo _{0.8} Al _{0.2} O ₂	4.5	169.25	121.63	47.62	28.14	292.98
LiCo _{0.8} Al _{0.2} O ₂	4.75	193.52	132.42	61.10	31.57	292.98
LiCo _{0.8} Al _{0.2} O ₂	4.75	194.84	133.40	61.44	31.53	292.98

The addition of Al to LiCoO₂ was found to have a significant deleterious effect on both the charge and discharge capacity regardless of the cutoff potential. Furthermore, Table 5-III shows a clear relationship between the irreversible capacity loss in the first cycle and the amount of Al in the positive electrode material. Since all the synthesized materials have similar surface areas, the decrease in discharge capacity and increase in irreversible loss cannot be primarily attributed to surface area effects. Figure 5-12 (a-e) shows the 1st, 5th, 10th and 15th cycle voltage profiles of the cycling cells for each group 1 material. From the voltage profiles of cLCO (Figure 5-12 (a)) and LiCoO₂ (Figure 5-12 (b)) it is clear that while all of the phase transitions were completely reversible on the first cycle, they rapidly become less distinct or non-existent with

cycling. By even the 5th cycle, the signature hexagonal to monoclinic to hexagonal transformations were absent from the voltage profile. The voltage profiles were particularly useful for understanding the impedance development during cycling, which was determined by the polarization and hysteresis in the potential curves. cLCO and LiCoO₂ both had only moderate impedance growth in the first 15 cycles, and the rate of impedance growth appeared to be slowing down as cycling progressed. However, as the Al content in the electrode material increased, so did the total impedance after 15 cycles. Moreover, materials with higher Al substitution such as LiCo_{0.9}Al_{0.1}O₂ and LiCo_{0.8}Al_{0.2}O₂ continued to have rapid impedance growth even after 10 cycles. The amplified impedance growth that scales with the magnitude of the Al substitution into LiCoO₂ was largely responsible for the poor electrochemical cycling performance of the Al-substituted electrodes. Figure 5-13 (a, d) shows the % discharge capacity retention when charged to 4.5 and 4.75 V, respectively. Al substitution into LiCoO₂ had a profound negative impact on the material's capacity retention, especially when charged to 4.75 V.

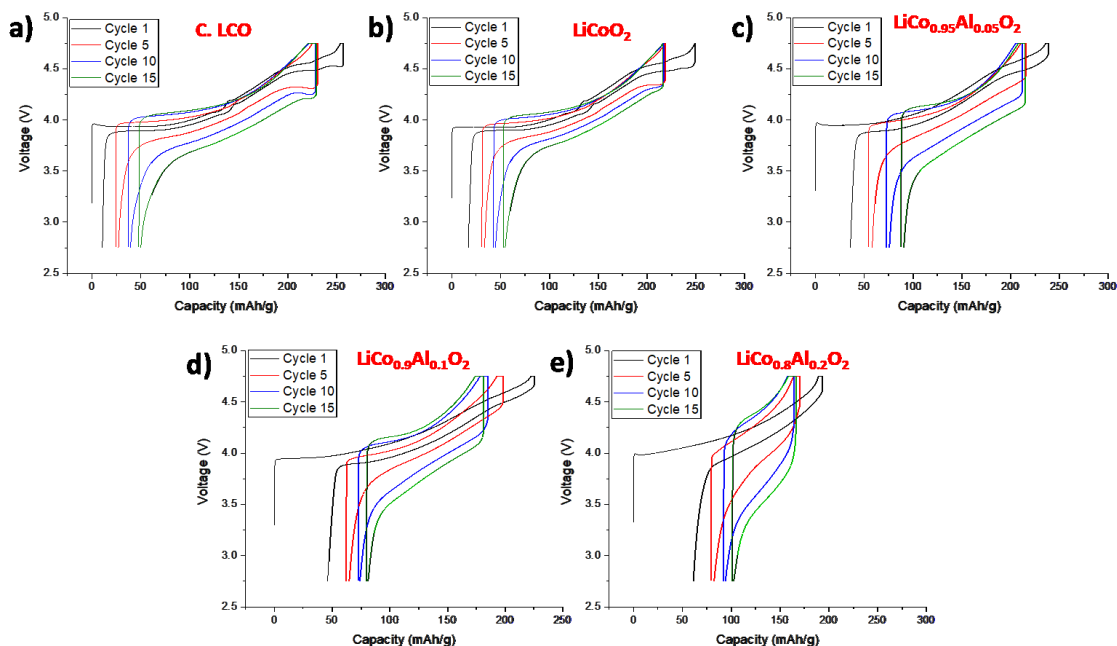


Figure 5-12: The voltage vs. capacity curves of the 1st, 5th, 10th and 15th cycles from a 4.75 V cycling cell is shown for (a) C. LCO, (b) LiCoO₂, (c) LiCo_{0.95}Al_{0.05}O₂, (d) LiCo_{0.9}Al_{0.1}O₂, and (e) LiCo_{0.8}Al_{0.2}O₂. Each cell was charged to 4.75 V at 20 mA/g, held at 4.75 V until the current went below 10 mA/g, and then was discharged at 10 mA/g to 2.75 V, all at room temperature.

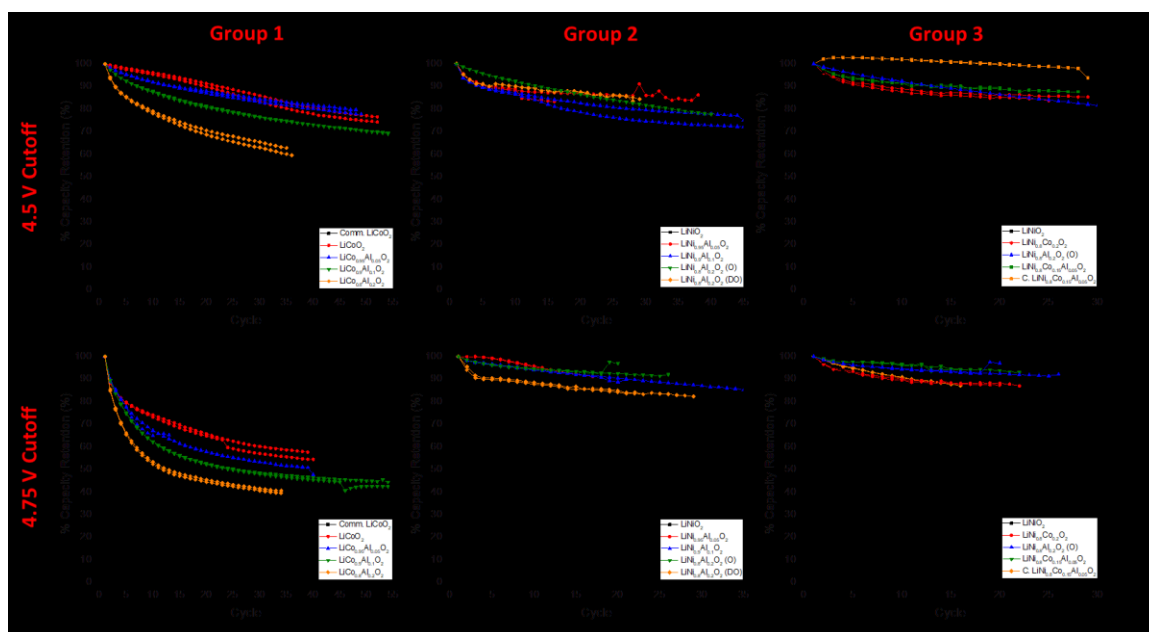


Figure 5-13: The % discharge capacity retention during cycling for cells charged to 4.5 V (a-c) and 4.75 V (d-f). The results for the (a, d) group 1, (b, e) group 2, and (c, f) group 3 materials are presented. The % capacity retention was calculated by normalizing the discharge capacity of each cycle to the cell's first cycle discharge capacity.

5.4.2.4 Dissolution: $\text{Li}_x\text{Co}_{1-y}\text{Al}_y\text{O}_2$

To investigate the impact that Al substitution had on surface chemistry stability, additional coin cells were charged to 4.75 V at 25 mA/g and held under potentiostatic conditions for 10 h at 60°C. As previously reported, at this high state of charge and elevated temperature, HF etching of the positive electrode material becomes accelerated and transition metal dissolution from the positive electrode becomes prevalent.²⁴⁴ For each positive electrode material duplicate cells were tested and the average % Ni and % Co dissolution results are presented in Table 5-IV. It is important to note that the ICP-OES measurement only determines the amount of Ni and Co dissolved from the positive electrode and then reduced on the negative electrode. It doesn't quantify any of the dissolved transition metals that were still in the electrolyte when the cell was disassembled.

Table 5-IV: Ni and Co transition metal dissolution results determined by ICP-OES. Coin cells using each positive electrode material were charged to 4.75 V at 25 mA/g, held at a constant potential (4.75 V) for 10 h, all while in a 60°C incubator. In an Ar-filled glovebox the cells were disassembled, the negative electrode and adjacent separator were removed and then dissolved in an acidic solution. The Ni and Co concentration in the resulting solution was then measured by ICP-OES, and the average % Ni and % Co dissolution from each positive electrode material is presented. The % Ni and % Co dissolution from the baseline samples was below the instrument's detection limit.

Material	Average % Ni Dissolved	Average % Co Dissolved
Comm. LiCoO ₂	-	3.83
LiCoO ₂	-	5.24
LiCo _{0.95} Al _{0.05} O ₂	-	2.80
LiCo _{0.9} Al _{0.1} O ₂	-	2.48
LiCo _{0.8} Al _{0.2} O ₂	-	1.77
LiNiO ₂	0.97	-
LiNi _{0.95} Al _{0.05} O ₂	0.82	-
LiNi _{0.9} Al _{0.1} O ₂	1.01	-
LiNi _{0.8} Al _{0.2} O ₂ (O)	0.28	-
LiNi _{0.8} Al _{0.2} O ₂ (DO)	2.08	-
LiNiO ₂	0.97	-
LiNi _{0.8} Co _{0.2} O ₂	1.75	1.86
LiNi _{0.8} Al _{0.2} O ₂ (O)	0.28	-
LiNi _{0.8} Co _{0.15} Al _{0.05} O ₂	1.78	1.77
C. LiNi _{0.8} Co _{0.15} Al _{0.05} O ₂	0.82	0.68
Co3O4	-	0.05
NiO	10.21	-
Baseline	N/A	N/A

Despite being at 4.75 V and 60°C for only 10 h, significant Co dissolution was measured for all group 1 materials. LiCoO₂ (5.24%) had substantially more of its initial Co lost than did cLCO (3.83%), because of its higher electrode-electrolyte interfacial area. 5% Al substitution for Co enabled LiCo_{0.95}Al_{0.05}O₂ (2.80%) to have a 47% reduction in Co dissolution relative to LiCoO₂ (5.24%). Additional Al substitution in LiCo_{0.9}Al_{0.1}O₂ (2.48%) and LiCo_{0.8}Al_{0.2}O₂ (1.77%) was

effective in further reducing the Co dissolution significantly. A Co_3O_4 reference material was found to have exceedingly low (0.05%) Co dissolution, indicating the impressive stability of Co in the cobalt spinel and inferior stability of the layered oxides in such an aggressive environment. This result is consistent with that reported for cobalt spinel coated LiCoO_2 .²⁵⁵ The Co dissolution was directly related to the corrosion current, which resulted from parasitic electrode-electrolyte reactions during the 4.75 V potentiostatic hold. Figure 5-14 shows the current profiles for the ICP-OES cells for all materials. The increase in current during the potentiostatic hold, which is clearly seen in the LiCoO_2 cells (Figure 5-14 (a)), was from the exothermic electrode-electrolyte reactions and transition metal dissolution that were extensively described in a previous report.⁶⁶ As a result of the lower surface area, less parasitic current was measured for cLCO relative to LiCoO_2 , which supports its lower Co dissolution measurement. In confirmation with the dissolution results, as the concentration of the Al in $\text{LiCo}_{1-y}\text{Al}_y\text{O}_2$ increased the corrosion current decreased substantially.

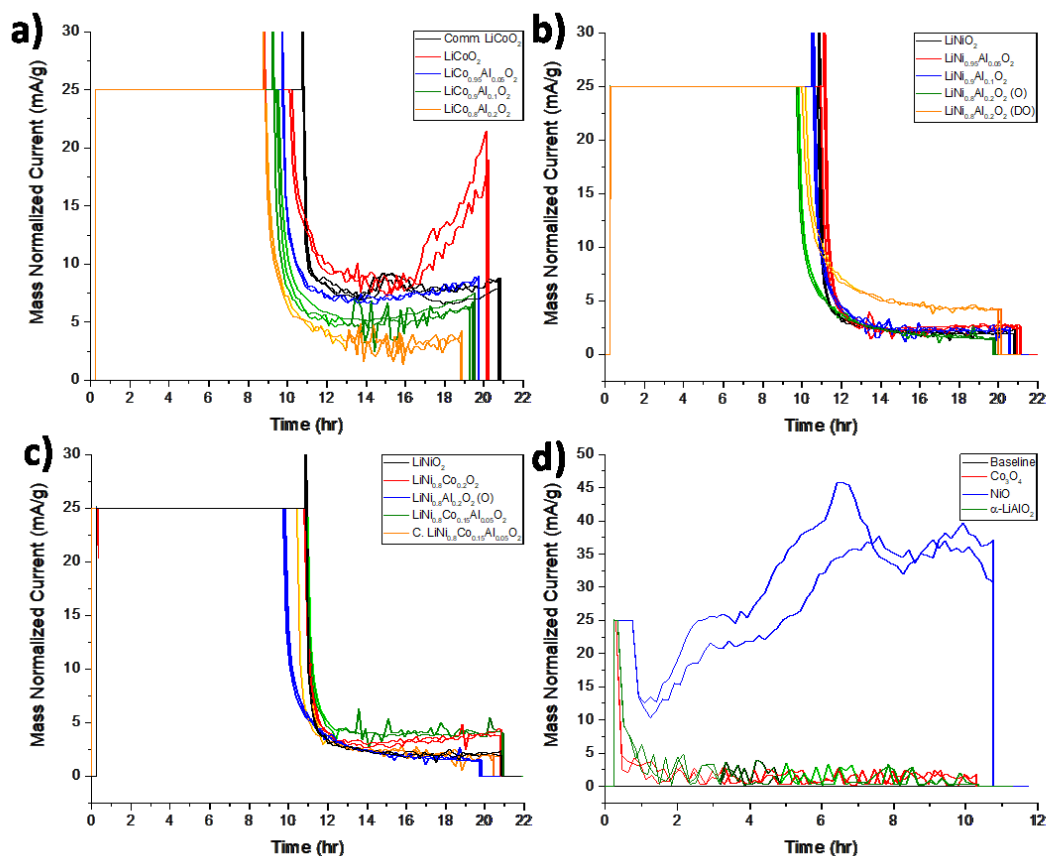


Figure 5-14: The current profiles for all of the ICP-OES coin cells listed in Table I. The group 1, 2 and 3 materials are shown in (a), (b), and (c), respectively, while the reference materials are presented in (d). Cells were charged to 4.75 V at a constant current (25 mA/g), and then held at constant potential (4.75 V) for 10 h, all while in a 60°C incubator. Some cells show a temporary increase in current at the beginning of the potentiostatic segment, but the current was never above 25 mA/g for more than 1 data point (10 sec).

Even though Al substitution into LiCoO_2 had many beneficial effects such as, suppressed phase and structural changes, improved average Li^+ diffusivities, and reduced Co dissolution at high states of charge, the Al-substituted LiCoO_2 materials had substantially increased first cycle irreversible losses and worse cycling performance. This poor cycling stability occurs despite the Al-substituted materials being sufficiently oxidized, and the irreversible loss not being attributed to the reaction kinetics. As a result, the source of the degradation in electrochemical performance

was likely of electronic or internal structural origin, and will be elaborated upon in the discussion section.

5.4.3 Group 2: $\text{LiNi}_{1-y}\text{Al}_y\text{O}_2$

5.4.3.1 Electrochemical Characterization: $\text{Li}_x\text{Ni}_{1-y}\text{Al}_y\text{O}_2$

By characterizing LiNiO_2 , $\text{LiNi}_{0.95}\text{Al}_{0.05}\text{O}_2$, $\text{LiNi}_{0.9}\text{Al}_{0.1}\text{O}_2$, $\text{LiNi}_{0.8}\text{Al}_{0.2}\text{O}_2$ (O), and $\text{LiNi}_{0.8}\text{Al}_{0.2}\text{O}_2$ (DO), (group 2) in a similar systematic way as the group 1 materials, an in-depth understanding of the role that Al has on structural transformations and subsequent cycling performance on LiNiO_2 was investigated. Tested identically to the results presented in Figure 5-4, the dQ/dV and PITT results for all group 2 materials are shown in Figure 5-15 (a-c).

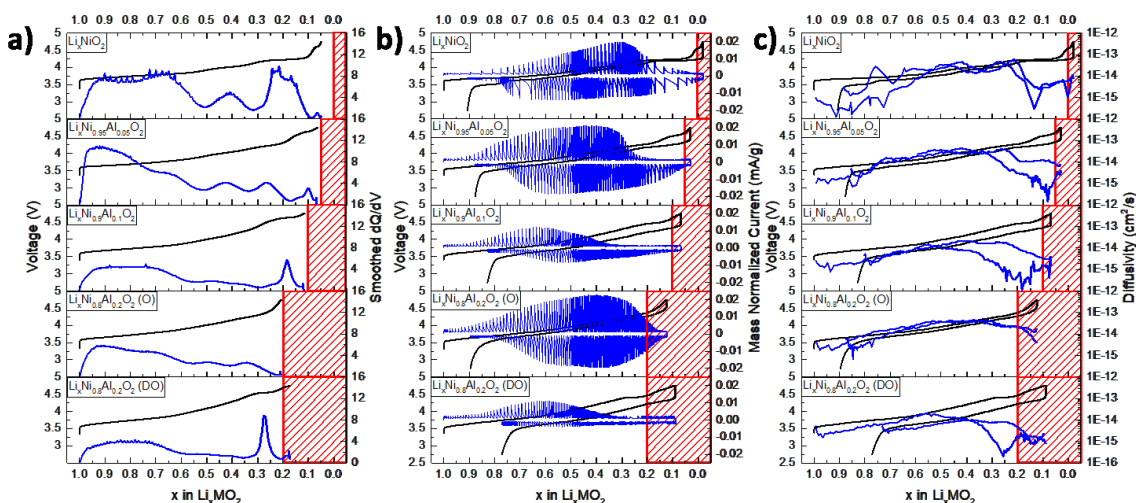


Figure 5-15: (a) The (a) voltage (black) and differential charge (blue) profiles from the first charge of coin cells that were cycled at a constant current of 5 mA/g between 4.75 – 2.75 V are shown for all group 2 materials. Duplicate cells were cycled under PITT conditions (10 mV steps, 1 mA/g current cutoff) and the resulting first cycle (b) voltage (black) and current (blue) profiles, and (c) the voltage (black) and diffusivity (blue) plots of each material are also presented. The red boxes in the three graphs denote the theoretically inaccessible lithiation regions based on the amount of transition metals that can be electrochemically oxidized in each material.

Consistent with earlier reports, the delithiation of LiNiO_2 proceeded within a single phase and is shown by the broad dQ/dV peak centered at $x = 0.9$ in panel 1 of Figure 5-15 (a).^{14,256}

Similar to LiCoO_2 , during this highly lithiated region, the Li^+ diffusivity (Figure 5-15 (c)) of

LiNiO₂ was relatively low ($\sim 1\text{E-}15$ to $1\text{E-}16$ cm²/s). The Li_xNiO₂ structural transition to the monoclinic phase began at $\sim x = 0.75$ (3.764 V) and is shown by the wide differential charge peak at $x = 0.65$. In contrast to LiCoO₂, the monoclinic phase in LiNiO₂ is stable for a much larger lithiation range. The transformation back to a rhombohedral structure is represented by the dQ/dV peak at $\sim x = 0.41$ (4.010 V). This single rhombohedral phase was stable until $x = 0.24$ (4.207 V), where a two phase reaction is obtained. Throughout the monoclinic and single rhombohedral phase structures the Li⁺ diffusivity of LiNiO₂ was high ($\sim 1\text{E-}13$ to $1\text{E-}14$ cm²/s), which was a result of the ample lithium vacancies and expanded c axis. The transition to this phase was enormously sluggish with diffusion decreasing by almost two orders of magnitude. At the very end of the charging process, a final peak in the differential charge plot was observed at $\sim x = 0.06$. This peak could be indicative of the ongoing transition to the fully delithiated structure. All structural transitions in LiNiO₂ were highly reversible as demonstrated by the very small hysteresis in the PITT voltage profile, and plateaus at similar lithiations and potentials. The LiNiO₂ phase transitions documented here are in good agreement with previous observations.^{14,105,241,256}

Similar to the LiCo_{1-y}Al_yO₂ ($y > 0$) materials, the substitution of Al for the Ni in LiNiO₂ decreased the intensity of the phase transitions and smoothed out the voltage profile. However, in the 5% Al-substituted material, LiNi_{0.95}Al_{0.05}O₂, there was still very distinct differential charge peaks associated with each phase transition, and the voltage profile of the PITT cell remained highly faceted. As with LiNiO₂, the final phase transition in LiNi_{0.95}Al_{0.05}O₂ was accompanied with a very significant decrease in diffusion, but in contrast with LiNiO₂, this transition seems to occur with greater hysteresis. As more Al was substituted into the Li_xNiO₂ structure, the lower state of charge ($x > 0.2$) phase transitions became less apparent even though they are within the smaller delithiation range induced by the Al substitution. Interestingly, as 5 and 10% Al was substituted into LiNiO₂ the final dQ/dV peak's intensity grew substantially, but this peak was not visible for LiNi_{0.8}Al_{0.2}O₂ (O). As previously indicated this peak was correlated to the final

delithiation of the material and not only did the magnitude of this peak change with the amount of Al substitution, but so did its position. In Li_xNiO_2 this peak was located at $x = 0.06$ (4.605 V), while it was measured at $x = 0.10$ (4.641 V) for $\text{Li}_x\text{Ni}_{0.95}\text{Al}_{0.05}\text{O}_2$, and at $x = 0.18$ (4.633 V) for $\text{Li}_x\text{Ni}_{0.9}\text{Al}_{0.1}\text{O}_2$. Although this peak was measured on $\text{Li}_x\text{Ni}_{0.8}\text{Al}_{0.2}\text{O}_2$ (DO) at $x = 0.19$ (4.710 V), it was not found on $\text{LiNi}_{0.8}\text{Al}_{0.2}\text{O}_2$ (O).

The shift in the lithiation at which this final dQ/dV peak occurs was directly related to the amount of Al substitution. When there was less Ni in the structure as a result of Al substitution, full oxidation of the positive electrode occurs at lower lithiation values since Al is electrochemically inactive. In agreement with previous findings, the amount of Al shifts the voltage profile higher so that the potential at which this transition occurs was correlated to the amount of Al in the structure.^{134,141,142} We specifically find this increase in slope and average voltage with Al substitution readily apparent at $x < 0.3$. The reason why this final delithiation peak was not observed for $\text{LiNi}_{0.8}\text{Al}_{0.2}\text{O}_2$ (O) but was found in $\text{LiNi}_{0.8}\text{Al}_{0.2}\text{O}_2$ (DO) may be related to the homogeneity of the Ni and Al mixing. At the end of charging, the homogeneous $\text{LiNi}_{0.8}\text{Al}_{0.2}\text{O}_2$ (O) material still had ~20.8% of its initial Li remaining in the structure. As a result, $\text{LiNi}_{0.8}\text{Al}_{0.2}\text{O}_2$ (O) was not delithiated enough for the final transition to be observed. Conversely, in $\text{LiNi}_{0.8}\text{Al}_{0.2}\text{O}_2$ (DO) the transition metal mixing was poor so the material had “Ni-rich” and “Al-rich” domains. Thus while the “Ni-rich” domains were capable of some phase transition, the “Al-rich” domains were not, and the dQ/dV plot, which is an averaged measurement of the material, only shows a small peak. The inhomogeneity of the transition metal ions in $\text{LiNi}_{0.8}\text{Al}_{0.2}\text{O}_2$ (DO) is clearly shown by the EDS images in Figure 5-16 (b-d). In contrast to the poor Ni and Al mixing in $\text{LiNi}_{0.8}\text{Al}_{0.2}\text{O}_2$ (DO), $\text{LiNi}_{0.8}\text{Al}_{0.2}\text{O}_2$ (O) was observed to have a homogenous distribution of Ni and Al (Figure 5-16 (f-h)).

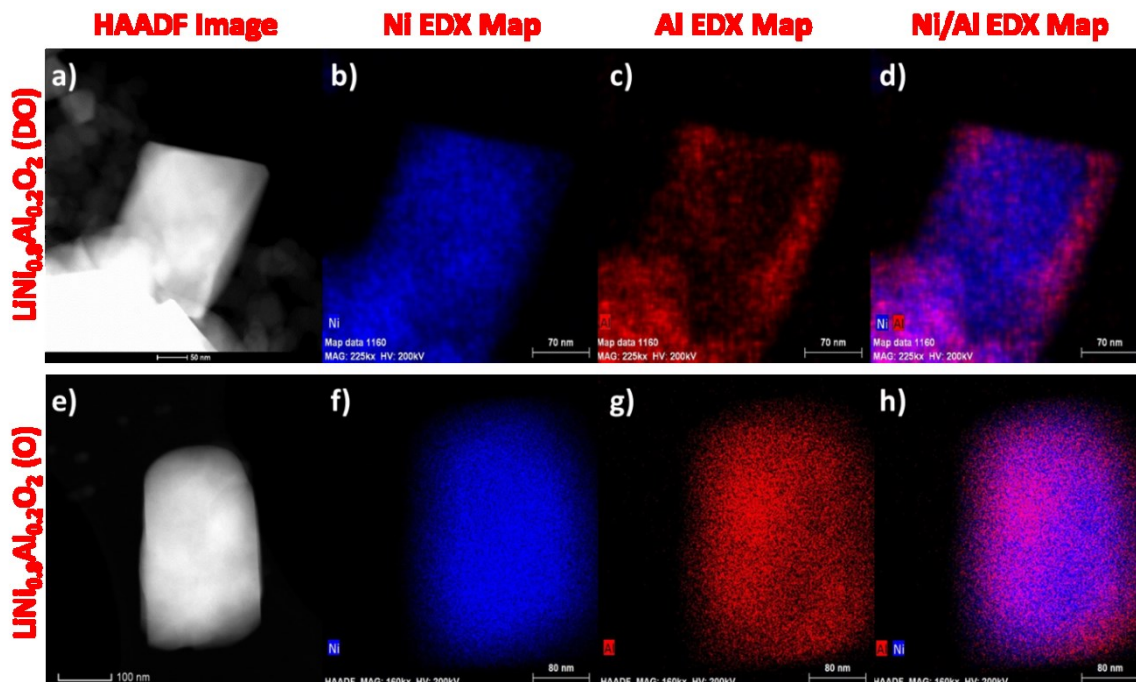


Figure 5-16: (a) A HAADF image of a representative $\text{LiNi}_{0.8}\text{Al}_{0.2}\text{O}_2$ (DO) particle and EDS maps of the (b) Ni, (c) Al, and (d) Ni and Al signals is shown. A similar HAADF image and EDS maps are given for $\text{LiNi}_{0.8}\text{Al}_{0.2}\text{O}_2$ (O) in (e-h), respectively. The EDS images show relatively poor Ni and Al mixing for $\text{LiNi}_{0.8}\text{Al}_{0.2}\text{O}_2$ (DO) and a homogenous distribution for $\text{LiNi}_{0.8}\text{Al}_{0.2}\text{O}_2$ (O).

Like LiNiO_2 , $\text{LiNi}_{0.95}\text{Al}_{0.05}\text{O}_2$ and $\text{LiNi}_{0.8}\text{Al}_{0.2}\text{O}_2$ (O) have very little hysteresis in the PITT voltage profiles. While it was expected for the poorly mixed $\text{LiNi}_{0.8}\text{Al}_{0.2}\text{O}_2$ (DO) sample to have a substantial voltage hysteresis, it was surprising to find a larger hysteresis in $\text{LiNi}_{0.9}\text{Al}_{0.1}\text{O}_2$ than in $\text{LiNi}_{0.8}\text{Al}_{0.2}\text{O}_2$ (O). This indicates that $\text{LiNi}_{0.9}\text{Al}_{0.1}\text{O}_2$ may also have some “Ni-rich” and “Al-rich” domains, although not nearly to the same degree as $\text{LiNi}_{0.8}\text{Al}_{0.2}\text{O}_2$ (DO). When there was good transition metal mixing, the addition of Al to LiNiO_2 did not negatively impact the Li^+ diffusivity. Instead, $\text{LiNi}_{0.95}\text{Al}_{0.05}\text{O}_2$ and $\text{LiNi}_{0.8}\text{Al}_{0.2}\text{O}_2$ (O) show similar average Li^+ diffusivities as LiNiO_2 . In fact the $\text{LiNi}_{0.8}\text{Al}_{0.2}\text{O}_2$ (O) sample exhibited diffusivities almost an order of magnitude larger than LiNiO_2 towards the end of charge.

5.4.3.2 Structural Characterization: $\text{Li}_x\text{Ni}_{1-y}\text{Al}_y\text{O}_2$

To confirm the difference in structural transitions suggested by the electrochemical characterization, *in-situ* XRD cells made of each group 2 material were fabricated and tested identically to the group 1 positive electrode materials and are presented in Figure 5-17 (a-e). The calculated c and a lattice parameters of each group 2 material are shown in Figure 5-19. In agreement with the differential charge and PITT results, the initial two phase structure in LiNiO_2 (Figure 5-17 (a)) was not easily observed by *in-situ* XRD. Instead, the delithiation reaction appeared to be topotactic until the monoclinic phase starts forming at approximately $x = 0.75$. While the structural change to and from the monoclinic phase isn't easily apparent from the (003) peak contour plot, an increase in the (003) peak breadth was observed when $0.75 \geq x \geq 0.36$. This supports the lithiation range over which the monoclinic region was observed in the dQ/dV cells. Near the end of charge ($x = 0.16$), a two phase region appears as the delithiation reaction starts to create empty lithium planes. As LiNiO_2 proceeds to higher states of charge, the intensity of the new peak (at $\sim 19.8^\circ$) increases substantially and the original (003) peak gradually disappeared. As the lithiation in LiNiO_2 approached 0 the contraction of the c axis plateaus and the c parameter stabilizes at 13.400 Å (Figure 5-19). The relative change to the c axis was much smaller for LiNiO_2 (Figure 5-7 (b)) than for LiCoO_2 (Figure 5-7 (a)). Regardless, the *in-situ* XRD results for LiNiO_2 at the end of charge were best refined to NiO_2 with either a $R\bar{3}m$ or $C2/m$ structure, but cannot be distinguished because of the insufficient scan resolution to observe peak splitting. The $C2/m$ structure has been previously associated to NiO_2 .^{154,254} Unlike the CdI_2 ($P-3m1$) structure that is achieved by CoO_2 , the octahedral environment of the Li site in the $C2/m$ structure does not share faces and as a result more closely resembles the $R\bar{3}m$ ($O3$) structure. As such, the environment is stable for new, residual Li^+ or even Ni ions to occupy octahedral sites. A brief elaboration on the differences between the $C2/m$, $R\bar{3}m$, and $P-3m1$ structures is provided in the following paragraphs and shown in Figure 5-18.

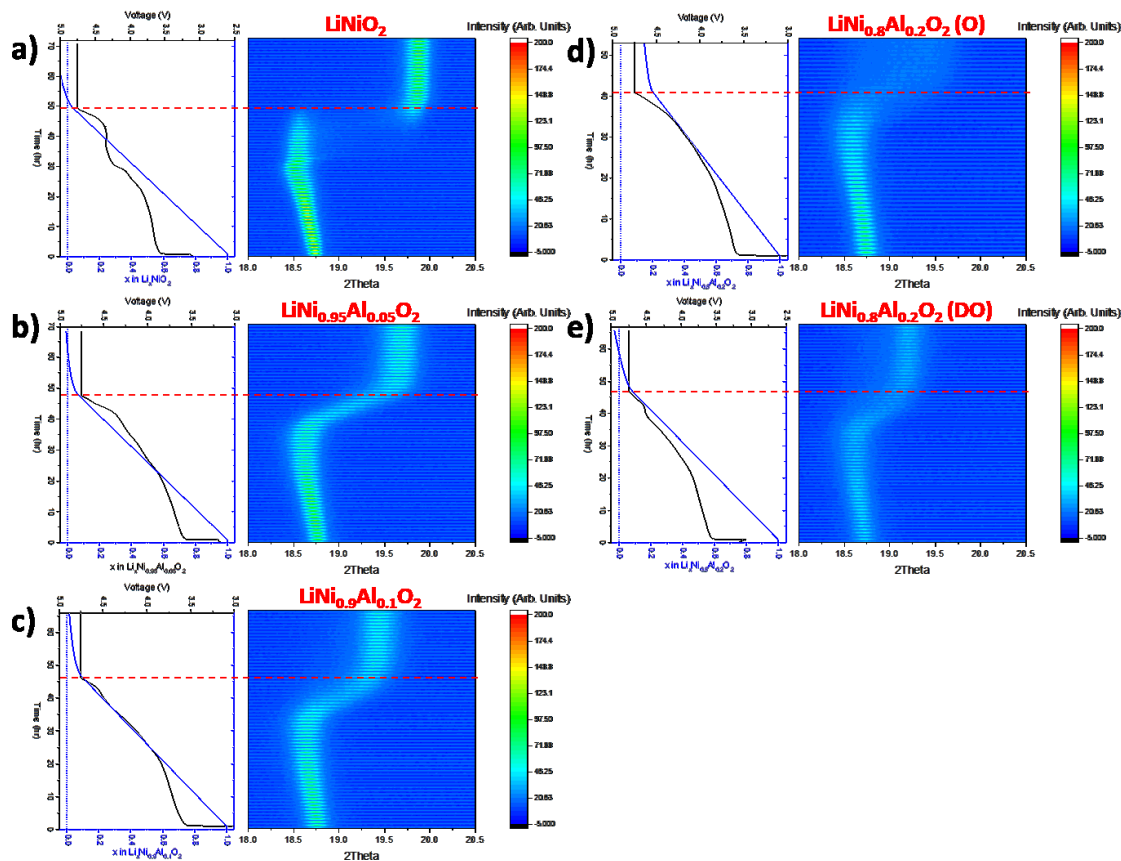


Figure 5-17: In-situ XRD contour plots of the (003) peak and corresponding electrochemical profiles for (a) LiNiO_2 , (b) $\text{LiNi}_{0.95}\text{Al}_{0.05}\text{O}_2$, (c) $\text{LiNi}_{0.9}\text{Al}_{0.1}\text{O}_2$, (d) $\text{LiNi}_{0.8}\text{Al}_{0.2}\text{O}_2$ (O), and (e) $\text{LiNi}_{0.8}\text{Al}_{0.2}\text{O}_2$ (DO). Cells were charged at a constant current of $C/50$ to 4.75 V, and then held at constant potential indefinitely, all while 1 h XRD scans were continuously running. To avoid missing any features, the experimental parameters were chosen such that $\Delta x \leq 0.02$ for every scan. A red dashed line corresponding to when the potential reached 4.75 V is superimposed on each sub-figure to enable easy comparison between materials.

While it has been well established that when fully delithiated, Li_xCoO_2 has a structural transition to the P-3m1 space group which is denoted as the O1 structure. In this O1 configuration (Figure S9 (c, f)), the Co atoms from neighboring layers align directly above one another, and only two unique oxygen positions are present which gives the structure is AB AB packing sequence. However, this structure has not been observed for NiO_2 (fully delithiated Li_xNiO_2), and is generally considered to be a consequence of the additional divalent transition metal in the Li 3a

site that is prevalent for LiNiO_2 -based materials. Instead, a structural transition from the original rhombohedral ($\text{R}\bar{3}\text{m}$) to a monoclinic (C2/m) phase has been observed.^{154,254}

A comparison of the Reitveld determined crystal structures for NiO_2 fit to a C2/m and $\text{R}\bar{3}\text{m}$ space group as well as CoO_2 in a P-3m1 structure is presented in Figure S9. The authors that determined that the structure of NiO_2 was C2/m claimed that this structure was a distortion of the CdI_2 structure and could thus be considered to be O1. While it is true that NiO_2 in the C2/m space group (Figure S9 (a, d)) does have an AB stacking sequence similar to CoO_2 in the P-3m1 space group (Figure S9 (c, f)), there are substantial differences between the two structures. The necessary distortion to the P-3m1 structure to form C2/m causes a substantial increase in the β angle from 90° to $\sim 126^\circ$. Relative to the (001) plane, this forces the neighboring NiO_2 (or CoO_2) slabs to shift and offset themselves. As a result of this shift, the interlayer octahedral environment (3a site in $\text{R}\bar{3}\text{m}$) is changed from face sharing in P-3m1 to edge sharing in C2/m . The specific environment of this octahedral position is critically relevant for insertion materials, because it is this site which will accommodate Li ions upon reduction of the material. Because the interlayer octahedral sites in C2/m have edge sharing with the adjacent interlayer octahedral sites, from the perspective of Li^+ intercalation the structure more closely resembles $\text{R}\bar{3}\text{m}$ (O3) than P-3m1 (O1). Thus, in the context of electrochemical positive electrode materials it is misleading to consider the C2/m structure as an O1-type structure when it can be more acutely described as O3-type.

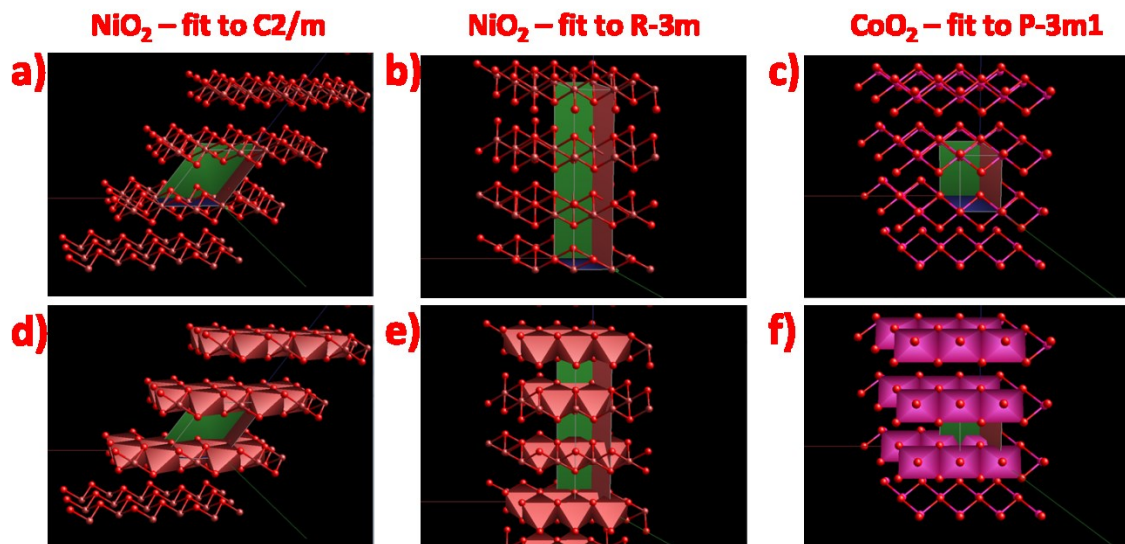


Figure 5-18: Visualizations of the Reitveld calculated crystal structures for (a, d) NiO_2 fit to $C2/m$, (b, e) NiO_2 fit to $R\bar{3}m$, and (c, f) CoO_2 fit to $P-3m1$ are shown. For each structure, images with (a-c) and without (d-f) the transition metal octahedra are provided. Oxygen, Ni and Co atoms are represented by red, maroon, and pink balls, respectively. All structures are oriented so that the a axis (red line) is directed to the left, and the b axis (green line) is indirectly positioned towards the reader.

Compared to LiNiO_2 , the Al-substituted LiNiO_2 materials had broader peaks, smoother phase transformations and smaller changes to the lattice parameters. The *in-situ* XRD diffraction result for $\text{Li}_x\text{Ni}_{0.95}\text{Al}_{0.05}\text{O}_2$ (Figure 5-17 (b)) appeared to behave similarly to Li_xNiO_2 when $x > 0.3$, but at higher states of charge the (003) peak in $\text{Li}_x\text{Ni}_{0.95}\text{Al}_{0.05}\text{O}_2$ had a gradual and continuous shift to higher angles. As more Al was substituted into LiNiO_2 , the peak shift representing the structural transition towards the highly delithiated phase decreased and occurred more progressively. 5% Al substitution was sufficient to prevent any ambiguity over the formation of a $C2/m$ phase as in LiNiO_2 , and instead a highly delithiated phase retaining the $O3 R\bar{3}m$ structure was clearly observed. From Figure 5-19 (a) it can be seen that Al was added to LiNiO_2 the host materials began to have their c axes contract at lower states of charge as opposed to going through a distinct two phase reaction. Figure 5-7 (b) makes it evident that the relative change to the c axis decreased steadily as more Al was substituted into the structure. The final single phase c spacing for the Al-substituted materials was markedly larger than that of pure LiNiO_2 . This was

likely because at the end of charge there is more Li remaining in $\text{LiNi}_{1-y}\text{Al}_y\text{O}_2$ ($y > 0$) than in LiNiO_2 .

The a lattice parameter of the fully lithiated materials was observed to be highly dependent on the Al concentration, and as more Ni was replaced with Al the a parameter systematically decreased. However, Figure 5-7 (e) shows that during delithiation the relative change to the a parameter was not strongly related to the concentration of Al in the host material. Since $\text{LiNi}_{0.8}\text{Al}_{0.2}\text{O}_2$ (O) was homogeneously mixed the a lattice was significantly smaller than for $\text{LiNi}_{0.9}\text{Al}_{0.1}\text{O}_2$, but the a parameter for $\text{LiNi}_{0.8}\text{Al}_{0.2}\text{O}_2$ (DO) was larger than $\text{LiNi}_{0.9}\text{Al}_{0.1}\text{O}_2$ because of the presence of “Ni-rich” and “Al-rich” domains. In contrast to the LiCoO_2 -based materials, none of the group 2 materials had an increase in the a lattice parameter during charging. Instead, the a parameter for all of the Al-substituted Li_xNiO_2 electrodes decreased until $x \sim 0.2$ and then remained constant.

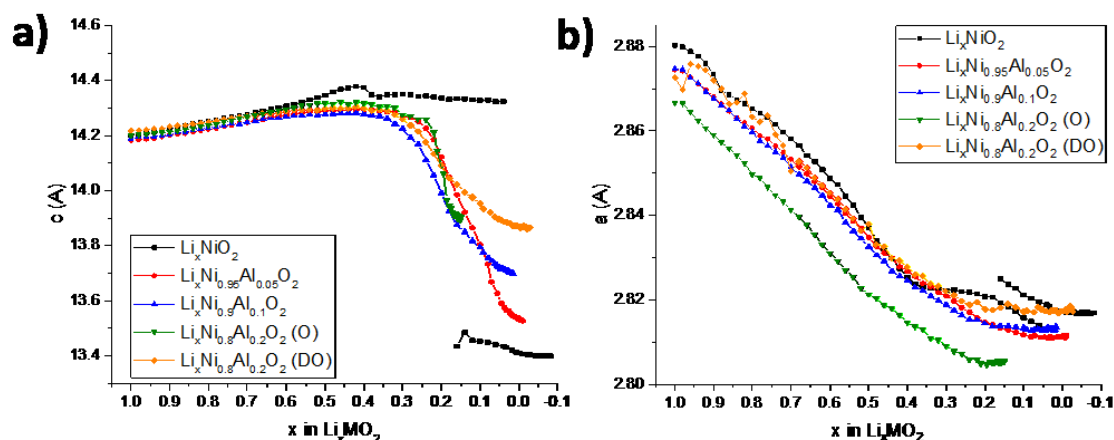


Figure 5-19: Calculated (a) c and (b) a lattice parameters as a function of delithiation for the in-situ XRD experiments of LiNiO_2 (black), $\text{LiNi}_{0.95}\text{Al}_{0.05}\text{O}_2$ (red), $\text{LiNi}_{0.9}\text{Al}_{0.1}\text{O}_2$ (blue), $\text{LiNi}_{0.8}\text{Al}_{0.2}\text{O}_2$ (O) (green), and $\text{LiNi}_{0.8}\text{Al}_{0.2}\text{O}_2$ (DO) (orange) positive electrodes. Lattice parameters were calculated from a rhombohedral unit cell using the peak locations of the (003) and (101) peaks.

Identically to the group 1 materials, all group 2 positive electrodes were PITT charged to 4.75 V and disassembled for *ex-situ* XRD analysis. The charging profiles for these materials are

shown in Figure S5 (b), while the (003) and (104) peak regions of the resulting *ex-situ* scans are shown in Figure 5-20. Despite not being the most delithiated group 2 material, the (003) and (104) peaks for LiNiO_2 were shifted to significantly higher angles than any of the Al-substituted materials. As observed with the *in-situ* XRD samples, the peak shift to higher angles was a result of the transitions to a C2/m structure that occur at the highest states of charge. The coulombic charge results from Table 5-II show that $\text{Li}_x\text{Ni}_{0.95}\text{Al}_{0.05}\text{O}_2$ ($x = 0.020$) was slightly more delithiated than Li_xNiO_2 ($x = 0.047$) at the end of charge, yet both the (003) and (104) peaks for $\text{Li}_x\text{Ni}_{0.95}\text{Al}_{0.05}\text{O}_2$ were observed at lower angles than in Li_xNiO_2 . When higher concentrations of Al substitution was used ($\text{LiNi}_{0.9}\text{Al}_{0.1}\text{O}_2$ or $\text{LiNi}_{0.8}\text{Al}_{0.2}\text{O}_2$) the peak shift to higher angles was even more muted. These results support the relationship determined by the *in-situ* experiments. As more Al was added into the LiNiO_2 structure the degree of structural transformation in the positive electrode material diminishes, *even at equivalent states of delithiation*. The OCV after 1 h, presented in Table 5-II, demonstrates a strong relationship between the quantity of the Al ions and the OCV. In agreement with the group 1 materials, as the Al content in $\text{LiNi}_{1-y}\text{Al}_y\text{O}_2$ increased the OCV voltage 1 h after being PITT charged to 4.75 V also increased. Like the group 1 materials, no trend between the amount of Al in the positive electrode structure and the % Ni oxidation could be determined. This can be attributed to the non-negligible amount parasitic reactions that were occurring on these materials at higher states of charge, and explain why the observed % Ni oxidation for some of these materials were beyond the theoretical limit.

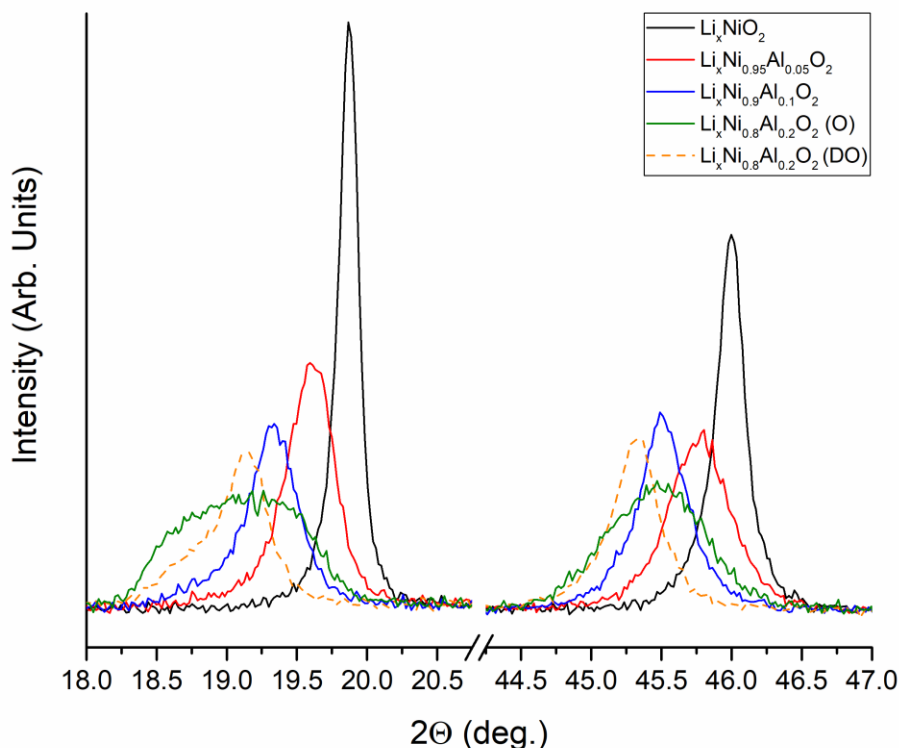


Figure 5-20: Ex-situ XRD scans of positive electrodes that were charged to 4.75 V under PITT conditions (10 mV step, 1 mA/g cutoff). Results are presented in the regions of the (003) (18-21.5°) and (104) (42-47°) peaks for LiNiO_2 (black), $\text{LiNi}_{0.95}\text{Al}_{0.05}\text{O}_2$ (red), $\text{LiNi}_{0.9}\text{Al}_{0.1}\text{O}_2$ (blue), $\text{LiNi}_{0.8}\text{Al}_{0.2}\text{O}_2$ (O) (green), and $\text{LiNi}_{0.8}\text{Al}_{0.2}\text{O}_2$ (DO) (orange). All coin cells were disassembled in an Ar-filled glovebox and the XRD samples were sealed with a Kapton film to temporarily prevent hydrogen intercalation upon exposure to ambient atmosphere.

The potential and heat flux profiles determined by *operando* microcalorimetry are displayed in Figure 5-21. In contrast to the group 1 materials the LiNiO_2 -based group 2 materials each had an exothermic heat flux as charging began. Li_xNiO_2 did become slightly endothermic at $x \approx 0.75$, which was associated with the beginning of the monoclinic phase. While the intensity of the heat flux peaks associated with the hexagonal to monoclinic to hexagonal phase transformations was much weaker for LiNiO_2 than for LiCoO_2 , it was still visible. The less distinct transitions to and from the monoclinic phase for LiNiO_2 was in agreement with the dQ/dV, PITT, and *in-situ* XRD results. During charging to 4.75 V, the heat flux for all Al-

substituted LiNiO_2 materials remained exothermic, and showed no signs of the structural transformations related to the monoclinic phase. The temporary region during charging where $\text{LiNi}_{0.9}\text{Al}_{0.1}\text{O}_2$ was endothermic was due to a small temperature deviation ($< 0.1^\circ\text{C}$) in the microcalorimeter chamber and was not associated to the electrode material. At higher potentials ($> 4.3\text{ V}$), the heat flux of each LiNiO_2 -based material rapidly became more exothermic, and continued to increase until the end of charge. The only exception to this rule was the $\text{LiNi}_{0.8}\text{Al}_{0.2}\text{O}_2$ (O) sample which maintained a very low exothermic reaction for the majority of the delithiation and finally resulted in a slight (approx. 50% less than other samples) exothermic rise at the end of delithiation towards 4.75 V. Knowing that the ionic transport was improved within the relevant region of lithiation in $\text{LiNi}_{0.8}\text{Al}_{0.2}\text{O}_2$ (O), we can state that a majority of the exotherm was related to the kinetics of the reaction. Throughout the entirety of the discharge to 2.75 V, all group 2 materials remained exothermic, although the $\text{LiNi}_{0.8}\text{Al}_{0.2}\text{O}_2$ (O) sample much less so. Since the entropic changes of the positive electrode should be the dominant influence on the heat flux, the heat flux during discharge is expected to be equal and opposite to the heat flux during charge, so some of the heat generated may be related to parasitic reactions or impedance.

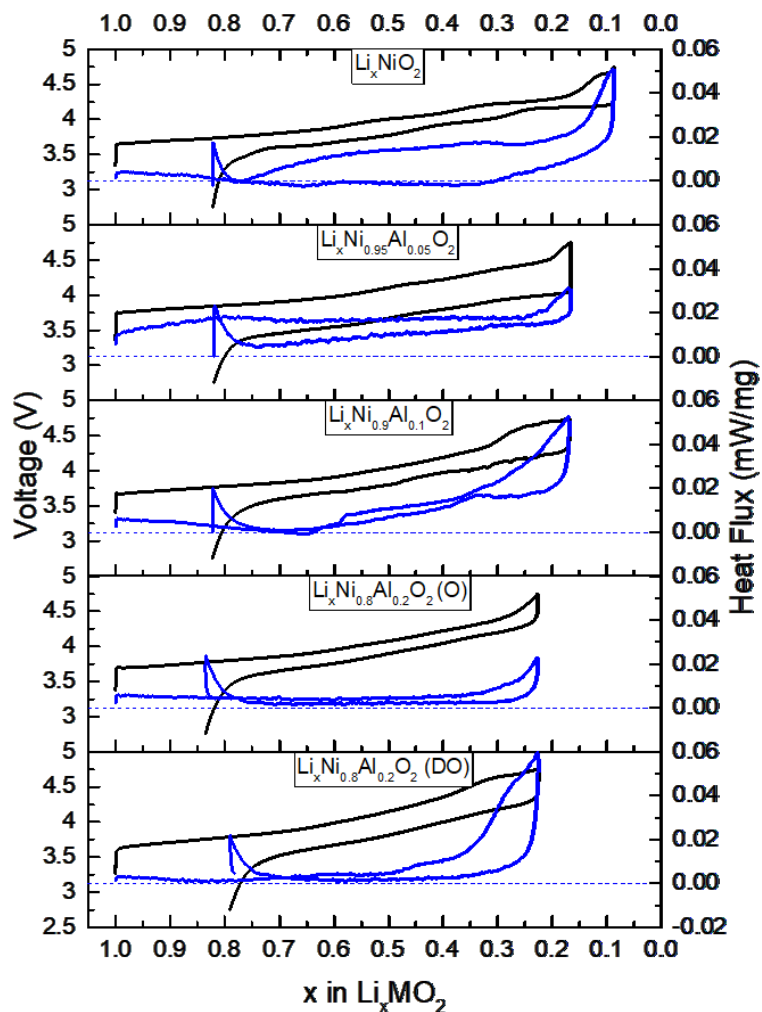


Figure 5-21: Operando isothermal microcalorimetry voltage (black) and heat flux (blue) measurements are presented during the first cycle for each group 2 material. Coin cells were cycled at a constant current (25 mA/g) between 4.75 V and 2.75 V, while the chamber was isothermal at 30°C.

5.4.3.3 Cycling Performance: $\text{Li}_x\text{Ni}_{1-y}\text{Al}_y\text{O}_2$

The electrochemical cycling performance for each group 2 positive electrode material was evaluated by coin cells that were made and cycled identically to the results shown in Figure 5-11 for group 1. The discharge capacity vs. cycle number results for cells containing a group 2 positive electrode are shown in Figure 5-22, and the associated first cycle charge/discharge capacities as well as the irreversible loss are provided in Table 5-V. For cells charged to 4.5 V

and 4.75 V, the first cycle discharge capacity decreased systematically with increasing Al content. In contrast to the $\text{LiCo}_{1-y}\text{Al}_y\text{O}_2$ materials, the % irreversible loss (Table 5-V) during the first cycle did not necessarily increase with higher Al substitution. While $\text{LiNi}_{0.95}\text{Al}_{0.05}\text{O}_2$ did have a higher first cycle irreversible capacity loss than LiNiO_2 when a 4.5 V cutoff potential was implemented, a steady decrease in the irreversible loss was observed as the Al content was increased beyond 5%. In contrast, when a 4.75 V cutoff potential was used the first cycle irreversible losses for $\text{LiNi}_{0.95}\text{Al}_{0.05}\text{O}_2$ and $\text{LiNi}_{0.8}\text{Al}_{0.2}\text{O}_2$ (O) were lower than for LiNiO_2 , but $\text{LiNi}_{0.9}\text{Al}_{0.1}\text{O}_2$ and $\text{LiNi}_{0.8}\text{Al}_{0.2}\text{O}_2$ (DO), which are both somewhat inhomogeneous, had increased capacity losses.

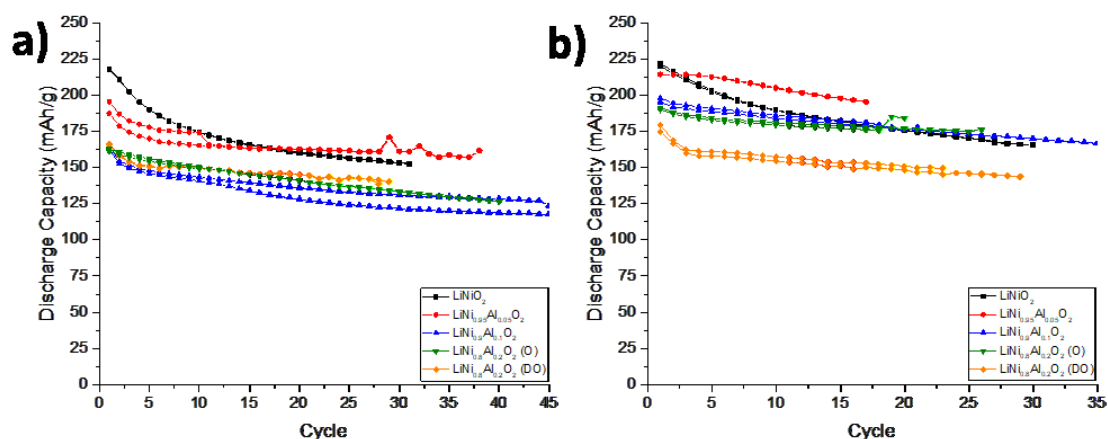


Figure 5-22: Discharge capacity vs. cycle results for coin cells charged to either (a) 4.5 V or (b) 4.75 V. Cells were charged at 20 mA/g to V_{\max} (4.5 or 4.75 V), held at a constant potential until the current dropped below 10 mA/g, and were then discharged at 10 mA/g to 2.75 V, all at room temperature. Duplicate cells of each positive electrode material were made to ensure reproducibility.

Table 5-V: First cycle charge capacity, discharge capacity, and irreversible loss for each coin cell shown in Figure 5-22. The theoretical capacity (assuming Al is electrochemically active) is given for each material.

Material	V _{max}	First Cycle Charge Capacity (mAh/g)	First Cycle Discharge Capacity (mAh/g)	Irreversible Loss (mAh/g)	Irreversible Loss (%)	Theoretical Capacity (mAh/g)
LiNiO ₂	4.5	255.18	217.78	37.40	14.66	274.52
LiNiO ₂	4.5	255.30	218.33	36.97	14.48	274.52
LiNiO ₂	4.75	265.52	221.92	43.60	16.42	274.52
LiNiO ₂	4.75	262.41	220.13	42.28	16.11	274.52
LiNi _{0.95} Al _{0.05} O ₂	4.5	233.67	187.40	46.27	19.80	279.05
LiNi _{0.95} Al _{0.05} O ₂	4.5	241.31	195.43	45.88	19.01	279.05
LiNi _{0.95} Al _{0.05} O ₂	4.75	255.69	214.51	41.18	16.11	279.05
LiNi _{0.95} Al _{0.05} O ₂	4.75	237.38	197.54	39.84	16.78	279.05
LiNi _{0.9} Al _{0.1} O ₂	4.5	205.82	164.62	41.20	20.02	283.74
LiNi _{0.9} Al _{0.1} O ₂	4.5	206.58	162.92	43.66	21.13	283.74
LiNi _{0.9} Al _{0.1} O ₂	4.75	243.13	195.06	48.07	19.77	283.74
LiNi _{0.9} Al _{0.1} O ₂	4.75	248.38	198.13	50.25	20.23	283.74
LiNi _{0.8} Al _{0.2} O ₂ (O)	4.5	194.43	161.15	33.28	17.12	293.59
LiNi _{0.8} Al _{0.2} O ₂ (O)	4.5	196.48	162.92	33.55	17.08	293.59
LiNi _{0.8} Al _{0.2} O ₂ (O)	4.75	232.90	191.40	41.50	17.82	293.59
LiNi _{0.8} Al _{0.2} O ₂ (O)	4.75	232.51	190.03	42.48	18.27	293.59
LiNi _{0.8} Al _{0.2} O ₂ (DO)	4.5	197.04	165.68	31.36	15.92	293.59
LiNi _{0.8} Al _{0.2} O ₂ (DO)	4.5	196.57	166.08	30.49	15.51	293.59
LiNi _{0.8} Al _{0.2} O ₂ (DO)	4.75	240.03	179.38	60.65	25.27	293.59
LiNi _{0.8} Al _{0.2} O ₂ (DO)	4.75	229.09	174.54	54.55	23.81	293.59

Figure 5-22 shows that LiNiO₂ had very poor cycling stability when either a 4.5 or 4.75 V cutoff potential was used. The cycling instability of LiNiO₂ was likely caused by the strong two phase reaction that occurs at high states of charge, which results in a significant incoherence of strain along the phase boundary. The significant improvement in % capacity retention for even a slightly substituted 5% Al sample is consistent with the elimination of this two phase region. Beyond the two phase reaction, theoretical loss of oxygen at the surface can result in a more resistive cathode-electrolyte interface layer, and the subsequent propensity for divalent Ni atoms to migrate into the 3a site may further impede the Li⁺ diffusivity. It is evident from the % capacity retention results in Figure 5-13 (b, e) that all Al-substituted LiNiO₂ materials were markedly more stable and had substantially better capacity retention than LiNiO₂. Interestingly, little

difference was observed in the capacity retention at either cutoff potential between $\text{LiNi}_{0.95}\text{Al}_{0.05}\text{O}_2$, $\text{LiNi}_{0.9}\text{Al}_{0.1}\text{O}_2$, and $\text{LiNi}_{0.8}\text{Al}_{0.2}\text{O}_2$ (O), which indicates that only enough Al needed to eliminate the two phase reaction towards C2/m was necessary.

In contrast to LiCoO_2 , Figure 5-23 shows that the voltage profile of LiNiO_2 remained highly faceted even after 15 cycles to 4.75 V. Furthermore, after the first cycle LiNiO_2 had negligible impedance development, and unlike Al-substituted LiCoO_2 , substituting Al for Ni in LiNiO_2 actually decreased the amount of impedance development. The 15th cycle voltage profile of $\text{LiNi}_{0.8}\text{Al}_{0.2}\text{O}_2$ (O) (Figure 5-23 (d)) looks nearly identical to the 5th cycle, indicating the stability of the electrode's impedance with extended cycling. The lack of impedance development on $\text{LiNi}_{0.9}\text{Al}_{0.1}\text{O}_2$ and $\text{LiNi}_{0.8}\text{Al}_{0.2}\text{O}_2$ (O) electrodes was why those materials had little capacity fade after the initial cycles. $\text{LiNi}_{0.8}\text{Al}_{0.2}\text{O}_2$ (DO) experiences large changes to its voltage profile after the first cycle. Even though the general shape of the voltage profile remains, there was much less hysteresis after the first cycle and there was little impedance growth after the 5th cycle. This was in sharp contrast to $\text{LiCo}_{0.8}\text{Al}_{0.2}\text{O}_2$ (Figure 5-12 (e)), which continued to have substantial impedance development after its 5th cycle.

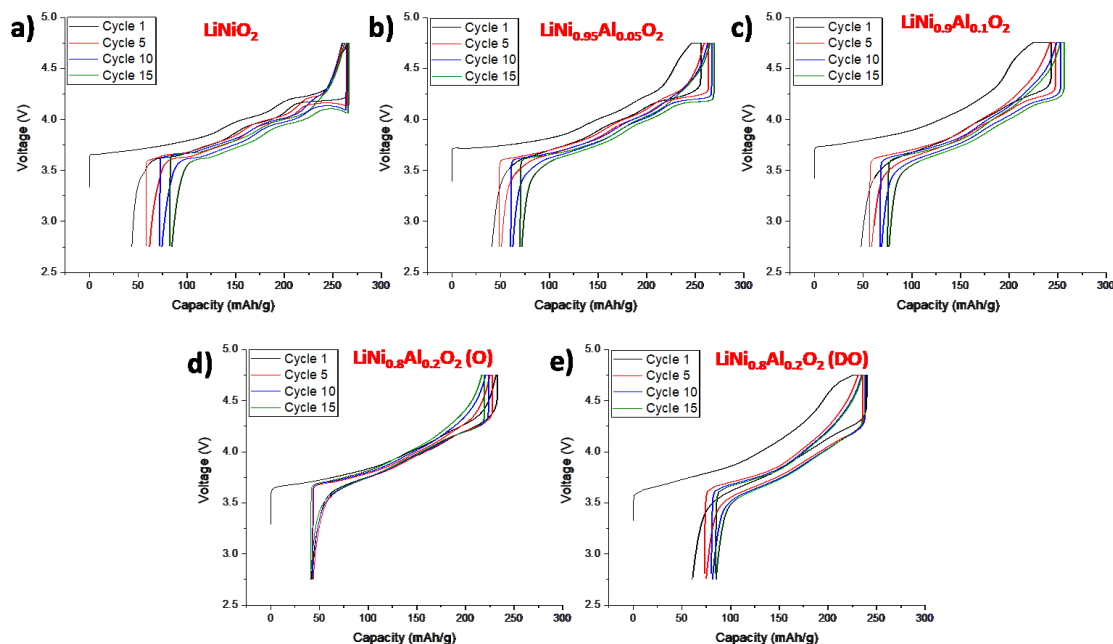


Figure 5-23: The voltage vs. capacity curves of the 1st, 5th, 10th and 15th cycles from a 4.75 V cycling cell is shown for (a) LiNiO_2 , (b) $\text{LiNi}_{0.95}\text{Al}_{0.05}\text{O}_2$, (c) $\text{LiNi}_{0.9}\text{Al}_{0.1}\text{O}_2$, (d) $\text{LiNi}_{0.8}\text{Al}_{0.2}\text{O}_2$ (O), and (e) $\text{LiNi}_{0.8}\text{Al}_{0.2}\text{O}_2$ (DO). Each cell was charged to 4.75 V at 20 mA/g, held at 4.75 V until the current went below 10 mA/g, and then was discharged at 10 mA/g to 2.75 V, all at room temperature.

5.4.3.4 Dissolution: $\text{Li}_x\text{Ni}_{1-y}\text{Al}_y\text{O}_2$

Similar to LiCoO_2 , Al substitution into LiNiO_2 was found to have stabilized the structure against HF attack and impede Ni dissolution. Table 5-IV lists the average % Ni dissolution from each group 2 material after being charged to and held at 4.75 V for 10 at 60°C. Surprisingly, LiNiO_2 (0.97%) had substantially lower transition metal dissolution than LiCoO_2 (5.24%). This was particularly surprising since NiO has a % Ni dissolution of 10.21% and highly delithiated LiNiO_2 -based materials are known to transform into a rocksalt-like structure that is Ni^{2+} rich at the surface.^{223,257,258} Similar to the group 1 materials, as Al was substituted into LiNiO_2 the magnitude of Ni dissolution generally decreased. The average % Ni dissolution in $\text{LiNi}_{0.95}\text{Al}_{0.05}\text{O}_2$, $\text{LiNi}_{0.9}\text{Al}_{0.1}\text{O}_2$, and $\text{LiNi}_{0.8}\text{Al}_{0.2}\text{O}_2$ (O) positive electrodes was 0.82%, 1.01%, and an amazingly low 0.28%, respectively. Only $\text{LiNi}_{0.9}\text{Al}_{0.1}\text{O}_2$ and $\text{LiNi}_{0.8}\text{Al}_{0.2}\text{O}_2$ (DO), which had an

average Ni dissolution of 2.08%, didn't follow the trend of decreasing Ni dissolution with increasing Al content. Because these two materials have "Ni-rich" domains, with low Al contents, it was expected that they would have more Ni dissolution than some of the other $\text{LiNi}_{1-y}\text{Al}_y\text{O}_2$ ($y > 0$) materials. However it was unexpected that $\text{LiNi}_{0.8}\text{Al}_{0.2}\text{O}_2$ (DO) would have a significantly higher Ni dissolution rate than LiNiO_2 , suggesting that somehow the inhomogeneous Ni/Al mixing actively increased the propensity for Ni dissolution.

Unlike the LiCoO_2 -based materials, none of the group 2 materials had a noteworthy increase in current during the 10 h potentiostatic segment. Yet, the corrosion current results in Figure 5-14 (b) still show a rough trend that as more Al was substituted into LiNiO_2 the parasitic current decreased. Both the dissolution results and the corrosion current data indicate that Co was more catalytic towards the electrolyte and more likely to dissolve from the positive electrode than Ni. Similar to the group 1 materials, Al substitution into LiNiO_2 suppressed phase and structural transformations, reduced the variability in the Li^+ diffusivity, and stabilized the structure against HF etching. In stark contrast to the Al substitution for Co in LiCoO_2 , which was found to significantly reduce the cycling capacity, adding Al to LiNiO_2 had beneficial effects on the cycling stability by minimizing the rapid capacity fade and impedance development in LiNiO_2 .

5.4.4 Group 3: 20% Substituted LiNiO_2

5.4.4.1 Electrochemical Characterization: 20% Substituted LiNiO_2

Presently, most state of the art positive electrodes for secondary Li-ion batteries consist of a Ni-rich layered oxide material.¹³¹ These materials have a LiNiO_2 base structure with varying amounts of Al, Co, or Mn substituted for Ni. Among the most commonly used compounds are $\text{LiNi}_{0.8}\text{Co}_{0.15}\text{Al}_{0.05}\text{O}_2$ or $\text{LiNi}_x\text{Mn}_y\text{Co}_z\text{O}_2$ (where $x + y + z = 1$).^{5,131} For this study, $\text{LiNi}_{0.8}\text{Co}_{0.15}\text{Al}_{0.05}\text{O}_2$ was investigated as a model commercial positive electrode material with the objective of understanding the role that both Co and Al have in improving its electrochemical

performance. As previously indicated, cNCA (commercially produced $\text{LiNi}_{0.8}\text{Co}_{0.15}\text{Al}_{0.05}\text{O}_2$) was used to benchmark the $\text{LiNi}_{0.8}\text{Co}_{0.15}\text{Al}_{0.05}\text{O}_2$ sample that was synthesized in-house. $\text{LiNi}_{0.8}\text{Co}_{0.2}\text{O}_2$ and $\text{LiNi}_{0.8}\text{Al}_{0.2}\text{O}_2$ (O), which have 20% of the Ni substituted for either Co or Al, were studied alongside cNCA, $\text{LiNi}_{0.8}\text{Co}_{0.15}\text{Al}_{0.05}\text{O}_2$, and LiNiO_2 , and together make up the group 3 materials.

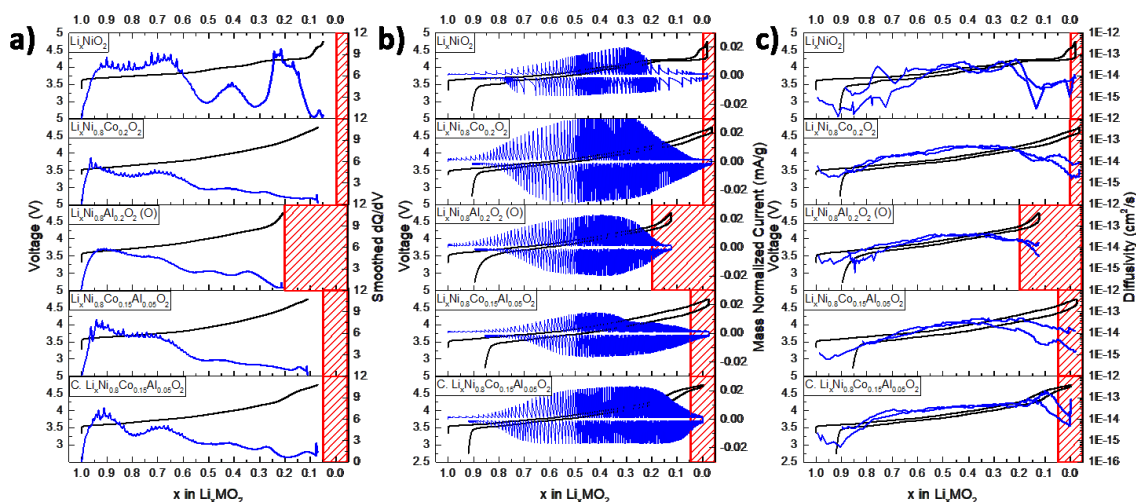


Figure 5-24: The (a) voltage (black) and differential charge (blue) profiles from the first charge of coin cells that were cycled at a constant current of 5 mA/g between 4.75 – 2.75 V are shown for all group 3 materials. Duplicate cells were cycled under PITT conditions (10 mV steps, 1 mA/g current cutoff) and the resulting first cycle (b) voltage (black) and current (blue) profiles, and (c) the voltage (black) and diffusivity (blue) plots of each material are also presented. The red boxes in the three graphs denote the theoretically inaccessible lithiation regions based on the amount of transition metals that can be electrochemically oxidized in each material.

Panel 2 of Figure 5-24 (a) presents the differential charge results for $\text{LiNi}_{0.8}\text{Co}_{0.2}\text{O}_2$, where 20% of the Ni in LiNiO_2 (panel 1) was substituted for Co. The impact of 20% Co substitution into LiNiO_2 is qualitatively similar to the strong effect of 20% Al substitution already discussed in the results of the group 2 materials. While barely visible, $\text{Li}_x\text{Ni}_{0.8}\text{Co}_{0.2}\text{O}_2$ did show a small dQ/dV peak associated with the monoclinic to rhombohedral phase transitions that was observed at $\sim x = 0.43$ (3.976 V). The weak differential charge peaks for $\text{LiNi}_{0.8}\text{Al}_{0.2}\text{O}_2$ (O) and $\text{LiNi}_{0.8}\text{Co}_{0.2}\text{O}_2$ suggest that Al and Co substitution into LiNiO_2 makes the monoclinic structural transition less favorable. Relative to LiNiO_2 , in $\text{LiNi}_{0.8}\text{Co}_{0.2}\text{O}_2$ this peak not only occurs in a more

lithiated state but was also much less intense. Also similar to $\text{LiNi}_{0.8}\text{Al}_{0.2}\text{O}_2$ (O), the 20% Co in $\text{LiNi}_{0.8}\text{Co}_{0.2}\text{O}_2$ caused the dQ/dV peak representative of the transition to a new hexagonal phase to be shifted to a higher lithiation. This peak was observed at $\sim x = 0.28$ (4.185 V) in $\text{Li}_x\text{Ni}_{0.8}\text{Co}_{0.2}\text{O}_2$, which wasn't nearly as high as in $\text{Li}_x\text{Ni}_{0.8}\text{Al}_{0.2}\text{O}_2$ (O) ($\sim x = 0.34$, 4.234 V) but was still a significant shift from Li_xNiO_2 ($\sim x = 0.24$, 4.207 V). However, because Co can be oxidized, all of the Li in $\text{Li}_x\text{Ni}_{0.8}\text{Co}_{0.2}\text{O}_2$ can be extracted during charging and a small peak in the dQ/dV profile was measured at $\sim x = 0.10$ (4.637 V). In comparison to Li_xNiO_2 , this peak in $\text{Li}_x\text{Ni}_{0.8}\text{Co}_{0.2}\text{O}_2$ occurs when there was more Li in the structure ($x = 0.10$ vs. $x = 0.06$) but the electrode potential was higher (4.637 V vs. 4.605 V). Excluding the final delithiation dQ/dV peak, which wasn't observed in $\text{LiNi}_{0.8}\text{Al}_{0.2}\text{O}_2$ (O) because the material couldn't be completely delithiated, the substitution of 20% of either Al or Co for Ni caused less defined structural transitions and shifted these transitions to a higher lithiation.

The potential, current and Li^+ diffusivity profiles obtained from the PITT cells of the group 3 materials are shown in Figure 5-24 (b-c). Like LiNiO_2 , $\text{LiNi}_{0.8}\text{Co}_{0.2}\text{O}_2$ and $\text{LiNi}_{0.8}\text{Al}_{0.2}\text{O}_2$ (O) had very low hysteresis in their potential, current, and Li^+ diffusivity profiles, indicative of the high reversibility of the reactions that occurred during charging. In contrast to Li_xNiO_2 , which had a relatively flat voltage when $x \geq 0.75$, $\text{LiNi}_{0.8}\text{Co}_{0.2}\text{O}_2$ and $\text{LiNi}_{0.8}\text{Al}_{0.2}\text{O}_2$ (O) had more sloped profiles and a typical Cottrellian response at each potential step. At high states of charge a two phase reaction was observed when $0.20 \geq x \geq 0.06$ in Li_xNiO_2 , but is clearly single phase in $\text{Li}_x\text{Ni}_{0.8}\text{Co}_{0.2}\text{O}_2$ and $\text{Li}_x\text{Ni}_{0.8}\text{Al}_{0.2}\text{O}_2$ (O). In tandem with smoothing the voltage profile during charging and discharging, substituting 20% Co or Al for Ni improved the Li^+ diffusivity, particularly in the lithiation ranges where two phase transformations were observed in LiNiO_2 . The dQ/dV and PITT results clearly showed that all substitutions into LiNiO_2 dramatically reduced the intensity of the phase transformations.

$\text{LiNi}_{0.8}\text{Co}_{0.15}\text{Al}_{0.05}\text{O}_2$, which is isostructural to LiNiO_2 but has a mixture of Co and Al substituted for 20% of the Ni, was expected to show properties between $\text{LiNi}_{0.8}\text{Co}_{0.2}\text{O}_2$ and $\text{LiNi}_{0.8}\text{Al}_{0.2}\text{O}_2$ (O). The differential charge plots for cNCA and $\text{LiNi}_{0.8}\text{Co}_{0.15}\text{Al}_{0.05}\text{O}_2$, presented in Figure 5-24 (a), are very similar to $\text{LiNi}_{0.8}\text{Co}_{0.2}\text{O}_2$, and clearly different from LiNiO_2 . Like $\text{LiNi}_{0.8}\text{Co}_{0.2}\text{O}_2$ and $\text{LiNi}_{0.8}\text{Al}_{0.2}\text{O}_2$ (O), cNCA and $\text{LiNi}_{0.8}\text{Co}_{0.15}\text{Al}_{0.05}\text{O}_2$ had smooth, gradual voltage profiles, and small dQ/dV peaks associated with the monoclinic to rhombohedral and the rhombohedral to hexagonal transitions. Also similar to $\text{LiNi}_{0.8}\text{Co}_{0.2}\text{O}_2$, both cNCA and $\text{LiNi}_{0.8}\text{Co}_{0.15}\text{Al}_{0.05}\text{O}_2$ had small dQ/dV peaks assumed to be associated with structural transformation towards the highly delithiated phase, located at $\sim x = 0.11$ (4.646 V) and $\sim x = 0.14$ (4.642 V), respectively. However, the intensity of this peak was much larger for cNCA than for either $\text{LiNi}_{0.8}\text{Co}_{0.15}\text{Al}_{0.05}\text{O}_2$ or $\text{LiNi}_{0.8}\text{Co}_{0.2}\text{O}_2$. Both cNCA and $\text{LiNi}_{0.8}\text{Co}_{0.15}\text{Al}_{0.05}\text{O}_2$ also had similar voltage profiles and show a Cottrellian current response over the entire lithiation range investigated.

A slightly larger voltage hysteresis was observed for $\text{LiNi}_{0.8}\text{Co}_{0.15}\text{Al}_{0.05}\text{O}_2$ relative to cNCA, and was attributed to the higher surface area of $\text{LiNi}_{0.8}\text{Co}_{0.15}\text{Al}_{0.05}\text{O}_2$ which caused more polarization from increased electrode-electrolyte reactions. While the Li^+ diffusivities for cNCA and $\text{LiNi}_{0.8}\text{Co}_{0.15}\text{Al}_{0.05}\text{O}_2$ generally follow the same trends, on average the Li^+ diffusivity for $\text{LiNi}_{0.8}\text{Co}_{0.15}\text{Al}_{0.05}\text{O}_2$ was incrementally lower than cNCA, which is also associated with the differences in the particle size of the materials. Major differences between the Li^+ diffusivities of cNCA and $\text{LiNi}_{0.8}\text{Co}_{0.15}\text{Al}_{0.05}\text{O}_2$ arose when $0.3 > x > 0.05$. The Li^+ diffusivity of $\text{LiNi}_{0.8}\text{Co}_{0.15}\text{Al}_{0.05}\text{O}_2$ began to decrease at a lower state of charge ($\sim x = 0.3$) than cNCA ($\sim x = 0.1$). Additionally, at $\sim x = 0.15$ the Li^+ diffusivity of $\text{LiNi}_{0.8}\text{Co}_{0.15}\text{Al}_{0.05}\text{O}_2$ suddenly decreased, while it increased for cNCA at the same lithiation. This contrast is clearly correlated to the larger feature in the dQ/dV profile of cNCA at $x = \sim 0.11$ relative to the corresponding peaks for $\text{LiNi}_{0.8}\text{Co}_{0.15}\text{Al}_{0.05}\text{O}_2$ or $\text{LiNi}_{0.8}\text{Co}_{0.2}\text{O}_2$. As the Ni-Co-Al ternary materials approached full

delithiation ($x < 0.1$), they all showed similar decreases in the Li^+ diffusivity, indicating that as the remaining Li ions become scarce the Li^+ diffusivity declines irrespective of the specific transition metal chemistry or particle size.

$\text{LiNi}_{0.8}\text{Co}_{0.15}\text{Al}_{0.05}\text{O}_2$, like $\text{LiNi}_{0.8}\text{Co}_{0.2}\text{O}_2$ and $\text{LiNi}_{0.8}\text{Al}_{0.2}\text{O}_2$ (O), had reduced structural transformations and less variation in the Li^+ diffusivity compared to LiNiO_2 . The differential charge and PITT results for $\text{LiNi}_{0.8}\text{Co}_{0.15}\text{Al}_{0.05}\text{O}_2$ were similar to $\text{LiNi}_{0.8}\text{Co}_{0.2}\text{O}_2$, with the main difference being that $\text{LiNi}_{0.8}\text{Co}_{0.15}\text{Al}_{0.05}\text{O}_2$ was slightly more lithiated at the end of charge because of the 5% Al substitution. The Li^+ diffusivity when $1 > x > 0.8$ was much lower for Li_xNiO_2 than for any of the other group 3 materials, indicating the Al and Co substitution into LiNiO_2 improved the Li^+ diffusivity even at low states of charge.

5.4.4.2 Structural Characterization: 20% Substituted LiNiO_2

In-situ XRD results for all group 3 materials during charging to 4.75 V, and at constant potential (4.75 V) are presented in Figure 5-25 (a-e). The calculated c and a lattice parameters are shown in Figure 5-26, while the % change in the lattice parameters are shown in Figure 5-7 (c,f). Each 20%-substituted LiNiO_2 material had a single phase reaction throughout the entire lithiation range. While phase evolutions were observed in every material at high states of charge, the structural transformations were always gradual and none of the substituted materials had a two phase transition. Because of its larger particle size, cNCA (Figure 5-25 (e)) had narrower and more intense diffraction peaks as well as better contrast relative to the background signal than $\text{LiNi}_{0.8}\text{Co}_{0.15}\text{Al}_{0.05}\text{O}_2$ (Figure 5-25 (d)) did.

Despite cNCA having a slightly smaller a axis, the variation of the a lattice parameter during delithiation was nearly identical for cNCA and the more nanostructured $\text{LiNi}_{0.8}\text{Co}_{0.15}\text{Al}_{0.05}\text{O}_2$. Qualitatively, the change in the c axis during charging was consistent between cNCA and $\text{LiNi}_{0.8}\text{Co}_{0.15}\text{Al}_{0.05}\text{O}_2$, but the magnitude of the expansion and contraction was

much larger for cNCA (Figure 5-7 (c)). The % change of the c lattice parameter was smaller for $\text{LiNi}_{0.8}\text{Co}_{0.15}\text{Al}_{0.05}\text{O}_2$ than for cNCA because either $\text{LiNi}_{0.8}\text{Co}_{0.15}\text{Al}_{0.05}\text{O}_2$ had more Ni in the 3a site, which made the structure more rigid or because the true degree of delithiation was slightly less in $\text{LiNi}_{0.8}\text{Co}_{0.15}\text{Al}_{0.05}\text{O}_2$ relative to cNCA.

The c lattice parameters for each electrode, displayed in Figure 5-26 (a), make evident the differences that Al and Co ions have on LiNiO_2 . When fully charged, $\text{LiNi}_{0.8}\text{Al}_{0.2}\text{O}_2$ (O) only had a 2.09% contraction of the c lattice, whereas the c axis of $\text{LiNi}_{0.8}\text{Co}_{0.2}\text{O}_2$ decreased by 5.48%. $\text{LiNi}_{0.8}\text{Co}_{0.15}\text{Al}_{0.05}\text{O}_2$, which has 5% Al and 15% Co substitution for Ni, had a 4.35% contraction of its c parameter which is between the results for $\text{LiNi}_{0.8}\text{Al}_{0.2}\text{O}_2$ (O) and $\text{LiNi}_{0.8}\text{Co}_{0.2}\text{O}_2$. A comparison of the $\text{LiNi}_{0.8}\text{Co}_{0.15}\text{Al}_{0.05}\text{O}_2$ and $\text{LiNi}_{0.8}\text{Co}_{0.2}\text{O}_2$ materials revealed that Al ions were more efficient at minimizing the c axis structural change than Co ions, *even at the same lithiation*. At lower states of charge ($x > 0.2$) little difference was observed in the % change of the a lattice parameter (Figure 5-7 (f)) between cNCA, $\text{Li}_x\text{Ni}_{0.8}\text{Co}_{0.15}\text{Al}_{0.05}\text{O}_2$, and $\text{Li}_x\text{Ni}_{0.8}\text{Co}_{0.2}\text{O}_2$ during delithiation. While the higher Al content in $\text{LiNi}_{0.8}\text{Al}_{0.2}\text{O}_2$ (O) did cause a smaller a parameter, the relative change compared to $\text{LiNi}_{0.8}\text{Co}_{0.15}\text{Al}_{0.05}\text{O}_2$ or $\text{LiNi}_{0.8}\text{Co}_{0.2}\text{O}_2$ was minimal and there was no fundamental change in the trend during delithiation.

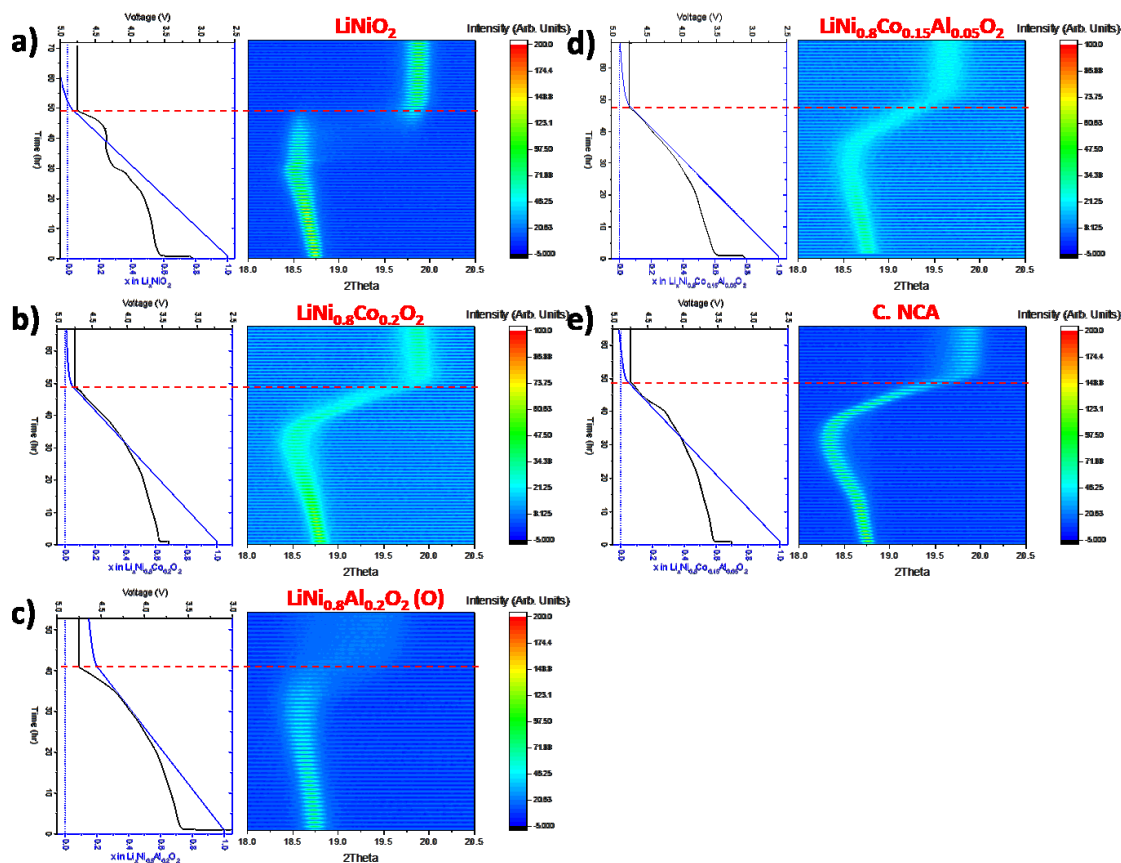


Figure 5-25: In-situ XRD contour plots of the (003) peak and corresponding electrochemical profiles for (a) LiNiO_2 , (b) $\text{LiNi}_{0.8}\text{Co}_{0.2}\text{O}_2$, (c) $\text{LiNi}_{0.8}\text{Al}_{0.2}\text{O}_2$ (O), (d) $\text{LiNi}_{0.8}\text{Co}_{0.15}\text{Al}_{0.05}\text{O}_2$, and (e) cNCA. Cells were charged at a constant current of $C/50$ to 4.75 V, and then held at constant potential indefinitely, all while 1 h XRD scans were continuously running. To avoid missing any features, the experimental parameters were chosen such that $\Delta x \leq 0.02$ for every scan. A red dashed line corresponding to when the potential reached 4.75 V is superimposed on each sub-figure to enable easy comparison between materials.

Analysis of Figure 5-26 (b) shows an expansion of the a lattice parameter for cNCA, $\text{Li}_x\text{Ni}_{0.8}\text{Co}_{0.15}\text{Al}_{0.05}\text{O}_2$, and $\text{Li}_x\text{Ni}_{0.8}\text{Co}_{0.2}\text{O}_2$ at very high states of charge ($x < \sim 0.15$). Even though $\text{LiNi}_{0.8}\text{Al}_{0.2}\text{O}_2$ (O) was fully oxidized, it may not have been sufficiently delithiated for the a parameter to increase. However, it was previously shown that even for the $\text{LiNi}_{1-y}\text{Al}_y\text{O}_2$ materials that could reach such high states of charge, none of the a parameters for any of the $\text{LiNi}_{1-y}\text{Al}_y\text{O}_2$ materials (Figure 5-19 (b)) had a similar expansion during delithiation. Contrastingly, all of the $\text{Li}_x\text{Co}_{1-y}\text{Al}_y\text{O}_2$ materials (Figure 5-6 (b)) show an increasing a axis when $x < \sim 0.5$. For cNCA,

$\text{LiNi}_{0.8}\text{Co}_{0.15}\text{Al}_{0.05}\text{O}_2$, and $\text{LiNi}_{0.8}\text{Co}_{0.2}\text{O}_2$, the lithiation point at which the a axis began to expand appears to be correlated to the amount of Co in the electrode. Because of its lower redox potential, the Ni ions should have been oxidized to 4+ before Co.¹⁰³ Thus, the expansion of the a lattice parameter seems to only occur when Co was being oxidized, which is in agreement with the a lattice parameter results of the group 1 and 2 materials. The *in-situ* XRD results of $\text{Li}_{1-x}\text{Ni}_{0.8}\text{Co}_{0.15}\text{Al}_{0.05}\text{O}_2$ and $\text{Li}_{1-x}\text{Co}_{1/3}\text{Ni}_{1/3}\text{Mn}_{1/3}\text{O}_2$ by Yoon *et al.* also show an expansion of the a parameter at higher states of charge, and that the increase of the a parameter occurs at lower states of charge for $\text{Li}_{1-x}\text{Co}_{1/3}\text{Ni}_{1/3}\text{Mn}_{1/3}\text{O}_2$, than for $\text{Li}_{1-x}\text{Ni}_{0.8}\text{Co}_{0.15}\text{Al}_{0.05}\text{O}_2$ because of its higher Co content.¹³⁸

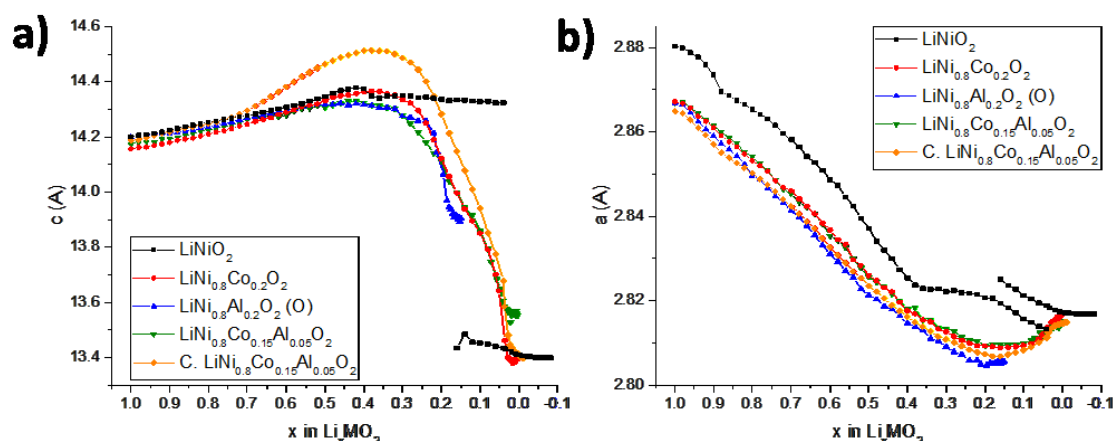


Figure 5-26: Calculated (a) c and (b) a lattice parameters as a function of delithiation for the *in-situ* XRD experiments of LiNiO_2 (black), $\text{LiNi}_{0.8}\text{Co}_{0.2}\text{O}_2$, $\text{LiNi}_{0.8}\text{Al}_{0.2}\text{O}_2$ (O)(blue), $\text{LiNi}_{0.8}\text{Co}_{0.15}\text{Al}_{0.05}\text{O}_2$ (red)(green), and cNCA (orange) positive electrodes. Lattice parameters were calculated from a rhombohedral unit cell using the peak locations of the (003) and (101) peaks.

The (003) and (104) regions of the *ex-situ* XRD scans of positive electrodes that were charged to 4.75 V under PITT conditions are presented in Figure 5-27. The associated charging profiles are provided in Figure S5 (c) while the OCV, final lithiation and % Ni/Co oxidation results are listed in Table 5-II. LiNiO_2 and $\text{LiNi}_{0.8}\text{Co}_{0.2}\text{O}_2$, which have no Al in their structures and can be fully delithiated, had the highest angle (003) and (104) peaks of all group 3 materials.

Similar to LiNiO_2 , at the end of charge $\text{LiNi}_{0.8}\text{Co}_{0.2}\text{O}_2$ was indexed to a NiO_2 -type material in either the $R\bar{3}m$ or $C2/m$ space groups. Even though $\text{Li}_x\text{Ni}_{0.8}\text{Co}_{0.2}\text{O}_2$ has less Li in its structure ($x = 0.015$) than the Li_xNiO_2 *ex-situ* XRD sample ($x = 0.047$), the (003) and (104) peaks were still measured at lower angles. This confirms that substitution of Co for Ni induced a contraction in the c lattice parameter and helped resist large structural changes, without preventing full delithiation of the material. In agreement with the conclusions drawn from sections 5.4.2 and 5.4.3, Al substitution limited the structural transformations that occurred at the highest states of charge and prevented the (003) and (104) peaks from completely shifting to higher angles. cNCA and $\text{LiNi}_{0.8}\text{Co}_{0.15}\text{Al}_{0.05}\text{O}_2$, which substituted 5% Al for Co in $\text{LiNi}_{0.8}\text{Co}_{0.2}\text{O}_2$, had peak positions at slightly lower angles than $\text{LiNi}_{0.8}\text{Co}_{0.2}\text{O}_2$. In the $\text{LiNi}_{0.8}\text{Al}_{0.2}\text{O}_2$ (O and DO) samples, where all of the Co in $\text{LiNi}_{0.8}\text{Co}_{0.2}\text{O}_2$ was exchanged for Al, the peak positions were observed at even lower angles. At a full state of charge, all Al substituted materials conclusively had a partially delithiated $R\bar{3}m$ structure.

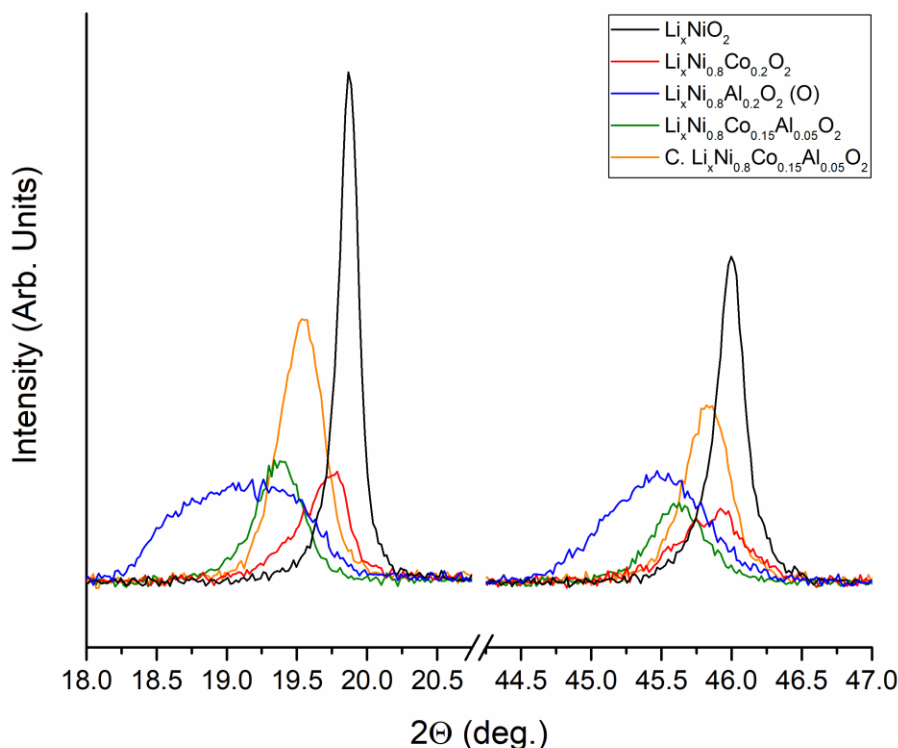


Figure 5-27: Ex-situ XRD scans of positive electrodes that were charged to 4.75 V under PITT conditions (10 mV step, 1 mA/g cutoff). Results are presented in the regions of the (003) (18-21.5°) and (104) (42-47°) peaks for LiNiO_2 (black), $\text{LiNi}_{0.8}\text{Co}_{0.2}\text{O}_2$ (red), $\text{LiNi}_{0.8}\text{Al}_{0.2}\text{O}_2$ (O) (blue), $\text{LiNi}_{0.8}\text{Co}_{0.15}\text{Al}_{0.05}\text{O}_2$ (green), and cNCA (orange). All coin cells were disassembled in an Ar-filled glovebox and the XRD samples were sealed with a Kapton film to temporarily prevent hydrogen intercalation upon exposure to ambient atmosphere.

The OCV of $\text{LiNi}_{0.8}\text{Co}_{0.2}\text{O}_2$ (4.646 V) was substantially higher than LiNiO_2 (4.466 V) likely due to the presence of Co, which oxidized at higher potentials than Ni and shifted the equilibrium voltage profile higher. As was previously discussed, the OCV of $\text{LiNi}_{1-y}\text{Al}_y\text{O}_2$ was raised as the amount of Al in the structure increased. Comparison of $\text{LiNi}_{0.8}\text{Co}_{0.2}\text{O}_2$, $\text{LiNi}_{0.8}\text{Co}_{0.15}\text{Al}_{0.05}\text{O}_2$, and $\text{LiNi}_{0.8}\text{Al}_{0.2}\text{O}_2$ demonstrated that substituting Ni with Co instead of Al can increase the OCV even further. In particular, $\text{LiNi}_{0.8}\text{Co}_{0.2}\text{O}_2$ (4.646 V) had an incrementally higher OCV than $\text{LiNi}_{0.8}\text{Co}_{0.15}\text{Al}_{0.05}\text{O}_2$ (4.637 V) despite being at a slightly lower state of charge, and had a substantially higher OCV than $\text{LiNi}_{0.8}\text{Al}_{0.2}\text{O}_2$ (O) (4.613 V). Thus for LiNiO_2 -based

electrodes at similar states of charge, Co ions were more effective in raising the OCV than Al ions.

The *operando* microcalorimetry results of the group 3 materials are presented in Figure 5-28. Similar to the Al-substituted LiNiO_2 materials, cNCA, $\text{LiNi}_{0.8}\text{Co}_{0.15}\text{Al}_{0.05}\text{O}_2$, and $\text{LiNi}_{0.8}\text{Co}_{0.2}\text{O}_2$ were exothermic when charging began and showed no heat flux peaks related to the monoclinic phase. All group 3 materials had very little hysteresis in the heat flux profiles, which is in agreement with the effect of Al substitution observed in the microcalorimetry results of the group 1 and 2 materials. The lack of observable phase changes or hysteresis in the heat flux profiles supports the conclusion that Co and Al substitution into LiNiO_2 suppressed phase changes within the electrode material. In general, the heat flux profiles for cNCA, $\text{LiNi}_{0.8}\text{Co}_{0.15}\text{Al}_{0.05}\text{O}_2$, and $\text{LiNi}_{0.8}\text{Co}_{0.2}\text{O}_2$ were always exothermic, and in good agreement with the LiNiO_2 -based group 2 materials. The negative heat flux region between $0.85 \geq x \geq 0.54$ during the discharge of $\text{Li}_x\text{Ni}_{0.8}\text{Co}_{0.15}\text{Al}_{0.05}\text{O}_2$ was due to a small drift in the heat flux measurement and was not representative of the material showing endothermic behavior. Of particular note was that the $\text{LiNi}_{0.8}\text{Co}_{0.2}\text{O}_2$ exhibited much lower exothermic signal at the end of charge than all the corresponding synthesized (high surface area) materials. The only material which was comparable was the much lower surface area cNCA.

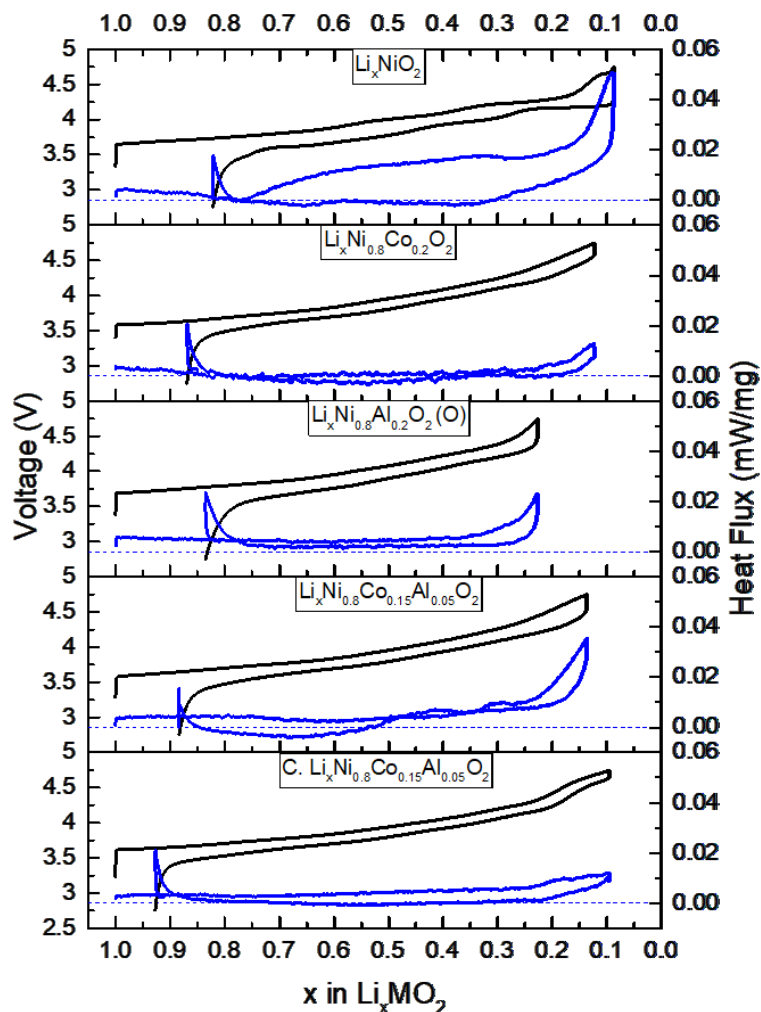


Figure 5-28: Operando isothermal microcalorimetry voltage (black) and heat flux (blue) measurements are presented during the first cycle for each group 3 material. Coin cells were cycled at a constant current (25 mA/g) between 4.75 V and 2.75 V, while the chamber was isothermal at 30°C.

5.4.4.3 Cycling Performance: 20% Substituted LiNiO₂

The cycling capacity and % capacity retention results of the group 3 materials are shown in Figure 5-29 and Figure 5-13 (c, f), respectively. The first cycle charge capacity, discharge capacity, and irreversible loss are presented in Table 5-VI. When 4.5 V was used as the upper cutoff potential, LiNiO₂ has the highest first cycle discharge capacity, but realized very poor cycling stability. The first cycle discharge capacities for LiNi_{0.8}Co_{0.15}Al_{0.05}O₂ and LiNi_{0.8}Co_{0.2}O₂

were higher than for cNCA. However, as is evident from Figure 5-29 (a), the discharge capacities for $\text{LiNi}_{0.8}\text{Co}_{0.15}\text{Al}_{0.05}\text{O}_2$ and $\text{LiNi}_{0.8}\text{Co}_{0.2}\text{O}_2$ drop during the first few cycles, while the discharge capacity of cNCA actually increased slightly. As a result, for the majority of the cycles studied the discharge capacity of cNCA is ~ 14 mAh/g higher than $\text{LiNi}_{0.8}\text{Co}_{0.15}\text{Al}_{0.05}\text{O}_2$ and ~ 22 mAh/g above $\text{LiNi}_{0.8}\text{Co}_{0.2}\text{O}_2$. The difference in cycling behavior between cNCA and $\text{LiNi}_{0.8}\text{Co}_{0.15}\text{Al}_{0.05}\text{O}_2$ during the first few cycles can be attributed the difference in the surface areas of the two materials, and is discussed in more detail later.

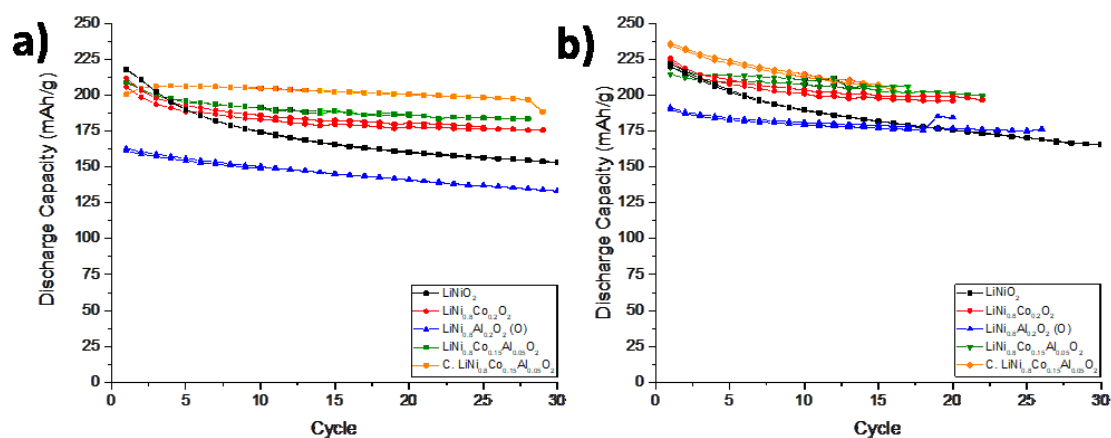


Figure 5-29: Discharge capacity vs. cycle results for coin cells charged to either (a) 4.5 V or (b) 4.75 V. Cells were charged at 20 mA/g to V_{max} (4.5 or 4.75 V), held at a constant potential until the current dropped below 10 mA/g, and were then discharged at 10 mA/g to 2.75 V, all at room temperature. Duplicate cells of each positive electrode material were made to ensure reproducibility.

Table 5-VI: First cycle charge capacity, discharge capacity, and irreversible loss for each coin cell shown in Figure 5-29. The theoretical capacity (assuming Al is electrochemically active) is given for each material.

Active Material	Vmax	First Cycle Charge Capacity (mAh/g)	First Cycle Discharge Capacity (mAh/g)	Irreversible Loss (mAh/g)	Irreversible Loss (%)	Theoretical Capacity (mAh/g)
LiNiO ₂	4.5	255.18	217.78	37.40	14.66	274.52
LiNiO ₂	4.5	255.30	218.33	36.97	14.48	274.52
LiNiO ₂	4.75	265.52	221.92	43.60	16.42	274.52
LiNiO ₂	4.75	262.41	220.13	42.28	16.11	274.52
LiNi _{0.8} Co _{0.2} O ₂	4.5	238.59	211.78	26.81	11.24	274.39
LiNi _{0.8} Co _{0.2} O ₂	4.5	230.83	205.73	25.1	10.87	274.39
LiNi _{0.8} Co _{0.2} O ₂	4.75	251.2	224.42	26.78	10.66	274.39
LiNi _{0.8} Co _{0.2} O ₂	4.75	252.08	225.89	26.19	10.39	274.39
LiNi _{0.8} Al _{0.2} O ₂ (O)	4.5	194.43	161.15	33.28	17.12	293.59
LiNi _{0.8} Al _{0.2} O ₂ (O)	4.5	196.48	162.92	33.55	17.08	293.59
LiNi _{0.8} Al _{0.2} O ₂ (O)	4.75	232.90	191.40	41.50	17.82	293.59
LiNi _{0.8} Al _{0.2} O ₂ (O)	4.75	232.51	190.03	42.48	18.27	293.59
LiNi _{0.8} Co _{0.15} Al _{0.05} O ₂	4.5	224.78	209.22	15.56	6.92	278.95
LiNi _{0.8} Co _{0.15} Al _{0.05} O ₂	4.5	224.92	208.86	16.06	7.14	278.95
LiNi _{0.8} Co _{0.15} Al _{0.05} O ₂	4.75	241.11	214.65	26.46	10.97	278.95
LiNi _{0.8} Co _{0.15} Al _{0.05} O ₂	4.75	247.46	219.05	28.41	11.48	278.95
C. LiNi _{0.8} Co _{0.15} Al _{0.05} O ₂	4.5	220.61	200.79	19.82	8.98	278.95
C. LiNi _{0.8} Co _{0.15} Al _{0.05} O ₂	4.5	220.33	200.72	19.61	8.90	278.95
C. LiNi _{0.8} Co _{0.15} Al _{0.05} O ₂	4.75	253.03	234.62	18.41	7.28	278.95
C. LiNi _{0.8} Co _{0.15} Al _{0.05} O ₂	4.75	254.77	236.13	18.64	7.32	278.95

With a 4.5 V potential limit, cNCA and LiNi_{0.8}Co_{0.15}Al_{0.05}O₂ showed similar capacity loss rates after the first 5 cycles, which was associated to the identical chemistries between the two materials. As the materials were charged to 4.75 V (Figure 5-29 (b)), cNCA initially maintained a higher discharge capacity but exhibited a much more rapid decay in capacity retention than LiNi_{0.8}Co_{0.15}Al_{0.05}O₂. Relative to the other group 3 materials, LiNi_{0.8}Al_{0.2}O₂ (O) had significantly lower discharge capacities on every cycle, which was attributed to it only being capable of having 0.8 Li extracted per formula unit. However, LiNi_{0.8}Al_{0.2}O₂ (O) had very good cycling stability, especially at 4.75 V (Figure 5-13 (f)), and experienced less capacity fade than all of the other group 3 materials.

As a result of being able to have all of its Li deintercalated, LiNi_{0.8}Co_{0.2}O₂ had higher first cycle charging and discharging capacities than LiNi_{0.8}Co_{0.15}Al_{0.05}O₂, although, the cycling

stability of $\text{LiNi}_{0.8}\text{Co}_{0.15}\text{Al}_{0.05}\text{O}_2$ was slightly higher than $\text{LiNi}_{0.8}\text{Co}_{0.2}\text{O}_2$ in both potential windows. $\text{LiNi}_{0.8}\text{Co}_{0.15}\text{Al}_{0.05}\text{O}_2$ and $\text{LiNi}_{0.8}\text{Co}_{0.2}\text{O}_2$, which both had higher surface areas than cNCA, likely experienced significantly more parasitic electrode-electrolyte reactions on the first charge relative to cNCA. These parasitic surface reactions caused the development of a larger cathode-electrolyte interface and increased the charge transfer impedance. The impact of these reactions is evident by the higher irreversible loss (Table 5-VI) and lower initial discharge capacities for $\text{LiNi}_{0.8}\text{Co}_{0.15}\text{Al}_{0.05}\text{O}_2$ and $\text{LiNi}_{0.8}\text{Co}_{0.2}\text{O}_2$. The reduced amount of parasitic reactions on cNCA had a beneficial effect on the material's discharge capacity and cycling stability. At the same time, because cNCA had a larger particle size than the synthesized materials it was more susceptible to fracturing, especially when subjected to the enormous structural changes upon charging to 4.75 V. As the material fractures, new surfaces were created, which in turn, parasitically react with the electrolyte.

A larger change in the c axis was expected to degrade the material's cycling stability since there would repeatedly be increased strain on the lattice. When charged to 4.5 V, cNCA and $\text{LiNi}_{0.8}\text{Co}_{0.15}\text{Al}_{0.05}\text{O}_2$ had similar relative contractions in the c lattice parameter (Figure 5-7), and nearly identical cycling stabilities. In contrast, when the materials were charged to 4.75 V cNCA had a substantially larger change in the c axis compared to $\text{LiNi}_{0.8}\text{Co}_{0.15}\text{Al}_{0.05}\text{O}_2$, and could explain why cNCA had a worse cycling stability than $\text{LiNi}_{0.8}\text{Co}_{0.15}\text{Al}_{0.05}\text{O}_2$. Direct comparison of the cycling capabilities for these materials shows that cNCA and $\text{LiNi}_{0.8}\text{Co}_{0.15}\text{Al}_{0.05}\text{O}_2$ had similar initial charge capacities and % irreversible losses, but that the discharge capacity for cNCA was higher, while $\text{LiNi}_{0.8}\text{Co}_{0.15}\text{Al}_{0.05}\text{O}_2$ had markedly better cycling stability. The lower discharge capacity for $\text{LiNi}_{0.8}\text{Co}_{0.15}\text{Al}_{0.05}\text{O}_2$ during the first few cycles was due to the higher impedance from the increased electrode-electrolyte reactions. As shown in Figure 5-26 (a), $\text{LiNi}_{0.8}\text{Co}_{0.15}\text{Al}_{0.05}\text{O}_2$ had substantially smaller variation in the c axis compared to cNCA, which is expected to induce a reduced amount of particle cracking and improve the material's cycling stability. Thus,

while the difference in the initial electrochemical performance between cNCA and $\text{LiNi}_{0.8}\text{Co}_{0.15}\text{Al}_{0.05}\text{O}_2$ can be attributed to the effect of surface reactions, the discrepancy in the extended cycling stability was mainly determined by the structural changes within each material.

The impedance development for the group 3 materials during the first 15 cycles is displayed in Figure 5-30 (a-e). cNCA , $\text{LiNi}_{0.8}\text{Co}_{0.15}\text{Al}_{0.05}\text{O}_2$, $\text{LiNi}_{0.8}\text{Co}_{0.2}\text{O}_2$, and $\text{LiNi}_{0.8}\text{Al}_{0.2}\text{O}_2$ (O) each had little impedance growth after the first cycle and then nearly no change to the voltage profile after the 5th cycle. All of the substituted group 3 materials showed a reduction in the impedance growth compared to LiNiO_2 , which confirmed the role that Al and Co ions had on stabilizing the LiNiO_2 structure. The very low impedance development on these materials confirmed the high structural stability of these electrode materials even when being charged to such high potentials.

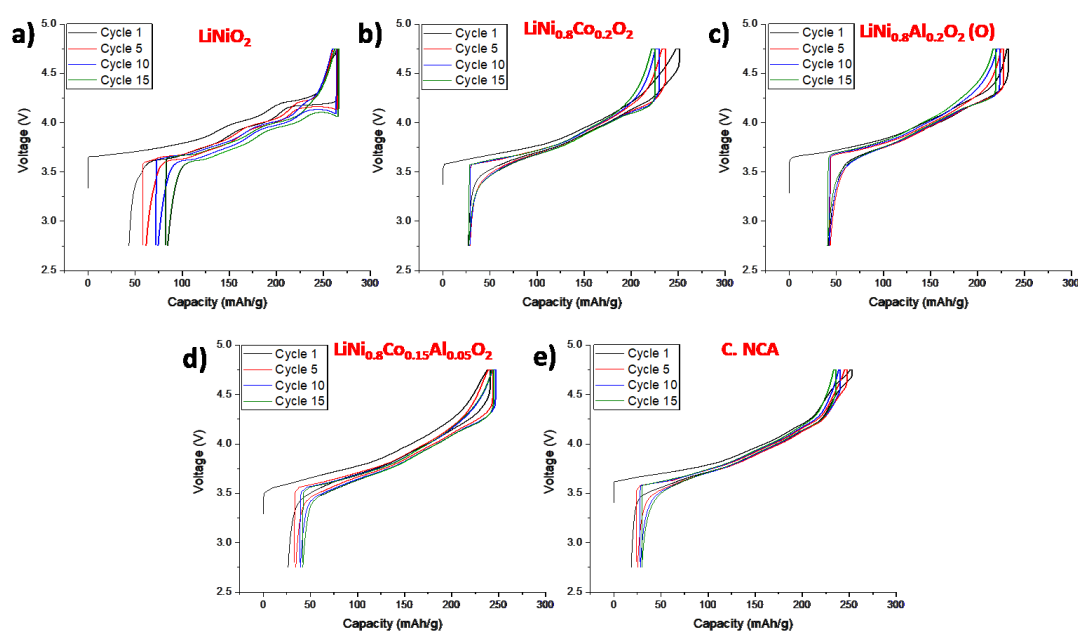


Figure 5-30: The voltage vs. capacity curves of the 1st, 5th, 10th and 15th cycles from a 4.75 V cycling cell is shown for (a) LiNiO_2 , (b) $\text{LiNi}_{0.8}\text{Co}_{0.2}\text{O}_2$, (c) $\text{LiNi}_{0.8}\text{Al}_{0.2}\text{O}_2$ (O), (d) $\text{LiNi}_{0.8}\text{Co}_{0.15}\text{Al}_{0.05}\text{O}_2$, and (e) C. NCA. Each cell was charged to 4.75 V at 20 mA/g, held at 4.75 V until the current went below 10 mA/g, and then was discharged at 10 mA/g to 2.75 V, all at room temperature.

5.4.4.4 Dissolution: 20% Substituted LiNiO₂

The Ni and Co dissolution results for the group 3 materials, presented in Table 5-IV, support the previously drawn conclusions. cNCA has much lower Ni and Co dissolution than LiNi_{0.8}Co_{0.15}Al_{0.05}O₂ because of its significantly lower surface area. LiNi_{0.8}Co_{0.15}Al_{0.05}O₂ and LiNi_{0.8}Co_{0.2}O₂, which had similar surface areas, had nearly identical % Ni and % Co dissolution. In contrast to the much lower dissolution observed for 5% Al substitution into LiCoO₂ or LiNiO₂, substituting Co for Ni was found to have significantly increased the amount of transition metal dissolution relative to LiNiO₂. It seems that Co catalyzes dissolution regardless of whether it is the sole transition metal, substituted into LiNiO₂ or in a mixture with both Ni and Al ions. From the three materials with both Ni and Co ions, it's evident that there was no preferential dissolution between Ni and Co. Although 5% Al substitution was very effective in lowering the dissolution rates of LiCoO₂ and LiNiO₂, it was not beneficial for LiNi_{0.8}Co_{0.2}O₂.

The corrosion current results, presented in Figure 5-14 (c), show a small increase in current for LiNi_{0.8}Co_{0.15}Al_{0.05}O₂ and LiNi_{0.8}Co_{0.2}O₂ relative to the expected delithiation current profile. This increase in parasitic reactions with the electrolyte may be induced by the Co ions in both materials. The group 1 and 2 materials showed that only the Co-rich materials had any increase in corrosion current, and that the Ni-rich materials, even without any Al substitution, did not have an increase in parasitic current. The substantially higher corrosion current as well as Ni and Co dissolution in LiNi_{0.8}Co_{0.15}Al_{0.05}O₂ and LiNi_{0.8}Co_{0.2}O₂ compared to LiNiO₂ or LiNi_{0.95}Al_{0.05}O₂, suggests that Co substitution into Ni-rich materials degrades the material's resistance to HF attack. In Co-substituted Ni-rich materials, not only did the Co ions dissolve into the electrolyte, but the Co ions seemed to increase the propensity for the Ni ions to dissolve as well. The higher Ni dissolution in LiNi_{0.8}Co_{0.15}Al_{0.05}O₂ and LiNi_{0.8}Co_{0.2}O₂ relative to LiNiO₂ and LiNi_{0.95}Al_{0.05}O₂ may have been from the increased surface porosity or degraded surface structure that was likely to occur with Co dissolution.

5.5 Discussion

5.5.1 Influence of Al

As was clearly shown with the group 1 and 2 materials, Al substitution into LiCoO_2 or LiNiO_2 had a very significant impact on preventing phase transformations and in reducing the structural changes to the electrode material during delithiation and subsequent lithiation. Suppression of the structural transitions and variation in the lattice parameters during charging and discharging was directly correlated to the amount of Al in the electrode material. The 5% Al in $\text{LiCo}_{0.95}\text{Al}_{0.05}\text{O}_2$ was sufficient to prevent the formation of the O1 phase that was observed for cLCO and LiCoO_2 at full states of charge. Even though 5% Al substitution in LiNiO_2 lowered the Ni content on the 3a site to 0.026, the Al was sufficient to maintain the $R\bar{3}m$ structure at a full state of charge. When more Al was substituted into either LiCoO_2 or LiNiO_2 , the phase transformations became less distinct, and the crystal structure became more rigid. LiCoO_2 , LiNiO_2 , and the 20% Al-substituted versions of each base material were discharged down to 0.5 V (not shown) and the Al ions caused no additional phase transformations and didn't impede the full transformations to Co/Ni metal and Li_2O . This confirms that Al substitution for Co and Ni did not distort the phase transformations of these electrode materials, even when completely lithiated. As a result of the beneficial effects that Al substitution had on the phase progression of $\text{LiCo}_y\text{Al}_{1-y}\text{O}_2$ and $\text{LiNi}_y\text{Al}_{1-y}\text{O}_2$, a stabilization of the Li^+ diffusivity in Al-substituted materials was observed, especially when lower Al concentrations were used. Al substitution substantially reduced the magnitude of the transition metal dissolution that occurs when the electrode material was near full delithiation (Table 5-IV) for both the LiCoO_2 and LiNiO_2 -based materials.

Despite the favorable effects of Al substitution into LiCoO_2 , Figure 5-11 shows that inserting Al for Co did not improve the electrode's cycling capacity or stability, and instead increased the first cycle irreversible capacity loss. Based on the structural considerations, Al-

substituted LiCoO_2 materials should have superior cycling performance to LiCoO_2 at high states of charge. As shown in Figure 5-7 (a, d) Al substitution into LiCoO_2 the reduced structural changes that occurred during delithiation to 4.75 V, and prevented the formation of the O1 phase, even at equivalent states of charge. While $\text{LiCo}_{0.95}\text{Al}_{0.05}\text{O}_2$ and $\text{LiCo}_{0.9}\text{Al}_{0.1}\text{O}_2$ still had substantial changes to the a and c lattice parameters during charging, the unit cell dimensions in $\text{LiCo}_{0.8}\text{Al}_{0.2}\text{O}_2$ were relatively invariant. The terrible electrochemical performance and high irreversible capacity loss of $\text{LiCo}_{0.8}\text{Al}_{0.2}\text{O}_2$ was particularly surprising because $\text{LiCo}_{0.8}\text{Al}_{0.2}\text{O}_2$ was structurally very stable and the phase transitions were reversible. While the cycling stability was very poor when cycled to either cutoff potential it was markedly worse when charged to 4.75 V, indicating a high voltage degradation mechanism. No structural decomposition was observed by *in-situ* XRD or PITT experiments when $\text{LiCo}_{0.8}\text{Al}_{0.2}\text{O}_2$ was charged to 4.75 V. Furthermore, the first cycle Li^+ diffusivity in $\text{LiCo}_{0.8}\text{Al}_{0.2}\text{O}_2$ was similar to the other Co-rich materials, suggesting that the material wasn't initially kinetically limited. Thus, the impedance that developed during cycling must be a result of changes to the $\text{LiCo}_{0.8}\text{Al}_{0.2}\text{O}_2$ material. When charged and held at 4.75 V under aggressive thermal conditions, $\text{LiCo}_{0.8}\text{Al}_{0.2}\text{O}_2$ also had substantially less transition metal dissolution (Table 5-IV) or corrosion current (Figure 5-14 (a)) than the other group 1 materials. To determine if the capacity degradation was related to electrode reactions with the electrolyte salt, $\text{LiCo}_{0.8}\text{Al}_{0.2}\text{O}_2$ electrodes were also cycled with a 1M LiBF_4 EC:DMC (1:1) electrolyte. All cells were cycled identically to the previously presented 1M LiPF_6 EC:DMC (1:1) cells (Figure 5-11), and the charge and discharge capacities for both electrolytes are shown in Figure 5-31 (a) and (b), respectively. Changing the electrolyte salt had minimal impact on the cycling stability. In both electrolytes, $\text{LiCo}_{0.8}\text{Al}_{0.2}\text{O}_2$ electrodes had a very high first cycle irreversible capacity (> 60 mAh/g), and poor cycling stability. Regardless of the electrolyte used, all $\text{LiCo}_{0.8}\text{Al}_{0.2}\text{O}_2$ cells had a discharge capacity below 100 mAh/g by the 5th cycle. The LiBF_4 electrolyte is known to contain substantially less H_2O , which subsequently degrades into HF, than its LiPF_6 corollary.^{66,129} Since a similar cycling performance for $\text{LiCo}_{0.8}\text{Al}_{0.2}\text{O}_2$ was observed for both salts, the acid induced

degradation mechanism of the positive electrode was eliminated as the cause of the poor electrochemical capabilities during the initial cycles. In summary, these results indicate that the degradation of the electrochemical performance when Al was added to LiCoO_2 isn't from transition metal dissolution of the positive electrode and subsequent poisoning of the negative electrode, or from increased electrolyte decomposition.

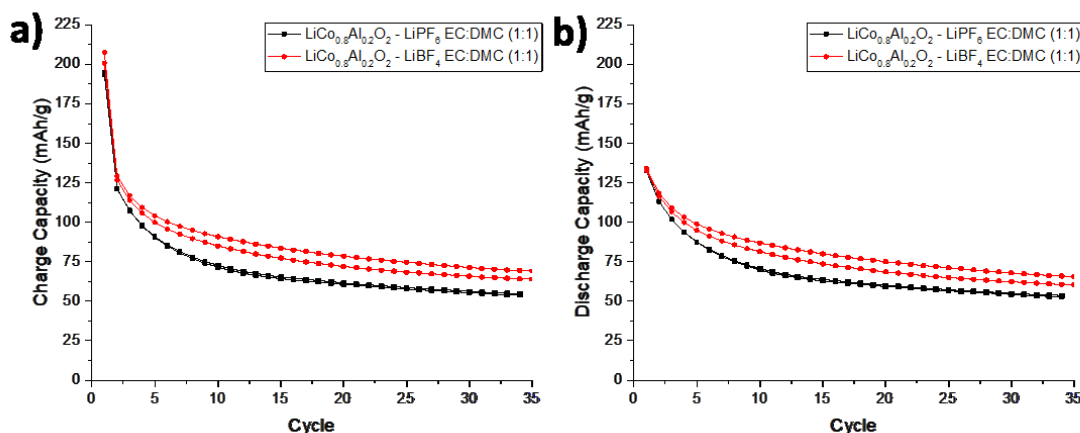


Figure 5-31: (a) Charge and (b) discharge capacities vs. cycle # results for coin cells with $\text{LiCo}_{0.8}\text{Al}_{0.2}\text{O}_2$ positive electrodes. Cells were made with either 1M LiPF_6 EC:DMC (1:1) (black), or 1M LiBF_4 EC:DMC (1:1) (red). Electrodes were charged at 20 mA/g to 4.75 V, held at a constant potential until the current dropped below 10 mA/g, and were then discharged at 10 mA/g to 2.75 V, all while at room temperature. Duplicate cells with each electrolyte were made to ensure reproducibility.

While structural degradation for any of the $\text{LiCo}_{1-y}\text{Al}_y\text{O}_2$ materials wasn't observed on the first cycle, there was evidence of increased impedance development (Figure 5-12 (e)) upon additional cycling. Moreover, exceptionally high irreversible capacities for Al-substituted LiCoO_2 , especially $\text{LiCo}_{0.8}\text{Al}_{0.2}\text{O}_2$, were observed on both the first and subsequent cycles and was correlated to the severe impedance growth of these materials (Figure 5-12 (e)). This suggests that the Al-substituted LiCoO_2 materials underwent some transformation during cycling that had profound negative consequences on the materials' electrochemical capabilities. In contrast, when Al was added into LiNiO_2 the cycling stability improved markedly (Figure 5-22). When cycling

with an upper cutoff potential of 4.75 V, $\text{LiNi}_{0.95}\text{Al}_{0.05}\text{O}_2$ had a higher discharge capacity and lower capacity degradation rate than LiNiO_2 after only 3 cycles. Even increased Al concentrations (10 and 20%), which substantially decreased the electrode's theoretically obtainable capacity, were observed to have better cycling performance than LiNiO_2 when charged to 4.75 V. While $\text{LiNi}_{0.8}\text{Al}_{0.2}\text{O}_2$ (O) initially had a lower capacity than LiNiO_2 , after only 17 cycles $\text{LiNi}_{0.8}\text{Al}_{0.2}\text{O}_2$ (O) maintained a higher discharge capacity and a greater stability with additional cycling. Furthermore, Al substitution into LiNiO_2 was very effective in reducing the impedance development (Figure 5-23), and the Ni dissolution from the fully delithiated electrodes (Table 5-IV).

5.5.2 Influence of Co

Like $\text{LiNi}_{0.8}\text{Al}_{0.2}\text{O}_2$ (O), 20% Co substitution for Ni increased the average voltage profile, and reduced the degree of structural transformations during charging. In contrast to substituting LiNiO_2 with Al, using Co doesn't replace any of the Ni atoms with an electrochemically inactive element, and preserves the ability to fully delithiate the electrode. As a result, much higher discharge capacities were obtained with $\text{LiNi}_{0.8}\text{Co}_{0.2}\text{O}_2$ electrodes relative to $\text{LiNi}_{0.8}\text{Al}_{0.2}\text{O}_2$ (O) or LiNiO_2 . Furthermore the cycling stability was significantly better for $\text{LiNi}_{0.8}\text{Co}_{0.2}\text{O}_2$ and after 20 cycles of charging up to 4.75 V the discharge capacity of $\text{LiNi}_{0.8}\text{Co}_{0.2}\text{O}_2$ (199 mAh/g) was much higher than that of either LiNiO_2 (176 mAh/g) or $\text{LiNi}_{0.8}\text{Al}_{0.2}\text{O}_2$ (O) (177 mAh/g). The improved electrochemical performance at high states of charge of LiNiO_2 with Co substitution may be attributed to the decreased structural transformations. As is evident from Figure 5-4 and Figure 5-15 the final oxidation plateau for LiCoO_2 is ~ 0.3 V above that for LiNiO_2 . Co substitution was effective in suppressing phase transformations and in minimizing the lattice strain that is associated with them. The cumulative effect of these two phenomena was that the $\text{LiNi}_{0.8}\text{Co}_{0.2}\text{O}_2$ material was more stable at high states of charge and can reversibly cycle in this region

substantially better than LiNiO_2 , despite the fact that the substitution of Co markedly increased the degree of transition metal dissolution.

5.5.3 Influence of Co and Al

Comparison of $\text{LiNi}_{0.8}\text{Co}_{0.15}\text{Al}_{0.05}\text{O}_2$ and $\text{LiNi}_{0.8}\text{Co}_{0.2}\text{O}_2$ gave direct insight into the role that the 5% Al substitution had on the electrochemical performance of layered oxides with both Ni and Co ions. Despite being electrochemically inactive and thus preventing extraction of all of the electrode's lithium, 5% Al substitution into $\text{LiNi}_{0.8}\text{Co}_{0.2}\text{O}_2$ increased the discharge capacity and improved the cycling stability slightly. The *in-situ* XRD results, displayed in Figure 5-25 and Figure 5-26, show that $\text{LiNi}_{0.8}\text{Co}_{0.15}\text{Al}_{0.05}\text{O}_2$ has a smaller change in its unit cell parameters when charged to 4.75 V than $\text{LiNi}_{0.8}\text{Co}_{0.2}\text{O}_2$. This increased structural stability was the key reason why the cycling performance of $\text{LiNi}_{0.8}\text{Co}_{0.15}\text{Al}_{0.05}\text{O}_2$ incrementally exceeded that of $\text{LiNi}_{0.8}\text{Co}_{0.2}\text{O}_2$ at high potentials.

While the cycling stability of layered oxide electrodes near full state of charge was dictated by multiple factors, some aspects were more influential than others. The structural changes that occurred during cycling, particularly in the *c* axis, and the electrode impedance development are identified as the primary factors affecting the cycling stability at higher states of charge. Relative to LiNiO_2 , Co and Al-substituted LiNiO_2 materials clearly demonstrated the beneficial impact that reducing structural transformations had on the electrochemical performance. By decreasing the degree of structural change during charging to 4.75 V, the Co and Al atoms considerably reduced the impedance development, and improved the cycling stability of the Ni-rich electrodes.

5.5.4 Transition Metal – Oxygen Bonding at High States of Charge

The different effect that Al substitution had on LiCoO_2 and LiNiO_2 was likely associated with the fundamental differences between Co and Ni. Two models are presently considered to

explain these fundamental differences. In the first model, the Co and Ni atoms are conceptualized to behave with highly ionic bonds, while the second model investigates a degree of covalency in the transition metal-oxygen bonding. When fully oxidized, a large ionic size difference between Co^{4+} and Ni^{4+} ions is expected, where Co^{4+} is smaller than Ni^{4+} , and both ions are substantially smaller than Al^{3+} . A smaller transition metal radius will contract the metal octahedra layer and weaken the Al-O bonds by pulling the oxygen electron density closer to the more positively charged cation (Co^{4+} or Ni^{4+}). The shorter the transition metal ionic radius is, the more the oxygen's electron density will be shifted towards the transition metal and away from the neighboring Al ion. The weaker Al-O bonds reduces the energy barrier limiting Al migration to the nearby tetrahedral site and subsequent hop to the adjacent 3a octahedral site. Consequentially, when Al-substituted LiCoO_2 is highly charged and the Co ions are predominantly in the 4+ valence state, Al ions should be more likely to migrate into the tetrahedral or 3a octahedral sites. Once in these sites, the Al atoms would be a significant barrier to Li^+ diffusion and severely hinder the electrochemical performance. This phenomenon is expected to scale with Al concentration, and be less prevalent in Al substituted LiNiO_2 because the less ionic Ni^{4+} doesn't weaken the Al-O bonds to the same degree as Co^{4+} does.

In the second scenario, where the transition metal-oxygen bond is considered to be at least partially covalent, oxygen charge compensation becomes possible at high states of charge.^{98,259} An anticipated problem with oxygen charge compensation is that it will likely result in oxygen gas evolution, especially on the particle's surface.^{200,260} It has been previously observed in highly delithiated layered oxide materials, that when O_2 is evolved from the surface, the resulting structure will have a transition metal densification in the surface and subsurface regions.^{171,222} As a result, spinel-like and rocksalt-like structures are formed and these structures drastically increase the positive electrode's impedance, causing substantially worse electrochemical performance.^{66,140}

First-principles calculations^{108,109,261} and experimental studies^{106,107,110–112,254} have observed that oxygen charge compensation occurs during the delithiation of some layered oxide compounds. The presence of oxygen charge compensation is dependent on the overlap of the cation and oxygen ion's electron band states.¹⁰⁹ When there is sufficient overlap of the cation and anion electron bands, the cation's *d* energy levels will accept an electronic transfer from the anionic *sp* levels.^{109,254,261} When this happens, the transition metal is more electronegative than the oxygen atoms so holes will appear on the *sp* bands during charging instead of the *d* bands.²⁵⁴ Since the electron energy levels of Co^{3+} have significant overlap with the oxygen electron energy states Co-based layered oxide materials, like LiCoO_2 , are observed to have extensive oxygen charge compensation during delithiation.^{107,109–111} However, Ni-based layered oxides, such as LiNiO_2 , have little electron band overlap with oxygen and as a result Ni is the electrochemically active ion during oxidation.¹⁰⁹ The NMR and XAS results from Yoon *et al.* shows that during charging of $\text{Li}_{1-x}\text{Co}_{1/3}\text{Ni}_{1/3}\text{Mn}_{1/3}\text{O}_2$, the Mn atoms remain in their initial 4+ state, while the Ni ions are oxidized from 2+ to 4+, the Co^{3+} ions are only slightly oxidized and the remaining charge is compensated by the oxygen ions. By experimentally comparing $\text{Li}_{1-x}\text{Co}_{1/3}\text{Ni}_{1/3}\text{Mn}_{1/3}\text{O}_2$ and $\text{Li}_{1-x}\text{Ni}_{0.5}\text{Mn}_{0.5}\text{O}_2$, they determined that the oxygen atoms were only electrochemically active when Co was present in the structure.^{106,112} It is important to note that when Co is in the positive electrode material, both cobalt and oxygen oxidation occur during delithiation, and that the charge transfer throughout delithiation cannot be solely explained by the oxygen charge compensation.^{110,111}

The change of the *a* lattice parameter that was observed for all positive electrode materials containing Co is likely related to the oxidation of oxygen ions. Particularly interesting is that during charging to high states of charge, the *a* parameter in Li_xCoO_2 -based materials contracted until $x \sim 0.5$, and then expanded with further delithiation. Previous studies which focused on the lower state of charge region determined that the initial delithiation of LiCoO_2

causes an increase in the covalency of the Co-O bonds.^{107,111} This increased bond covalency and partial oxidation of the Co^{3+} ions causes a contraction of the Co octahedra and a decreased a lattice parameter. At higher states of charge the Co-O bonds become more covalent since the Co d and O $2p$ orbitals overlap, and at some critical oxidation point oxygen oxidation should become preferential to oxidation of the Co ions.¹⁰⁸ As the electron density around the oxygen ions is reduced, the attractive forces between the transition metal and O ions should decrease and result in a longer bond length. Since the oxygen charge compensation mechanism becomes prevalent at higher states of charge (after some Co oxidation) an expanding a axis is anticipated in this lithiation region. No expansion of the a lattice parameter was observed for LiNiO_2 -based materials, because there was insufficient overlap between the Ni and O orbitals.¹⁰⁹ The group 3 materials clearly demonstrated that for LiNiO_2 -based materials an expansion of the a lattice parameter was only observed when there was Co substitution. Furthermore, the point in which the a parameter began to expand appears to be correlated to when Co oxidation occurs. Since Ni oxidizes at lower potentials than Co, the increase of the a parameter for cNCA, $\text{Li}_x\text{Ni}_{0.8}\text{Co}_{0.15}\text{Al}_{0.05}\text{O}_2$ and $\text{Li}_x\text{Ni}_{0.8}\text{Co}_{0.2}\text{O}_2$ when $x < \sim 0.2$ can be likely associated to the oxidation of Co. Thus, the expanding a lattice parameter that was measured at higher states of charge for all of the positive electrode materials with Co ions can be attributed to increased charge compensation by the oxygen ions. Interestingly, it was observed that Al substitution into LiCoO_2 and LiNiO_2 had no impact on the expansion of the a axis.

Since Al is electrochemically inactive and remains in the 3+ state, in the Al-substituted LiCoO_2 materials none of the charge is accommodated by the Al ions, and the Al-O bonds would remain relatively unchanged during cycling.²⁶¹ Thus, it is theorized that the oxygen atoms surrounding an Al ion should have considerably reduced redox activity, which in turn would force the oxygen atoms distant from an Al ion to be more electrochemically active. Due to the strong covalency induced by the Al-O bond, oxygen ions that are bonded to both Co and Al ions

would have more “ionic” Co-O bonds and a diminished role in the charge compensation process. By localizing the oxygen charge compensation activity to oxygen atoms that aren’t adjacent to Al ions, an increased susceptibility for oxygen evolution is expected because the electrochemically active oxygen ions would experience a larger change in charge, and a subsequent decrease in stability. As a result, Al substitution would impede the reversibility of the oxygen charge transfer and promote oxygen gas evolution.⁹⁸ Furthermore, the reduced charge of oxidized oxygen ions should lower the energy barrier for transition metal movement into the neighboring tetrahedral or 3a octahedral sites. These structural changes would explain why the electrochemical performance of Al-substituted LiCoO₂ was progressively worse, and why the impedance growth increased as more Al was added into the material. The oxygen oxidation that occurs during delithiation results in a smaller effective charge on the oxygen ions, which has been theoretically and experimentally demonstrated to increase the propensity for oxygen evolution from the positive electrode.^{98,262,263} Since the charge transfer to oxygen ions is only observed in appreciable amounts when Co is present, this degradation mechanism would be negligible in LiNiO₂-based positive electrodes, unless they are substituted with Co.

Regardless of whether the transition metal-oxygen bonds were ionic or covalent, Al substitution for Co is shown to induce a larger degradation of the electrochemical performance than Al substitution for Ni. The poor cycling capabilities of the Al-substituted LiCoO₂ materials were likely associated to the propensity for Al atoms in LiCo_{1-y}Al_yO₂ to migrate to the tetrahedral or 3a octahedral sites. This structural degradation mechanism would become progressively more influential when the electrode was repeatedly cycled to very high potentials, and explains the high irreversible loss, and increased impedance development of Al-substituted LiCoO₂ relative to the pure LiCoO₂ material.

5.5.5 Summary

Table 5-VII provides a succinct overview of the physical and electrochemical characterization results for each positive electrode material at 4.5 and 4.75 V. From the table, key relationships between the changes to each material's structure and electrochemical performance when near a full state of charge can be identified, and an understanding of what determines a material's cycling stability at such high states of charge can be elucidated. It is evident from the % capacity retention after 15 cycles and the % irreversible loss on the first cycle (Table 5-VII) that LiNiO₂ has terrible electrochemical stability relative to the Al-substituted materials. The two phase reaction and large change in the *c* parameter causes the structural degradation of LiNiO₂ at high states of charge. In contrast, Al substitution into LiNiO₂ stabilized the layered structure at high potentials and drastically reduced the structural transformations between 4.5 V and a full state of charge, even for 5% Al substitution. Moreover, Al substitution reduced the transition metal dissolution while maintaining the Li⁺ diffusivity. As a result, the cycling stability of the LiNi_{1-y}Al_yO₂ materials further improved as the Al content increased beyond 5%.

*Table 5-VII: For each positive electrode material, important structural and electrochemical results at 4.5 V and at full state of charge are given (4.75 V). The lithiation (x)/%TM oxidation results are from the ex-situ XRD samples, and the listed values are from the end of the potentiostatic hold at each potential. The OCV results are from the same cells and were taken 1 h after the charging commenced. The % change in the *c* parameter and unit cell volume results were calculated with the in-situ XRD results at 4.5 V and at the end of charge, while the Li⁺ diffusivity data is from the PITT experiments shown in Figures 2, 7, and 13. * denotes a two phase transition between 4.5 and 4.75 V, and ** signifies that two phases were present simultaneously.*

Material	Lithiation (x) / % TM oxidation at 4.5 V	Lithiation (x) / % TM oxidation at 4.75 V	Change in lithiation (x) / % TM oxidation between 4.5 and 4.75 V	% Capacity after 15 cycles to 4.5 V / 4.75 V / difference	% first cycle irreversible loss on cycle to 4.5 V / 4.75 V / difference	% change in <i>c</i> parameter between 4.5 and 4.75 V	% change in unit cell volume between 4.5 and 4.75 V	% TM dissolution (% Ni / % Co)	Change in Li ⁺ diffusivity between 4.5 and 4.75 V (cm ² /s)	% change in Li ⁺ diffusivity between 4.5 and 4.75 V	OCV at 4.75 V (V)
C. LiCoO ₂ *	0.269 / 73.07%	0.016 / 98.37%	0.253 / 25.3%	94.4 / 72.9 / -21.5	2.20 / 4.14 / 1.94	-10.86	-6.59	N/A / 3.83%	-3.69E-14	-92.02	4.592
LiCoO ₂ *	0.289 / 71.06%	0.051 / 94.89%	0.238 / 27.83%	93.9 / 69.8 / -24.1	4.37 / 6.73 / 2.36	-10.73	-6.49	N/A / 5.24%	-3.11E-14	-93.11	4.579
LiCo _{0.95} Al _{0.05} O ₂	0.306 / 73.07%	0.111 / 93.55%	0.195 / 20.48%	89.9 / 61.5 / -28.4	12.14 / 14.83 / 2.69	-5.25	-1.78	N/A / 2.80%	-3.58E-14	-94.71	4.648
LiCo _{0.9} Al _{0.1} O ₂	0.347 / 72.59%	0.167 / 92.55%	0.180 / 19.96%	84.2 / 56.0 / -28.2	16.81 / 20.01 / 3.20	-3.83	-3.54	N/A / 2.48%	-2.44E-14	-92.78	4.682
LiCo _{0.8} Al _{0.2} O ₂	0.404 / 74.44%	0.252 / 93.48%	0.152 / 19.04%	74.3 / 48.2 / -26.1	28.09 / 31.53 / 3.44	-0.44	-0.38	N/A / 1.77%	-6.01E-15	-79.39	4.654
LiNiO ₂ *	0.072 / 92.84%	0.047 / 95.31%	0.025 / 2.47%	76.2 / 82.6 / 6.4	14.48 / 16.11 / 1.63	-6.49 / -0.37**	-6.29 / -0.73**	0.97% / N/A	4.98E-15	181.09	4.466
LiNi _{0.95} Al _{0.05} O ₂	0.099 / 94.85%	0.020 / 103.12%	0.079 / 8.27%	87.3 / 92.2 / 4.9	19.01 / 16.11 / -2.90	-2.83	-2.91	0.82% / N/A	1.72E-15	208.23	4.501
LiNi _{0.9} Al _{0.1} O ₂	0.249 / 83.48%	0.175 / 91.69%	0.074 / 8.21%	84.6 / 92.4 / 7.8	20.02 / 19.77 / -0.25	-2.09	-2.16	1.01% / N/A	6.33E-16	76.54	4.535
LiNi _{0.8} Al _{0.2} O ₂ (O)	0.242 / 94.71%	0.207 / 99.11%	0.035 / 4.40%	89.2 / 93.2 / 4.0	17.08 / 17.82 / 0.74	-1.52	-1.54	0.28% / N/A	-8.70E-15	-67.97	4.613
LiNi _{0.8} Al _{0.2} O ₂ (DO)	0.220 / 97.56%	0.116 / 110.54%	0.104 / 12.98%	88.1 / 86.7 / -1.4	15.51 / 23.81 / 8.30	-1.61	-1.65	2.08% / N/A	-1.73E-15	-68.11	4.588
LiNi _{0.5} Co _{0.5} O ₂	0.117 / 88.30%	0.015 / 98.46%	0.102 / 10.16%	89.2 / 93.2 / 4.0	10.87 / 10.39 / -0.48	-3.84	-3.30	1.75% / 1.86%	-6.11E-15	-72.74	4.646
LiNi _{0.8} Co _{0.15} Al _{0.05} O ₂	0.106 / 94.12%	0.009 / 104.32%	0.097 / 10.20%	90.5 / 94.4 / 3.9	6.92 / 10.97 / 4.05	-3.09	-2.62	1.78% / 1.77%	-2.16E-15	-59.34	4.637
C. LiNi _{0.8} Co _{0.15} Al _{0.05} O ₂	0.173 / 87.06%	0.057 / 99.29%	0.116 / 12.23%	100.8 / 87.8 / -13.0	8.90 / 7.28 / -1.62	-4.83	-4.31	0.82% / 0.68%	-5.73E-14	-92.42	4.725

In comparison to LiNiO_2 , LiCoO_2 had substantially worse stability when cycled to 4.75 V, and after 15 cycles it only retained 69.8% of its capacity, significantly lower than the 82.6% retained by LiNiO_2 . This poor cycling performance can be mainly attributed to the two phase reaction to the O1 phase and the massive c parameter change that accompanied it. This is a much harsher two phase transition than the deleterious C2/m transition observed in LiNiO_2 . The substantial Co dissolution and increased parasitic reactions present on LiCoO_2 at high states of charge also contributed to the diminished stability. Despite preventing the two phase reaction at the end of charge, reducing the Co dissolution, and preserving the reaction kinetics, Al substitution into LiCoO_2 , in contrast to LiNiO_2 , severely degraded the electrodes' stability (Table 5-VII). For the $\text{LiCo}_{1-y}\text{Al}_y\text{O}_2$ materials, accessing very high states of charge possibly promoted the migration of Al ions into the tetrahedral sites, which caused the degradation of the material's electrochemical capabilities. As more Al was substituted into the structure, the more pronounced this failure mechanism became.

The cycling stability at high states of charge for the Ni-Co-Al ternary mixtures was also dependent on the phase transitions between 4.5 and 4.75 V. Comparison of $\text{LiNi}_{0.95}\text{Al}_{0.05}\text{O}_2$, $\text{LiNi}_{0.8}\text{Co}_{0.2}\text{O}_2$, and $\text{LiNi}_{0.8}\text{Co}_{0.15}\text{Al}_{0.05}\text{O}_2$ is beneficial because all three materials have similar theoretical capacities. As with Al, Co substitution into LiNiO_2 was effective at eliminating the high state of charge two phase reactions and in reducing the c lattice parameter variation. In contrast to Al substitution, Co increased the amount of transition metal dissolution, which is due to the catalytic nature of Co. While Al substitution into $\text{LiNi}_{0.8}\text{Co}_{0.2}\text{O}_2$ didn't reduce the magnitude of Ni/Co dissolution, it definitively minimized the lattice changes and improved the cycling stability. Confirmation of the importance that the structural changes have on the cycling stability is apparent in the comparison of cNCA and $\text{LiNi}_{0.8}\text{Co}_{0.15}\text{Al}_{0.05}\text{O}_2$. cNCA showed a feature in the dQ/dV and PITT profiles at ~ 4.6 V that was substantially more prominent than the similar feature in $\text{LiNi}_{0.8}\text{Co}_{0.15}\text{Al}_{0.05}\text{O}_2$ or $\text{LiNi}_{0.8}\text{Co}_{0.2}\text{O}_2$. Since Table 5-VII rules out all other

possibilities, this high state of charge structural transition can be attributed to the worse cycling stability of cNCA relative to $\text{LiNi}_{0.8}\text{Co}_{0.15}\text{Al}_{0.05}\text{O}_2$ and $\text{LiNi}_{0.8}\text{Co}_{0.2}\text{O}_2$ when charged to 4.75 V.

The results presented herein help answer the critical questions regarding whether Ni-Co-Al ternary mixtures like $\text{LiNi}_{0.8}\text{Co}_{0.15}\text{Al}_{0.05}\text{O}_2$ are the best positive electrode materials. As previously mentioned, the substitution of Co into LiNiO_2 had mixed results. However, this work was not an exhaustive evaluation of the impact that Co may have on the performance of the electrode material. Other aspects, such as the electronic conductivity or the impact on transition metal occupation of the 3a site, were not fully investigated and may prove to be critically important properties. Nevertheless, of all the materials studied, $\text{LiNi}_{0.8}\text{Co}_{0.15}\text{Al}_{0.05}\text{O}_2$ and $\text{LiNi}_{0.8}\text{Co}_{0.2}\text{O}_2$, had the best cycling stability near full delithiation.

While it is well documented that carbonate electrolytes are unstable at potentials ≥ 4.5 V and that transition metal dissolution from the positive electrode can degrade a cell's functionality, neither of these failure mechanisms were found to be the primary reason for poor electrochemical performance of layered oxide materials operating near full delithiation.^{61,264} The PITT measurements showed that differences in electrochemical performance between positive electrode materials at such high states of charge couldn't be attributed to differences in the Li^+ diffusivity or to kinetic limitations. Table 5-VII also shows that the % change in the c parameter or in the unit cell volume between 4.5 and 4.75 V was largely independent of the each material's cycling stability. Furthermore, the change in lithiation and amount of transition metal oxidation between 4.5 and 4.75 V was also unrelated to the electrochemical performance. Instead, the cycling stability of these layered oxide materials at or near full delithiation was mainly dependent on the intrinsic structural stability of the positive electrode material. Specifically, the elimination of a two phase reaction at the end of charge and the prevention of transition metal migration into undesired sites was identified as the primary factors dictating the cycling stability. Thus, for optimal performance at such high states of charge it is critically important that, first and foremost,

the positive electrode material is devoid of two phase transitions with significant lattice mismatch, robust enough to withstand the large single phase structural evolution and the correlated stresses that occur during cycling, as well as preventing internal migration of metal ions to unfavorable sites. After this foundation is established, long term impedance evolution from failure modes originating at the surface needs to be addressed.

5.6 Conclusions

The cycling capacity and stability of the layered oxide positive electrodes near full delithiation was determined to be primarily attributed to the intrinsic stability of the electrode material. Using an extensive array of electrochemical techniques along with *in-situ* XRD and *operando* microcalorimetry, the impact of Al substitution on the structural and electrochemical properties at very high states of charge for LiCoO₂ and LiNiO₂ is shown. While Al substitution into both LiCoO₂ and LiNiO₂-based positive electrodes was observed to stabilize the structural evolution during delithiation, reduce parasitic reactions, and restrict transition metal dissolution, only adding Al to LiNiO₂ improved the electrode's electrochemical performance. Al substitution into LiCoO₂ was ineffective in stabilizing the capacity degradation when cycling to high potentials likely because of changes to the material's electronic structure and the subsequent increase in the charge compensation activity of oxygen ions. Furthermore, at high states of charge Al was observed to migrate into tetrahedral sites and impede the electrochemical reversibility of the electrode. In contrast, both 20% Al or Co substitution into LiNiO₂ was found to significantly reduce the structural transitions and increase the stability during cycling. LiNi_{0.8}Co_{0.15}Al_{0.05}O₂, which has both Al and Co ions, was shown to have superior electrochemical performance than LiNi_{0.8}Al_{0.2}O₂ and LiNi_{0.8}Co_{0.2}O₂ at very high states of charge, which can be attributed to the increased structural stability gained by the mixture of both ions. The results presented herein enhance the collective understanding of how the transition metal chemistry affects the stability and electrochemical performance of layered oxide electrodes at or near full delithiation.

Utilization of the lessons derived from this work will aid in the identification of new positive electrode materials that will minimize the gap between the theoretical and practically obtained electrode energy densities.

5.7 Acknowledgements

The authors would like to acknowledge Gerbrand Ceder for useful discussions. This work was supported as part of NECCES, an Energy Frontier Research Center funded by the U.S. Department of Energy, Office of Science, Office of Basic Energy Sciences under Award No. DE-SC0012583.

6 CONCLUDING REMARKS

The investigations described in chapters 3-5 made significant progress towards understanding the complex behavior of the positive electrode and electrolyte at very high states of charge. Results presented in chapter 3 show the structural degradation of the positive electrode's surface and the corresponding increase in impedance when near full delithiation. The electrode-electrolyte reactions at these potentials induced an immense amount of transition metal dissolution that was sufficiently high to alloy with the negative electrode and shift the entire cell's potential. The CEI and degree of transition metal dissolution was found to be substantially higher when LiPF_6 instead of LiBF_4 was used as the electrolyte salt. The increased magnitude of electrode and electrolyte decomposition when LiPF_6 was used indicates that the HF acid attack degradation mechanism was the main cause of the instability at high potentials. This mechanism is derived from the degradation of the fluorinated salts by reactions with moisture.

The atmospheric exposure work shown in chapter 4 supports these results. The biggest detriments to the electrochemical performance of NCA were the surface impurity species with hydrogen, particularly H_2O and LiHCO_3 , which would react with LiPF_6 producing HF. In contrast

to previous studies, Li_2CO_3 was not found to significantly hamper the cycling stability. In fact, nearly all of the degradation in the electrochemical performance of positive electrodes due to ambient exposure can be attributed to surface impurity species other than Li_2CO_3 . Annealing, even at lower temperatures ($\leq 500^\circ\text{C}$), was observed to be highly effective in removing surface impurity species and in restoring the electrode's cycling capabilities. Furthermore, room temperature growth of Li_2CO_3 on layered oxide materials was determined to be negligible in the absence of moisture. Direct reaction between CO_2 and a layered oxide positive electrode won't readily occur at room temperature, even in a dry CO_2 atmosphere. It was also demonstrated that the positive electrode's OCV can be used as a quick, and low cost measure of the amount of the surface impurity species present.

Despite the critical impacts that the electrode-electrolyte reactions and surface impurity species have on the electrochemical performance of layered oxides at high states of charge, the intrinsic stability of the positive electrode is the most important factor on the cycling stability and reversible capacity. Al substitution into both LiCoO_2 and LiNiO_2 reduced the amount of transition metal dissolution, electrolyte decomposition, and the structural changes during charging and discharging without limiting the Li^+ diffusivity or reaction kinetics. Yet, the electrochemical performance of $\text{LiCo}_{1-y}\text{Al}_y\text{O}_2$ was severely degraded as the Al content increased. However, the cycling stability of $\text{LiNi}_{1-y}\text{Al}_y\text{O}_2$ increased markedly with more Al substitution. This discrepancy was determined to be caused by the different changes to the electronic states of highly delithiated LiCoO_2 and LiNiO_2 -based materials. Because the Co d orbitals overlap with the oxygen $2p$ orbitals at high states of charge the oxygen ions participate in a charge compensation mechanism that promotes oxygen loss and degradation of the positive electrode structure. In spite of this, mixed substitution of Co and Al into LiNiO_2 was effective in improving the material's structural stability and electrochemical performance.

In conjunction, this work took a holistic approach towards understanding the intricate reactions and mechanisms occurring between the positive electrode and electrolyte at very high

potentials. While further work is needed, and is proposed in the following chapter, these results make significant advancements to the collective comprehension of the failure mechanisms of layered oxide positive electrode's when near full delithiation. Lessons derived from this work may be valuable in the quest to develop enhanced positive electrode materials that can be effectively operated at very high states of charge.

7 FUTURE WORK

7.1 Impact from Substitution with Mn and Other Transition Metals

Recently, $\text{LiNi}_x\text{Mn}_y\text{Co}_z\text{O}_2$ ($x + y + z = 1$) positive electrodes have received substantial research and commercial implementation due to their relatively low cost and high energy densities. Furthermore, numerous previous reports have studied the substitution of other transition metals into LiCoO_2 and LiNiO_2 -based materials in an effort to improve the properties of the positive electrode material. In an effort to fully characterize and understand the roles of Ni, Co and Al ions in a layered oxide material, additional transition metals were excluded from the material fabrication and analysis presented in this thesis. Using the characterization and analysis template for positive electrode materials previously discussed, it would be insightful to study the effect of Mn and other transition metal substitution into LiCoO_2 and LiNiO_2 -based materials. Particular focus on the structural and chemical stability of these materials at high states of charge could be beneficial to understanding the fundamental mechanisms of these materials at such high states of charge and in designing a new generation of positive electrode materials.

7.2 Effect of Electrolyte Composition

While ample investigation into the effects that the electrolyte salt and solvent chemistries have on the electrode-electrolyte reactions was completed, the results still left important questions unanswered. Additional work is necessary to fully understand the role that the electrolyte chemistry has on the composition of the CEI, the structural degradation on the positive electrode's surface and on inducing transition metal dissolution from layered oxide materials. Particular focus should be given to understanding the role that the electrolyte solvent has in enabling transition metal dissolution by forming complexes with transition metal ion species and allowing ionic migration throughout the cell. Other important questions to be answered by future studies include whether non-fluorinated salts are more stable on the positive electrode surface at such high states of charge, and if electrolyte additives can be effectively employed to quickly

develop a passivating CEI that reduces the charge transfer impedance development that occurs with prolonged time at high potentials.

7.3 Role of Positive Electrode Surface Coatings

An additional approach to minimizing the electrode-electrolyte reactions and preserving the electrode's structure involves coating the electrode material with a protective barrier. While the use of surface coatings on layered oxide materials has already been demonstrated and contains promising results, there still remain many critical unanswered questions. Comprehensive analysis of various surface coatings on high state of charge positive electrode materials would be acutely beneficial to the practical utilization of layered oxide materials near full delithiation. Future work should evaluate the structural and chemical stability of the surface coatings and of the positive electrode host materials at high states of charge, and compare the results to the bare positive electrode materials. Specific attention should be given to how these coatings affect the electrochemical capabilities of the electrode material, particularly to how the coating impacts the Li^+ transfer from the electrolyte to the electrode's bulk.

REFERENCES

1. Etacheri, V., Marom, R., Elazari, R., Salitra, G. & Aurbach, D. Challenges in the development of advanced Li-ion batteries: a review. *Energy Environ. Sci.* **4**, 3243–3262 (2011).
2. Scherson, D. A. & Palencsár, A. Batteries and Electrochemical Capacitors. *Electrochem. Soc. Interface* **15**, 17–22 (2006).
3. Liu, C., Li, F., Ma, L.-P. & Cheng, H.-M. Advanced materials for energy storage. *Adv. Mater.* **22**, E28–62 (2010).
4. SolRayo - Energy Storage Systems. at <http://solrayo.com/SolRayo/Li-Ion_Batteries.html>
5. Blomgren, G. E. The Development and Future of Lithium Ion Batteries. *J. Electrochem. Soc.* **164**, A5019–A5025 (2017).
6. Burns, R. A. *Fundamentals of Chemistry*. (Prentice Hall, 2002).
7. Gaskell, D. R. *Introduction to the Thermodynamics of Materials*. (Taylor and Francis, 2008).
8. Ponrouch, A. *et al.* Non-aqueous electrolytes for sodium-ion batteries. *J. Mater. Chem. A* **3**, 22–42 (2015).
9. Zhang, S. S. A review on the separators of liquid electrolyte Li-ion batteries. *J. Power Sources* **164**, 351–364 (2007).
10. Johnson Matthey Battery Systems. How cells work. at <<http://www.jmbatterysystems.com/technology/cells/how-cells-work>>
11. Nitta, N., Wu, F., Lee, J. T. & Yushin, G. Li-ion battery materials: Present and future. *Mater. Today* **18**, 252–264 (2015).
12. Placke, T., Kloepsch, R., Dühnen, S. & Winter, M. Lithium ion, lithium metal, and alternative rechargeable battery technologies: the odyssey for high energy density. *J. Solid State Electrochem.* **21**, 1939–1964 (2017).
13. Nishi, Y. *Lithium-Ion Batteries*. *Lithium-Ion Batteries* (2014). doi:10.1016/B978-0-444-59513-3.00002-9
14. Ohzuku, T., Ueda, A. & Nagayama, M. Electrochemistry and Structural Chemistry of LiNiO₂ (R3m) for 4 Volt Secondary Lithium Cells. *J. Electrochem. Soc.* **140**, 1862 (1993).
15. Ohzuku, T. & Brodd, R. J. An overview of positive-electrode materials for advanced lithium-ion batteries. *J. Power Sources* **174**, 449–456 (2007).
16. Batteries, H. O. F., Library, D. E. & Companies, T. M. *Handbook of batteries*. Cell (2004). doi:10.1016/0378-7753(86)80059-3
17. Amatucci, G. G., Tarascon, J. M. & Klein, L. C. CoO₂, The End Member of the LiCoO₂ Solid Solution. *Electrochem. Soc.* **143**, 1114–1123 (1996).
18. Ueda, A. & Ohzuku, T. Solid-State Redox Reactions of LiCoO₂ (R3m) for 4 Volt Secondary Lithium Cells. *J. Electrochem. Soc.* **141**, 2010 (1994).
19. Sina, M. *et al.* Structural phase transformation and Fe valence evolution in FeO_xF_{2-x}/C nanocomposite electrodes during lithiation and de-lithiation processes. *J. Mater. Chem. A* **1**, 11629–11640 (2013).
20. Yamakawa, N., Jiang, M., Key, B. & Grey, C. P. Identifying the local structures formed during lithiation of the conversion material, iron fluoride, in a Li ion battery: A solid-state NMR, X-ray diffraction, and pair distribution function analysis study. *J. Am. Chem. Soc.* **131**, 10525–10536 (2009).
21. Ellis, B. L., Lee, K. T. & Nazar, L. F. Positive electrode materials for Li-Ion and Li-batteries. *Chem. Mater.* **22**, 691–714 (2010).
22. Badway, F., Cosandey, F., Pereira, N. & Amatucci, G. G. Carbon Metal Fluoride

- Nanocomposites. *J. Electrochem. Soc.* **150**, A1318 (2003).
23. Plitz, I. *et al.* Structure and Electrochemistry of Carbon-Metal Fluoride Nanocomposites Fabricated by Solid-State Redox Conversion Reaction. *J. Electrochem. Soc.* **152**, A307 (2005).
 24. Bervas, M. *et al.* Investigation of the Lithiation and Delithiation Conversion Mechanisms of Bismuth Fluoride Nanocomposites. *J. Electrochem. Soc.* **153**, A799 (2006).
 25. Cabana, J., Monconduit, L., Larcher, D. & Palacin, M. R. Beyond intercalation-based Li-ion batteries: The state of the art and challenges of electrode materials reacting through conversion reactions. *Adv. Mater.* **22**, 170–192 (2010).
 26. Fuller, T. F. Simulation and Optimization of the Dual Lithium Ion Insertion Cell. *J. Electrochem. Soc.* **141**, 1 (1994).
 27. Vetter, J. *et al.* Ageing mechanisms in lithium-ion batteries. *J. Power Sources* **147**, 269–281 (2005).
 28. Ma, L. *et al.* Ternary and Quaternary Electrolyte Additive Mixtures for Li-Ion Cells That Promote Long Lifetime, High Discharge Rate and Better Safety. *J. Electrochem. Soc.* **161**, A1261–A1265 (2014).
 29. Wang, H., Jang, Y., Huang, B., Sadoway, D. R. & Chiang, Y. TEM Study of Electrochemical Cycling-Induced Damage and Disorder in LiCoO₂ Cathodes for Rechargeable Lithium Batteries. *J. Electrochem. Soc.* **146**, 473–480 (1999).
 30. Chikkannanavar, S. B., Bernardi, D. M. & Liu, L. A review of blended cathode materials for use in Li-ion batteries. *J. Power Sources* **248**, 91–100 (2014).
 31. Agrawal, R. C. & Pandey, G. P. Solid polymer electrolytes: Materials designing and all-solid-state battery applications: An overview. *J. Phys. D: Appl. Phys.* **41**, (2008).
 32. Ohzuku, T. Formation of Lithium-Graphite Intercalation Compounds in Nonaqueous Electrolytes and Their Application as a Negative Electrode for a Lithium Ion (Shuttlecock) Cell. *J. Electrochem. Soc.* **140**, 2490 (1993).
 33. Buqa, H., Goers, D., Holzapfel, M., Spahr, M. E. & Novák, P. High Rate Capability of Graphite Negative Electrodes for Lithium-Ion Batteries. *J. Electrochem. Soc.* **152**, A474 (2005).
 34. Kaskhedikar, N. A. & Maier, J. Lithium storage in carbon nanostructures. *Adv. Mater.* **21**, 2664–2680 (2009).
 35. Levi, M. D. & Aurbach, D. Diffusion Coefficients of Lithium Ions during Intercalation into Graphite Derived from the Simultaneous Measurements and Modeling of Electrochemical Impedance and Potentiostatic Intermittent Titration Characteristics of Thin Graphite Electrodes. *J. Phys. Chem. B* **101**, 4641–4647 (1997).
 36. Markevich, E., Levi, M. D. & Aurbach, D. Comparison between potentiostatic and galvanostatic intermittent titration techniques for determination of chemical diffusion coefficients in ion-insertion electrodes. *J. Electroanal. Chem.* **580**, 231–237 (2005).
 37. Persson, K. *et al.* Lithium diffusion in graphitic carbon. *J. Phys. Chem. Lett.* **1**, 1176–1180 (2010).
 38. Qi, Y., Guo, H., Hector, L. G. & Timmons, A. Threefold Increase in the Young's Modulus of Graphite Negative Electrode during Lithium Intercalation. *J. Electrochem. Soc.* **157**, A558 (2010).
 39. Hochgatterer, N. S. *et al.* Silicon/Graphite Composite Electrodes for High-Capacity Anodes: Influence of Binder Chemistry on Cycling Stability. *Electrochem. Solid-State Lett.* **11**, A76 (2008).
 40. Aurbach, D. *et al.* An analysis of rechargeable lithium-ion batteries after prolonged cycling. *Electrochim. Acta* **47**, 1899–1911 (2002).
 41. Zhong, K. *et al.* MnO powder as anode active materials for lithium ion batteries. *J. Power Sources* **195**, 3300–3308 (2010).
 42. Poizot, P., Laruelle, S., Grugeon, S. & Tarascon, J.-M. Rationalization of the Low-

- Potential Reactivity of 3d-Metal-Based Inorganic Compounds toward Li. *J. Electrochem. Soc.* **149**, A1212 (2002).
43. Tarascon, J.-M., Poizot, P., Laruelle, S., Grugeon, S. & Dupont, L. Nano-sized transition-metal oxides as negative-electrode materials for lithium-ion batteries. *Nature* **407**, 496–499 (2000).
 44. Poizot, P., Laruelle, S., Grugeon, S., Dupont, L. & Tarascon, J.-M. From the vanadates to 3d-metal oxides negative electrodes. *Ionics (Kiel)*. **6**, 321–330 (2000).
 45. Obrovac, M. N., Dunlap, R. A., Sanderson, R. J. & Dahn, J. R. The Electrochemical Displacement Reaction of Lithium with Metal Oxides. *J. Electrochem. Soc.* **148**, A576 (2001).
 46. Do, J. S. & Weng, C. H. Preparation and characterization of CoO used as anodic material of lithium battery. *J. Power Sources* **146**, 482–486 (2005).
 47. Hatchard, T. D. & Dahn, J. R. In Situ XRD and Electrochemical Study of the Reaction of Lithium with Amorphous Silicon. *J. Electrochem. Soc.* **151**, A838 (2004).
 48. Chandrasekaran, R., Magasinski, A., Yushin, G. & Fuller, T. F. Analysis of Lithium Insertion/Deinsertion in a Silicon Electrode Particle at Room Temperature. *J. Electrochem. Soc.* **157**, A1139 (2010).
 49. Ding, N. *et al.* Determination of the diffusion coefficient of lithium ions in nano-Si. *Solid State Ionics* **180**, 222–225 (2009).
 50. Xie, J. *et al.* Li-ion diffusion in amorphous Si films prepared by RF magnetron sputtering: A comparison of using liquid and polymer electrolytes. *Mater. Chem. Phys.* **120**, 421–425 (2010).
 51. Hy, S., Chen, Y., Liu, J., Rick, J. & Hwang, B. In situ surface enhanced Raman spectroscopic studies of solid electrolyte interphase formation in lithium ion battery electrodes. **256**, 324–328 (2014).
 52. Wang, G. X., Ahn, J. H., Yao, J., Bewlay, S. & Liu, H. K. Nanostructured Si-C composite anodes for lithium-ion batteries. *Electrochem. commun.* **6**, 689–692 (2004).
 53. Beck, F. & Rüetschi, P. Rechargeable batteries with aqueous electrolytes. *Electrochim. Acta* **45**, 2467–2482 (2000).
 54. Luo, J. Y., Cui, W. J., He, P. & Xia, Y. Y. Raising the cycling stability of aqueous lithium-ion batteries by eliminating oxygen in the electrolyte. *Nat. Chem.* **2**, 760–765 (2010).
 55. Li, W., Dahn, J. R. & Wainwright, D. S. Rechargeable Lithium Batteries with Aqueous Electrolytes. *Science (80-.)*. **264**, 1115–1118 (1994).
 56. Manickam, M., Singh, P., Issa, T. B., Thurgate, S. & De Marco, R. Lithium insertion into manganese dioxide electrode in MnO₂/Zn aqueous battery: Part I. A preliminary study. *J. Power Sources* **130**, 254–259 (2004).
 57. Blint, R. J. Binding of Ether and Carbonyl Oxygens to Lithium Ion. *J. Electrochem. Soc.* **142**, 696 (1995).
 58. Ue, M. Mobility and Ionic Association of Lithium Salts in a Propylene Carbonate-Ethyl Methyl Carbonate Mixed Solvent. *J. Electrochem. Soc.* **142**, 2577 (1995).
 59. Park, M., Zhang, X., Chung, M., Less, G. B. & Sastry, A. M. A review of conduction phenomena in Li-ion batteries. *J. Power Sources* **195**, 7904–7929 (2010).
 60. Wang, R. L. & Dahn, J. R. Computational Estimates of Stability of Redox Shuttle Additives for Li-Ion Cells. *J. Electrochem. Soc.* **153**, A1922 (2006).
 61. Xu, K. Nonaqueous liquid electrolytes for lithium-based rechargeable batteries. *Chem. Rev.* **104**, 4303–4417 (2004).
 62. Tarascon, J. M., Tarascon, J. M., Armand, M. & Armand, M. Issues and challenges facing rechargeable lithium batteries. *Nature* **414**, 359–367 (2001).
 63. Gmitter, A. J., Plitz, I. & Amatucci, G. G. High Concentration Dinitrile , 3-Alkoxypropionitrile , and Linear Carbonate Electrolytes Enabled by Vinylene and

- Monofluoroethylene Carbonate Additives. **159**, 370–379 (2012).
64. Pereira, N., Ruotolo, M. C., Lu, M. Y., Badway, F. & Amatucci, G. G. Elevated temperature performance of high voltage $\text{Li}_{1+y}\text{Mn}_{1.5}\text{Ni}_{0.5}\text{O}_{4-x}\text{F}_x$ spinel in window-shifted Li-ion cells. *J. Power Sources* **338**, 145–154 (2016).
 65. Hagh, N. M. & Amatucci, G. G. Effect of cation and anion doping on microstructure and electrochemical properties of the $\text{LiMn}_{1.5}\text{Ni}_{0.5}\text{O}_{4-\delta}$ spinel. *J. Power Sources* **256**, 457–469 (2014).
 66. Faenza, N. V. *et al.* Electrolyte-Induced Surface Transformation and Transition-Metal Dissolution of Fully Delithiated $\text{LiNi}_{0.8}\text{Co}_{0.15}\text{Al}_{0.05}\text{O}_2$. *Langmuir* **33**, (2017).
 67. du Pasquier, A. *et al.* An update on the high temperature ageing mechanism in LiMn_2O_4 - based Li-ion cells. *J. Power Sources* **81–82**, 54–59 (1999).
 68. Schmidt, M. *et al.* Lithium fluoroalkylphosphates: A new class of conducting salts for electrolytes for high energy lithium-ion batteries. *J. Power Sources* **97–98**, 557–560 (2001).
 69. Galiński, M., Lewandowski, A. & Stępnia, I. Ionic liquids as electrolytes. *Electrochim. Acta* **51**, 5567–5580 (2006).
 70. Fergus, J. W. Ceramic and polymeric solid electrolytes for lithium-ion batteries. *J. Power Sources* **195**, 4554–4569 (2010).
 71. Seki, S. *et al.* Degradation mechanism analysis of all-solid-state lithium polymer secondary batteries by using the impedance measurement. *J. Power Sources* **146**, 741–744 (2005).
 72. Matoba, Y., Matsui, S., Tabuchi, M. & Sakai, T. Electrochemical properties of composite polymer electrolyte applied to rechargeable lithium polymer battery. *J. Power Sources* **137**, 284–287 (2004).
 73. Yang, K. Y., Fung, K. Z. & Leu, I. C. Study on the structural change and lithium ion conductivity for the perovskite-type $\text{LaAlO}_3\text{-La}_{0.50}\text{Li}_{0.50}\text{TiO}_3$ solid solution. *J. Alloys Compd.* **438**, 207–216 (2007).
 74. Savitha, T. *et al.* Structural and ionic transport properties of $\text{Li}_2\text{AlZr}[\text{PO}_4]_3$. *J. Power Sources* **157**, 533–536 (2006).
 75. Kanno, R., Hata, T., Kawamoto, Y. & Irie, M. Synthesis of a new lithium ionic conductor, thio-LISICON-lithium germanium sulfide system. *Solid State Ionics* **130**, 97–104 (2000).
 76. Tomita, Y., Matsushita, H., Kobayashi, K., Maeda, Y. & Yamada, K. Substitution effect of ionic conductivity in lithium ion conductor, $\text{Li}_3\text{INBR}_6 - x\text{CL}_x$. *Solid State Ionics* **179**, 867–870 (2008).
 77. Thangadurai, V., Schwenzel, J. & Weppner, W. Tailoring ceramics for specific applications: A case study of the development of all-solid-state lithium batteries. *Ionics (Kiel)*. **11**, 11–23 (2005).
 78. Hamon, Y. *et al.* Influence of sputtering conditions on ionic conductivity of LiPON thin films. *Solid State Ionics* **177**, 257–261 (2006).
 79. Kennedy, J. H. & Zhang, Z. Further Characterization of $\text{SiS}_2\text{-Li}_2\text{S}$ Glasses Doped with Lithium Halide. *J. Electrochem. Soc.* **135**, 859–862 (1988).
 80. Inada, T. *et al.* Fabrications and properties of composite solid-state electrolytes. *Solid State Ionics* **158**, 275–280 (2003).
 81. Chowdari, B. V. R., Subba Rao, G. V. & Lee, G. Y. H. XPS and ionic conductivity studies on $\text{Li}_2\text{O-Al}_2\text{O}_3\text{-(TiO}_2 \text{ or GeO}_2\text{)-P}_2\text{O}_5$ glass-ceramics. *Solid State Ionics* **136–137**, 1067–1075 (2000).
 82. Seino, Y. *et al.* Synthesis of phosphorous sulfide solid electrolyte and all-solid-state lithium batteries with graphite electrode. *Solid State Ionics* **176**, 2389–2393 (2005).
 83. Jacke, S., Song, J., Cherkashinin, G., Dimesso, L. & Jaegermann, W. Investigation of the solid-state electrolyte/cathode LiPON/ LiCoO_2 interface by photoelectron spectroscopy. *Ionics (Kiel)*. **16**, 769–775 (2010).

84. Edström, K., Gustafsson, T. & Thomas, J. O. The cathode-electrolyte interface in the Li-ion battery. *Electrochim. Acta* **50**, 397–403 (2004).
85. Aurbach, D. *et al.* Review on electrode-electrolyte solution interactions, related to cathode materials for Li-ion batteries. *J. Power Sources* **165**, 491–499 (2007).
86. Jow, T. R., Marx, M. B. & Allen, J. L. Distinguishing Li⁺ Charge Transfer Kinetics at NCA/Electrolyte and Graphite/Electrolyte Interfaces, and NCA/Electrolyte and LFP/Electrolyte Interfaces in Li-Ion Cells. *J. Electrochem. Soc.* **159**, A604–A612 (2012).
87. Zhuang, Q. *et al.* An electrochemical impedance spectroscopic study of the electronic and ionic transport properties of LiCoO₂ cathode. *Chinese Sci. Bull.* **52**, 1187–1195 (2007).
88. Lee, S., Seung, C., Amine, K. & Sun, Y. Improvement of long-term cycling performance of Li[Ni_{0.8}Co_{0.15}Al_{0.05}]O₂ by AlF₃ coating. *J. Power Sources* **234**, 201–207 (2013).
89. Abraham, D. P. *et al.* Microscopy and Spectroscopy of Lithium Nickel Oxide-Based Particles Used in High Power Lithium-Ion Cells. *J. Electrochem. Soc.* **150**, A1450–A1456 (2003).
90. Karki, K. *et al.* Tuning the Activity of Oxygen in LiNi_{0.8}Co_{0.15}Al_{0.05}O₂ Battery Electrodes. *ACS Appl. Mater. Interfaces* **8**, 27762–27771 (2016).
91. Watanabe, S., Kinoshita, M., Hosokawa, T., Morigaki, K. & Nakura, K. Capacity fade of LiAl_yNi_{1-x-y}Co_xO₂ cathode for lithium-ion batteries during accelerated calendar and cycle life tests (surface analysis of LiAl_yNi_{1-x-y}Co_xO₂ cathode after cycle tests in restricted depth of discharge ranges). *J. Power Sources* **258**, 210–217 (2014).
92. Shim, J., Kostecki, R., Richardson, T., Song, X. & Striebel, K. a. Electrochemical analysis for cycle performance and capacity fading of a lithium-ion battery cycled at elevated temperature. *J. Power Sources* **112**, 222–230 (2002).
93. Robert, R., Bünzli, C., Berg, E. J. & Novák, P. Activation Mechanism of LiNi_{0.80}Co_{0.15}Al_{0.05}O₂: Surface and Bulk Operando Electrochemical, Differential Electrochemical Mass Spectromet. *Chem. Mater.* **27**, 526–536 (2015).
94. Zhuang, G. V. *et al.* Li₂CO₃ in LiNi_{0.8}Co_{0.15}Al_{0.05}O₂ cathodes and its effects on capacity and power. *J. Power Sources* **134**, 293–297 (2004).
95. Hwang, S. *et al.* Investigation of Changes in the Surface Structure of Li_xNi_{0.8}Co_{0.15}Al_{0.05}O₂ Cathode Materials Induced by the Initial Charge. *Chem. Mater.* **26**, 1084–1092 (2014).
96. Yoon, W. S., Grey, C. P., Balasubramanian, M., Yang, X. Q. & McBreen, J. In situ X-ray absorption spectroscopic study on LiNi_{0.5}Mn_{0.5}O₂ cathode material during electrochemical cycling. *Chem. Mater.* **15**, 3161–3169 (2003).
97. Amatucci, G. G. & Pereira, N. Fluoride based electrode materials for advanced energy storage devices. *J. Fluor. Chem.* **128**, 243–262 (2007).
98. Chen, H., Dawson, J. A. & Harding, J. H. Effects of cationic substitution on structural defects in layered cathode materials LiNiO₂. *J. Mater. Chem. A* **2**, 7988 (2014).
99. Laubach, S. *et al.* Changes in the crystal and electronic structure of LiCoO₂ and LiNiO₂ upon Li intercalation and de-intercalation. *Phys. Chem. Chem. Phys.* **11**, 3010 (2009).
100. Liu, H. S., Zhang, Z. R., Gong, Z. L. & Yang, Y. Origin of Deterioration for LiNiO₂ Cathode Material during Storage in Air. *Electrochem. Solid-State Lett.* **7**, A190–A193 (2004).
101. Krause, L. J., Jensen, L. D. & Dahn, J. R. Measurement of Parasitic Reactions in Li Ion Cells by Electrochemical Calorimetry. *J. Electrochem. Soc.* **159**, A937–A943 (2012).
102. Hoang, K. & Johannes, M. Defect Physics and Chemistry in Layered Mixed Transition Metal Oxide Cathode Materials: (Ni,Co,Mn) vs (Ni,Co,Al). *Chem. Mater.* **28**, 1325–1334 (2016).
103. Radin, M. D. *et al.* Narrowing the Gap between Theoretical and Practical Capacities in Li-Ion Layered Oxide Cathode Materials. *Adv. Energy Mater.* **1602888**, 1–33 (2017).
104. Amatucci, G. G., Tarascon, J. M. & Klein, L. C. Cobalt dissolution in LiCoO₂-based non-aqueous rechargeable batteries. *Solid State Ionics* **83**, 167–173 (1996).

105. Arroyo y de Dompablo, M. E., Van der Ven, A. & Ceder, G. First-principles calculations of lithium ordering and phase stability on Li_xNiO_2 . *Phys. Rev. B* **66**, 64112 (2002).
106. Yoon, W.-S. *et al.* Combined NMR and XAS Study on Local Environments and Electronic Structures of Electrochemically Li-Ion Deintercalated $\text{Li}_{1-x}\text{Co}_{1/3}\text{Ni}_{1/3}\text{Mn}_{1/3}\text{O}_2$ Electrode System. *Electrochem. Solid-State Lett.* **7**, A53 (2004).
107. Graetz, J. *et al.* Electronic structure of chemically-delithiated LiCoO_2 studied by electron energy-loss spectrometry. *J. Phys. Chem. B* **106**, 1286–1289 (2002).
108. Seo, D. H. *et al.* The structural and chemical origin of the oxygen redox activity in layered and cation-disordered Li-excess cathode materials. *Nat. Chem.* **8**, 692–697 (2016).
109. Ceder, G., Aydinol, M. K. & Kohan, A. F. Application of first-principles calculations to the design of rechargeable Li-batteries. *Comput. Mater. Sci.* **8**, 161–169 (1997).
110. Dahéron, L. *et al.* Electron Transfer Mechanisms upon Lithium Deintercalation from LiCoO_2 to CoO_2 Investigated by XPS. *Chem. Mater.* **20**, 583–590 (2008).
111. Yoon, W. S. *et al.* Oxygen contribution on Li-ion intercalation-deintercalation in LiCoO_2 investigated by O K-edge and Co L-edge X-ray absorption spectroscopy. *J. Phys. Chem. B* **106**, 2526–2532 (2002).
112. Yoon, W. S. *et al.* Investigation of the charge compensation mechanism on the electrochemically Li-ion deintercalated $\text{Li}_{1-x}\text{Co}_{1/3}\text{Ni}_{1/3}\text{Mn}_{1/3}\text{O}_2$ electrode system by combination of soft and hard X-ray absorption spectroscopy. *J. Am. Chem. Soc.* **127**, 17479–17487 (2005).
113. Chebiam, R. V., Prado, F. & Manthiram, A. Soft Chemistry Synthesis and Characterization of Layered $\text{Li}_{1-x}\text{Ni}_{1-y}\text{Co}_y\text{O}_{2-\delta}$ ($0 \leq x \leq 1$ and $0 \leq y \leq 1$). *Chem. Mater.* **13**, 2951–2957 (2001).
114. Ratnakumar, B. V., Smart, M. C. & Surampudia, S. Electrochemical impedance spectroscopy and its applications to lithium ion cells. *Batter. Conf. Appl. Adv. 2002. Seventeenth Annu.* 273–277 (2002). doi:10.1109/BCAA.2002.986414
115. Jow, T. R., Marx, M. B. & Allen, J. L. Distinguishing Li^+ Charge Transfer Kinetics at NCA/Electrolyte and Graphite/Electrolyte Interfaces, and NCA/Electrolyte and LFP/Electrolyte Interfaces in Li-Ion Cells. *J. Electrochem. Soc.* **159**, A604 (2012).
116. Orsini, F., Dolle, M. & Tarascon, J. M. Impedance study of the Li^0 /electrolyte interface upon cycling. *Solid State Ionics* **135**, 213–221 (2000).
117. Zhuang, Q. *et al.* LiCoO_2 electrode/electrolyte interface of Li-ion batteries investigated by electrochemical impedance spectroscopy. *Sci. China, Ser. B Chem.* **50**, 776–783 (2007).
118. Zhang, S. S., Xu, K. & Jow, T. R. Electrochemical impedance study on the low temperature of Li-ion batteries. *Electrochim. Acta* **49**, 1057–1061 (2004).
119. Aurbach, D. Common Electroanalytical Behavior of Li Intercalation Processes into Graphite and Transition Metal Oxides. *J. Electrochem. Soc.* **145**, 3024 (1998).
120. Arora, P. & White, R. E. Capacity Fade Mechanisms and Side Reactions in Lithium-Ion Batteries. *J. Electrochem. Soc.* **145**, 3647–3667 (1998).
121. Aurbach, D. *et al.* The Study of Surface Phenomena Related to Electrochemical Lithium Intercalation into Li_xMO_y Host Materials ($\text{M} = \text{Ni}, \text{Mn}$). *J. Electrochem. Soc.* **147**, 1322–1331 (2000).
122. Liu, H., Yang, Y. & Zhang, J. Investigation and improvement on the storage property of $\text{LiNi}_{0.8}\text{Co}_{0.2}\text{O}_2$ as a cathode material for lithium-ion batteries. *J. Power Sources* **162**, 644–650 (2006).
123. Xia, J. *et al.* A Study of Li-Ion Cells Operated to 4.5 V and at 55°C. *J. Electrochem. Soc.* **163**, 2399–2406 (2016).
124. Wang, H. *et al.* CO_2 and O_2 Evolution at High Voltage Cathode Materials of Li-Ion Batteries: A Differential Electrochemical Mass Spectrometry Study. *Am. Chem. Soc.* 6197–6201 (2014).
125. Haik, O. *et al.* On the Surface Chemistry of LiMO_2 Cathode Materials ($\text{M} = [\text{MnNi}]$ and

- [MnNiCo]): Electrochemical, Spectroscopic, and Calorimetric Studies. *J. Electrochem. Soc.* **157**, A1099 (2010).
126. Jarry, A. *et al.* The Formation Mechanism of Fluorescent Metal Complexes at the $\text{Li}_x\text{Ni}_{0.5}\text{Mn}_{1.5}\text{O}_{4-\delta}$ /Carbonate Ester Electrolyte Interface. *J. Am. Chem. Soc.* **137**, 3533–3539 (2015).
 127. Blyr, A. *et al.* Self-Discharge of $\text{LiMn}_2\text{O}_4/\text{C}$ Li-Ion Cells in Their Discharged State. **145**, (1998).
 128. Aoshima, T., Okahara, K., Kiyohara, C. & Shizuka, K. Mechanisms of manganese spinels dissolution and capacity fade at high temperature. *J. Power Sources* **97–98**, 377–380 (2001).
 129. Du Pasquier, A. *et al.* Mechanism for Limited 55° C Storage Performance of $\text{Li}_{1.05}\text{Mn}_{1.95}\text{O}_4$ Electrodes. *J. Electrochem. Soc.* **146**, 428–436 (1999).
 130. Mijung, N., Lee, Y. & Cho, J. Water Adsorption and Storage Characteristics of Optimized LiCoO_2 and $\text{LiNi}_{1/3}\text{Co}_{1/3}\text{Mn}_{1/3}\text{O}_2$ Composite Cathode Material for Li-Ion Cells. *J. Electrochem. Soc.* **153**, A935 (2006).
 131. Pillot, C. The Rechargeable Battery Market and Main Trends 2016-2025. *Adv. Automot. Batter. Conf.* (2016).
 132. Rougier, A., Saadoun, I., Gravereau, P., Willmann, P. & Delmas, C. Effect of cobalt substitution on cationic distribution in $\text{LiNi}_{1-y}\text{Co}_y\text{O}_2$ electrode materials. *Solid State Ionics* **90**, 83–90 (1996).
 133. Zhecheva, E. & Stoyanova, R. Stabilization of the layered crystal structure of LiNiO_2 by Co-substitution. *Solid State Ionics* **66**, 143–149 (1993).
 134. Zhong, Q. & von Sacken, U. Crystal structures and electrochemical properties of $\text{LiAl}_y\text{Ni}_{1-y}\text{O}_2$ solid solution. *J. Power Sources* **54**, 221–223 (1995).
 135. Guilmard, M., Croguennec, L. & Delmas, C. Thermal Stability of Lithium Nickel Oxide Derivatives. Part II: $\text{Li}_x\text{Ni}_{0.70}\text{Co}_{0.15}\text{Al}_{0.15}\text{O}_2$ and $\text{Li}_x\text{Ni}_{0.90}\text{Mn}_{0.10}\text{O}_2$ ($x = 0.50$ and 0.30). Comparison with $\text{Li}_x\text{Ni}_{1.02}\text{O}_2$ and $\text{Li}_x\text{Ni}_{0.89}\text{Al}_{0.16}\text{O}_2$. *Chem. Mater.* **15**, 4484–4493 (2003).
 136. Ohzuku, T., Ueda, A. & Kouguchi, M. Synthesis and Characterization of $\text{LiAl}_{1/4}\text{Ni}_{3/4}\text{O}_2$ ($R\bar{3}m$) for Lithium-Ion (Shuttlecock) Batteries. **142**, 4033–4039 (1995).
 137. Mohanty, D. *et al.* Modification of Ni-Rich FCG NMC and NCA Cathodes by Atomic Layer Deposition: Preventing Surface Phase Transitions for High-Voltage Lithium-Ion Batteries. *Sci. Rep.* **6**, 1–16 (2016).
 138. Yoon, W. S., Chung, K. Y., McBreen, J. & Yang, X. Q. A comparative study on structural changes of $\text{LiCo}_{1/3}\text{Ni}_{1/3}\text{Mn}_{1/3}\text{O}_2$ and $\text{LiNi}_{0.8}\text{Co}_{0.15}\text{Al}_{0.05}\text{O}_2$ during first charge using in situ XRD. *Electrochem. commun.* **8**, 1257–1262 (2006).
 139. Grenier, A. *et al.* Reaction Heterogeneity in $\text{LiNi}_{0.8}\text{Co}_{0.15}\text{Al}_{0.05}\text{O}_2$ Induced by Surface Layer. *Chem. Mater.* [acs.chemmater.7b02236](https://doi.org/10.1021/acs.chemmater.7b02236) (2017).doi:10.1021/acs.chemmater.7b02236
 140. Sallis, S. *et al.* Surface degradation of $\text{Li}_{1-x}\text{Ni}_{0.80}\text{Co}_{0.15}\text{Al}_{0.05}\text{O}_2$ cathodes: Correlating charge transfer impedance with surface phase transformations. *Appl. Phys. Lett.* **108**, 5–9 (2016).
 141. Ohzuku, T., Yanagawa, T., Kouguchi, M. & Ueda, A. Innovative insertion material of $\text{LiAl}_{1/4}\text{Ni}_{3/4}\text{O}_2$ ($R\bar{3}m$) for lithium-ion (shuttlecock) batteries. *J. Power Sources* **68**, 131–134 (1997).
 142. Julien, C. Electrochemical performances of layered $\text{LiM}_{1-y}\text{M}_y\text{O}_2$ ($M=\text{Ni, Co}$; $M'=\text{Mg, Al, B}$) oxides in lithium batteries. *Solid State Ionics* **135**, 121–130 (2000).
 143. Amin, R., Ravnsbaek, D. B. & Chiang, Y.-M. Characterization of Electronic and Ionic Transport in $\text{Li}_{1-x}\text{Ni}_{0.8}\text{Co}_{0.15}\text{Al}_{0.05}\text{O}_2$ (NCA). *J. Electrochem. Soc.* **162**, A1163–A1169 (2015).
 144. Gabrielli, G. & Axmann, P. Study of $\text{LiNi}_{0.5}\text{Mn}_{1.5}\text{O}_4$ Morphological Features for Reduced Electrolyte Decomposition at High Potential. **163**, 470–476 (2016).
 145. Joachin, H., Kaun, T. D., Zaghbi, K. & Prakash, J. Electrochemical and Thermal Studies

- of Carbon-Coated LiFePO₄ Cathode. *J. Electrochem. Soc.* **156**, A401–A406 (2009).
146. Downie, L. E. & Dahn, J. R. Determination of the Voltage Dependence of Parasitic Heat Flow in Lithium Ion Cells Using Isothermal Microcalorimetry. *J. Electrochem. Soc.* **161**, A1782–A1787 (2014).
 147. Visbal, H. *et al.* The influence of the carbonate species on LiNi_{0.8}Co_{0.15}Al_{0.05}O₂ surfaces for all-solid-state lithium ion battery performance. *J. Power Sources* **269**, 396–402 (2014).
 148. Wang, H., Jang, Y., Huang, B., Sadoway, D. R. & Chiang, Y. TEM Study of Electrochemical Cycling-Induced Damage and Disorder in LiCoO₂ Cathodes for Rechargeable Lithium Batteries. *J. Electrochem. Soc.* **146**, 473 (1999).
 149. Sun, Y.-K., Yoon, C. S., Myung, S.-T., Belharouak, I. & Amine, K. Role of AlF₃ Coating on LiCoO₂ Particles during Cycling to Cutoff Voltage above 4.5 V. *J. Electrochem. Soc.* **156**, A1005 (2009).
 150. Woo, S.-U., Yoon, C. S., Amine, K., Belharouak, I. & Sun, Y.-K. Significant Improvement of Electrochemical Performance of AlF₃-Coated LiNi_{0.8}Co_{0.1}Mn_{0.1}O₂ Cathode Materials. *J. Electrochem. Soc.* **154**, A1005 (2007).
 151. Liu, L. *et al.* Electrochemical and In Situ Synchrotron XRD Studies on Al₂O₃-Coated LiCoO₂ Cathode Material. *J. Electrochem. Soc.* **151**, A1344 (2004).
 152. Mauger, J.-F., Ralbovsky, P., Widawski, G. & Ye, P. *Evaluation of a Complete Coin Cell Battery Using the MMC 274 Nexus with Coin Cell Module.* Netzsch (2013).
 153. Metrohm Ion Analysis. *756/831 KF Coulometer Instructions for Use.* (2003).
 154. Seguin, L. *et al.* Structural study of NiO₂ and CoO₂ as end members of the lithiated compounds by in situ high resolution X-ray powder diffraction. *J. Power Sources* **81–82**, 604–606 (1999).
 155. Kim, Y. J., Cho, J., Kim, T.-J. & Park, B. Suppression of Cobalt Dissolution from the LiCoO₂ Cathodes with Various Metal-Oxide Coatings. *J. Electrochem. Soc.* **150**, A1723 (2003).
 156. Lee, K. T., Jeong, S. & Cho, J. Roles of surface chemistry on safety and electrochemistry in lithium ion batteries. *Acc. Chem. Res.* **46**, 1161–1170 (2013).
 157. A. Blyr *et al.* Self-Discharge of LiMn₂O₄/C Li-Ion Cells in Their Discharged State. *Electrochem. Soc.* **145**, 194–209 (1998).
 158. Martha, S. K. *et al.* A short review on surface chemical aspects of Li batteries: A key for a good performance. *J. Power Sources* **189**, 288–296 (2009).
 159. Täubert, C., Fleischhammer, M., Wohlfahrt-Mehrens, M., Wietelmann, U. & Buhrmester, T. LiBOB as Electrolyte Salt or Additive for Lithium-Ion Batteries Based on LiNi_{0.8}Co_{0.15}Al_{0.05}O₂/Graphite. *J. Electrochem. Soc.* **157**, A721 (2010).
 160. Kim, G.-Y. & Dahn, J. R. ARC Studies of the Effects of Electrolyte Additives on the Reactivity of Delithiated Li_{1-x}[Ni_{1/3}Mn_{1/3}Co_{1/3}]O₂ and Li_{1-x}[Ni_{0.8}Co_{0.15}Al_{0.05}]O₂ Positive Electrode Materials with Electrolyte. *J. Electrochem. Soc.* **161**, A1394–A1398 (2014).
 161. Wang, D. Y. *et al.* A Systematic Study of Electrolyte Additives in Li[Ni_{1/3}Mn_{1/3}Co_{1/3}]O₂ (NMC)/Graphite Pouch Cells. *J. Electrochem. Soc.* **161**, A1818–A1827 (2014).
 162. Wang, Y., Jiang, J. & Dahn, J. R. The reactivity of delithiated Li(Ni_{1/3}Co_{1/3}Mn_{1/3})O₂, Li(Ni_{0.8}Co_{0.15}Al_{0.05})O₂ or LiCoO₂ with non-aqueous electrolyte. *Electrochem. commun.* **9**, 2534–2540 (2007).
 163. Hu, L., Zhang, Z. & Amine, K. Electrochemical investigation of carbonate-based electrolytes for high voltage lithium-ion cells. *J. Power Sources* **236**, 175–180 (2013).
 164. Abraham, D. P., Twisten, R. D. & Balasubramanian, M. Surface changes on LiNi_{0.8}Co_{0.2}O₂ particles during testing of high-power lithium-ion cells. **4**, 620–625 (2002).
 165. Hwang, S., Kim, S. M., Bak, S. M., Cho, B. W. & Chung, K. Y. Investigating Local Degradation and Thermal Stability of Charged Nickel - Based Cathode Materials through Real - Time Electron Microscopy. *Appl. Mater. Interfaces* **6**, 15140–15147 (2014).
 166. Kobayashi, H. *et al.* Investigation of positive electrodes after cycle testing of high-power

- Li-ion battery cells II. An approach to the power fading mechanism using hard X-ray photoemission spectroscopy. *J. Power Sources* **174**, 795–799 (2007).
167. Makimura, Y., Zheng, S., Ikuhara, Y. & Ukyo, Y. Microstructural Observation of $\text{LiNi}_{0.8}\text{Co}_{0.15}\text{Al}_{0.05}\text{O}_2$ after Charge and Discharge by Scanning Transmission Electron Microscopy. *J. Electrochem. Soc.* **159**, A1070–A1073 (2012).
 168. Tsujikawa, T., Yabuta, K., Matsushita, T., Arakawa, M. & Hayashi, K. A Study on the Cause of Deterioration in Float-Charged Lithium-Ion Batteries Using LiMn_2O_4 as a Cathode Active Material. *J. Electrochem. Soc.* **158**, A322–A325 (2011).
 169. Nonaka, T., Okuda, C., Seno, Y., Koumoto, K. & Ukyo, Y. X-ray absorption study on $\text{LiNi}_{0.8}\text{Co}_{0.15}\text{Al}_{0.05}\text{O}_2$ cathode material for lithium-ion batteries. *Ceram. Int.* **34**, 859–862 (2008).
 170. Xia, H., Lu, L., Meng, Y. S. & Ceder, G. Phase Transitions and High-Voltage Electrochemical Behavior of LiCoO_2 Thin Films Grown by Pulsed Laser Deposition. *J. Electrochem. Soc.* **154**, A337 (2007).
 171. Lin, F. *et al.* Surface reconstruction and chemical evolution of stoichiometric layered cathode materials for lithium-ion batteries. *Nat. Commun.* **5**, 3529 (2014).
 172. Chen, K., Unsworth, G. & Li, X. Measurements of heat generation in prismatic Li-ion batteries. *J. Power Sources* **261**, 28–37 (2014).
 173. Saito, Y. *et al.* Comparative study of thermal behaviors of various lithium-ion cells. *J. Power Sources* **97–98**, 688–692 (2001).
 174. Saito, Y., Shikano, M. & Kobayashi, H. Heat generation behavior during charging and discharging of lithium-ion batteries after long-time storage. *J. Power Sources* **244**, 294–299 (2013).
 175. Kobayashi, Y. *et al.* Precise Electrochemical Calorimetry of LiCoO_2 /Graphite Lithium-Ion Cell. *J. Electrochem. Soc.* **149**, A978–A982 (2002).
 176. Lu, W., Belharouak, I., Vissers, D. & Amine, K. In Situ Thermal Study of $\text{Li}_{1+x}[\text{Ni}_{1/3}\text{Co}_{1/3}\text{Mn}_{1/3}]_{1-x}\text{O}_2$ Using Isothermal Micro-calorimetric Techniques. *J. Electrochem. Soc.* **153**, A2147 (2006).
 177. Bang, H., Yang, H., Sun, Y. K. & Prakash, J. In Situ Studies of $\text{Li}_x\text{Mn}_2\text{O}_4$ and $\text{Li}_x\text{Al}_{0.17}\text{Mn}_{1.83}\text{O}_{3.97}\text{S}_{0.03}$ Cathode by IMC. *J. Electrochem. Soc.* **152**, A421 (2005).
 178. Rao, L. Heat-Generation Rate and General Energy Balance for Insertion Battery Systems. *J. Electrochem. Soc.* **144**, 2697 (1997).
 179. Bernardi, D. A General Energy Balance for Battery Systems. *J. Electrochem. Soc.* **132**, 5 (1985).
 180. Thomas, K. E. & Newman, J. Heats of mixing and of entropy in porous insertion electrodes. *J. Power Sources* **119–121**, 844–849 (2003).
 181. Thomas, K. E. & Newman, J. Thermal Modeling of Porous Insertion Electrodes. *J. Electrochem. Soc.* **150**, A176–A192 (2003).
 182. Srinivasan, R., Carson Baisden, a., Carkhuff, B. G. & Butler, M. H. The five modes of heat generation in a Li-ion cell under discharge. *J. Power Sources* **262**, 93–103 (2014).
 183. Lu, W. & Prakash, J. In Situ Measurements of Heat Generation in a Li/Mesocarbon Microbead Half-Cell. *J. Electrochem. Soc.* **150**, A262–A266 (2003).
 184. Lu, W., Belharouak, I., Liu, J. & Amine, K. Thermal properties of $\text{Li}_{4/3}\text{Ti}_{5/3}\text{O}_4/\text{LiMn}_2\text{O}_4$ cell. *J. Power Sources* **174**, 673–677 (2007).
 185. Miyashiro, H. *et al.* Improvement of Degradation at Elevated Temperature and at High State-of-Charge Storage by ZrO_2 Coating on LiCoO_2 . *J. Electrochem. Soc.* **153**, A348–A353 (2006).
 186. Yang, H. & Prakash, J. Determination of the Reversible and Irreversible Heats of a $\text{LiNi}_{0.8}\text{Co}_{0.15}\text{Al}_{0.05}\text{O}_2$ /Natural Graphite Cell Using Electrochemical-Calorimetric Technique. *J. Electrochem. Soc.* **151**, A1222–A1229 (2004).
 187. Lu, W., Yang, H. & Prakash, J. Determination of the reversible and irreversible heats of

- LiNi_{0.8}Co_{0.2}O₂/mesocarbon microbead Li-ion cell reactions using isothermal microcalorimetry. *Electrochim. Acta* **51**, 1322–1329 (2006).
188. Li, J., Downie, L. E., Ma, L., Qiu, W. & Dahn, J. R. Study of the Failure Mechanisms of LiNi_{0.8}Mn_{0.1}Co_{0.1}O₂ Cathode Material for Lithium Ion Batteries. *J. Electrochem. Soc.* **162**, A1401–A1408 (2015).
 189. Downie, L. E., Hyatt, S. R. & Dahn, J. R. The Impact of Electrolyte Composition on Parasitic Reactions in Lithium Ion Cells Charged to 4.7 V Determined Using Isothermal Microcalorimetry. *Electrochem. Soc.* **163**, A35–A42 (2016).
 190. van Bommel, A., Krause, L. J. & Dahn, J. R. Investigation of the Irreversible Capacity Loss in the Lithium-Rich Oxide Li[Li_{1/5}Ni_{1/5}Mn_{3/5}]O₂. *J. Electrochem. Soc.* **158**, A731 (2011).
 191. Downie, L. E., Nelson, K. J., Petibon, R., Chevrier, V. L. & Dahn, J. R. The Impact of Electrolyte Additives Determined Using Isothermal Microcalorimetry. *ECS Electrochem. Lett.* **2**, A106–A109 (2013).
 192. Downie, L. E., Hyatt, S. R., Wright, A. T. B. & Dahn, J. R. Determination of the Time Dependent Parasitic Heat Flow in Lithium Ion Cells Using Isothermal Microcalorimetry. *J. Phys. Chem. C* **118**, 29533–29541 (2014).
 193. Hagh, N. M., Cosandey, F., Rangan, S., Bartynski, R. & Amatucci, G. G. Electrochemical Performance of Acid-Treated Nanostructured LiMn_{1.5}Ni_{0.5}O_{4-δ} Spinel at Elevated Temperature. *Electrochem. Soc.* **157**, A305–A319 (2010).
 194. Tarascon, J. M., Gozdz, A. S., Schmutz, C., Shokoohi, F. & Warren, P. C. Performance of Bellcore's plastic rechargeable Li-ion batteries. *Solid State Ionics* **86–88**, 49–54 (1996).
 195. Kobayashi, Y. *et al.* Precise Electrochemical Calorimetry of LiCoO₂/Graphite Lithium-Ion Cell. *J. Electrochem. Soc.* **149**, A978 (2002).
 196. Watanabe, S., Kinoshita, M. & Nakura, K. Capacity fade of LiNi_(1-x-y)Co_xAl_yO₂ cathode for lithium-ion batteries during accelerated calendar and cycle life test. I. Comparison analysis between LiNi_(1-x-y)Co_xAl_yO₂ and LiCoO₂ cathodes in cylindrical lithium-ion cells during long term storage test. *J. Power Sources* **247**, 412–422 (2014).
 197. Van der Ven, A. First-Principles Evidence for Stage Ordering in Li_xCoO₂. *J. Electrochem. Soc.* **145**, 2149 (1998).
 198. Chang, C. Synthesis and electrochemical characterization of LiMO₂ (M=Ni, Ni_{0.75}Co_{0.25}) for rechargeable lithium ion batteries. *Solid State Ionics* **112**, 329–344 (1998).
 199. Pereira, N. *et al.* Stoichiometric, Morphological, and Electrochemical Impact of the Phase Stability of Li_xCoO₂. *J. Electrochem. Soc.* **152**, A114–A125 (2005).
 200. Kumai, K., Miyashiro, H., Kobayashi, Y., Takei, K. & Ishikawa, R. Gas generation mechanism due to electrolyte decomposition in commercial lithium-ion cell. *J. Power Sources* **81–82**, 715–719 (1999).
 201. Andersson, a. M. *et al.* Surface Characterization of Electrodes from High Power Lithium-Ion Batteries. *J. Electrochem. Soc.* **149**, A1358–A1369 (2002).
 202. Borodin, O. & Jow, T. R. Quantum Chemistry Studies of the Oxidative Stability of Carbonate, Sulfone and Sulfonate-Based Electrolytes Doped with BF₄⁻, PF₆⁻ Anions. *Trans. E C S Soc. Electrochem.* **33**, 77–84 (2011).
 203. Choi, N. S. *et al.* Degradation of spinel lithium manganese oxides by low oxidation durability of LiPF₆-based electrolyte at 60°C. *Solid State Ionics* **219**, 41–48 (2012).
 204. Bi, Y. *et al.* Stability of Li₂CO₃ in cathode of lithium ion battery and its influence on electrochemical performance. *RSC Adv.* **6**, 19233–19237 (2016).
 205. Tasaki, K. *et al.* Solubility of Lithium Salts Formed on the Lithium-Ion Battery Negative Electrode Surface in Organic Solvents. *J. Electrochem. Soc.* **156**, A1019–A1027 (2009).
 206. Campion, C. L., Li, W. & Lucht, B. L. Thermal Decomposition of LiPF₆-Based Electrolytes for Lithium-Ion Batteries. *J. Electrochem. Soc.* **152**, A2327–A2334 (2005).
 207. Ellis, L. D., Xia, J., Louli, A. J. & Dahn, J. R. Effect of Substituting LiBF₄ for LiPF₆ in

- High Voltage Lithium-Ion Cells Containing Electrolyte Additives. *J. Electrochem. Soc.* **163**, 1686–1692 (2016).
208. Imhof, R. & Novak, P. Oxidative Electrolyte Solvent Degradation in Lithium-Ion Batteries - An In Situ Differential Electrochemical Mass Spectrometry Investigation. *J. Electrochem. Soc.* **146**, 1702–1706 (1999).
 209. Saito, Y., Shikano, M. & Kobayashi, H. State of charge (SOC) dependence of lithium carbonate on $\text{LiNi}_{0.8}\text{Co}_{0.15}\text{Al}_{0.05}\text{O}_2$ electrode for lithium-ion batteries. *J. Power Sources* **196**, 6889–6892 (2011).
 210. Lin, C. K., Ren, Y., Amine, K., Qin, Y. & Chen, Z. In situ high-energy X-ray diffraction to study overcharge abuse of 18650-size lithium-ion battery. *J. Power Sources* **230**, 32–37 (2013).
 211. MacNeil, D. D. & Dahn, J. R. The Reaction of Charged Cathodes with Nonaqueous Solvents and Electrolytes: I. $\text{Li}_{0.5}\text{CoO}_2$. *J. Electrochem. Soc.* **148**, A1205 (2001).
 212. Kim, J., Hong, Y., Ryu, S., Kim, M. G. & Cho, J. Washing Effect of a $\text{LiNi}_{0.83}\text{Co}_{0.15}\text{Al}_{0.02}\text{O}_2$ Cathode in Water. *Electrochem. Solid-State Lett.* **9**, A19–A23 (2006).
 213. Matsumoto, K., Kuzuo, R., Takeya, K. & Yamanaka, A. Effects of CO_2 in air on Li deintercalation from $\text{LiNi}_{1-x-y}\text{Co}_x\text{Al}_y\text{O}_2$. *J. Power Sources* **81–82**, 558–561 (1999).
 214. Shizuka, K., Kiyohara, C., Shima, K. & Takeda, Y. Effect of CO_2 on layered $\text{Li}_{(1+z)}\text{Ni}_{(1-x-y)}\text{Co}_{(x)}\text{M}_{(y)}\text{O}_2$ (M = Al, Mn) cathode materials for lithium ion batteries. *J. Power Sources* **166**, 233–238 (2007).
 215. Zhang, X. *et al.* Aging of $\text{LiNi}_{1/3}\text{Mn}_{1/3}\text{Co}_{1/3}\text{O}_2$ cathode material upon exposure to H_2O . *J. Power Sources* **196**, 5102–5108 (2011).
 216. Song, S.-W., Zhuang, G. V & Ross, P. N. Surface Film Formation on $\text{LiNi}_{0.8}\text{Co}_{0.15}\text{Al}_{0.05}\text{O}_2$ Cathodes Using Attenuated Total Reflection IR Spectroscopy. *J. Electrochem. Soc.* **151**, A1162–A1167 (2004).
 217. Dupin, J.-C., Gonbeau, D., Vinatier, P. & Levasseur, A. Systematic XPS studies of metal oxides, hydroxides and peroxides. *Phys. Chem. Chem. Phys.* **2**, 1319–1324 (2000).
 218. Kobayashi, H., Emura, S., Arachi, Y. & Tatsumi, K. Investigation of inorganic compounds on the surface of cathode materials using Li and O K-edge XANES. *J. Power Sources* **174**, 774–778 (2007).
 219. Shizuka, K. *et al.* Effect of CO_2 on Layered $\text{Li}_{(1+z)}\text{Ni}_{(1-x-y)}\text{Co}_{(x)}\text{M}_{(y)}\text{O}_2$ (M = Al, Mn) Cathode Materials. *Trans. E C S Soc. Electrochem.* **11**, 7–13 (2008).
 220. Li, W., McKinnon, W. R. & Dahn, J. R. Lithium Intercalation from Aqueous Solutions. *MRS Proc.* **369**, 69 (1994).
 221. Chen, Z. & Dahn, J. R. Improving the Capacity Retention of LiCoO_2 Cycled to 4.5V by Heat-Treatment. *Electrochem. Solid-State Lett.* **7**, A11 (2004).
 222. Armstrong, a. R. *et al.* Demonstrating oxygen loss and associated structural reorganization in the lithium battery cathode $\text{Li}[\text{Ni}_{0.2}\text{Li}_{0.2}\text{Mn}_{0.6}]\text{O}_2$. *J. Am. Chem. Soc.* **128**, 8694–8698 (2006).
 223. Faenza, N. V. *et al.* Electrolyte-Induced Surface Transformation and Transition-Metal Dissolution of Fully Delithiated $\text{LiNi}_{0.8}\text{Co}_{0.15}\text{Al}_{0.05}\text{O}_2$. *Langmuir* **acs.langmuir.7b00863** (2017). doi:10.1021/acs.langmuir.7b00863
 224. Ménétrier, M. *et al.* ^7Li and ^1H MAS NMR Observation of Interphase Layers on Lithium Nickel Oxide Based Positive Electrodes of Lithium-Ion Batteries. *Electrochem. Solid-State Lett.* **7**, A140 (2004).
 225. Aurbach, D. *et al.* The Study of Electrolyte Solutions Based on Ethylene and Diethyl Carbonates for Rechargeable Li Batteries. *J. Electrochem. Soc.* **142**, 2882 (1995).
 226. Ward, J. W. A Spectroscopic Study of the Surface of Zeolite Y . II. Infrared Spectra of Structural Hydroxyl Groups and Adsorbed Water on Alkali , Alkaline Earth , and Rare Earth Ion-Exchanged Zeolites. *J. Phys. Chem.* **73**, 4211–4223 (1968).

227. Parker, S. F., Refson, K., Bewley, R. I. & Dent, G. Assignment of the vibrational spectra of lithium hydroxide monohydrate, $\text{LiOH} \cdot \text{H}_2\text{O}$. **941**, 1–8 (2011).
228. Jones, L. H. The Infrared Spectra and Structure of LiOH , $\text{LiOH} \cdot \text{H}_2\text{O}$ and the Deuterium Species. Remark on Fundamental Frequency of OH^- . **217**, (2011).
229. Wickersheim, K. A. Infrared Absorption Spectrum of Lithium Hydroxide. *J. Chem. Phys.* **31**, 863–869 (1959).
230. Aurbach, D. The Surface Chemistry of Lithium Electrodes in Alkyl Carbonate Solutions. *J. Electrochem. Soc.* **141**, L1 (1994).
231. Mosqueda, H. a, Vazquez, C., Bosch, P. & Pfeiffer, H. Chemical Sorption of Carbon Dioxide (CO_2) on Lithium Oxide (Li_2O). *Chem. Mater.* **18**, 2307–2310 (2006).
232. Kozen, A. C. *et al.* Atomic layer deposition and in situ characterization of ultraclean lithium oxide and lithium hydroxide. *J. Phys. Chem. C* **118**, 27749–27753 (2014).
233. Shkrob, I. A. *et al.* Chemical Weathering of Layered Ni-Rich Oxide Electrode Materials : Evidence for Cation Exchange. **164**, (2017).
234. Grosvenor, A. P., Biesinger, M. C., Smart, R. S. C. & McIntyre, N. S. New interpretations of XPS spectra of nickel metal and oxides. *Surf. Sci.* **600**, 1771–1779 (2006).
235. Sun, Y., Song, X., Wang, J. & Yu, J. Preparation of Li_2CO_3 by gas-liquid reactive crystallization of LiOH and CO_2 . *Cryst. Res. Technol.* **47**, 437–442 (2012).
236. Yi, W., Yan, C. & Ma, P. Crystallization kinetics of Li_2CO_3 from LiHCO_3 solutions. *J. Cryst. Growth* **312**, 2345–2350 (2010).
237. Liu, H., Yang, Y. & Zhang, J. Reaction mechanism and kinetics of lithium ion battery cathode material LiNiO_2 with CO_2 . *J. Power Sources* **173**, 556–561 (2007).
238. Moshtev, R., Zlatilova, P., Vasilev, S., Bakalova, I. & Kozawa, A. Synthesis, XRD characterization and electrochemical performance of overlithiated LiNiO_2 . *J. Power Sources* **81–82**, 434–441 (1999).
239. Amatucci, G. G., Tarascon, J. M., Larcher, D. & Klein, L. C. Synthesis of electrochemically activer LiCoO_2 and LiNiO_2 at 100°C . *Solid State Ionics* **84**, 169–180 (1996).
240. Chen, Z., Lu, Z. & Dahn, J. R. Staging Phase Transitions in Li_xCoO_2 . *J. Electrochem. Soc.* **149**, A1604 (2002).
241. Croguennec, L., Poullierie, C. & Delmas, C. NiO_2 Obtained by Electrochemical Lithium Deintercalation from Lithium Nickelate: Structural Modifications. *J. Electrochem. Soc.* **147**, 1314 (2000).
242. Bak, S. M. *et al.* Correlating structural changes and gas evolution during the thermal decomposition of charged $\text{Li}_x\text{Ni}_{0.8}\text{Co}_{0.15}\text{Al}_{0.05}\text{O}_2$ cathode materials. *Chem. Mater.* **25**, 337–351 (2013).
243. Jang, Y., Huang, B., Wang, H., Sadoway, D. R. & Ceder, G. $\text{LiAl}_y\text{Co}_{1-y}\text{O}_2$ ($R\bar{3}m$) Intercalation Cathode for Rechargeable Lithium Batteries. *J. Electrochem. Soc.* **146**, 862–868 (1999).
244. Faenza, N. V *et al.* Growth of Ambient Induced Surface Impurity Species on Layered Positive Electrode Materials and Impact on Electrochemical Performance. *J. Electrochem. Soc.* **164**, A3727–A3741 (2017).
245. Kalyani, P., Kalaiselvi, N., Renganathan, N. G. & Raghavan, M. Studies on $\text{LiNi}_{0.7}\text{Al}_{0.3-x}\text{Co}_x\text{O}_2$ solid solutions as alternative cathode materials for lithium batteries. *Mater. Res. Bull.* **39**, 41–54 (2004).
246. Kim, J. & Amine, K. A comparative study on the substitution of divalent, trivalent and tetravalent metal ions in $\text{LiNi}_{1-x}\text{M}_x\text{O}_2$ ($\text{M} = \text{Cu}^{2+}$, Al^{3+} and Ti^{4+}). **104**, 33–39 (2002).
247. Buta, S., Morgan, D., Ven, A. Van Der, Aydinol, M. K. & Ceder, G. Phase Separation Tendencies of Aluminum-Doped Transition-Metal Oxides ($\text{LiAl}_{1-x}\text{M}_x\text{O}_2$) in the α - NaFeO_2 Crystal Structure. **146**, 4335–4338 (1999).
248. Chen, C. H. *et al.* Aluminum-doped lithium nickel cobalt oxide electrodes for high-power

- lithium-ion batteries. *J. Power Sources* **128**, 278–285 (2004).
249. Croguennec, L. *et al.* Segregation tendency in layered aluminum-substituted lithium nickel oxides. *Chem. Mater.* **21**, 1051–1059 (2009).
 250. Kang, K. & Ceder, G. Factors that affect Li mobility in layered lithium transition metal oxides. *Phys. Rev. B - Condens. Matter Mater. Phys.* **74**, 1–7 (2006).
 251. Kim, J. R. & Amatucci, G. G. Structural and Electrochemical Investigation of Na⁺ Insertion into High-Voltage Spinel Electrodes. *Chem. Mater.* **27**, 2546–2556 (2015).
 252. Danek, V., Tarniowy, M. & Suski, L. Kinetics of the $\alpha \rightarrow \gamma$ phase transformation in LiAlO₂ under various atmospheres within the 1073–1173 K temperatures range. *J. Mater. Sci.* **39**, 2429–2435 (2004).
 253. Lin, S.-P., Fung, K.-Z., Hon, Y.-M. & Hon, M.-H. Effect of Al Addition on Formation of Layer-Structured LiNiO₂. *J. Solid State Chem.* **167**, 97–106 (2002).
 254. Tarascon, J. M. *et al.* In Situ Structural and Electrochemical Study of Ni_{1-x}Co_xO₂ Metastable Oxides Prepared by Soft Chemistry. *J. Solid State Chem.* **147**, 410–420 (1999).
 255. Jeong, S., Park, S. & Cho, J. High-Performance, Layered, 3D-LiCoO₂ Cathodes with a Nanoscale Co₃O₄ Coating via Chemical Etching. *Adv. Energy Mater.* **1**, 368–372 (2011).
 256. Delmas, C. *et al.* Lithium batteries: a new tool in solid state chemistry. *Int. J. Inorg. Mater.* **1**, 11–19 (1999).
 257. Yoon, W. S., Hanson, J., McBreen, J. & Yang, X. Q. A study on the newly observed intermediate structures during the thermal decomposition of nickel-based layered cathode materials using time-resolved XRD. *Electrochem. commun.* **8**, 859–862 (2006).
 258. Tatsumi, K. *et al.* Local atomic and electronic structures around Mg and Al dopants in LiNiO₂ electrodes studied by XANES and ELNES and first-principles calculations. *Phys. Rev. B - Condens. Matter Mater. Phys.* **78**, 1–8 (2008).
 259. Hy, S., Felix, F., Rick, J., Su, W. & Hwang, B. J. Direct In situ Observation of Li₂O Evolution on Li-Rich High-Capacity Cathode Material, Li[Ni_xLi_{(1-2x)/3}Mn_{(2-x)/3}]O₂ (0 ≤ x ≤ 0.5). *J. Am. Chem. Soc.* **2**, (2014).
 260. MacNeil, D. D. & Dahn, J. R. The Reactions of Li_{0.5}CoO₂ with Nonaqueous Solvents at Elevated Temperatures. *J. Electrochem. Soc.* **149**, A912–A919 (2002).
 261. Ceder, G. *et al.* Identification of cathode materials for lithium batteries guided by first-principles calculations. *Nature* **392**, 694–696 (1998).
 262. Dahn, J., Fuller, E., Obrovac, M. & Von Sacken, U. Thermal-Stability of Li_xCoO₂, Li_xNiO₂ and λ-MnO₂ and Consequences for the Safety of Li-Ion Cells. *Solid State Ionics* **69**, 265–270 (1994).
 263. Furushima, Y., Yanagisawa, C., Nakagawa, T., Aoki, Y. & Muraki, N. Thermal stability and kinetics of delithiated LiCoO₂. *J. Power Sources* **196**, 2260–2263 (2011).
 264. Yang, L., Ravdel, B. & Lucht, B. L. Electrolyte Reactions with the Surface of High Voltage LiNi_{0.5}Mn_{1.5}O₄ Cathodes for Lithium-Ion Batteries. *Electrochem. Solid-State Lett.* **13**, A95 (2010).